Università degli Studi di Pavia Dipartimento di Scienze della Terra e dell'Ambiente

SCUOLA DI ALTA FORMAZIONE DOTTORALE MACRO-AREA SCIENZE E TECNOLOGIE

DOTTORATO DI RICERCA IN SCIENZE DELLA TERRA E DELL'AMBIENTE

Joan Lloret Quirante

Stratigraphic-sedimentary reconstruction in the Permian-Triassic succession of the Central-Eastern Southern Pyrenees: a multi-disciplinary approach

Anno Accademico 2015-2018

Ciclo XXXI

Coordinatore
Prof. Roberto Sacchi Tutors

Tutors

Prof. Ausonio Ronchi

Dr. José López Gómez

Co-tutor
Dr. Raúl De la Horra del Barco

*Als meus pares i a l'Andrea,
per el seu suport i amor constant.*

Acknowledgements

En la realización de esta tesis he tenido el placer de estar en el Departamento de Geodinámica, Estratigrafía y Paleontología en la Facultad de Ciencias Geológicas de la Universidad Complutense de Madrid, como también en el Igeo (CSIC-UCM, Madrid, España). Muchas gracias por acogerme en vuestras instalaciones y vuestra generosidad. Habría sido imposible realizar esta tesis sin la disponibilidad ni sin su profesionalidad. Un especial agradecimiento al subdirector del departamento Dr. Agustín Pieren Pidal y al vicedirector del IGEO el Dr. José López Gómez. A la Dra. Nieves Meléndez, que sin ella yo no habría empezado la tesis. También agradecer a los técnicos Aitor, Juan Carlos, Aida, …, de ambas instituciones que sin su dedicación nada hubiera sido posible.

Una mención especial merecen los colaboradores de los artículos y congresos derivados de esta tesis, Dr. Alfredo Arche, Dr. Bienvenido Díez y Dr. Gretter. No puedo olvidar a Manuel Juncal, con él hemos compartido trabajo de campo, congresos, publicaciones y las pesadillas de la tesis. Lejos de ser un gran colaborador has sido un gran apoyo y un inestimable amigo con quien espero seguir trabajando.

All'interno del Dipartimento di Scienze della Terra e dell'Ambiente ho incontrato un gruppo di persone fantastiche che mi hanno accolto in modo molto meraviglioso: sono venuto da un paese diverso ma non mi hanno mai fatto sentire straniero. Ho conosciuto i compagni del XXXI ciclo Niccolò Menegoni e Mattia Mazzucchelli un lontano 27 settembre del 2015 e a partire da allora abbiamo fatto un cammino comune, dividendo difficoltà e allegria. Sempre pronti a condividere con me un caffè o una birra. Grazie anche a tutti gli altri dottorandi e borsisti per le belle chiacchierate durante i pranzi o le cene e l'appoggio reciproco che ci siamo dati: Roberta Occhipinti, Chiara Amadori, Riccardo Inama, Yuri Panara, Alessandro Bonanno, Pierre Mueller, Aldo Bertone , Clausssi e Marchionda, tra tutti. Sono stati mesi impegnativi, però sappiate che ne è valsa la pena! Voglio anche ringraziare il magnifico gruppo di ricercatori con cui ho condiviso interessanti chiacchierate nonchè preoccupazioni: Dr. Alessio Sanfilippo, Dr. Matteo Maino, Dr. Antonio Langone e Dr. Massimiliano Bordoni.

En Madrid encontré un grupo excelente de doctorandos, becarios y excompañeros de Máster: Sonia Campos, Laura Martínez Parro, Maialen López, Dra. Violeta Borruel Abadia, Carlos Bueno, Francisco

Index

Summary

The research in this PhD thesis deals with the stratigraphic record of the Central-Eastern Southern Pyrenean continental basins of the Late Carboniferous – Early-Middle Triassic age. These basins were located in the Western peri-Tethyan domain. The Pyrenean and other basins located in the current Western Europe were supposed to develop under the same tectono-sedimentary regime and shape, and with a similar paleoenvironmental scenario. This work proposes a multidisciplinary study to unravel the complex tectonic and depositional record in this area, provide some hints on its chronostratigraphy and reconstruct the paleoenvironments that characterized the continental successions in this crucial time-frame.

The Upper Carboniferous-Lower Triassic sedimentary record in the Central-Eastern Southern Pyrenees is organized in five formal stratigraphic units, some of them bounded by angular unconformities. Due to the complex geological setting, several approaches have been used together. The adopted method was selected in order to obtain the most detailed information and reconstruct the original conditions of these basins and their later refill. The main approach followed was based on the stratigraphy and the sedimentology studies. On this basis, other approaches, such as palynology, paleopedology, isotopic analyses and clay mineralogy from claystone, were attempted in both the Erill Castell-Estac Basin and the neighbouring basins (Castejón-Laspaúles, Gramós and Castellar-Camprodón). Detailed field made it possible to define facies, facies associations and the architectural elements of the deposits. Detailed syn-sedimentary faulting was also measured with the scope to constrain the relationship between the sedimentation and the tectonics. When the stratigraphic units were clearly characterized and their vertical and lateral relations were well established, a detailed sampling was performed for the other approaches used. The stratigraphic units were then joined in

sedimentary cycles (SC) bounded by angular unconformities. The sedimentary record of each SC shows significant changes in the paleoenvironmental conditions. The first sedimentary cycle (Late Carboniferous-Early Permian) is characterized by isolated sub-basins and it is strongly linked with intense volcanic activity. In the upper part of this cycle, fluvial and lacustrine sediments were deposited in a transtensive tectonic context, and again during a strong volcanic outpouring. In the second sedimentary cycle (Middle Permian), the sub-basins started to merge due to the continuation of transtensive tectonic context. The main deposits in this cycle represent playa-lake and fluvial environments with negligible volcanic influence. Finally, after a long-lasting stratigraphic gap, the third sedimentary cycle (Early-Middle Triassic) is represented by meandering fluvial systems with isolated lacustrine environments and no volcanic influence.

The age of the units was constrained thanks to their newly discovered palynological content. These fossils represent an important biostratigraphic tool for correlation across the SW European basins. The age obtained by one sporomorph association found in the basal Grey Unit (SC1) was Gzhelian (Upper Carboniferous). The spores and pollen contained in the Transition Unit (SC1) indicate an Asselian age (Early Permian). The second sedimentary cycle is represented by the Lower Red Unit (LRU), which was assigned to an Artinskian age, based on palynological data. Finally, the Lower Triassic deposits contained pollen and spores too, and the age ascribed was upper-middle Anisian.

The pedogenic activity during the development of the Central-Eastern Pyrenean basins also revealed important information. Even though paleopedology is poorly used, it served to achieve paleoclimatic and paleoenvironmental indicators. The study of paleosoils enabled me to understand the relationship between tectonics, vegetation, climate and the paleotopography of the Permian-Triassic basins. The presence of Andisols, Alfisols, Aridisols and Entisols during the deposition of the Lower Red Unit,

in the middle Cisuralian, indicates wet and dry climatic conditions (even monsoonal) due to the presence of humid and dry paleosols. During the late Cisuralian-early Guadalupian, represented by the Upper Red Unit deposition, the climate inferred was more monsoonal to because of the presence of Entisols, Alfisols and Andisols. During the Anisian, represented by the Buntsandstein facies deposition, Ultisols and Entisols were the most representative paleosols, leading to infer more arid climatic conditions. The pedogenic carbonate content made it possible to analyze the isotopic signature of $\delta^{13}C$ and $\delta^{18}O$. This carbonate was in balance with the atmosphere when it precipitated, and so its values are indicative of atmospheric changes. The results obtained show different isotopic signatures for each of the pedotypes studied, indicating variability in the pedogenesis and corroborating the pedogenic and sedimentary diagnosis in the field. Moreover, the isotopic values indicate a general trend, as the most positive values were in the deepest horizons. On the whole, the overall isotopic composition of Permian and Triassic paleosols in the Central-Eastern Southern Pyrenees fit well with the paleoenvironmental reconstructions provided by sedimentary facies. Furthermore, the isotopic compositions show significant differences between the isotopic composition of the Permian and Triassic carbonates. The findings obtained in this study fit with the global $\delta^{13}C$ curve for those times.

Clay mineralogy from several claystone layers in the studied stratigraphic units was another tool used in this research to obtain possibly valuable information on the variations in mineralogical associated with different climate conditions. It was observed that the basal units (GU and TU) contain halloysite mineral which, together with high percentages of other minerals like felspars (5-10%), is linked to strong volcanic activity under humid conditions. Quartz is present (15-40%) in all the units, indicating the intense erosion of the Palaeozoic basement during all the basin's development. The Permian units

(Transition, Lower Red and Upper Red) contain calcite (5-15%), which was probably related to pedogenic processes linked with semi-humid environments. The Lower Triassic claystones indicate an increase in quartz, probably related to another important tectonic event and renewed erosion of the Palaeozoic basement, linked to a more widespread extensional tectonic phase. In this latter unit, the absence of calcite confirms the more arid conditions.

All the results and observations contained within this PhD thesis improve the knowledge of the Central-Eastern Southern Pyrenees basin (which is composed of several smaller basins) and its geological history during the pristine phases of Pangea break-up. This initially started during the development of intermontane continental basins in the inner areas of the Hercynian belt and latter evolved as a sedimentary response to different tectonics regimes. The fossil content, particularly microfloras, may provide valuable chronostratigraphic information to correlate and compare the SW European basins' sedimentary record. An understanding of the paleogeographical location of these basins and the time which they were interconnected could shed more light to understand plate movements during the Late Carboniferous to Middle Triassic, a crucial time-interval represented by the break-up of Pangea supercontinent. The field evidences, provided by facies analysis and tectonic analysis, matches well with the isotopic content of paleosoils and the analysis of clay minerals analysis in order to reach a more accurate paleoenvironmental reconstruction for the studied time-interval.

1. Introduction

1.1 Preface

This PhD thesis has been realized in the Earth Science and Environmental Department of the University of Pavia and, in part (5 months) in the Igeo (CSIC-UCM, Madrid, Spain) and the Stratigraphy Department of the Complutense University (Madrid, Spain). It was supervised by Dr. Ausonio Ronchi from the University of Pavia, Dr. José López Gómez from the Igeo (CSIC-UCM, Madrid, Spain) and Dr. Raúl de la Horra Del Barco (University Complutense of Madrid, Spain). The author of this thesis received a PhD student grant from the University of Pavia and logistic and financial support from the CGL2014-52699-P project of the Ministerio de Economía y Competitividad (Spanish government). The fieldwork (more than 3 months) was carried out in the Central-Eastern Spanish Pyrenees in different periods during the PhD. Moreover, some of the results of this PhD thesis have been presented in two international congresses and other two national congresses.

1.2 General introduction

The Paleozoic-Mesozoic transition is one of the most studied geological events, as several factors made this timespan crucial for the life in the seas and emerging lands, and the paleoclimate and paleogeography implications for the entire world, such as the configuration of Pangea. The severest mass extinction in Earth history occurred precisely at the very end of the Permian (e.g., Erwin, 1994; Benton and Twitchett, 2003; Benton and Newell, 2014; Fig.1.2.1) and it was preceded by another major biotic crisis, at the end of the Guadalupian (Isozaki and Aljinović, 2009; Isozaki et al., 2011; Jost et al., 2014). About 90% of the marine genera became extinct (Erwin, 1994; Yin et al., 2007), with special severity in ammonoids (98%) and marine invertebrates (91%). The terrestrial biota was not exempt from extinction, as a 75% drop in biodiversity and a 62.9% loss in terrestrial families have been identified (Fig. 1.2.1; Benton, 1995; Benton and Newell, 2014). Plants and insects were also affected: for example, the Glossopteris flora of
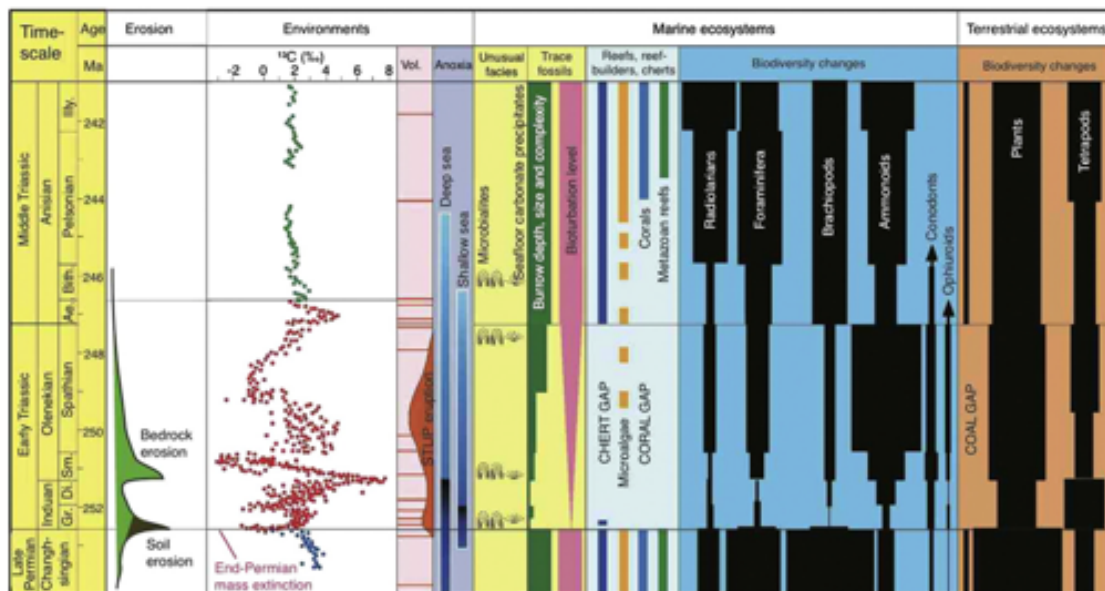
Figure 1.2.1. Environmental changes and biodiversity variations from the latest Permian to Middle Triassic. Arrows indicated on the conodont and ophiuroid range bars show increasing data into the Middle Triassic. The 'Erosion' column indicates hypothesised erosion of soil and bedrock from land to sea, after Algeo et al. (2011). Stratigraphic dates, carbon isotope fluctuations, Siberian Traps large igneous province (STLIP) eruption, anoxia ranges, trace fossil data, and reef, reef builder, chert and coal gap data are given in full detail in Chen and Benton (2012). Abbreviations: Ae., Aegean; Bith., Bithynian; Di., Dienerian; Gr., Griesbachian; Illy., Illyrian; Sm., Smithian; and Vol., volcanism. From Benton and Newell (2014).

Gondwana totally disappeared (Retallack, 1995), although vascular plants tended to be less affected by climatic and environmental changes (Cascales-Miñana and Cleal, 2014).

The Siberian Traps volcanic eruption is one of the most accepted explanations of the Permian-Triassic mass extinction (Wignall, 2001; Benton and Twitchett, 2003; Knoll et al., 2007; Retallack, 2013). Huge eruptions generated an increase in CO_2, SO_2 and thermogenic methane, resulting in various atmospheric and climatic changes (Wignall, 2001; Algeo et al., 2011; Benton and Newell, 2014; Fig. 1.2.2). The consequences of these gas increases were soil erosion produced by acid rain, global warming and an accelerated continental weathering. These factors not only affected the biosphere as the rocks deposited in this timespan also left several indicators. One piece of evidence linked to the biota crisis is the absence of coal over the Early Triassic (Veevers et al., 1994; Retallack et al., 1996), although the depositional systems which are sensitive to climatic conditions were affected (Arche and Lopez-Gomez, 2005; Smith and Botha, 2005). The
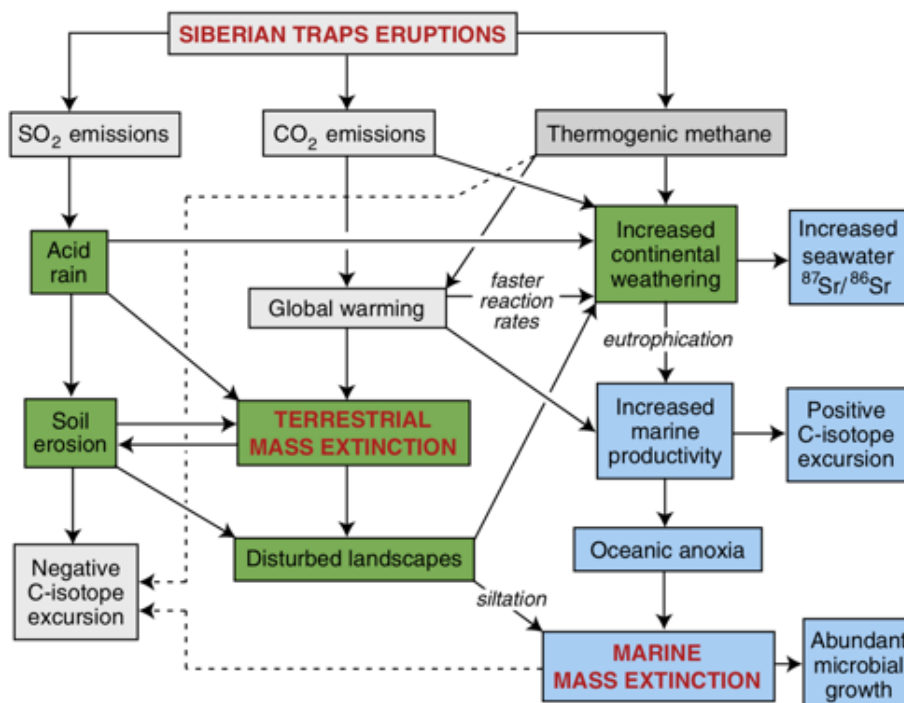
Figure 1.2.2. Model of likely environmental consequences of the Siberian Traps eruptions, showing the flows of consequences of global warming and acid rain. Causal links are indicated by solid arrows, and possible second-order controls on the negative carbonate C-isotope excursion at the EPME are indicated by dashed lines. Modified from Algeo et al. (2011), and based on an earlier version by Wignall (2001). From Benton and Newell (2014).

fluvial style through the P-T change substantially in several locations (e.g., Iberian Ranges, Urals, Karoo, China, India), from sandy-dominated meandering systems in the Late Permian to braided fluvial systems in the Early Triassic (Benton and Newell, 2014 and references therein). The Early to Middle Permian lacustrine deposits generally disappeared almost totally when the Triassic began. Another depositional feature of the PT boundary influenced by the climatic was the appearance of widespread aeolian facies in the late Early Triassic (e.g., Iberian Ranges, East Pyrenees, South Urals and Central Europe (Bourquin et al., 2007; 2011; Borruel-Abadia et al., 2015).

During the Late Carboniferous-Early Permian timespan the South-Western paleoeuropean paleogeographic domain (Fig. 1.2.3) was affected by the late- to post-Variscan tectonic phases and the subsequent chain collapse and dismemberment (Matte, 1986; Zwart, 1986; Echtler and Malavieille, 1990). Later on, the regional context was constrained by the global plate re-organization during the Early to Late Permian till the Triassic rifting (Puigdefàbregas and Souquet, 1986; Van Wees et al., 1998; Muttoni et al., 2009) characterized by a dextral mega-shear zone. The result was the birth of several small and large intramontane continental basins located in the current Western European area, in, for example, Sardinia, the Southern Alps, the Iberian Ranges, Southern and Central France and the Pyrenees (Fig. 1.2.4). These basins present similar sedimentological, stratigraphic, tectonic and paleontological features, which have given rise to tentative correlations (Cassinis et al., 2000; Roscher and Schneider, 2005; Virgili et al., 2006; Bourquin et al., 2011; Cassinis et al., 2012; Gretter et al., 2015; Lloret et al., 2018; Juncal et al., 2018; Fig. 1.2.4). However, the basin-fill of these dispersed basins often changes from on to the other (Gretter et al., 2015; Mujal et al., 2017b; Lloret et al., 2018) because of the intrinsic complexity of active tectonic basins, and this hinders and complicates any stratigraphic correlations. Furthermore, as in the Pyrenees, the

subsequent Alpine orogeny deformed the original configuration, thereby generating more structural complication.
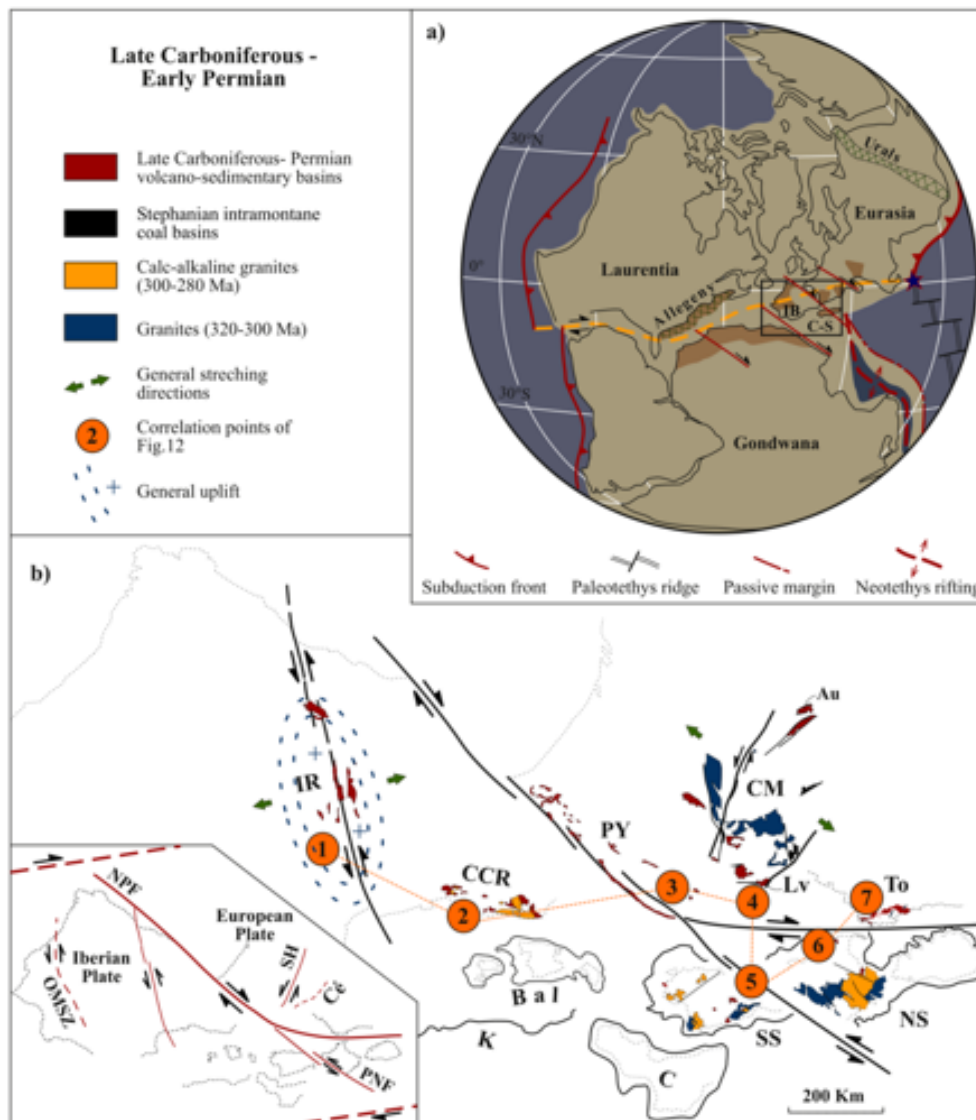
Figure 1.2.3. Palaeogeodynamic scheme by the Late Carboniferous-Early Permian times, redrawn after Domeier et al. (2012), and Matte (2001). a) Geometry of the Variscan belt (brown field). The dashed yellow line traces the dextral mega-shear zone affecting the Variscan chain during the time interval studied. The Early-Permian configuration of the stable transform-trench– ridge junction has also been highlighted by the blue star (Cassinis et al., 2012). b) Detail of the Southwestern European sector. The main strike–slip structures (Faure et al., 2009; De Vicente et al., 2009) are sketched in the little marginal box: Cé: Cévennes Fault; NPF: North Pyrenean Fault; PNF: Permian Nuoro Fault; SH: Sillon–Houiller Fault. OMSZ: Ossa–Morena Zone. Major basins and localities: Ar.B.: Aragonese Branch; Au: Autun Basin; Bal: Balearic Islands; C: Calabria; Cas.B.: Castilian Branch; CCR: Catalan Coastal Ranges; CM: Central Massif; IR: Iberian Ranges; K: Kabilies; Lv: Lodève Basin; NS: North Sardinia; PY: Pyrenees; SS: South Sardinia; To: Toulon–Cuers. From Gretter et al. (2015).

1.3. Aims of the project

The general aim of this thesis is to shed more light on some of the less studied Central-Eastern Spanish Pyrenean basins (which belong to the South-Western paleoeuropean domain), particularly the Erill Castell-Estac Basin. Even though some authors have studied single Pyrenean post-Variscan basins in detail, only a few conducted any of the multidisciplinary research involving the neighboring basins in a larger sector that permits regional correlation and more global inferences on a wider scale. In this thesis, tectono-stratigraphic, sedimentologic, paleopedologic and paleontologic insights have been used to understand the evolution of various Central-Eastern Pyrenean basins from the incipient Carboniferous post-Variscan phases to their final development in the Early-Middle Triassic in the Southern Pyrenean context.

The main approach of this thesis is stratigraphic and sedimentological: while the stratigraphic context was studied for all the basins, the sedimentology was studied in detail in the Erill Castell-Estac basin because it had been poorly described in this respect and the absance inside this trough of one of the stratigraphic unit (which is known in every other Pyrenean basin) made it the least completely understood and subject ripe for research. The aim of my sedimentary study was to understand how the deposits are organized and evaluate the paleoenvironmental conditions present during the deposition.

The Upper Carboniferous-Lower Triassic continental deposits in the Central-Eastern Southern Pyrenees were formally organized for 40 years into different units (Gisbert, 1981). A renewed and detailed sedimentological description of the single stratigraphic units and their vertical and lateral relationships has been presented in this research in order to distinguish the depositional facies and sedimentary styles of the considered basins in question over time, in the light of modern methodologies and concepts. Complex syn-depositional tectonic activity occurred during the deposition of

the sediments. Understanding the interplay between tectonics and stratigraphy made it possible to depict a tectono-stratigraphic model evolution. This approaches was used for the first time for the Erill Castell-Estac Basin, which actually represents a very good example for to unravelling the history of a basin. Once the basic stratigraphic relationships and paleoenvironments had been recognized, different approaches were been applied to the other Upper Carboniferous-Lower Triassic basins in the Central and Eastern Pyrenees. From this viewpoint, the analysis of paleosols and the study of clay mineralogy in the four studied basins can be considered as significant tools to provide key information at a wider scale about paleoclimatic conditions and regional correlations. Moreover, since the Permian and Triassic red beds proved difficult to distinguish in many cases due to the similarity of their facies, the characterization of the formal units' paleosols and clay mineralogy content provided features that allowed them to be distinguished unequivocally.

Another important objective of this research was to understand the pedogenic features of the paleosols located in the sedimentary record. This information was used in an attempted to constrain both paleoenvironmental and paleoclimatic conditions. Furthermore, isotopic analysis makes it possible to corroborate field diagnosis and provide the first isotopic analysis for the Late Variscan basins in the Pyrenees.

Finally, the paleontological content in the continental deposits also provides funamental information makes it possible to constrain the ages of the stratigraphic units more exactly. Accodingly, a total number of 67 samples were collecte for pollen analysis in the four basins. The samples were processed in collaboration with palynological experts from Vigo University (Spain) and several palynological associations were identified. This constitutes a significant contribution to the chronostratigraphy of the studied Pyrenean Permo-Carboniferous successions and widens the knowledge of the Western Paleotethys floristic associations.

1.4 Study area and geographic setting

The Pyrenees are a 430 km-long mountain range in the North of the Iberian Peninsula (Fig. 1.4.1). The studied sector is located on the Central-Eastern Southern side of the Pyrenees, encompassing about 170 km in the W-E direction. The Spanish Pyrenees are divided in two main geological zones, the axial one bearing the oldest rocks (early-middle Palaeozoic) and the southern part where the Mesozoic-Cenozoic cover occurs. The post-Variscan rocks represent the youngest geological record belonging to the axial zone. This is characterized by intense folding and thrusting generated by both the Variscan and the Alpine orogeny. The four studied basins (Castejón-Laspaúles, Erill Castell-Estac, Gramós and Camprodón-Castellar) present an elongate morphology following the E-W Pyrenees direction.

The main one basin studied is the Erill Castell-Estac, which is located in the Central Southern Pyrenees (squared in Fig. 1.4.1.). The total length of this basin is about 50 km and the highest topographical point is Tossal de Tuiro with 1766 meters of elevation. The Gramós and Camprodón-Castellar basins are located to the East, in the Eastern Catalan Pyrenees respectively. The fourth basin is the Castejón-Laspaúles which lies westward (Central Southern Pyrenees), in the Aragón region.
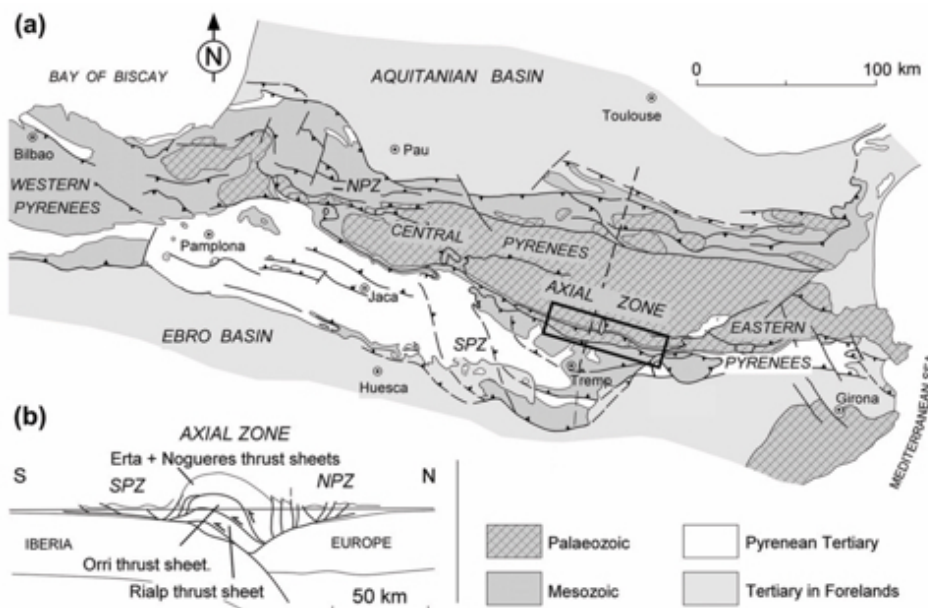
Figure 1.4.1. Geological map of the Pyrenees (a) and the tectonic interpretation of the Axial Zone (b). Modified from Saura and Teixell (2006).

The four basins and the stratigraphic sections (from West to East) carried out in this thesis are summarized in the Table 1.4.1, along with information about the approaches used in each section.

BASIN	SECTION	STRATIGRAPHY	SEDIMENTOLOGY	SYN-SED. TECTONICS	PEDOGENESIS	CLAY MINERALOGY	ISOTOPS	PALYNOLOGY
CASTEJÓN-LASPAÚLES	Villarrué-Suils	X			X	X	X	X
	Igüerri	X	X	X				X
	Gotarta	X	X	X	X	X	X	X
	Malpàs	X	X	X				
ERILL CASTELL-ESTAC	Castellars	X	X	X	X	X	X	X
	Sas	X	X	X	X	X	X	
	La Mola d'Amunt	X	X	X	X	X	X	X
	Collada de Pui Pavaller	X	X	X				
	Roca de les Creus	X	X	X				
	Estac	X	X	X				
	Baro	X	X	X				
GRAMÓS	Pallarols	X			X	X	X	X
CAMPRODÓN-CASTELLARS	Castellar de N'Hug	X			X	X	X	X

Table 1.4.1. Approaches carried out in each section of the basins studied.

1.5 Geological setting

The Late Palaeozoic sedimentary sequences of the Central-Eastern Southern Pyrenees filled basins whose development was primarily framed by late- to post-Variscan orogenic evolution. The Basins' inception began in the Late Carboniferous and their structuration continued throughout the Permian, within a transtensional regime that become more and more extensional, affecting the entire Variscan belt (e.g., Van Den Driessche and Brun, 1989; Echtler and Malavieille, 1990; Burg et al., 1994; Gaggero et al., 2007, 2017; Casini and Oggiano, 2008). More specifically, the overall geodynamic setting was a dextral megashear, with transtensional kinematics, which followed the compressional phases of the Variscan orogeny building (Casas et al., 1989; Muñoz, 1992). The transtenstentional-extentional Permian regime was then followed by a widespread Triassic extension.
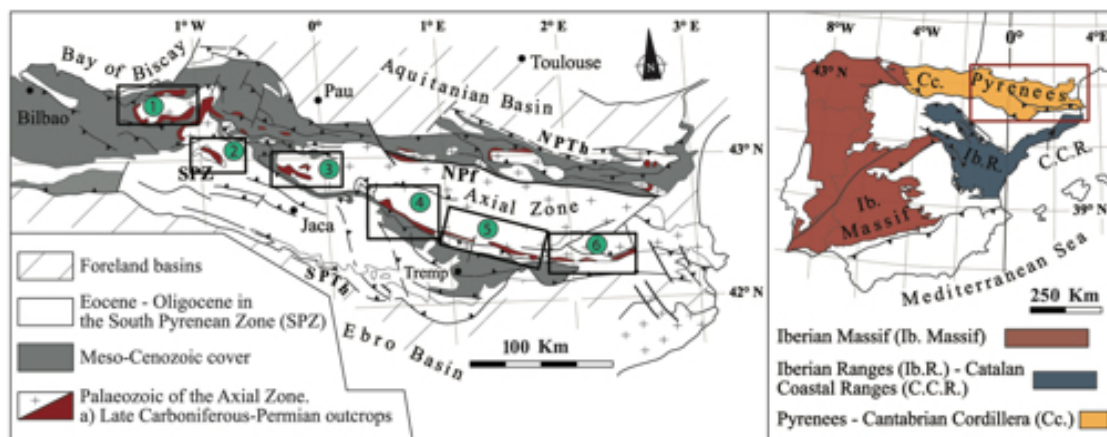
Figure 1.4.2. Geological setting. Geological sketch of the Iberian Peninsula showing the location of Pyrenees (right side of figure) and the Upper Carboniferous-Lower Permian basins (in red) attached to the southern border of the Axial Zone of the Pyrenees (left side of the figure). NPf: North Pyrenean fault; SPZ: South Pyrenean Zone; NPTh: North Pyrenean frontal thrust; SPTh: South Pyrenean frontal thrust. 1: Anayet Basin; 2: Aragón-Bearn Basin; 3: Castejón-Laspaúles Basin; 4: Erill Castell-Estac Basin; 5: Gramós Basin; 6: Castellar-Camprodón Basin. From Lloret et al. (2018).

The evolution of the sedimentary record in relation to syn-depositional tectonics in the Pyrenean Late Carboniferous-Early Triassic basins (Fig. 1.4.1) has never been described in detail until now. Previous studies of the Erill Castell-Estac and Gramós basins have focused mainly on sedimentological, structural and palaeontological analysis

(e.g., Mey et al., 1968; Nagtegaal, 1969; Gisbert, 1981, 1983; Besly and Collinson, 1991; Saura and Teixell, 2006; Fortuny et al., 2010, 2011; Voigt and Haubold, 2015; Mujal et al., 2016a,b, 2017a,b, 2018). From this perspective, our contribution aims to re-appraise the filling history in the Erill Castell-Estac Basin, a continental trough in the Centra-Eastern Southern Pyrenees.

These basins are strongly deformed nowadays due to the Alpine orogeny. Tentative reconstructions and retro-deformations have been carried out by Saura and Teixell (2006). Their study focused on the tectonics of the Erill Castell-Estac and Gramós basins and provided the first evidence of a half-graben morphology for such basins. Due to the difficulty of the tectonic setting, the authors did not discuss the original distance between the Northern Pyrenean Permian basins in France and the Southern Spanish basins. However it was clearly demonstrated (Saura, 2004; Saura and Teixell, 2006) that each basins had its own distinctive evolution, even though they existed under the same regime.

Our purpose is to highlight the significance of the different tectono-stratigraphic phases that occurred in an well developed and typical post-orogenic continental basin involved in the beginning of the Pangea break-up by combining different topics. In order to elucidate the relationship between tectonics and sedimentation, ten key stratigraphic profiles were measured at metre-detail, a detailed facies analysis was performed and tectonic data were integrated into a tectono-stratigraphic model. All these data allow us to define the sedimentary depositional evolution of the Erill Castell-Estac Basin through different tectonic phases and compare our results to the classic rifting model (Schlische and Olsen, 1990; Carroll and Bohacs, 1999).

1.6 Thesis outline

This thesis is organized as an ongoing PhD project. First of all, a detailed tectono-stratigraphic and sedimentological study of a Late Carboniferous-Lower Triassic basin was the main subject of this research. Using this detailed stratigraphic data, the study zone was enlarged to take in another three basins by applying other geological tools to constrain the paleoclimatic, paleoenvironmental and general evolution of the Central-Eastern Southern Pyrenean basins.

Chapter 2 provides a geological framework of the Late Paleozoic-Early Mesozoic continental successions in the Central-Eastern Southern Pyrenees, as well as introducing key aspects of the tools used in this multidisciplinary thesis and proviing an explanation for their usefulness.

Chapter 3 explains the materials and methodologies used for each approach applied in this study. It also details the criteria followed for sampling in the field, as well as the instrumental methodologies and technical details applied out in this thesis.

Chapter 4 presents the results obtained with the chronostratigraphic information provided by the palynology study. This study was carried out in collaboration of the PhD student Manuel Juncal under the supervision of Prof. Bienvenido Díez (Universidad de Vigo, Spain). The chapter is based on the paper published under the title: (1) "First palynological data of upper Carboniferous in the Oriental Pyrenees (Argestues, Lleida, Spain)" by Lloret, J. and Juncal, M. 2018. Geogaceta 64, 91-94; and another recently published paper entitled "New Upper Carboniferous palynofloras from Southern Pyrenees (NE Spain): Implications for palynological zonation of Western Europe" by Juncal, M., Lloret, J., Díez, J.B., López-Gómez, J., Ronchi, A., De la Horra, R., Barrenechea, J.F., Arche, A. (2018). Palaeogeography, Palaeoclimatology, Palaeoecology 516, 307-321. https://doi.org/10.1016/j.palaeo.2018.12.010. The

preliminary results of these works were presented as oral communications at the 2nd International Congress on the Permian and Triassic, Casablanca, Morocco, in April, 2018 and at the LXIV Scientific Session from the Geological Society of Spain. Ávila, on June 1 2018.

Chapter 5 is based on the sedimentological study of Erill Castell-Estac Basin. This chapter is derived from a published paper entitled: "Syn-tectonic sedimentary evolution of the continental Late Palaeozoic-Early Mesozoic Erill Castell-Estac Basin and its significance in the development of the Central Pyrenees Basin" by Lloret, J., Ronchi, A., López-Gómez, J., Gretter, N., De la Horra, R., Barrenechea, J.F., Arche, A. (2018). Sedimentary Geology 374, 134–157. https://doi.org/10.1016/j.sedgeo.2018.07.014.

The results and discussion of this chapter were also presented as oral communication at the 33rd International Meeting of Sedimentology (International Association of Sedimentology), Toulouse, France, October 2017. The preliminary results were previously presented as a poster communication in the 88th National Congress of the Italian Geological Society, Naples, Italy, September 2016.

Chapter 6 focuses on the paleosols study of the Permian and Triassic continental successions in the Central-Eastern Pyrenees which was performed in four basins. It is based on a paper in preparation, which aims to show the pedogenic evolution and its relationship with the paleoclimate. The preliminary results were presented as a poster shown at the 2nd International Congress on the Permian and Triassic, Casablanca, Morocco, April 2018.

Chapter 7 is based on the isotopic analysis of pedogenic carbonate of the Permian and Triassic paleosols. This part of the thesis provides the first isotopic analyses carried out in the Permian and Triassic of the Central-Eastern Southern Pyrenees zone. Part of

this chapter is included in the paper in preparation referring to the paleosols study mentioned the preceing chapter.

Chapter 8 contains a geochemical analysis of the clay mineralogy carried out in the Central-Eastern Pyrenees. This part of the thesis provides a mineralogical characterization of the different stratigraphic units and the paleoclimatic implications deduced. Part of this chapter is included in the paper in preparation referring to the paleosols study mentioned in the precedent chapter.

Chapter 9 consists of the syn-sedimentary tectonic study carried out in the Erill Castell-Estac Basin. This part of the thesis was included in the paper entitled: "Syn-tectonic sedimentary evolution of the continental late Palaeozoic-early Mesozoic Erill Castell-Estac Basin and its significance in the development of the central Pyrenees Basin" by Lloret, J., Ronchi, A., López-Gómez, J., Gretter, N., De la Horra, R., Barrenechea, J.F., Arche, A. (2018). Sedimentary Geology 374, 134–157. https://doi.org/10.1016/j.sedgeo.2018.07.014.

Chapter 10 is a general discussion on the various data presented in the preceding chapters. It is focuses on the paleoenvironmental reconstruction, the paleoclimatic evolution and regional evolution of the Central-Eastern Pyrenean basins.

Chapter 11 presents the general conclusions of the thesis and proposals for future research in the Pyrenees.

Appendix A: this contains the detailed stratigraphic columns undertaken in this PhD project and the position of the samples.

Appendix B: this contains the results and analytical data obtained from the isotopic study of paleosols.

Appendix C: this contains the tables with the results and analytical data obtained from de clay mineralogy study.

2. Framework

2.1 Late- to post Variscan geological context in the SW Europe

The geodynamic history of the Variscan orogeny involved a complex assembly of different microplates. The Variscan belt resulted from the Palaeozoic large-scale collisional event of the Northern part of the Gondwana supercontinent and the Southern margin of the Laurussia supercontinent (e.g., Scotese and Langford, 1995; Franke, 2000; Matte, 2001; Stampfli and Borel, 2002; Simancas et al., 2005; Johnston and Gutiérrez-Alonso, 2010; Stampfli et al., 2011; Pereira et al., 2014; Fig. 2.1.1). In this scenario, a transpressional-to-transtensional tectonic regime characterized the late to post-Variscan evolution, which contributed to the development of several strike-slip basins (e.g., Arthaud and Matte, 1977; Matte, 1986; Ménard and Molnar, 1988; Van Den Driessche and Brun, 1989; Echtler and Malavieille, 1990; Rey, 1993; Burg et al., 1994; Scotese, 2003). These continental basins were filled by clastic products (e.g., Glennie, 1990; Arche and López-Gómez, 1996; Maynard et al., 1997; López-Gómez et al., 2002; McCann et al., 2006). An extensive intraplate magmatism (e.g., Cortesogno et al., 1998; Neumann et al., 2004) with different episodes guided the emplacement of thick volcanic and sub-
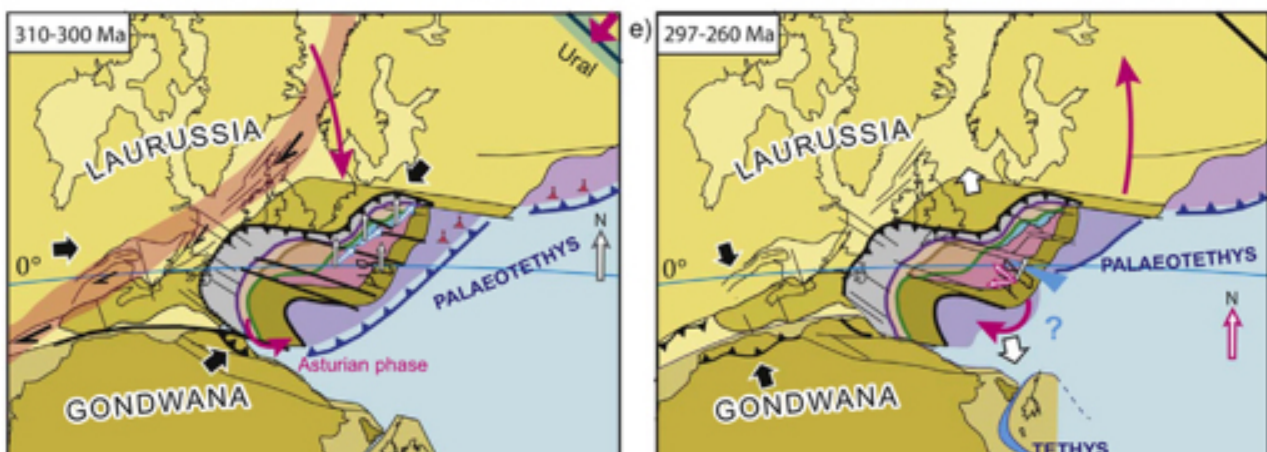
Figure 2.1.1. Paleotectonic map of the Variscan belt during the Carboniferous-Permian transition in the Western Paleotethys Ocean, from Edel et al. (2018).

volcanic bodies, filling the Permian-Carboniferous continental basins of the Pyrenees, the Southern Alps, Southern France and Sardinia (e.g., Cortesogno et al., 1998; Lago et al., 2004; Bourquin et al., 2011; Cassinis et al., 2012; Pereira et al., 2014; Gaggero et al., 2017).

The SW European basins stratigraphy has been studied by many authors (Gandin et al., 1982; Broutin, et al., 1992; Henk, 1992, 1993; Cassinis et al., 1995; Arche and López-Gómez, 1996; Cortesogno et al., 1998; López-Gómez et al., 2002; Schneider et al., 2006; Bourquin et al., 2007, 2011). Generally the stratigraphic record of the different basins places in this area contains continental deposits. The main characteristic of these basins are the unconformities between the formal stratigraphic formations. The beginning of these basins in most places is still uncertain, as well as the development of many of the lithostratigraphic formations. In the Early Permian the sedimentary record was unconnected between basins, and so, correlations between these basins remain still uncertain. For example, in the Nurra sector (Sardinia) and in the Provence (SE France) good correlations between formations and paleontological content have been identified (Cassinis et al., 2003), however, in Spain correlations between Central Iberian Ranges, Cantabrian Mountains and the Pyrenees Chain seems uncertainly nowadays. The tectonic context in the Iberian plate during the Permian was different for each zone (López-Gómez et al., 2002), so detailed correlations between formations have not been done up to now.

The Lower-Middle Triassic deposits are better fitted than the Permian ones in SW Europe correlations, as the tectonic extensive regime was quite more the same for all the regions. The extensive dynamic generated more connectivity between sectors, allowing more feasible lithostratigraphic correlations between different sectors. In addition, the Triassic chronostratigraphy is better known, so the age of the units are well constrained. Nevertheless, the continental sedimentation during the Permian-Triassic transition is not recorded in the W Palaeothehys (Bourquin et al., 2011; Ronchi et al., 2018).

16

The small and isolated basins of the Southern Pyrenees basin (Fig. 2.1.2) during the Late Carboniferous-Early Permian have been interpreted as graben or half-graben continental troughs (Gisbert, 1981, 1983; Bixel and Lucas, 1983; Martí, 1986; Soriano et al., 1996), associated with displacement along strike-slip faults (Speksnijder, 1985; Saura and Teixell, 2006). The Southern basin-bordering normal faults were active during the Late Carboniferous-Early Permian and acted as thrusts during the Cenozoic Alpine compression (e.g., Hartevelt, 1970; Sibuet et al., 2004; Saura and Teixell, 2006).

Figure 2.1.2. Paleogeographic situation of the Pyrenean basins during the lower Permian, modified from Blackey (2012).

2.2 Stratigraphy of the Upper Carboniferous – Lower Triassic continental deposits

The stratigraphic architecture of continental basins covers a wide and long-term time-span and typology in the general sedimentary record, generally controlled by plate tectonics and mantle dynamics (e.g., Allen and Allen, 2005). They also show a wide range of sedimentary possinilities. For instance, continental rift basins, such as those along the North-America Atlantic margins as well as the Cretaceous Congo basin or the Palaeozoic basins of Western China, share a common stratigraphic architecture characterized by initial period of fluvial sedimentation with the volume of sediments exceeding the basin capacity followed by lacustrine deposits spreading over a larger basin (e.g., Lefournier, 1980; Lambiase, 1990; Schlische and Olsen, 1990; Schlische, 1991; Harris et al., 2004).

The case of the stratigraphic subdivision of the Late Palaeozoic succession in the Pyrenees has been a matter of discussion over decades (e.g., Dalloni, 1930; Roger, 1965; Nagetgaal, 1969; Gisbert, 1981, 1983; Van Wees et al., 1998; López-Gómez et al., 2002; Vargas et al., 2009; Cantarelli et al., 2013; Gretter et al., 2015; Mujal et al., 2016b, 2017a, b, 2018). The first descriptions were mainly focused in the paleontological content (e.g., Dalloni, 1930). This latter work show the first age estimation for these deposits, an age that was referenced to the French basins terminology. Dalloni identified "Stephanian" deposits in Adrall-Pla de San Tirs, *Autunian* deposits in Gerri de la Sal and Triassic deposits in Guils. Ashauer (1934) identified for the first time the angular unconformities between Triassic, Permian and "Stephanian" deposits and provide detailed data about their stratigraphic features. After decades of scientific lacking, May (1968) and Nagtegaal (1969) which provided the first modern descriptions of the Upper Carboniferous-Lower Triassic basins in the Central-Eastern Southern Pyrenees. They separated the stratigraphic record in five lithostratigraphic units: Aguiró, Erill Castell, Malpàs, Peranera and

18

"Bunter" Formations). The naming of "Bunter" Fm. of the continental Triassic deposits indicates that they correlate these deposits with the German Triassic basins. In fact, the carbonate and evaporitic formations in the Southern Pyrenees are called Muschelkalk and Keuper Fm.

The current division used in the Central-Eastern Southern Pyrenees drives from other Gisbert's (1981) PhD thesis. This work represented a new vision of the sedimentology in the Southern Pyrenean basin based on detailed tectonic and stratigraphy studies that allowed to organize the sedimentary record using the concept of "tecto-sedimentary units" defined by Garrido-Megías (1973). This concept tries to group the deposits with similar paleoclimatic, volcanic and tectonic features. Therefore, from the 80's the classic "Formation" term is only used to correlate the old terminology with the one defined by Gisbert. The Late Carboniferous-Middle Triassic basins in the Central-Eastern Southern Pyrenees are divided into five "tecto-sedimentary units" (Fig. 2.2.1): Grey, Transition, Lower Red, Upper Red Units and Buntsandstein facies (Fig. 2.2.1). In some Western basins the Upper Red Unit (e.g., Erill Castell-Estac Basin, Castejón-Laspaúles Basin) does not crop out. The significance of this fact will be discussed later.

The Grey Unit (GU), mostly made up of volcanic and volcaniclastic rocks (Erill Castell Fm. of Mey et al., 1968; Nagtegaal, 1969), presents basal polygenic slope breccias (i.e., Aguiró Fm. of Mey et al., 1968; Nagtegaal, 1969) and fluvial-lacustrine deposits with coal-bearing plant fossils at the topmost (lower part of Malpàs Fm. of May et al., 1968; Nagtegaal, 1969). It rests unconformably over the basement and is ascribed to a Stephanian B-C age on the grounds of its flora (Broutin and Gisbert, 1985; Talens and Wagner, 1995; Mujal et al., 2018). Recent radiometric age data have assigned a late Kasimovian-early Gzhelian age to this unit (307.4 ± 1.4 Ma and 302.6 ± 2.6 Ma in Pereira et al., 2014).
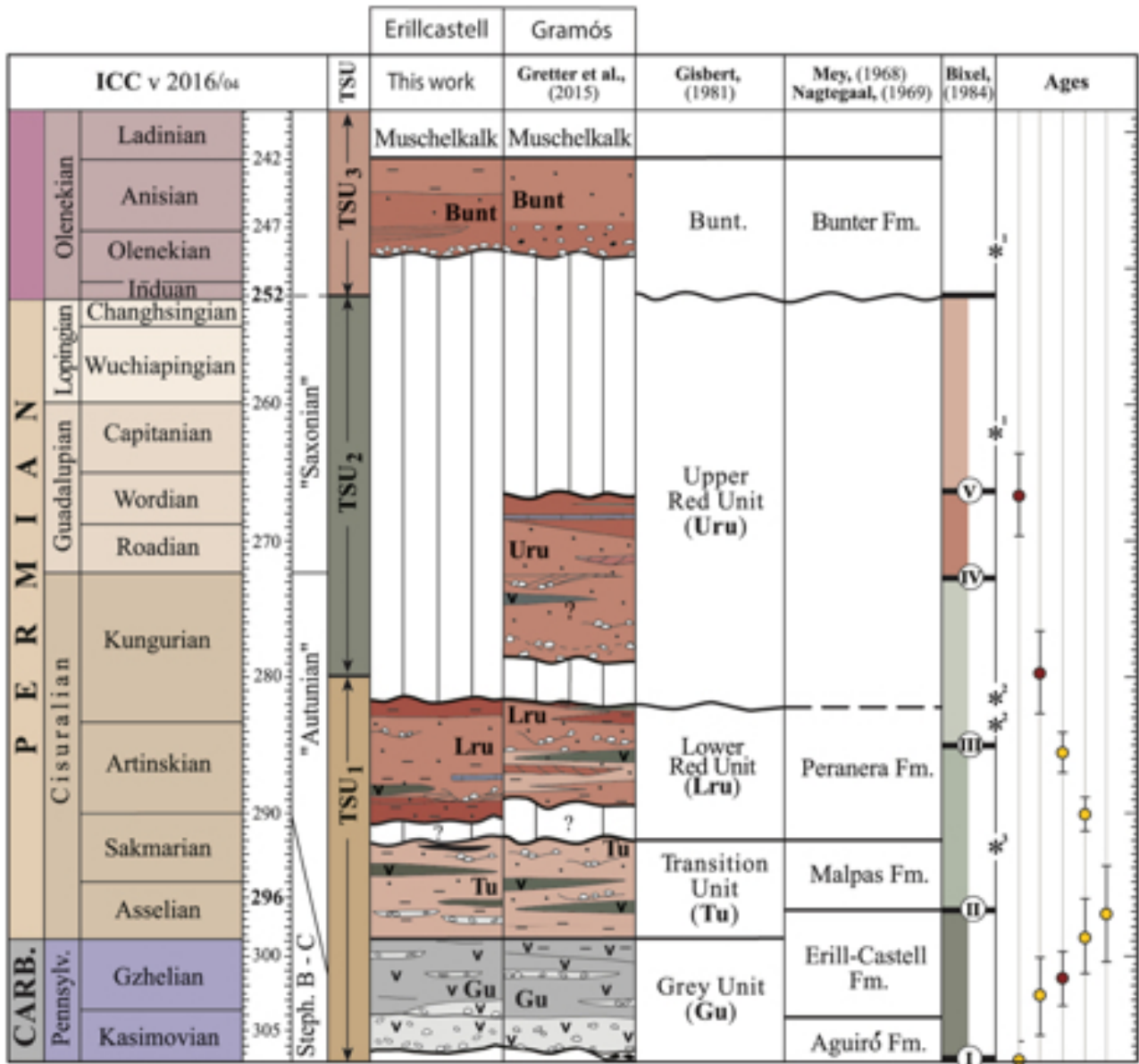
Figure 2.2.1. Chrono-lithostratigraphic scheme of post-Variscan formations in the Erill Castell and Gramós basins, based on Gisbert (1981), Mey et al. (1968) and Nagtegaal (1969), modified from Gretter et al. (2015). Bixel (1984) volcanic compositions, in asterisks: I Calc-alkaline andesites, II Calc-alkaline ultra-potassic andesites, III Alkaline rhyolites, IV Calc-alkaline andesites and V Alkaline basalts. Red points are the radiometric ages of intrusive rocks, and the yellow points are the radiometric age of volcanic rocks, both from Pereira et al. (2014). From Lloret et al. (2018).

The Transition Unit (TU) ("Permien alternant" by Broutin et al., 1994) corresponds to the upper part of the Malpàs Fm. of Mey et al. (1968) and Nagtegaal (1969). It is mostly characterized by a detrital succession of volcanic and volcaniclastic sequences, microconglomerates, sandstones and siltstones with interbedded coal levels. The TU rests conformably over the underlying GU (e.g., Gisbert, 1981; Gretter et al.,

2015; Mujal et al., 2018). Its age attribution is early-middle Autunian (Broutin and Gisbert, 1985); this is also supported by the Asselian ages for the Erill Castell ignimbrites (296.1 ±4.0 Ma in Pereira et al., 2014).

The Lower Red Unit (LRU) (i.e., the Peranera Formation of Roger, (1965); Mey et al., 1968; Nagtegaal, 1969), was described as alluvial fan sediments and meandering river flood-plain deposits (Gascón-Cuello and Gisbert, 1987) with volcaniclastic intercalations. The inferred age ranges from "late Autunian" to "post Autunian" (i.e., Sakmarian to lower Artinskian; Pellenard et al., 2017). An early Cisuralian age is inferred from its flora and plant remains (Dalloni, 1930; Roger, 1965; see also the "Flora of Gotarta" of Broutin and Gisbert, 1985), and by its tetrapod ichnoassociations that indicate an Artinskian (Mujal et al., 2016a,b, 2018). Recent radiometric age data, obtained from ignimbrites in the Castellar de n'Hug area, point to an Artinskian age (281.5±2.3 Ma and 283.4±1.9 Ma; Pereira et al., 2014).

The Upper Red Unit (URU) (i.e., the Peranera Formation of Roger, (1965); Mey et al., 1968; Nagtegaal, 1969) does not appear in Erill Castell-Estac Basin. It was described as red fluvial and lacustrine deposits composed of conglomerates, sandstone and siltstones (Gisbert, 1983; Gretter et al., 2015). This unit is organized in two fining upwards megasequences with interbedded volcanic bodies. The age of this unit is constrained as middle Permian by Mujal et al. (2016a) and as "Thüringien" based on a palynomorph assemblage (Broutin et al., 1988).

The fluvial Buntsandstein facies (Bunter Formation of Mey et al., 1968) represents the fifth and last unit of the continental Permian-Triassic sedimentary record at the Erill Castell-Estac Basin. It begins with coarse-grained oligomictic quartz-rich conglomerates and channel sand-sheets associated with braided fluvial systems (Anadón and Marzo, 1977; Gretter et al., 2015; Mujal et al., 2017a). The basal coarse levels are followed by

21

sandstones and shales related to meandering fluvial systems in a general fining upward sequence. The Buntsandstein can be observed unconformably overlying all preceding units, as well as the Palaeozoic basement. The upper part of this unit is represented by dark red siltsones and claystones levels that are below the carbonates in Muschelkalk facies. Initially, the palynomorph assemblages studied at the top of the coarse basal fluvial Buntsandstein deposits was interpreted as Thuringian age (e.g., Broutin et al., 1988: Calvet et al., 1993; Diez, 2000; Diez et al., 2005). Nowadays, this attribution has been recently changed to the late Olenekian on the basis of various new types of spores and pollens (Mujal et al., 2016b).

2.3 Southern Pyrenean basin configuration

The origin of the Late Palaeozoic-Lower Mesozoic basins in the Pyrenees has been a matter of discussion for some authors. Their mechanisms of formation are still not absolutely clear due to the geological difficulty of the zone. Since the 1970s, when the new modern geology started, several ideas and models have been proposed to explain the origin of these basins (Fig. 2.3.1), and this sections reviews the most important ones.

The first formal proposition was made by Soula et al. (1979) for the French Pyrenean Permian-Triassic basins. They used sand-box modelling to predict the occurrence of faulting under the specific conditions of Permian and Triassic Pyrenean basins. Their results led them to propose that this development occurred due to simple

a) Soula et al., 1979. French basins

Faults controlling the basin geometry

N

d) Gisbert (1981, 1986). Eastern Pyrenees

b) Bixel and Lucas (1983). Western Pyrenees

N060E
N110E

e) Saura and Teixell (2006). Noguères Zone

S   Triassic   Stephanian-Permian   N

Gramós basin

c) Speksnijdeer (1985). La Seu basin

Volcanic basins
f) Martí and Mitjavila (1988). Catalonian Pyrenees

passive caldera   active caldera

Figure 2.3.1. Different models proposed for the Permian-Triassic basins in the Pyrenees (modified from Soula, et al., 1979; Bixel and Lucas, 1983; Speksnijder, 1985; Gisbert, 1981; Martí and Mitjavila, 1988; Saura and Teixell, 2006).

shear activity along previous Variscan faults (Fig. 2.6.1). The conjugated-fault planes were subvertical, N 030º E and N 070º E striking. The opening of the basins took place by block rotation related to general sinistral shearing. Gretter et al. (2015) also hypothesized block rotation in the Easternmost Catalan basins, but with a dextral direction. These authors compared the results with San Andreas and Jacinto faults movements in the West of North America.

The next important work to elucidated basin origin evolution in this area was Bixel and Lucas (1983) which was based on Bixel's magmatic works (1983, 1984, 1987) in the French and Spanish Pyrenees. These works basically defined five volcanic events during the Late Carboniferous and Early Permian that were related to tectonic activity. The first event (1) is situated in the "Stephanian" deposits (Grey Unit) and contains two levels. The first is composed of acid levels of dacitic-rhyolitic levels, sometimes with an ignimbrite shape, while the second one is composed of basic rocks (andesitic) with a calco-alkaline composition. The second event (2) pertains to the "grey Autunian" deposits (TU). This is composed of calco-alkaline dacites. The third event (3) correspond to the "red Autunian" (LRU) and is composed of potassic peraluminic rhyolites. The fourth event (4) is placed between the "red Autunian*"* (LRU) and the "Saxonian" deposits (URU) and is composed of calco-alkaline volcanic rocks with alkaline affinity. Finally, the fifth event (5) is set in the upper part of the Upper Red Unit, below the basal Triassic conglomerate. The composition of these volcanic bodies is alkaline and represented by olivinitic basalts. On this basis, Bixel and Lucas (1983) proposed an E-W and N-S orientation half-grabens related to the transcurrent shear, with a strong volcanic influence. The basins were controlled by normal faults during the Stephanian under dextral shear and NE-SW-striking extensional faults. This system operated under an overall sinistral wrench regime (Fig. 2.3.1).

24

The Dutch geologist Speksnijder (1985) proposed a simple shear mechanism along E-W-striking for the La Seu sector (Central Catalan Pyrenees, current Gramós Basin). As a result, dextral faults generated a E-W oriented strike-slip grabens, with alternant stages of transtension and transpression that represented the internal basinal unconformities (Fig. 2.3.1). This work presents six major basin infill sequences that overlie each other unconformably, triggered by tectonic pulses. The author observed depocenters migration toward the East in space and time towards East.

Gisbert (1981, 1986) is the reference author for the stratigraphy of the Central.-Eastern Southern Pyrenees. In these works the sedimentary is reorganized into depositional stratigraphic units separated by unconformities. Using different criteria from Speksnijder (1985), Gisbert split the Erill Castell Fm. and Malpàs Fm. and reorganized them into the Grey and Transition Units. The so-called formations were originally divided according to lithostratigraphic criteria.

Saura and Teixell (2006) studied the faulting of some of the most representative Permian and Triassic basins in the Southern Pyrenees. Their palinspastic reconstructions they provided the first modern interpretation of the genesis of such basins. The main conclusion was that the shape was probably a half-graben morphology, while the current main thrusts (Erta and Orri thrust) were the border transtensive faults of the Erill Castell, Estac and Gramós basins.

Martí and Mitjavila (1988) focued their study on the volcanic role in the initial basin formation. Their study of the ignimbrites and the volcanic rocks indicates a highly explosive character with hydromagmatic mechanisms. On this basis, they proposde a volcanic passive caldera as the initial step of the formation of the Southern Pyrenean basins.

3. Materials and methodology

Several techniques have been used in this thesis to achieve the objectives of this project. Broadly speaking, the methodologies followed can be divided into fieldwork and laboratory/deskwork. There follows a etailed explanation of the workflow involved in each approach. The division of this chapter follows the organization of the thesis chapters.

3.1 Field work

Since the very start of the thesis, fieldwork has provided the main resource of data. There were many field trips during these three years of research. The firsts were prospective in nature, and they resulted in good outcrops where logging was the first step. The geological cartography followed for the first approach was that of the Instituto Geologico y Minero de España (IGME) and of the Institut Cartogràfic i Geològic de Catalunya (ICGC). The maps consulted were Campo (slide 212) and Pont de Suert (slide 213) of IGME with a 1:50.000 scale. The maps consulted from the ICGC was el Pont de Suert (slide 213 2-2, 64-20 with a 1:25.000 scale. Their geological resolution is not precise because the Permian and Lower Triassic units are usually grouped together (Fig. 3.1.1), and so a precise identification of the stratigraphic units was a key aspect of the fieldwork.

One important difficulty in the studied zone is the fragile deformation of the stratigraphic record due to the Alpine orogeny. Some research articles provide tectonic maps that have proved helped in the geological interpretation in the field (Hartevelt, 1970; Gisbert, 1981; Speksnijder, 1985; Soriano, 1996; Saura, 2004; Saura and Texiell, 2006). Stratigraphic repetitions abound, giving rise to significant confusion and complex tectonic frames. This made the site selection for the stratigraphic logs have been one of

the critical aspects of the field work. Thirteen detailed stratigraphic sections have been studied over four basins (Annex 1). From West to East (Figs. 1.4.2, 5.1.1, Appendix I figures; Tab. 1.4.1): Suils-Villarrué (Castejón-Laspaúles Basin); Igüerri, Gotarta, Malpàs, Castellars, Sas, La Mola d'Amunt, Collada de Pui Cavaller, Roca de les Creus, Baró and Estac (Erill Castell-Estac Basin); Rio Pallarols (Gramós Basin) and Castellar de N'Hug (Castellar-Camprodón Basin).
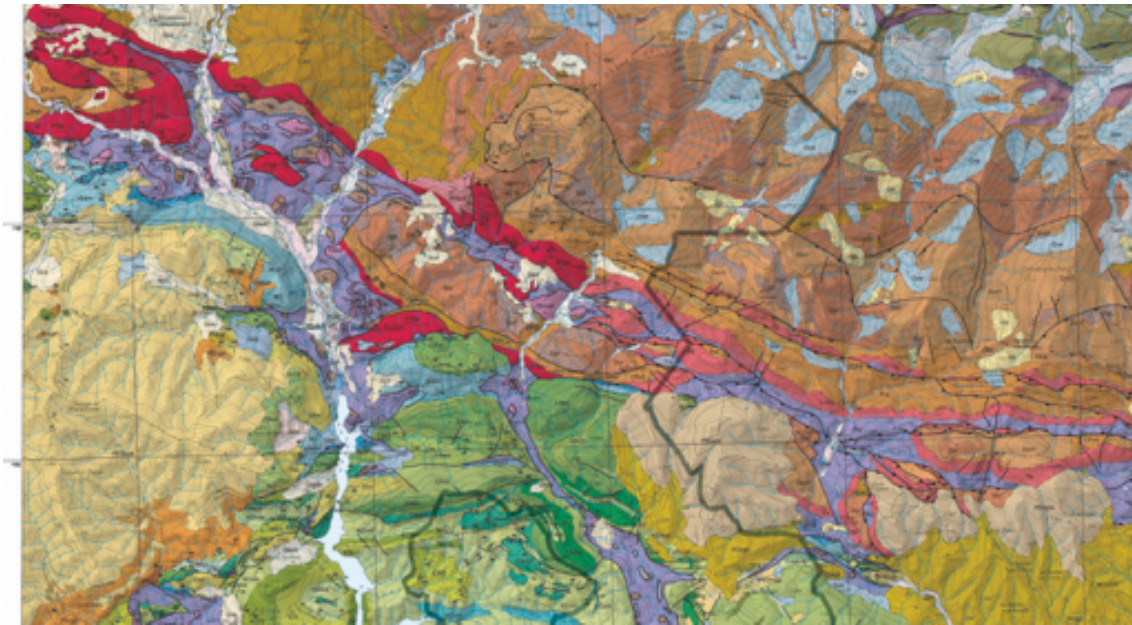
Figure 3.1.1. Geological map from ICGC (www.icgc.cat) of the Erill Castell-Estac Basin. Note the PTbc non-divided cartography for the Permian and Triassic rocks.

3.2 Sedimentology

This study is mainly based on sedimentary facies analysis, physical stratigraphy and architecture analysis of fluvial, lacustrine and volcaniclastic strata. New, detailed field mapping (Fig. 5.1.1) was performed taking into consideration previous tectonic studies (Soriano et al., 1996; Saura and Teixell, 2006). Ten detailed stratigraphic sections have been studied in the Erill Castell-Estac Basin (Fig. 5.1.1b), recording a total of ca. 3800 m for all the successions.

The facies (lithofacies) analyses (Tables 5.2.1 and 5.2.2) are based on macroscopic field evidence (Figs. 5.2.1 and 5.2.3) observed in this work, including: composition, thicknesses, strata geometry, colour, grain size, and sedimentary structures, following Miall's (1996, 2014) classification for fluvial and lacustrine deposits. This last deposits were not the focus of Miall's works, but are composed of the same lithology. Because for a synthetic nomenclature and understanding is used the same terminology. The lithofacies for the fluvial deposits traditionally are agruped into architectural elements. The architectural elements (Figs. 5.2.2 and 5.2.4) are defined according to their internal facies composition, related geometries, description of textures, composition and sedimentary structures. The study of these elements allow to understand the fluvial systems. For the volcanic and volcaniclastic lithofacies we followed the nomenclature proposed by Branney and Kokelaar (2002). This nomenclature is based on current ignimbritic deposits over the world. Despite some of the deposits studied here are not directly related with ignimbritic deposits it is considered a good solution. The interpretation of the volcanic and volcaniclastic elements is based on Martí's works (1986, 1988) in the Pyrenees. Some volcanic elements here described were previously described by Branney and Kokelaar (2002) in other parts of the world. The results obtained (Figs. 5.3.1 and 5.3.2) are compared in the discussion chapter with previous

publications in adjacent localities (Martí, 1996; Gretter et al., 2015; Mujal et al., 2017a, 2018).

3.3 Pollen analysis

The samples were processed in the laboratory of the Geosciences Department at the University of Vigo, with the invaluable assistance of Manuel Juncal (and his tutor Prof. J.B. Díez), using maceration procedures (HCl-HF-HCl techniques), following those outlined by Erdtman (1943), Wood et al. (1996) and Traverse (2007). The samples were processed by first adding HCl and HF to remove carbonate and silicate minerals (Fig. 3.3.1). No oxidising treatment was used, due to the fragility of the palynomorphs. A dispersing agent was subsequently added to facilitate filtering and sieving at 10µm. The palynological slides were analyzed in the Microscopy Labs at the University of Vigo with a Leica DM 2000 LED and the photos were taken with a Leica ICC50 W camera magnified x1000.
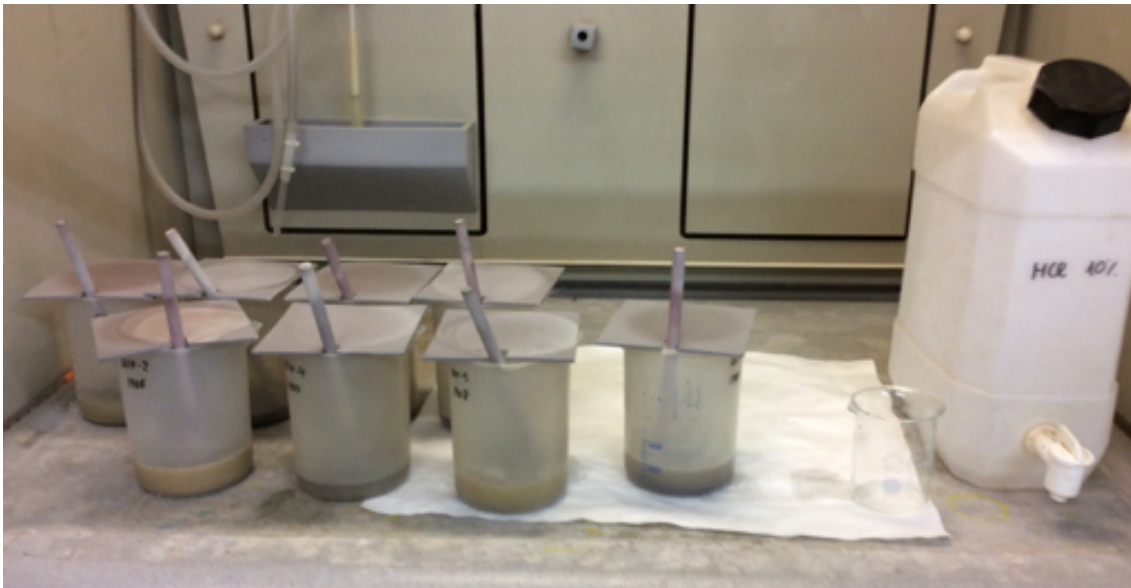
Figure 3.3.1. Pollen samples been processed in the laboratory at Universidad Complutense de Madrid, July 2016.

.

3.4 Pedology

The paleosols development depends of five main different factors: parental material, climate, activity of plants and animals, time of development, and topography (Retallack, 1984, 1988; Alonso-Zarza, 2003; Sheldon, 2005; De la Horra et al., 2008; Sheldon and Tabor, 2009; Alonso-Zarza et al., 2012; Li et al., 2016). In this study, a distribution of the pedotypes along the stratigraphic record of the Permian and the Triassic rocks is presented. The variation of the paleosols along Permian and Triassic rocks would imply variation of the factors that controlled their development. These factors are clue to understand the geologic processes that affected the Permian and Triassic rocks.

Five stratigraphic sections were detailed studied specifically for the pedogenic study: Villarrué-Suils, Gotarta, La Mola d'Amunt, Castellar de N'Hug and La Trava (Figs. 5.1.1, Appendix I). The main sedimentary structures of the sedimentary bodies were analyzed to interpret the parental material as well as the depositional environment. The pedogenic study have been carried out with field and petrographic observations following Retallack (1984, 1988) and Bullock et al. (1985) studies. The parameters that defined the paleosols identification were the presence of root traces or vegetation activity, the alteration of the parental material and the presence of indicators which confirm the aerial exposition and alteration of materials. In the field it was analyzed the parental material above and below the paleosols position and its stratigraphic position relative to the lithostratigraphic units. The thicknesses measurements of the whole soil and its horizons were done with a metric tape. Detailed field observations were completed with hand-samples for each horizon for the petrographic study. The pedogenic structures and features which are used to classify the pedotypes are based on Retallack's works (1984, 1988). The identification of horizons and the classification of the soils follows the main accepted works (Fig. 3.4.1: Retallack, 1984, 1988; Machette, 1985). The color

identification of each horizon is based on Munsell Colour Chart (Munsell, 1905). This

colour chart is recognized worldwide and used in many scientific fields.

Category	New Term	Description	Old Term
Master Horizons	O	Surface accumulation of organic materials (peat, lignite, coal), overlying clayey or sandy part of soil	O
	A	Usually has roots and a mixture of organic and mineral matter; forms the surface of those paleosols lacking an O horizon	A
	E	Underlies an O or A horizon and appears bleached because it is lighter colored, less organic, less sesquioxidic, or less clayey than underlying material	A2
	B	Underlies an A or E horizon and appears enriched in some material compared to both underlying and overlying horizons (because it is darker colored, more organic, more sesquioxidic or more clayey) or more weathered than other horizons	B
	K	Subsurface horizon so impregnated with carbonate that it forms a massive layer (developed to stage III or more of Table 4)	K
	C	Subsurface horizon, slightly more weathered than fresh bedrock; lacks properties of other horizons, but shows mild mineral oxidation, limited accumulation of silica carbonates, soluble salts or moderate gleying	C
	R	Consolidated and unweathered bedrock	R
Gradations Between Master Horizons	AB	Horizon with some characteristics of A and B, but with A characteristics dominant	A3
	BA	As above, but with B characteristics dominant	B1
	E/B	Horizon predominantly (more than 50%) of material like B horizon, but with tongues or other inclusions of material like an E horizon	A&B
Subordinate Descriptors	a	Highly decomposed organic matter	—
	b	Buried soil horizon (used only for pedorelict horizons with paleosols; otherwise redundant)	b
	c	Concretions or nodules	cn
	e	Intermediately decomposed organic matter	—
	f	Frozen soil, with evidence of ice wedges, dikes, or layers	f
	g	Evidence of strong gleying, such as pyrite or siderite nodules	g
	h	Illuvial accumulation of organic matter	h
	i	Slightly decomposed organic matter	—
	k	Accumulation of carbonates less than for K horizon	ca
	m	Evidence of strong original induration or cementation, such as avoidance by root traces in adjacent horizons	m
	n	Evidence of accumulated sodium, such as domed columnar peds or halite casts	sa
	o	Residual accumulation of sesquioxides	—
	p	Plowing or other comparable human disturbance	p
	q	Accumulation of silica	si
	r	Weathered or soft bedrock	ox
	s	Illuvial accumulation of sesquioxides	ir
	t	Accumulation of clay	t
	v	Plinthite (in place, pedogenic laterite)	—
	w	Colored or structural B horizon	—
	x	Fragipan (a layer originally cemented by silica or clay, and avoided by roots)	x
	y	Accumulation of gypsum crystals or crystal casts	cs
	z	Accumulation of other salts or salt crystal casts	sa

Figure 3.4.1. Identification and classification of pedogenic horizons defined by Retallack (1988).

3.5 Isotopic analysis

The samples used to do the isotopic analysis have been obtained in the field (Fig. 3.5.1). This was possible thanks to the previous stratigraphic, sedimentologic and pedologic work. All the samples have been carefully assigned to its stratigraphic unit. In addition, the parental material environment is supported by the sedimentologic analysis presented in the respective chapter. This fact is important to interpret the pedotype analyzed. Finally, the pedogenic study allow to know the distinctive horizons sampled.

The horizon B has been identified as the best level to guarantee the most representative isotopic composition (Cerling, 1984, 2009; Sheldon and Tabor, 2009; Sheldon et al., 2014; Hyland and Sheldon, 2016). This horizon is the most carbonate one and is considered as the maximum point of interaction between plants respiration, represented in the geological record as root traces. In this PhD project this fact is confirmed (see Chapter 6).

Figure 3.5.1. Field examples of the carbonate collected and samples for isotopic analysis.

The hand-samples have been collected along Castellar de N'Hug, Suils-Villarrué, La Mola, Castellar and Pallarols areas. The B horizon was identified following the pedotypes description done before. In the field were collected materials which contained

carbonate. These materials were mainly carbonate root traces and nodules. In order to corroborate the carbonate content samples to obtain thin-sections have been collected. To ensure a good representative sampling a duplicate set of samples has always been collected always.

Once is identified in thin-section the best point with the carbonate, it starts the procedure to obtain the isotopic signature of each sample. The next step is obtaining the dust of the carbonate to introduce them to the isotopic machine. The dust is obtained from the peg of the thin-section, taking into account the point which is interesting. The minimum weight needed is 300 micrograms.
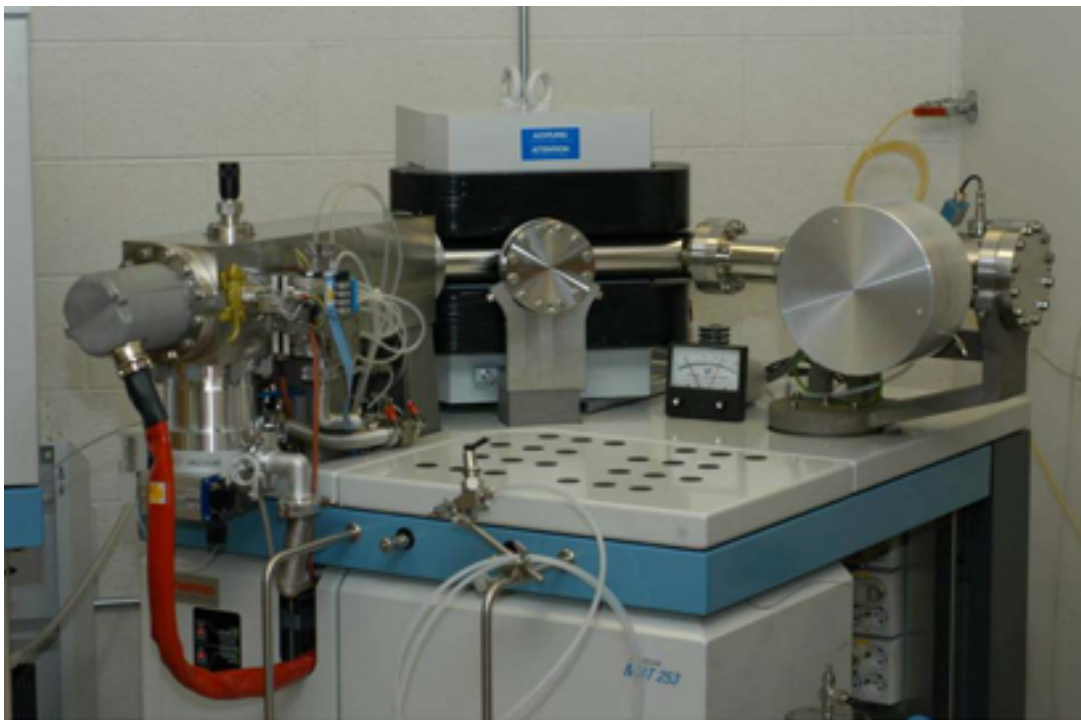
Figure 3.5.2. Stable isotopic laboratory in the UCM-CSIC.

40 isotopic analyses have been performed in the IGEO (UCM-CSIC) Stable Isotopic laboratory in Madrid under the supervision of Prof. Javier Martín-Chivelet. It was analyzed the stable C and O isotopic compositions in order to interpret variations on the paleosols horizons and types. The laboratory is full equipped with a Thermo Scientific^{TM} KIEL IV connected to a mass spectrometer of isotopic relationship Thermo

Scientific^{TM} MT253^{TM} and DELTA^{TM} (Fig. 3.5.2). Isotopic ratios were calibrated against the NBS-19 and Carrara standard and are reported as δ18O (‰) relative to the Vienna Pee Dee Belemnite (VPDB) standard. The analytical error of the instrument was better than ±0.01‰.

Stable isotope data are expressed in part per thousand (‰) deviations from international standards using the following equation:

$$\delta X = (R_{sample} / R_{standard} - 1) \times 1000$$

Where X = ^{13}C or ^{18}O, and R = ratio of heavy/light isotope content (^{13}C/^{12}C or ^{18}O/^{16}O).

3.5 Clay mineralogy

N. 88 samples for clay mineral analysis were collected at 5-10 meters intervals in fine deposits in the Sas, Castellars, Castellar de N'Hug and Villarrué-Suils sections. The field sampling involved collecting 100-200 gr of fines (very fine sandstone, or finer) from fresh rock outcrop. To avoid contamination of the samples, sampling zones with fluid alteration or a location close to fractures were ruled out.

The analysis was conducted in the UCM-CSIC laboratory in Madrid (Spain) under the supervision of Prof. José Barrenechea. The bulk sample mineralogy was obtained by X-ray diffraction (XRD) after grinding and homogenizaing the samples to b53 Am. Random-oriented powders were examined on a Siemens Kristalloflex 810 diffractometer, using Cu- Ka at 40 kV and 40 mA, a step size of 0.03 (82h), and time per step of 1s (scan rate of 1.88 2h/min). The clay mineral composition was determined on oriented aggregates of the b2 Am fraction obtained by sedimentation from an aqueous suspension onto glass slides. In some cases these were subjected to thermal treatment at 550 8C for 2h and to solvation with ethylene glycol (EG). A slower scan rate (1.28 2h/ min) was used between 28 and 138 2h in order to obtain better-defined peaks. Semi-quantitative analyses were performed, following the method proposed by Schultz (1964). The mineral identification involve the use of the diffraction angle of the most representative minerals (Table 3.5.1).

D₁ Å (2θ)	I₁ (%)	D₂ Å (2θ)	I₂ (%)	D₃ Å (2θ)	I₃ (%)	Mineral	Formula
2.883(30.99)	100	1.785(51.13)	60	2.191(41.17)	50	Dolomite	CaMg(CO3)2
3.035(29.40)	100	2.095(43.14)	18	2.285(39.40)	18	Calcite	CaCO3
3.176(28.07)	100	3.211(27.76)	30	3.752(23.69)	30	Albite	NaAlSi3O8
3.180(28.04)	100	4.020(22.09)	90	3.800(23.39)	80	Orthoclase	KAlSi3O8
3.200(27.86)	100	4.020(22.09)	80	3.740(23.77)	80	Oligoclase	(Na,Ca)(Si,Al)4O8
3.210(27.77)	100	3.180(28.04)	90	4.040(21.98)	80	Andesine	(Na,Ca)(Si,Al)4O8
3.211(27.76)	100	3.243(27.48)	90	4.106(21.63)	16	Anorthoclase	(Na,K)AlSi3O8
3.230(27.59)	100	10.500(8.41)	100	4.490(19.76)	80	Palygorskite	(Mg,Al)2Si4O10(OH)•4(H2O)
3.342(26.65)	100	4.257(20.85)	22	1.818(50.14)	14	Quartz	SiO2
3.430(25.96)	100	2.925(30.54)	80	5.610(15.78)	80	Analcime	NaAlSi2O6•(H2O)
3.580(24.85)	100	7.150(12.37)	100	2.330(38.61)	90	Dickite	Al2Si2O5(OH)4
4.180(21.24)	100	2.690(33.28)	30	2.452(36.62)	25	Goethite	Fe+++O(OH)
4.430(20.03)	100	2.560(35.02)	85	3.660(24.30)	40	Illite	(K,H3O)(Al,Mg,Fe)2(Si,Al)4O10[(OH)2,(H2O)]
4.470(19.85)	100	2.460(36.49)	90	2.970(30.06)	80	Chloritoid	(Fe++,Mg,Mn)2Al4Si2O10(OH)4
4.820(18.39)	100	4.340(20.45)	40	4.300(20.64)	20	Gibbsite	Al(OH)3
7.170(12.33)	100	1.490(62.26)	90	3.580(24.85)	80	Kaolinite	Al2Si2O5(OH)4
10.000(8.84)	100	4.360(20.35)	70	3.350(26.59)	40	Halloysite	Al2Si2O5(OH)4
10.500(8.41)	100	3.230(27.59)	100	4.490(19.76)	80	Palygorskite	(Mg,Al)2Si4O10(OH)•4(H2O)

Table.3.5.1. Summary of the mineralogical diffraction index to identify minerals the DRX diagram. Data from www.webmineral.com

3.6 Syn-sedimentary faulting

The kinematics of the faults in the case of the Pyrenees is a tangled issue. The sedimentary infill of the Erill Castell-Estac Basin was controlled by syn-sedimentary faults (Besly and Collinson, 1991) that probably were reactivations of previous pre-Hercynian faults (Poblet, 1991). However, the Alpine orogeny, which generated the formation of the present Pyrenees with mountains of 3.000 meters high, affected those structures, difficulting the precise kinematics characterization of the faults. In the field, we have analysed and described the direction and the dip of the faults, and we interpreted its kinematics based on the (a) Anderson (1905) model, which proposes that the faults with higher dip are related to normal faults and those with gentle dips should be correlated with inverse faults, and (b) the classic Riedel shear model, which describe the associated faults that occur in a strike-slip fault zone.

Two important aspects have to be considered in order to interpret the current directions of the original syn-sedimentary faults. The first is the Iberian Plate counter-clockwise rotation that occurred during the Cretaceous (e.g., Salas and Casas, 1993); the second is the possible rotation of original structures during the thrust sheet emplacement in the Alpine orogeny. With respect to the first consideration, the direction data obtained were accepted as valid, because all the Erill Castell-Estac Basin area would have rotated as one simple block. However, we have rotated the data obtained 30º clockwise to counteract the rotation of the Iberian plate. In order to avoid possible rotations between different thrust sheets, we have worked only in the Erta thrust sheet, with an interpreted SSW transport direction (Poblet, 1991; Muñoz, 1992). The angular relation of the different faults has been obtained as follows: firstly, we have obtained in the field all the dip and strike directions of all the units. Then, all the structural data have been successively restored to the horizontal starting from the Triassic to the Late Carboniferous. In this way we have obtained the original position of the faults affecting

38

each of the units. The software used to plot and restore the input data was Stereonet and we used the Fisher distribution included in the software to acquire mean vector directions. The age of the faults have been inferred from cartographic and field geometric and stratigraphic evidences. The syn-sedimentary character has been interpreted when a difference of thickness in the sediments has been observed between the two walls of a fault. A cross-section was also performed, together with a detailed analysis of thickness variations, in order to trace the depositional evolution of the basin. To infer the ages of stratigraphic units and the span of possible gaps we coupled geochronological data (Pereira et al., 2014) with the paleontological information (Dalloni, 1930; Broutin and Gisbert, 1985; Mujal et al., 2016 a, b). The isopach maps (10.1.2) were carried out with Surfer® software: input data are represented by field measurements of thicknesses and observed and inferred faults. Cartography was drawn on the basis of new field mapping, orthophoto interpretation and previous publications. The kriging interpolation method was the geostatistical method used to interpolate the input data and obtain the output isopach maps. The data used is based in our field work mapping and previous publications (Soriano et al., 1996; Saura, 2004; Saura and Teixell, 2006; Mujal et al., 2018). These data were also restored to the original position; the basin morphology is based on the half-graben typology proposed by the previous works.

4. Chronostratigraphy

4.1 Introduction

The climatic change which occurred during the Late Pennsylvanian-Permian produced an increase in the extinction rates of land plants (Cascales-Miñana and Cleal, 2014). The influence of aridification during this time is directly reflected by the variations in the constitution and distribution of floral associations (Ziegler, 1990; Kerp, 1996; DiMichele et al., 2001b; Wagner, 2004a, Schneider et al., 2006). In fact, in the Euramerican province this period has been interpreted as the "collapse of the rainforests" (DiMichele et al., 2009; Cleal et al., 2010, 2011; Sahney et al., 2010, Gulbranson et al., 2015). The replacement of hygrophytic ("Stephanian flora") by mesophytic and meso-xerophytic floras ("Autunian flora") that tolerated a seasonally dry climate has been documented. Conifers and other gymnosperms adapted to drier conditions and propagated progressively (e.g., DiMichele et al., 2001a; Looy et al., 2014) to become a dominant element in the landscapes until the Mesozoic.

In the Euramerican Province, the continental vegetation during the Pennsylvanian was a hygrophilous flora comprising pteridosperms, marattialean ferns, lycopsids, *Calamites* and *Cordaites* trees (DiMichele et al., 2006; Thomas and Cleal, 2017). In the Late Pennsylvanian-Early Permian, "Carboniferous hygrophilous flora" proliferated in the wet depressions (lowlands). Mesophilic, or even meso-xerophytic flora, whose most remarkable components were walchian conifers (Lemoigne and Doubinger, 1984) grew outside these areas (uplands), in dewatered habitats where the environmental conditions became less favourable for "Stephanian elements" (Broutin et al., 1986). This change in the flora was not isochronous across the Euramerican Province (e.g., Bouroz and Doubinger, 1977; Wagner, 1984; Broutin et al., 1990a; Kerp, 1996; Blake et al., 2002). The early appearance of "Autunian flora" in Carboniferous rocks has been reported in

40

outcrops from Western Europe (e.g., Lemoigne and Doubinger, 1984; Broutin and Gisbert, 1985; Broutin et al., 1986; Doubinger and Roy-Dias, 1985; Broutin et al., 1990a, DiMichele and Aronson, 1992; Kerp and Fichter, 1985; Martin-Closas and Galtier, 2005; Gand et al., 2013). Conversely, taxa from a Carboniferous-type wetland biome, interpreted as stream- and lake-side elements (DiMichele et al., 2006; Gand et al., 2013), reappear in Early Permian landscapes dominated by conifers (Broutin et al., 1990a; Galtier and Broutin, 1995). Records of Permian "mixed flora", including elements from more than one Palaeo-kingdom, may also appear in these above-cited environments (e.g., Broutin, 1986; Broutin et al., 1990b; Berthelin et al., 2003, 2006; Broutin and Berthelin, 2005; Sun, 2006; Cleal, 2016). This complex scenario was also affected by the phytogeographical provinciality that had a negative effect on the precise correlation between regional palynostratigraphic schemes (Stephenson, 2016).

The radiometric dating of those volcanic and volcaniclastic rocks provides an important tool for correlating palynological associations with absolutes ages. Correlating the age of microflora with other geochronological data (e.g., U–Pb dating, conodonts, macroflora, tetrapods footprints) would allow us to discern and validate the Palynological Zonation of Western Europe for the Late Carboniferous (Clayton et al., 1977). A deepening precision of our palynological knowledge for this period is essential to the correlation of the Carboniferous-Early Permian continental successions of Southwestern Europe (Eastern Equatorial Euramerica or Western Tethys) and to our understanding of the unconformities and hiatuses present in the Post-Variscan deposits, which are important in the correlation of basins (Cassinis et al., 2012; Gretter et al., 2015).

The Late Pennsylvanian-Early Permian palaeontological data from the Catalan (Central-Eastern Southern) Pyrenees has been described by previous authors in two main areas (Fig. 1). The Central Southern Pyrenees include the areas of Erill Castell, Malpás, Baró, Arcalis, Coll de Sas, Gotarta and Estac (Dalloni, 1930; Schmidt, 1931; Menéndez-

Amor, 1952; Nagtegaal, 1969; Álvarez-Ramis, 1985; Talens and Wagner, 1995; Wagner and Álvarez-Vázquez, 2010; Mujal et al., 2018). The main sections in the Eastern Pyrenees are Ogassa, Surroca, Coll de Jou, Coll de la Caritat and Camprodón (Faura, 1913, 1914; Dalloni, 1930; Jongmans, 1951; Álvarez-Ramis et al., 1969, 1971; Doubinger et al., 1978; Doubinger and Álvarez-Ramis, 1984; Broutin and Gisbert, 1985; Wagner, 2004b; Gómez-Alba, 2007; Martín-Closas and Martínez-Roig, 2007; Wagner and Álvarez-Vázquez, 2010). In both areas, understanding the Permo-Carboniferous transition is a challenge, due to the poor preservation of palynological remains and the fact that some studies were preliminary in nature (Broutin and Gisbert, 1985), or the location was uncertain (Alvarez-Ramis and Doubinger, 1987). Furthermore, the attribution of "Stephanian and Autunian flora" to validated chronostratigraphic units is very problematic. For example, Lloret and Juncal (2018) reported the appearance of microflora with "Autunian characteristics" in the Upper Carboniferous deposits of Argestues, Eastern Pyrenees.

Here is detailed all the chronostratigraphic information published in the Central-Eastern Southern Pyrenees (Tables 4.1.1, 4.1.2, 4.1.3):

Paleobotany (macroflora and microflora)			
Locality	**Unit**	**Age Proposed**	**References**
Palanca de Noves	Buntsandstein facies Unit	Anisian (Lower Triassic)	Díez et al. (2005)
Palanca de Noves	Buntsandstein facies Unit	Thuringian (Middle-Late Permian)	Díez (2000)
Les Nogueres-Cadí	Buntsandstein facies Unit	Anisian	Calvet et al. (1993)
Palanca de Noves	Buntsandstein facies Unit	Thuringian (Middle-Late Permian)	Broutin et al. (1988)
Campodrón	Lower Red Unit	"Autunian" (Early Permian)	Broutin and Gisbert (1985)
Gotarta	Lower Red Unit	"Autunian" (Early Permian)	Broutin and Gisbert (1985)
Arcalis	Transition Unit	"Autunian" (Early Permian)	Talens and Wagner (1995)
		"Autunian" (Early Permian)	Schmit (1931)
Baró	Transition Unit	Early Permian	Álvarez-Ramis (1985)
		"Autunian" (Early Permian)	Menendez-Amor (1952).
Coll de Jou	Transition Unit	"Middle-Upper Autunian" (late Gzhelian)	Wagner and Álvarez-Vázquez (2010)
		Stephanian B-C	Broutin and Gisbert (1985)
Coll de la Caritat	Transition Unit	Late Stephanian	Broutin and Gisbert (1985)
Malpás	Transition Unit (Malpás Fm)	Stephanian C	Wagner and Álvarez-Vázquez (2010)
		Late Stephanian C - "lower Autunian" (Early Permian)	Talens and Wagner (1995)
		Stephanian	Dalloni (1930); Nagtegaal (1969)
Estac	Uncertain	"Early Autunian" (Early Permian)	Álvarez-Ramis and Doubinger (1987)
Rio Pallarols/Gotarta	Grey Unit	Gzhelian	Lloret and Juncal (2018)
Coll de Sas	Grey Unit	Stephanian C	Mujal et al. (2018)
Surroca/Ogassa	Grey Unit	Stephanian C	Álvarez-Ramis et al. (1971); Doubinger et al. (1978); Doubinger and Álvarez-Ramis (1984); Martín-Closas and Martínez-Roig (2007); Wagner and Álvarez-Vázquez (2010)
		Late Stephanian	Dalloni (1930); Alvarez-Ramis et al. (1969); Álvarez-Ramis (1985)
		Middle Stephanian	Jongmans (1951)
		Stephanian (Surroca) – Late Stephanian (Ogassa)	Faura (1914)
		Upper Carboniferous	Faura (1913)
ErillCastell/Malpás	Grey Unit (Erill Castell Fm)	Cantabrian (Stephanian A)	Dalloni (1930); Talens and Wagner (1995)
Argestues	Grey Unit (Aguiró Fm)	Stephanian B	Broutin and Gisbert (1985)
Aguiró	Grey Unit (Aguiró Fm)	Asturian (Westphalian D)	Wagner and Álvarez-Vázquez (2010)
		Late Westphalian-Cantabrian (Stephanian A)	Talens and Wagner (1995)
		Westphalian D	Nagtegaal (1969)
		Middle-Upper Westphalian	Dalloni (1930)

Table 2.1.1. Summary of all the paleobotany chronostratigraphic information published

Tetrapod's footprints and bones			
Locality	**Unit**	**Age Proposed**	**References**
Coll de Terrers	Buntsandstein facies Unit	Early Triassic	Mujal et al. (2017b)
Erill Castell/Port del Cantó	Buntsandstein facies Unit	late Early Triassic	Mujal et al. (2017a)
Palanca de Noves	Buntsandstein facies Unit	Early Triassic	Mujal et al. (2016a)
Pla de St. Tirs/Noves de Segre	Upper Red Unit	"Late Permian"	Robles and Llompart (1987)
Noves/La Trava	Upper Red Unit	?Middle Permian (Wordian)	Mujal et al. (2016a)
Coll de Terrers	Upper Red Unit	"Late Permian"	Mujal et al. (2018)
La Mola d'Amunt	Lower Red Unit	Middle-Late early Permian (Artinskian)	Mujal et al. (2016b)

Table 2.1.2. Summary of all the tetrapod's footprints and bones chronostratigraphic information published

Radiometric dating			
Locality	**Unit**	**Age Proposed**	**References**
Castellar de N'Hug	Lower Red Unit	294,3±4,4	Pereira et a. (2014)
Erill Castell	Transition Unit	297,2±3,3	Pereira et a. (2014)
Estac	Uncertain (Grey/Transition Unit)	298,6±2,,5	Pereira et a. (2014)
Cadí	Grey Unit	302,6±2,6	Pereira et a. (2014)
Coll de Vanses	Grey Unit	307,4 ±1,4	Pereira et a. (2014)

Table 2.1.3. Summary of all radiometric published

4.2 Results

The chronostratigraphic information obtained in this PhD thesis comes from the palynological assemblages. Resulting of the fieldwork several samples have been collected, and some of them were positive. These data are a result of the collaboration with Manuel Juncal (PhD student) and Prof. Bienvenido Díaz from the Universidade de Vigo (Spain), who study the palynological assemblages of the Permian continental deposits.

4.2.1 Grey Unit

A palynological assemblage has extracted from the Grey Unit (Figs. 4.2.1 and 4.2.2):

Acanthotriletes echinatus (Knox) Potonié and Kremp 1955, *Acanthotriletes tenuispinosus* Naumova 1953, *Angulisporites splendidus* Bharadwaj 1954, *Apiculatisporis microacanthus* Andreyeva 1956, *Apiculatisporis parvispinosus* (Leschik) Schulz 1962, *Calamospora breviradiata* Kosanke 1950, Calamospora microrugosa (Ibrahim) Schopf, Wilson and Bentall 1944, *Calamospora pedata* Kosanke 1950, *Cirratriradites rarus* (Ibrahim) Schopf, Wilson and Bentall 1944, *Cyclogranisporites microgranus* Bharadwaj 1957, *Deltoidospora adnata* (Kosanke) McLean 1993 *Deltoidospora priddyi* (Berry) McGregor 1973, *Deltoidospora sphaerotriangula* (Loose) Ravn 1986, *Florinites junior* Potonié and Kremp 1956, *Florinites mediapudens* (Loose) Potonié and Kremp 1955, *Granulatisporites granulatus* Ibrahim 1933, *Granulatisporites minutus* Potonié and Kremp 1955, *Granulatisporites microgranifer* Ibrahim 1933, *Laevigatosporites perminutus* Alpern 1958, *Laevigatosporites vulgaris* (Ibrahim) Ibrahim 1933, *Latensina trileta* Alpern, 1958, *Lophotriletes microsaetosus* (Loose) Potonié and Kremp 1955, *Lundbladispora gigantea* (Alpern) Doubinger 1968, *Potonieisporites novicus* Bhardwaj 1964, *Potonieisporites simplex* Wilson 1962, *Punctatosporites minutus* Ibrahim 1933, *Punctatosporites punctatus* Ibrahim 1933,

Savitrisporites camptotus (Alpern) Doubinger 1968, *Vesicaspora wilsonii* (Schemel) Wilson and Venkatachala 1963, *Vestispora* cf. *cancellata* (Dybová and Jachowicz) Wilson and Venkatachala 1963, *Chromotriletes* sp., *Dictyotriletes* sp., *Endosporites* sp., *Guthoerlisporites* sp., *Lundbladispora* sp., *Maculatasporites* sp., *Nuskoisporites* sp., *Plicatipollenites* sp., *Potonieisporites* sp., *Spinosporites* sp., *Wilsonites* sp., and Unidentified disaccites.
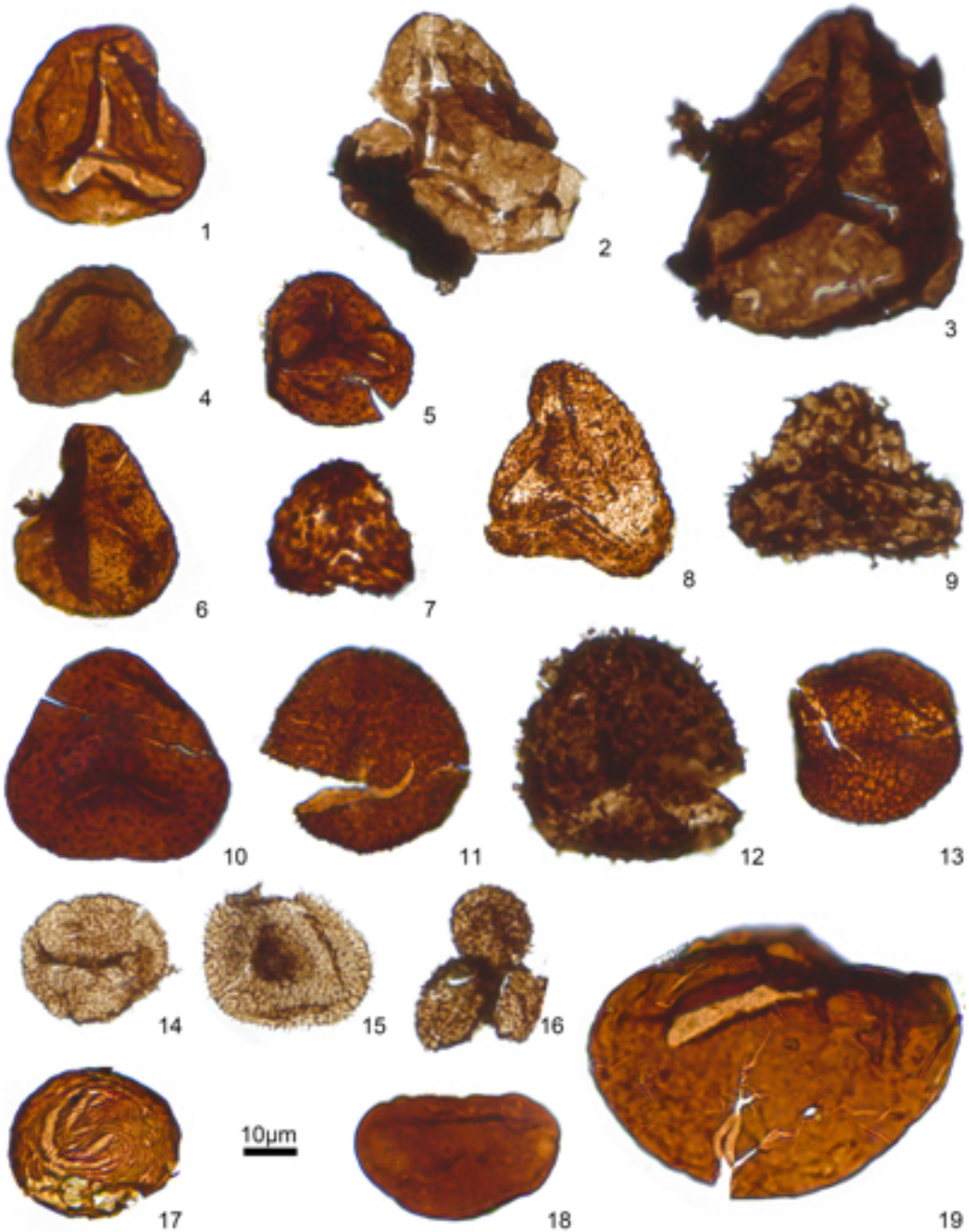
Figure 4.2.1. (previous page) GU palynological assemblage. 1: Deltoidospora priddyi. 2: Deltoidospora adnata. 3: Deltoidospora sphaerotriangula. 4: Granulatisporites minutus. 5: Granulatisporites granulatus. 6: Granulatisporites microgranifer. 7: Lophotriletes microsaetosus. 8: Acanthotriletes tenuispinosus. 9: Acanthotriletes echinatus. 10: Cyclogranisporites microgranus. 11: Apiculatisporis parvispinosus. 12: Apiculatisporis microacanthus. 13: Maculatasporites sp. 14: Punctatosporites punctatus. 15: Spinosporites sp. 16: Punctatosporites minutus. 17: Chromotriletes sp. 18: Laevigatosporites perminutus. 19: Laevigatosporites vulgaris. Modified from Juncal and Lloret (2018.)
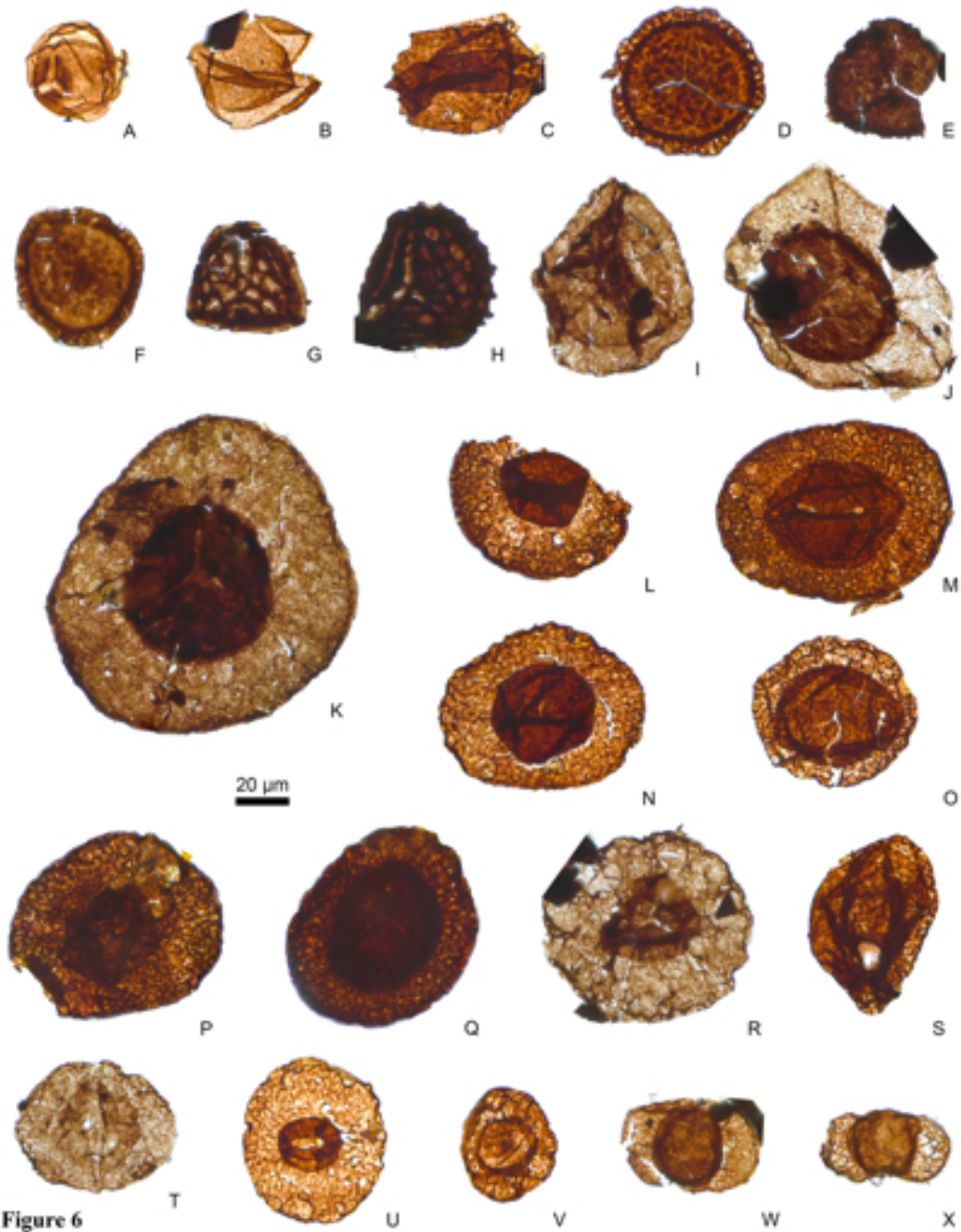
Figure 4.2.2. GU palynological assemblage. A: Calamospora breviradiata. B: Calamospora microrugosa. C: Calamospora pedata. D: Lundbladispora gigantea. E: Lundbladispora sp. F: Latensina trileta. G: Dictyotriletes sp. H: Savitrisporites camptotus. I: Angulisporites splendidus. J: Cirratriradites rarus. K: Endosporites sp. L: Potonieisporites simplex. M: Potonieisporites sp. N: Potonieisporites novicus. O: Plicatipollenites sp. P: Guthoerlisporites sp. Q: Nuskoisporites sp. R: Wilsonites sp. S: Vestispora cf. cancellata. T: Vesicaspora wilsonii. U: Florinites junior. V: Florinites mediapudens. W-X: Unidentified Disaccites. From Juncal et al. (2018).

4.2.2 Transition Unit

A palynological assemblage has extracted from several samples in the Transition Unit obtained from Gotarta section (Figs. 4.2.3, 4.2.4, 4.2.5 and 4.2.6).

The GT-01 sample (Fig. 4.2.3) has the following assemblage: *Apiculatisporis microacanthus* Andreyeva 1959, *Deltoidospora adnata* (Kosanke) McLean 1993, *Deltoidospora priddyi* (Berry) McGregor 1973, *Densosporites spinifer* Hoffmeister, Staplin and Malloy 1955, *Granulatisporites granulatus* Ibrahim 1933, *Granulatisporites minutus* Potonié and Kremp 1955, *Laevigatosporites perminutus* Alpern 1958, *Laevigatosporites vulgaris* (Ibrahim, Potonié and Kremp) Alpern and Doubinger 1973, *Lophotriletes ibrahimii* (Peppers) Pi-Radondy and Doubinger 1968, *Lophotriletes microsaetosus* (Loose) Potonié and Kemp 1955, *Lophotriletes parryensis* Utting 1994, *Savitrisporites camptotus* (Alpern) Doubinger 1968, *Calamospora* sp., *Deltoidospora* sp*., Densosporites* sp., *Granulatisporites* sp., *Punctatisporites* sp., *Punctatosporites* sp., *Raistrickia* sp., *Spinosporites* sp., and *Verrucosisporites* sp.

The GT-02 sample (Figs. 4.2.4, 4.2.5 and 4.2.6) contains: *Angulisporites splendidus* Bharadwaj 1954, *Calamospora breviradiata* Kosanke 1950, *Calamospora microrugosa* (Ibrahim) Schopf, Wilson and Bentall 1944, *Deltoidospora adnata* (Kosanke) McLean 1993*, Deltoidospora priddyi* (Berry) McGregor 1973, *Florinites junior* Potonié and Kremp 1956, *Florinites mediapudens* (Loose) Potonié and Kremp 1955, *Florinites millotti* Butterworth and Williams 1954, *Granulatisporites microgranifer* Ibrahim 1933, *Granulatisporites minutus* Potonié and Kremp 1955, *Granulatisporites parvus* (Ibrahim) Potonié and Kremp 1955, *Laevigatosporites perminutus* Alpern 1958, *Laevigatosporites vulgaris* (Ibrahim, Potonié and Kremp) Alpern and Doubinger 1973, *Latensina trileta* Alpern 1958, *Lophotriletes commissuralis* (Kosanke) Potonié and Kremp 1955, *Microreticulatisporites nobilis* (Wicher) Knox 1950, *Savitrisporites camptotus* (Alpern)

Doubinger 1968, *Spinosporites spinosus* Alpern 1958, *Calamospora* sp., *Cycadopites* sp., *Cyclogranisporites* sp., *Deltoidospora* sp., *Granulatisporites* sp., *Lundbladispora* sp., *Punctatisporites* sp. *Raistrickia* sp. *Spinosporites* sp., and unidentified spores, monosaccate and bisaccate pollen and lacustrine palynomorphs.
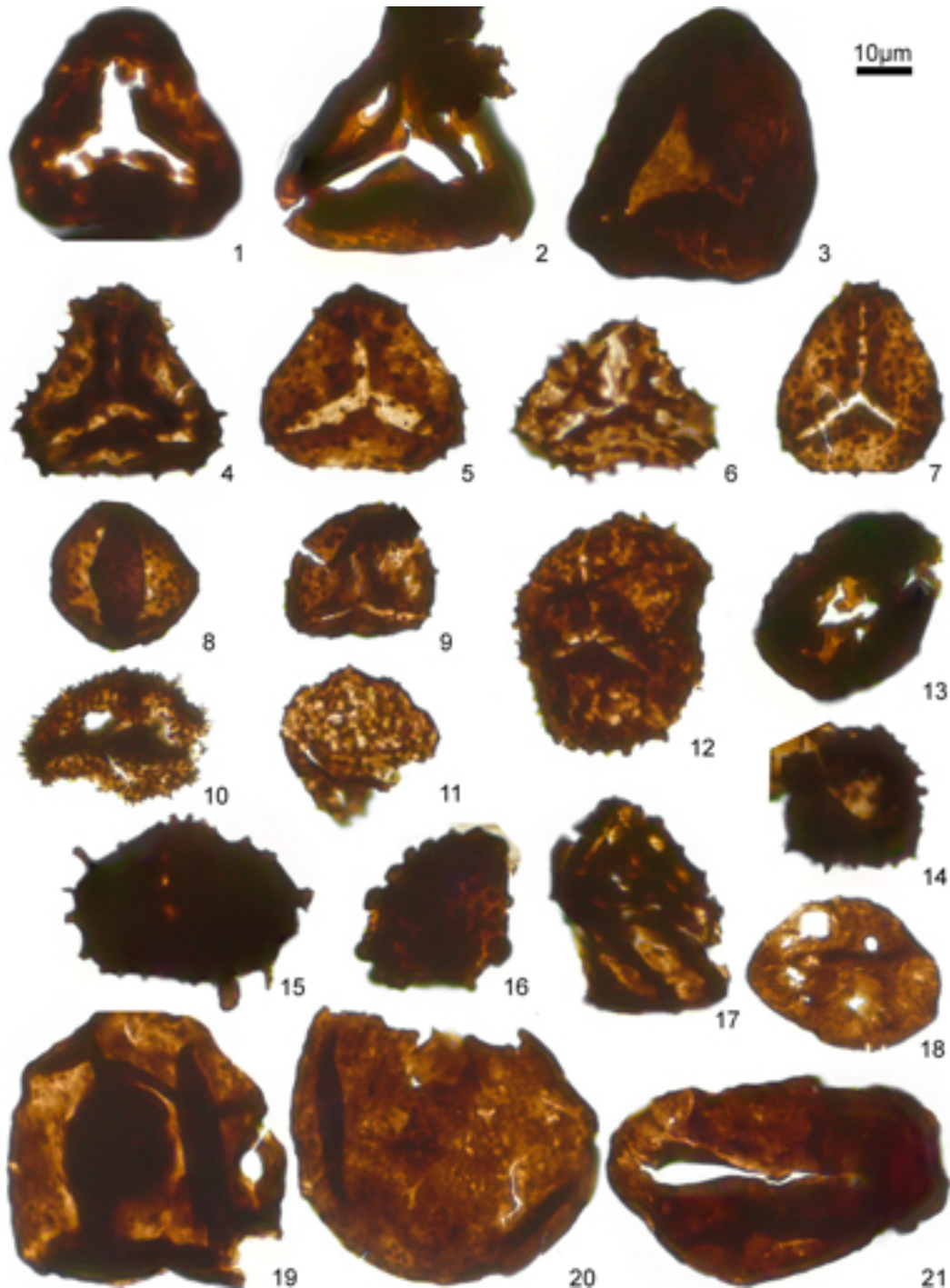
Figure 4.2.3. GT-01 palynogyical assemblage (TU). 1: Deltoidospora priddyi. 2: Deltoidospora sp. 3: Deltoidospora adnata. 4: Lophotriletes ibrahimii. 5: Lophotriletes parryensis. 6: Lophotriletes microsaetosus. 7: Granulatisporites granulatus. 8: Granulatisporites sp. 9: Granulatisporites minutus. 10: Spinosporites sp. 11: Punctatisporites sp. 12: Apiculatisporis microacanthus. 13: Densosporites sp. 14: Densosporites spinifer. 15: Raistrickia sp. 16: Verrucosisporites sp. 17: Savitrisporites camptotus. 18: Laevigatosporites perminutus. 19: Calamospora sp. 20: Punctatisporites sp. 21: Laevigatosporites vulgaris.
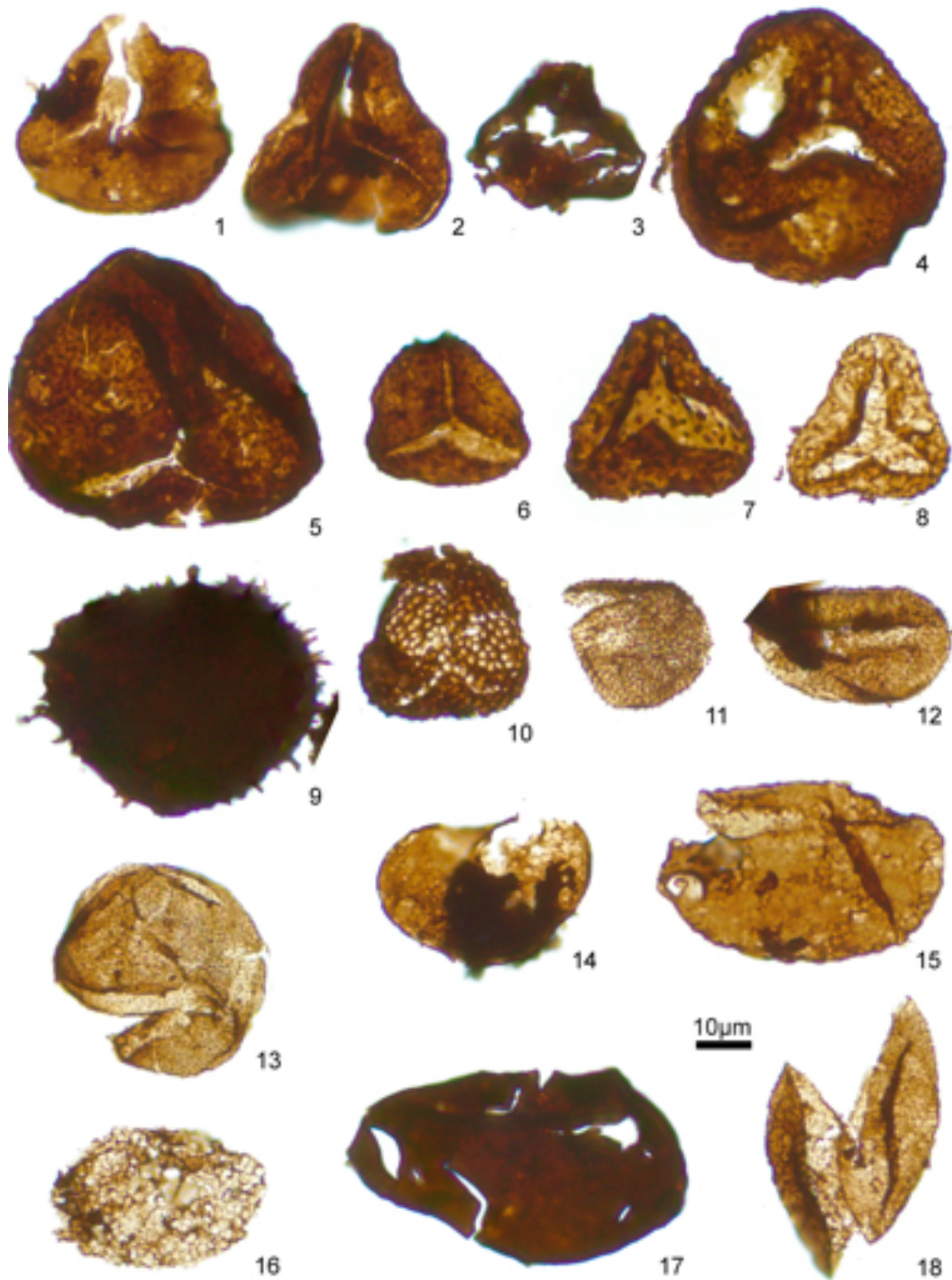
Figure 4.2.4. GT-02 palynological assemblage (TU). 1: Deltoidospora adnata. 2: Deltoidospora priddyi. 3. Deltoidospora sp. (Reworked) 4: Granulatisporites microgranifer. 5: Granulatisporites microgranifer. 6: Granulatisporites minutus. 7: Granulatisporites parvus. 8: Lophotriletes commissuralis. 9: Raistrickia sp. 10: Microreticulatisporites nobilis. 11: Spinosporites spinosus. 12: Spinosporites sp. 13: Cyclogranisporites sp. 14: Laevigatosporites perminutus. 15: Laevigatosporites vulgaris. 16: Laevigatosporites perminutus (Reworked). 17: Laevigatosporites vulgaris (Reworked). 18: Cycadopites sp.
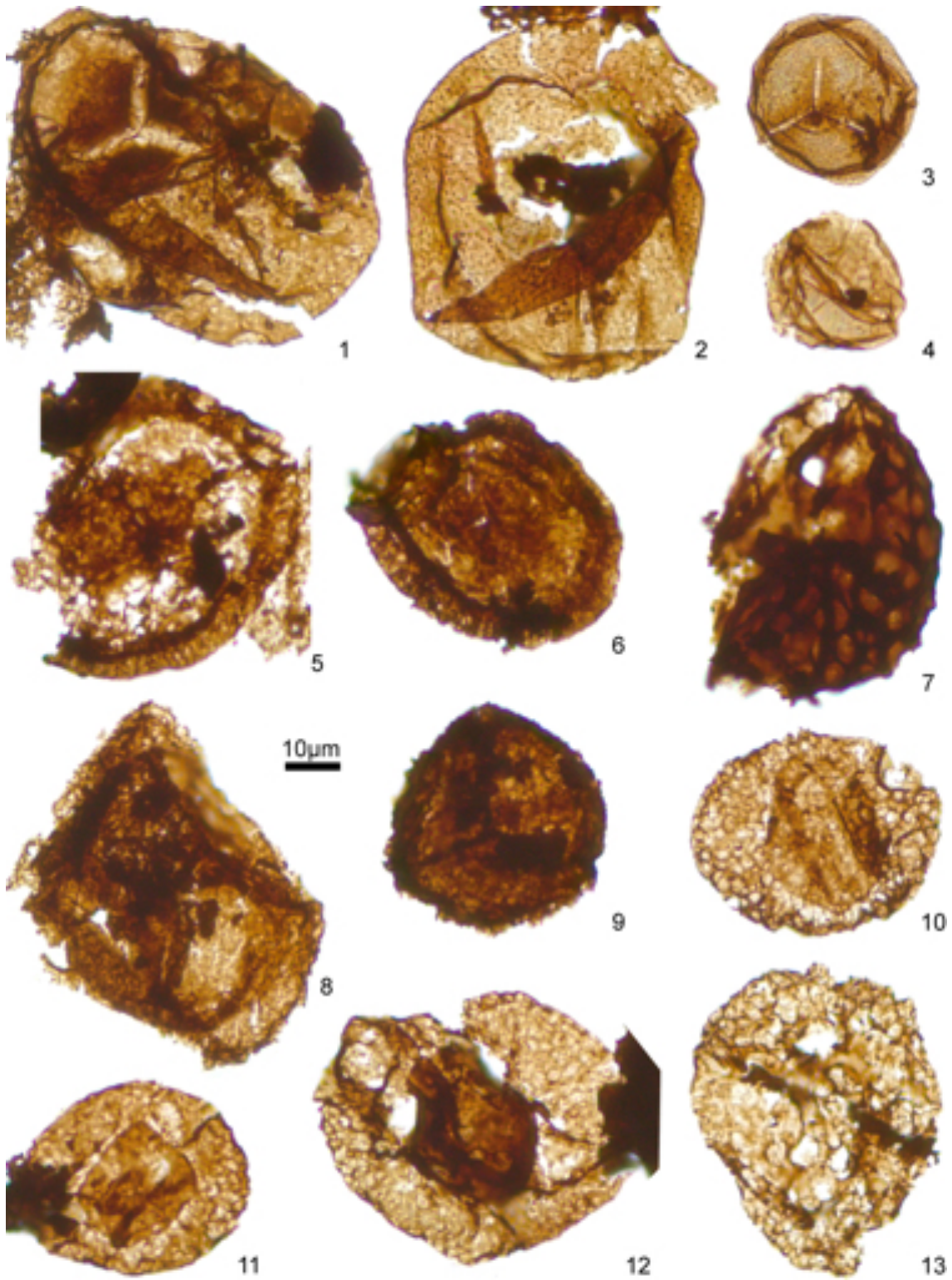
Figure 4.2.5. GT-02 palynological assemblage (TU). 1: Calamospora breviradiata. 2: Calamospora microrugosa. 3: Calamospora sp. 4: Calamospora sp. 5: Latensina trileta. 6: Latensina trileta. 7: Savitrisporites camptotus. 8: Angulisporites splendidus. 9: Lundbladispora sp. 10: Florinites mediapudens (Reworked). 11: Florinites junior. 12: Florinites junior. 13: Florinites millotti (Reworked).
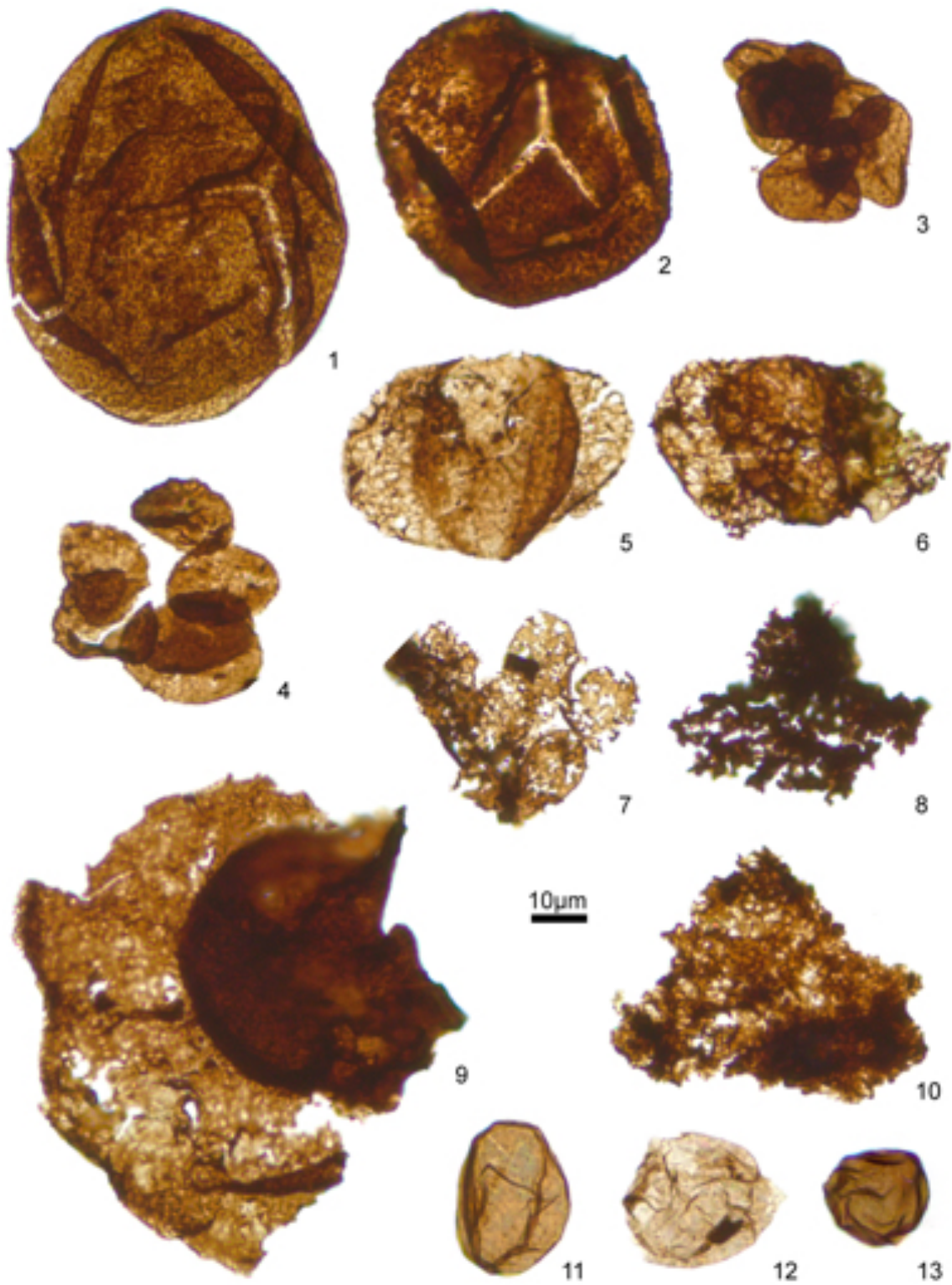
Figure 4.2.6. GT-02 palynological assemblage (TU). 1: Punctatisporites sp. 2: Punctatisporites sp. 3: Granulatisporites minutus 4: Granulatisporites sp. 5: Bisaccate pollen. 6: Bisaccate pollen (Reworked). 7: spores reworked. 8: Fern spore reworked. 9: Monosaccate pollen. 10: Fern spore reworked. 11: Lacustrine palynomorph. 12: Lacustrine palynomorph. 13: Lacustrine palynomorph.

The GT-04 sample (Figs. 4.2.7, 4.2.8 and 4.2.9) has the following palynological assemblage: *Acanthotriletes obtusosaetosus* (Luber and Waltz) Hart 1965, *Angulisporites splendidus* Bharadwaj, 1954, *Calamospora breviradiata* Kosanke 1950, *Crassispora kosankei* (Potonié and Kramp) Smith and Butterworth 1967, *Cirratriradites saturni* (Ibrahim) Schopf, Wilson and Bentall 1944, *Deltoidospora adnata* (Kosanke) McLean 1993*, Densosporites ruhus* Kosanke 1950, *Densosporites spinifer* Hoffmeister, Staplin and Malloy 1955, *Florinites junior* Potonié and Kremp 1956, *Florinites mediapudens* (Loose) Potonié and Kremp 1955, *Granulatisporites minutus* Potonié and Kremp 1955, *Laevigatosporites perminutus* Alpern 1958, *Laevigatosporites vulgaris* (Ibrahim, Potonié and Kremp) Alpern and Doubinger 1973, *Latensina trileta* Alpern 1958, *Lycospora granulata* Kosanke 1950, *Lycospora noctuina* Butterworth and Williams 1958, *Lycospora pusilla* (Ibrahim) Somers 1972, *Thymospora thiesseni* (Kosanke) Wilson and Venkatachala 1963, *Cadiospora* sp., *Calamospora* sp., *Chromotriletes* sp., *Cirratriradites* sp., *Cycadopites* sp., *Raistrickia* sp.,and *Nuskoisporites* sp.
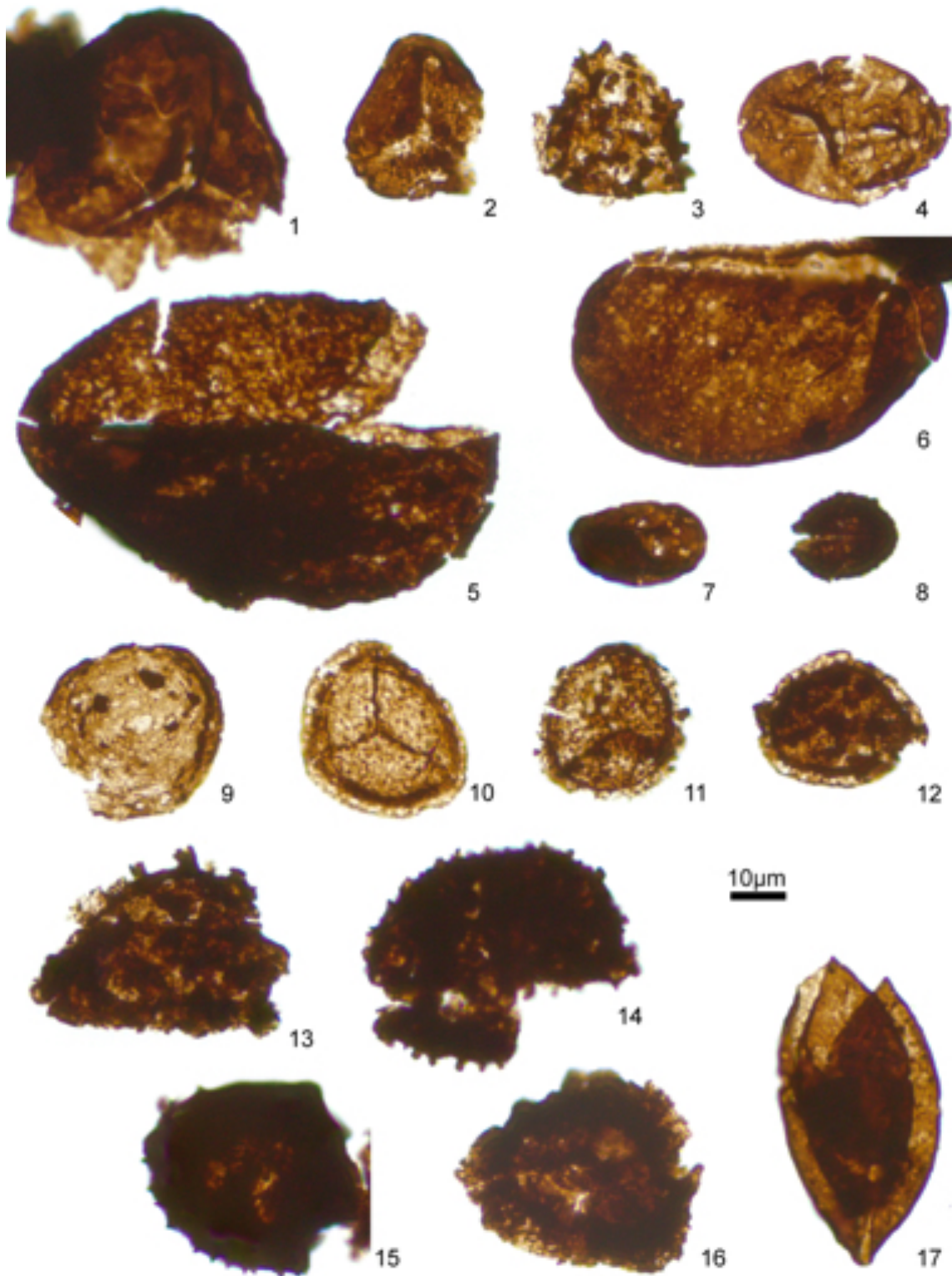
Figure 4.2.7. GT-04 palynological assemblage (TU). 1: Deltoidospora adnata. 2. Granulatisporites minutus. 3. Acanthotriletes obtusosaetosus. 4. Laevigatosporites perminutus. 5. Laevigatosporites vulgaris. 6. Laevigatosporites vulgaris. 7. Laevigatosporites perminutus. 8. Thymospora thiesseni. 9. Chromotriletes sp. 10. Lycospora pusilla. 11. Lycospora granulata. 12. Lycospora noctuina. 13. Raistrickia sp. 14. Raistrickia sp. 15. Densosporites spinifer. 1955 16. Densosporites ruhus. 17. Cycadopites sp.
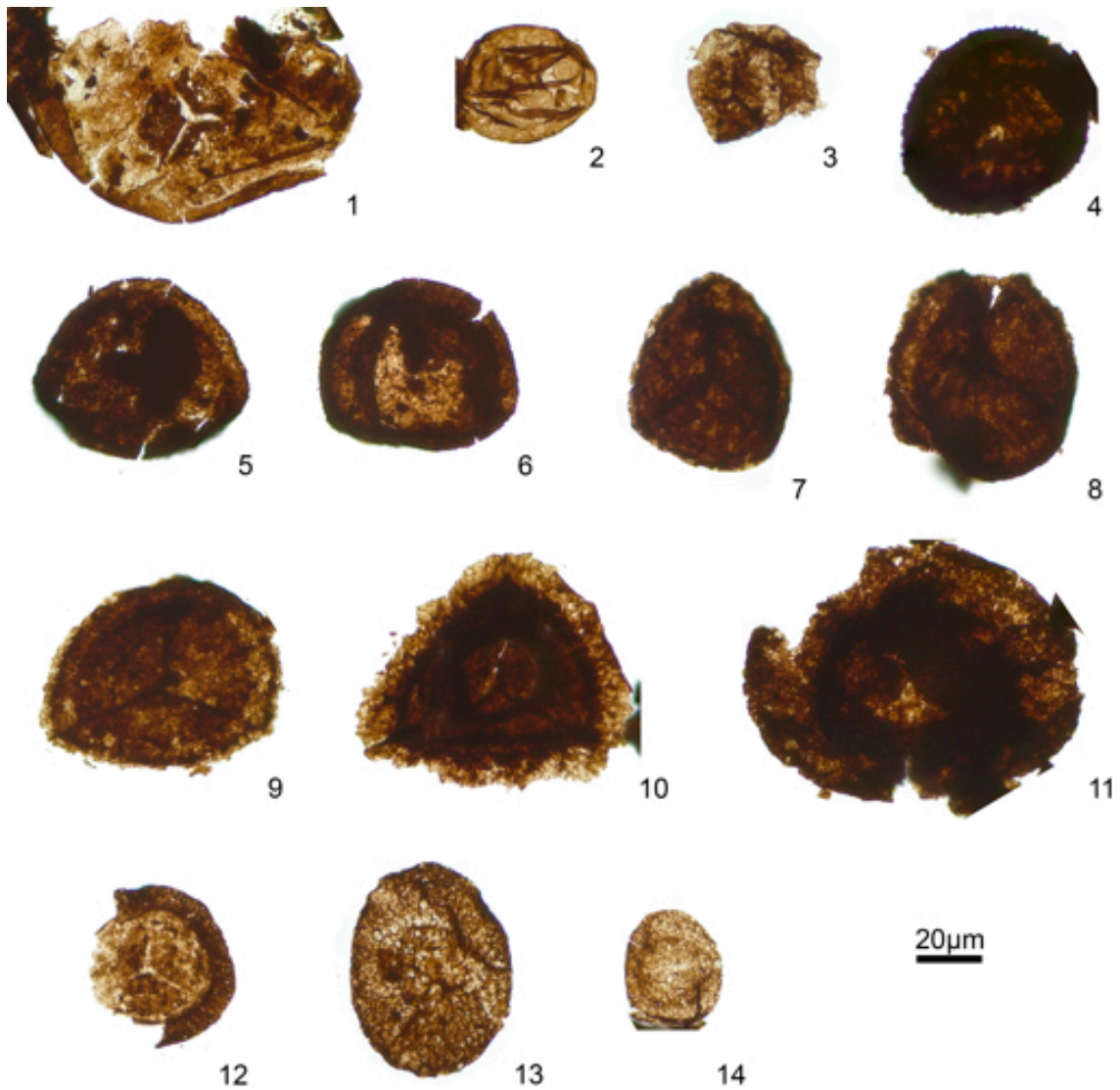
Figure 4.2.8. GT-04 palynological assemblage (TU). 1: Calamospora breviradiata. 2: Calamospora sp. 3. Calamospora sp. 4: Cadiospora sp. 5: Crassispora kosankei. 6: Crassispora kosankei. 7: Angulisporites splendidus. 8: Angulisporites splendidus. 9: Cirratriradites sp. 10: Cirratriradites saturni. 11: Nuskoisporites sp. 12: Latensina trileta. 13: Florinites junior. 14: Florinites mediapudens.

4.2.3 The Lower Red Unit

A palynological assemblage has extracted from one single sample, the GT-10 in the Gotarta section (Figs. 4.2.9, 4.2.10, 4.2.11 and 4.2.12). The assemblage obtained is the following: *Costapollenites ellipticus* Tshcudy and Kosanke 1966, *Falcisporites zapfei* (Potonié and Klaus) Leschik 1956, *Gardenasporites* cf. *heisseli* Klaus 1963, *Hamiapollenites bullaeformis* (Samoilovich) Jansonius 1962, *Hamiapollenites*

56

tractiferinus (Samoilovich) Jansonius 1962, *Illinites unicus* (Kosanke) Jansonius and Hills 1976, *Jugasporites delasaucei* (Potonie and Klaus) Leschik 1956, *Laevigatosporites vulgaris* (Ibrahim, Potonié and Kremp) Alpern and Doubinger 1973, *Lunatisporites albertae* (Jansonius) Fisher 1979, *Lunatisporites noviaulensis* (Leschik) Foster 1979, *Paravesicaspora splendens* (Leschik) Klaus 1963, *Potonieisporites magnus* Lele and Karim 1971, *Potonieisporites novicus* Bharadwaj 1954, *Protohaploxypinus globus* (Hart) Hart 1964, *Protohaploxypinus latissimus* (Luber) Samoilovich 1953, *Protohaploxypinus microcorpus* (Schaarschmidt) Clarke 1965, *Protohaploxypinus* cf. *perfectus* (Naumova) Samoilovich 1953, *Vesicaspora schemeli* Klaus 1963, *Vesicaspora wilsonii* (Schemel) Wilson and Venkatachala 1963, *Vestigisporites thomasi* (Pant) Hart 1960, *Vittatina costabilis* Wilson 1962, *Calamospora* sp., *Chromotriletes* sp., *Chordasporites* sp., *Gardenasporites* sp., *Hamiapollenites* sp., *Illinites* sp., *Jugasporites* sp., *Limitisporites* sp., *Lueckisporites* sp., *Lunatisporites* sp., *Nuskoisporites* sp., *Potonieisporites* sp., *Striatoabieites* sp., *Vesicaspora* sp., *Vittatina* sp., and Lacustrine palynomorph. cf. *Multiplicisphaeridium* sp.
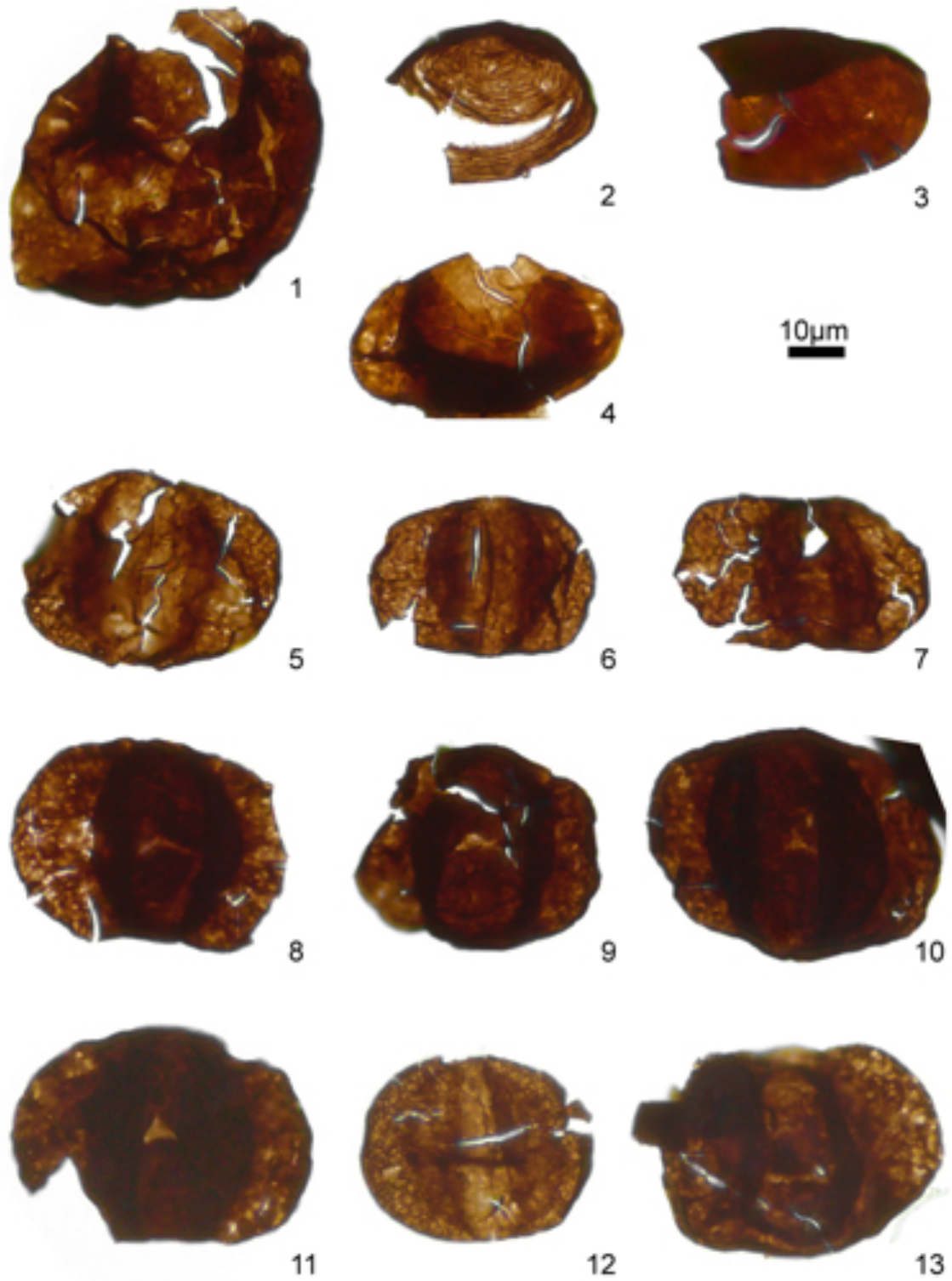
Figure 4.2.9. GT-10 palynological assemblage (LRU). 1: Calamospora sp. 2: Chromotriletes sp. 3: Laevigatosporites vulgaris 4: Paravesicaspora splendens. 5: Falcisporites zapfei. 6: Falcisporites zapfei. 7: Limitisporites sp. 8: Jugasporites delasaucei. 9: Jugasporites sp. 10: Illinites unicus. 11: Illinites sp. 12: Chordasporites sp. 13: Vestigisporites thomasi.

10µm
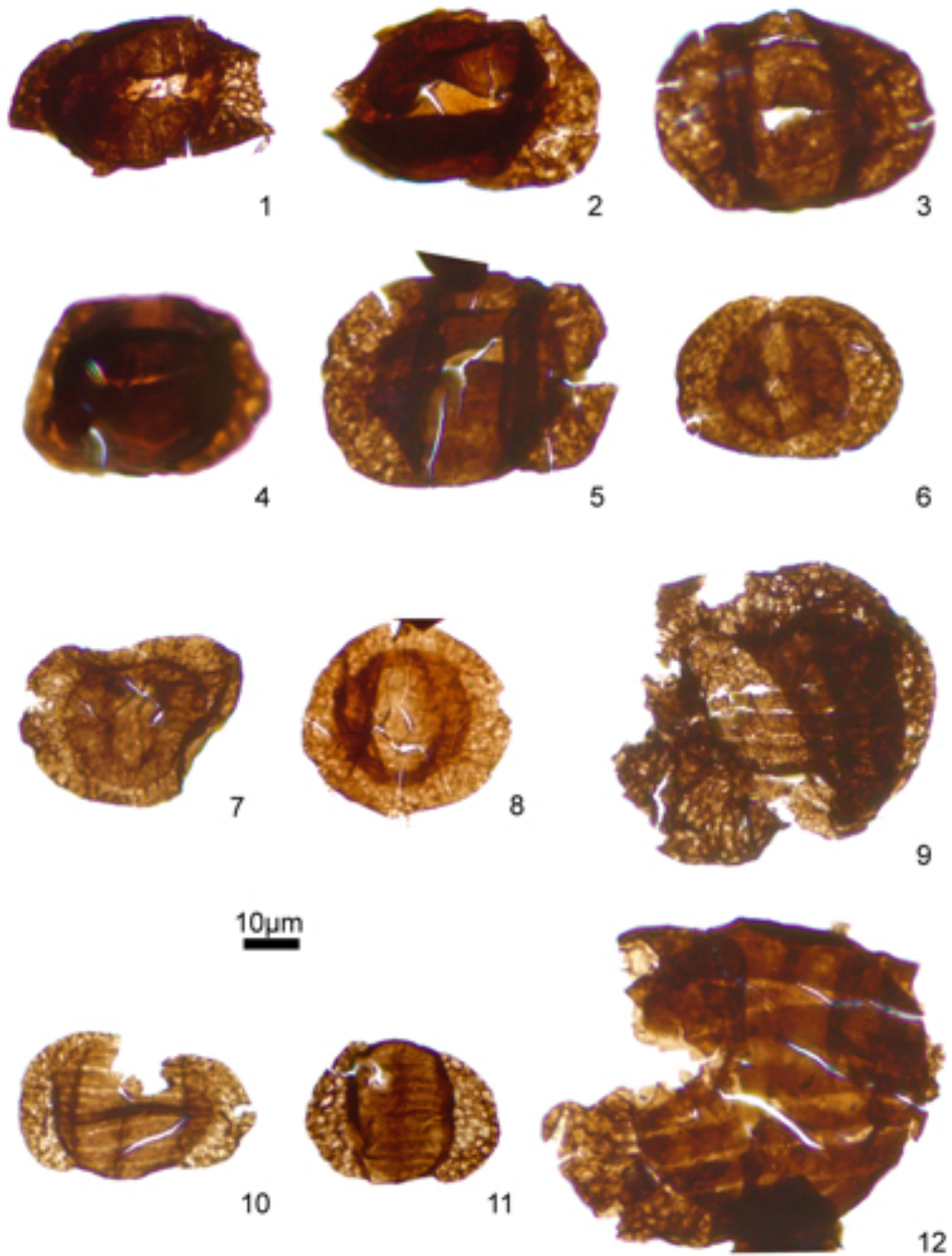
Figure 4.2.10. GT-10 palynological assemblage (LRU). 1: Lueckisporites sp. 2: Lueckisporites sp. 3: Lunatisporites noviaulensis. 4: Lunatisporites albertae. 5: Lunatisporites sp. 6: Vesicaspora wilsonii. 7: Vesicaspora schemeli. 8: Vesicaspora sp. 9: Protohaploxypinus microcorpus. 10: Protohaploxypinus globus. 11: Protohaploxypinus latissimus. 12: Protohaploxypinus cf. perfectus.

10μm
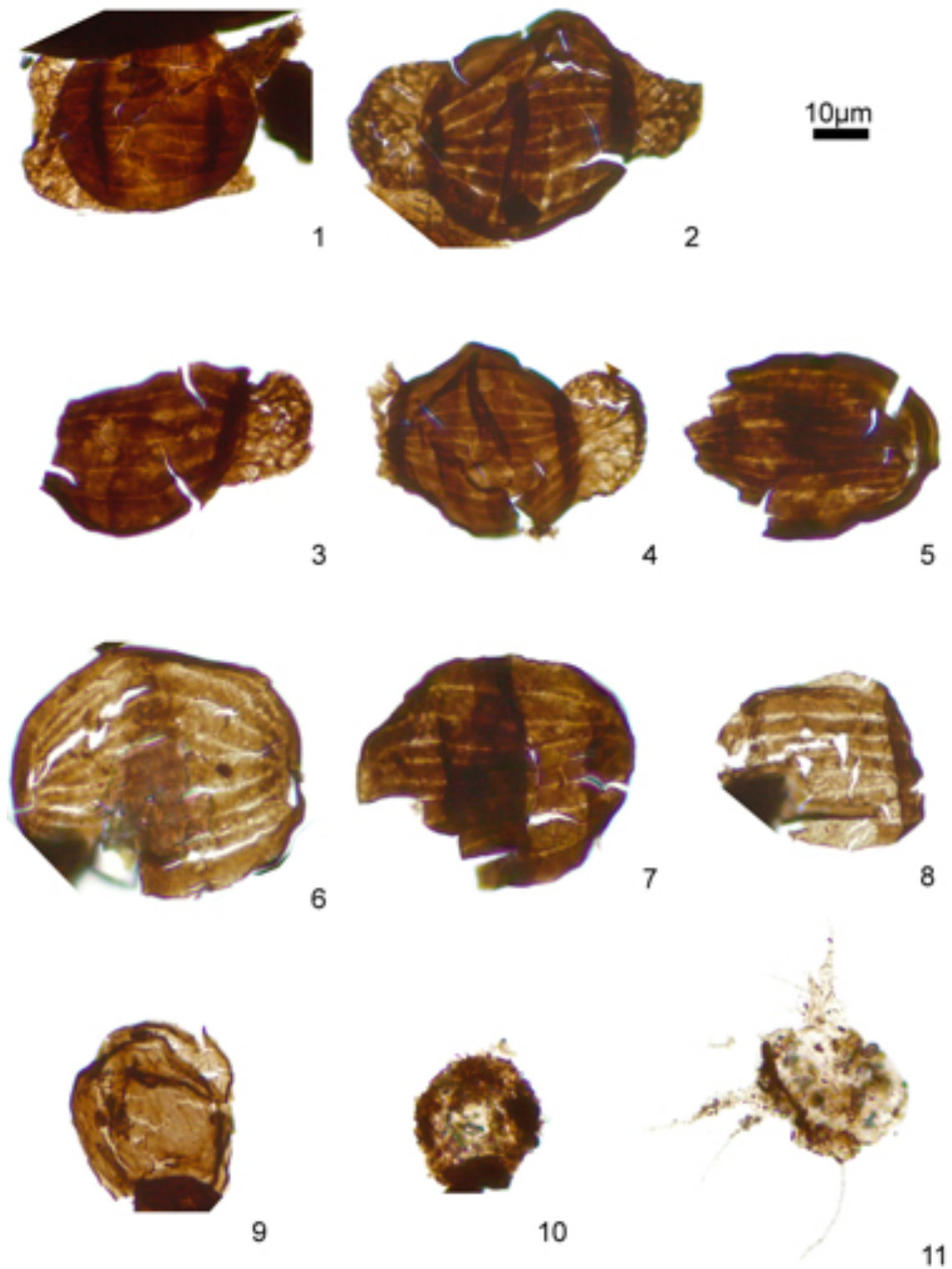
Figure 4.2.11. GT-10 palynological assemblage (LRU). 1: Striatoabieites sp. 2: Hamiapollenites bullaeformis. 3: Hamiapollenites tractiferinus. 4: Hamiapollenites sp. 5: Costapollenites ellipticus. 6: Vittatina costabilis. 7: Vittatina costabilis. 8: Vittatina sp. 9: Lacustrine palynomorph. 10: Lacustrine palynomorph. 11: cf. Multiplicisphaeridium sp.
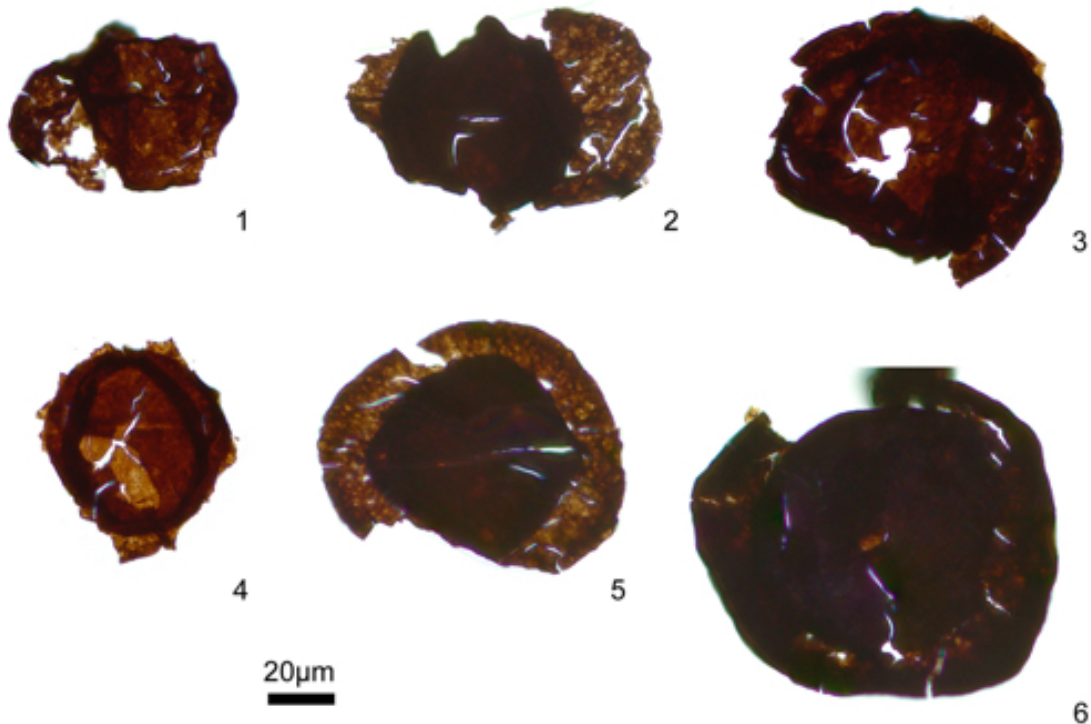
Figure 4.2.12. GT-10 palynological assemblage (LRU). 1: Gardenasporites cf. heisseli. 2: Gardenasporites sp. 3: Potonieisporites novicus. 4: Potonieisporites magnus. 5: Potonieisporites sp. 6: Nuskoisporites sp.

4.2.4 The Buntsandstein facies Unit

A palynological assemblage has extracted from one single sample, the SuilsP8 in the Suils section (Figs. 4.2.13 and 4.2.14). The assemblage obtained is the following: *Alisporites grauvogeli* Klaus 1964, *Alisporites opii* Daugherty 1941, *Calamospora tener* (Leschik) Mädler 1964, *Chordasporites singulichorda* Klaus 1960, *Hexasaccites muelleri* (Reinhardt and Schmitz) Adloff and Doubinger 1969, *Lunatisporites noviaulensis* (Leschik) Fisher 1979, *Microcachryidites sittleri* Klaus 1964, *Punctatisporites fungosus* Balme 1963, *Striatoabieites aytugii* (Visscher) Scheuring 1978, *Sulcosaccispora minuta* Klaus 1964, *Triadispora epigona* Klaus 1964, *Triadispora falcata* Klaus 1964, *Triadispora suspecta* Scheuring 1970, *Triadispora staplinii*

(Jansonius) Klaus 1964, *Triadispora plicata* Klaus 1964, *Voltziaceaesporites heteromorpha* Klaus 1964. *Lunatisporites* sp., *Punctatisporites* sp., *Vesicaspora* sp., Trisaccate pollen, and lacustrine palynomorphs.
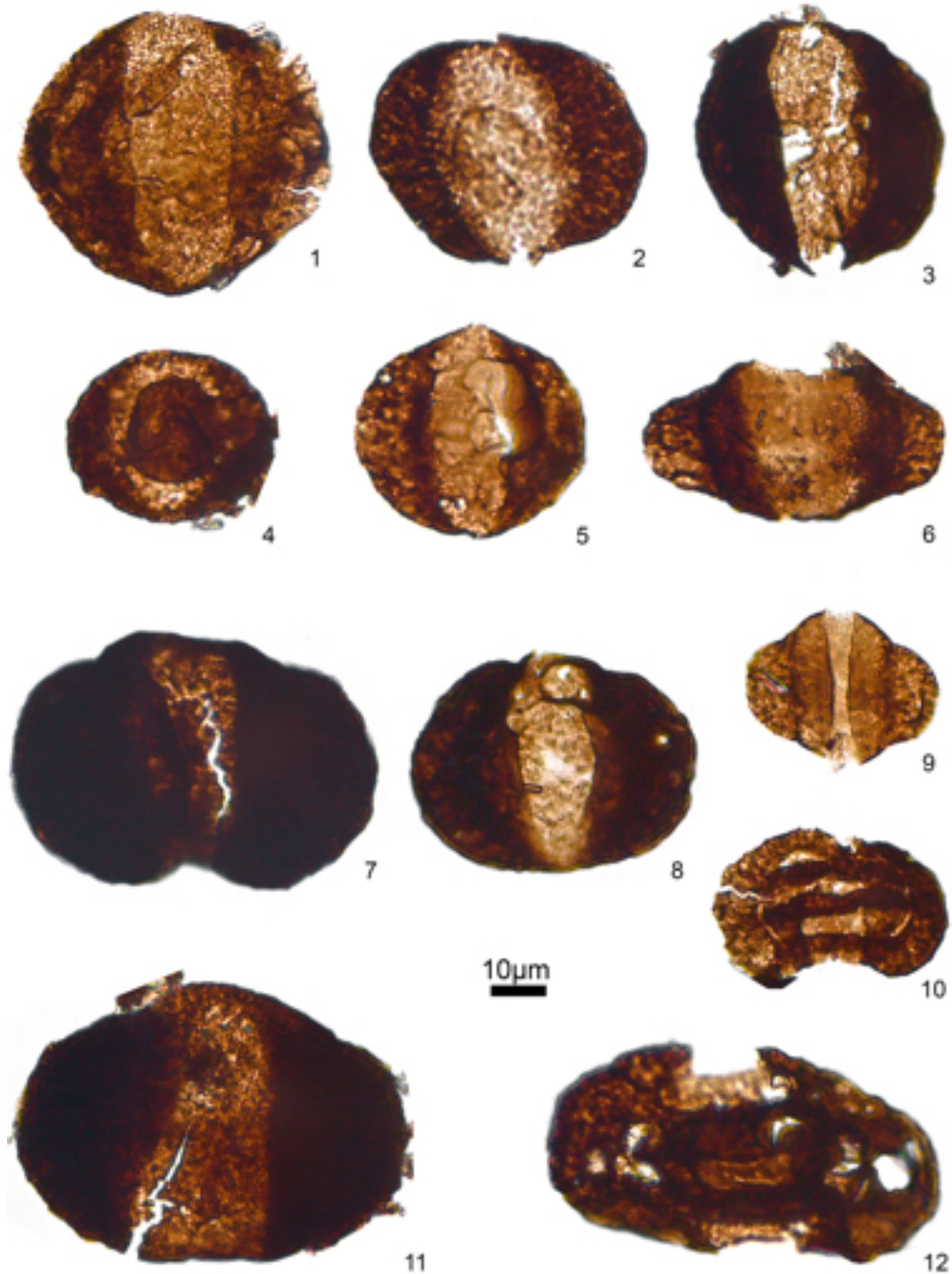
Figure 4.2.13. SuilsP8 palynological assemblage (Bunt). 1: Alisporites grauvogeli. 2: Alisporites grauvogeli. 3: Alisporites opii. 4: Triadispora epigona. 5: Triadispora plicata. 6: Triadispora falcata. 7: Triadispora suspecta. 8: Triadispora staplinii. 9: Microcachryidites sittleri. 10: Lunatisporites noviaulensis. 11: Voltziaceaesporites heteromorpha. 12: Lunatisporites sp.

Figure 4.2.14. SuilsP8 palynological assemblage (Bunt). 1: Chordasporites singulichorda. 2: Striatoabieites aytugii. 3: Vesicaspora sp. 4: Calamospora tener. 5: Sulcosaccispora minuta. 6: Hexasaccites muelleri. 7: Hexasaccites muelleri. 8: Punctatisporites fungosus. 9: Punctatisporites sp. 10: Trisaccate pollen 11: Lacustrine palynomorph 12: Lacustrine palynomorph.

4.3 Age assignation

4.3.1 Grey Unit age from palynology

The Grey Unit assemblage shows the presence the typical Upper Carboniferous ferns of the tedeleacean, zygoptetidaceae, gleicheniaceae and boctryopteridaceae groups (such as *Deltoidospora*, *Lophotriletes*, and *Spinosisporites*), the marattialean ferns (*Punctatosporites*) and lycopsids (*Lundbladispora*) are present here. The diversification of cordaite pollen (such as *Florinites* and *Latensina*) is also characteristic of this period.

The presence of monosaccate pollen such as *Guthoerlisporites* sp., *Nuskoisporites* sp., *Plicatipollenites* sp., *Potonieisporites simplex*, *Potonieisporites novicus* and the taxa *Angulisporites splendidus*, *Latensina trileta*, *Lundbladispora gigantea*, *Savitrisporites camptotus* and *Dictyotriletes* sp. (with Stephanian affinity, Juncal et al., 2019), in the studied samples suggests a Gzhelian age (Fig. 4.3.1). Moreover, the Grey Unit microfloral assemblage is comparable with the "Zone inférieure" of Broutin (1986), which is equivalent to the microflora of Assise d'Igornay (Doubinger, 1974) dated as late Gzhelian (299.91 ± 0.38Ma, Pellenard et al., 2017).

This age also fits very well with the absolute radiometric ages provided by Pereira et al. (2014), obtained from volcanic rocks interbedded in the Grey Unit deposits in the two neighbouring areas of Coll de Vanses (304.6 ±1.5 Ma) and the Cadí Ignimbrite (300.4 ±1.4 Ma, Table 2.1.3).

4.3.2 Transition Unit age from palynology

The Transition Unit presents Upper Carboniferous taxa with Stephanian affinity, such as *Angulisporites splendidus*, *Crassispora kosankei*, *Densosporites suhus*, *Densosporites spinifer*, *Latensina trileta*, *Savitrisporites camptotus*, *Florinites*

mediapudens, *Florinites junior, Spinosporites spinosus*, *Thymospora thiesseni* and *Lycospora* spp. The presence of fern spores such as *Acanthotriletes*, *Deltoidospora*, *Granulatisporites*, *Lophotriletes* and *Microreticulatisporites*, which are linked to the Carboniferous hygrophilous microflora, are indicative of a humid period.
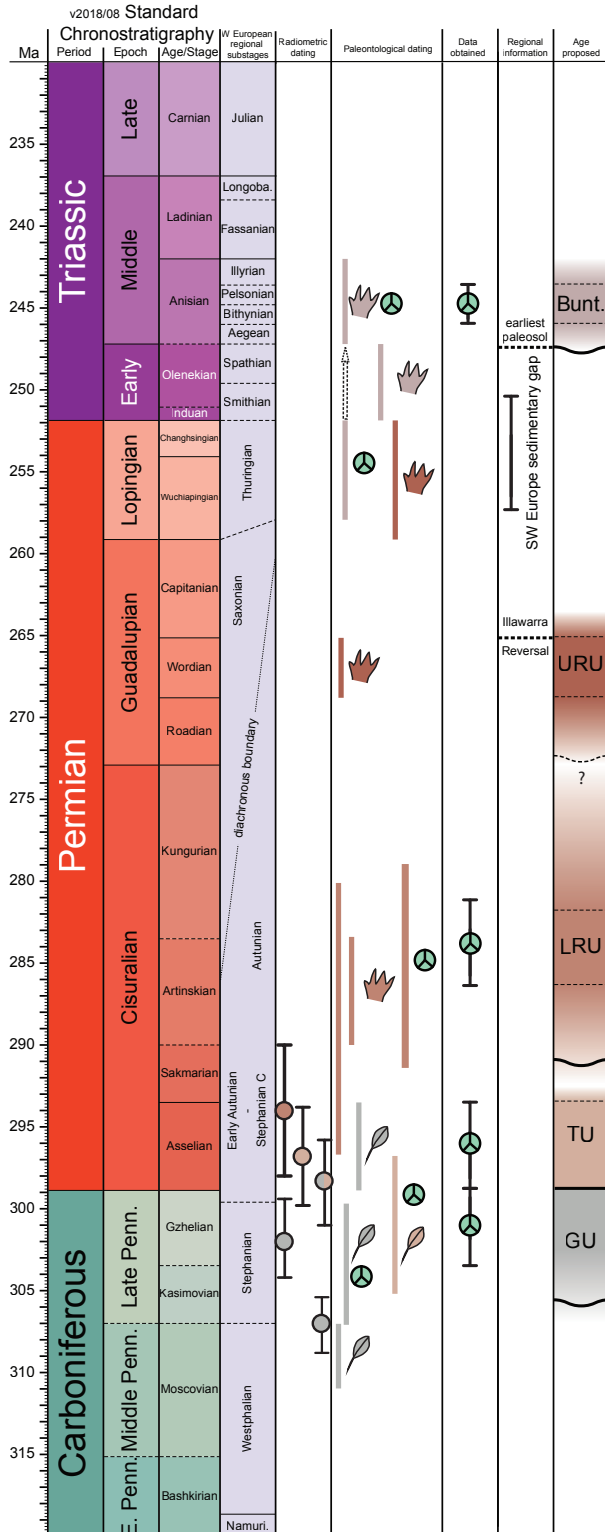
Figure 4.3.1. Age inferred of the stratigraphic units of the Central-Eastern Southern Pyrenees from the palynological data obtained and other biostratigraphic data (Tables. 2.1.2, 2.1.3).

65

The TU assemblages could be equivalent to the *Angulisporites splendidus-Latensina trileta* (ST) zone of Clayton et al., (1977) with a Stephanian A-B age (Fig. 4.3.1), but the radiometric dating from Estac ignimbrites indicate an Asselian age (296,2 ±3,1 Ma, 296,1 ±4,0 Ma; Pereira et al., 2014).

This singular difference in age between the two dating methods due to the fact that the isolated basins of the Central-Eastern Southern Pyrenees acted as a refuge with more favourable conditions for the Carboniferous hygrophilous flora, delaying the appearance of the meso-xerophytic floras. This reappearance of the Carboniferous-type wetland biome (Paquette et al., 1980; Broutin, 1986; Broutin et al., 1990a; Galtier and Broutin, 1995) in landscapes dominated by conifers is interpreted as stream and lakeside elements (DiMichele et al., 2006; Gand et al., 2013).

4.3.3 Lower Red Unit age from palynology

The microflora of the LRU assemblage shares characteristics with that of Zone A2 (Asselian-Sakmarian age) and Zone A3 (Kungurian-Roadian age) from Doubinger (1974) for the Autunian microflora of the Autun, Blanzy, l'Aumance, Brive and Lodève Basins, which are equivalent to the Bissacates striatiti (DS) Zone of Clayton et al. (1977), with a "Late Autunian" age (Sakmarian-Artinskian age) due to the presence of bisaccated pollen, striated taxa, and *Vittatina* spp. The microflora of Zone 2 is characteristic of Assise de Muse (Doubinger, 1974), recently dated as Asselian age (298.57 ±0.38 - 298.05 ±0.39 Ma) by Pellenard et al. (2017), and the Tuilière and Usclas, Saint-Privat, from the Lodève Basin (Doubinger, et al., 1987), dated as Sakmarian age (Tuilière - Loiras Fm., 293.85 ±0.10 Ma. Michel et al., 2015). The microflora of Zone 3 is equivalent to the

Gourd du Diable in Brive Basin (Doubinger, 1971) and the Charmoy schists of Blazy Basin (Doubinger, 1968) with a Kungurian-Roadian age (Doubinger, 1974).

Therefore, an intermediate age between Zone A2 and Zone A3 (Doubinger, 1974) could be suggested for sample GT-10.

We also compare LRU with the Artinskian to Ufimian palynological assemblages from the central Southern Alps, Italy (Cassinis and Doubinger, 1992). This work presents two palynological studies of the Collio and Tregiovo formation. The age range for the Permian volcanic activity of the Collio Basin in Eastern Lombardy was constrained from single-zircon U-Pb ages as early uppermost Artinskian-Kungurian age (283 ±1 to 281 ±2 Ma, Schaltegger and Brack 1999, 2007; Marocchi et al., 2008). The volcanic rocks of the Tregiovo basin were also radiometrically dated at 274.1 ±1.6 Ma and 276.5 ±1.1 Ma (e.g., Avanzini et al., 2007; Marocchi et al., 2008), attributing the Tregiovo Fm to the middle Kungurian.

The LRU assemblage is related to the Collio Fm assemblage and lower assemblage of Tregiovo Fm. Moreover, in the Gotarta Section, the presence of the Autunian Zone 2 palynomorphs (Doubinger, 1974) is accompanied by *Falcisporites zapfei*, *Jugasporites delasaucei*, *Lunatisporites noviaulensis* and *Paravesicaspora splendens*. That indicates a late Artinskian-Kungurian age for the LRU assemblage.

The age assigned to the LRU assemblage (Fig. 4.3.1) is consistent with the absolute radiometric age provided by Pereira et al. (2014), obtained from volcanic rocks interbedded in the Lower Red Unit deposits (283.4 ±1.9 Ma age. Pereira et al., 2014).

4.3.4 Buntsandstein Unit age from palynology

The sample SuilsP8 has an Anisian age due to the presence of the guide taxon *Hexasaccites muelleri.* The taxon *Voltziaceaesporites heteromorpha* indicates that the

sample cannot be younger than Pelsonian. The presence of the taxa *Alisporites grauvogeli, Microcachryidites sittleri* and *Striatoabieites aytugii* suggests an age close to the Bithynian-Pelsonian transit (Fig. 4.3.1). The presence of the taxa *Calamospora tener, Chordasporites singulichorda, Lunatisporites noviaulensis*, *Punctatisporites fungosus*, *Sulcosaccispora minuta* and *triadispora* spp. is consistent with this conclusion.

This microflora is equivalent to the "Eslida assemblage" (from Eslida Fm., SE Iberian Ranges, Spain. Juncal et al., 2018), due to the presence of *Alisporites grauvogeli*, *Alisporites opii*, *Calamospora tener*, *Hexasaccites muelleri*, *Lunatisporites noviaulensis*, *Punctatisporites fungosus* and *Voltziaceaesporites heteromorpha*. This assemblage corresponds to the *Voltziaceaesporites heteromorpha* Assemblage Zone, from boreholes in the Buntsandstein Strata of Western and Central Poland (Orlowska-Zwolinska, 1984, 1985; Kürschner and Herngreen, 2010) that is equivalent in age to the Triassic sections from the Southern Alps (Brugman 1986; Roghi 1995) and Assemblage A from the Dont Formation of the Kühwiesenkopf section (Kustatscher and Roghi, 2006; Kustatscher et al., 2006).

5. Sedimentology of Erill Castell-Estac Basin

5.1 Introduction

The sedimentology have been used for several authors to understand the depositional environment in the past (Kindle, 1917; Nevin and Trainer, 1927; Allen, 1963; Langford and Chan, 1989). The paleoenvironments reveals potential climatic issues as well as key information to reconstruct the paleogeography (Rust et al., 1985; Platt, 1989; Bourquin et al., 2007, 2011; Durand and Boruquin, 2013). From this basis the sedimentological study of Erill Castell-Estac Basin is one of the main objectives of this PhD thesis.

In spite the good preservation of the outcrops in the Central-Eastern Southern Pyrenees few works detailed sedimentological works have been published (Mey et al., 1968; Nagtegaal, 1969; Gisbert, 1981; Besly and Collinson 1991; Gretter et al., 2015). In particular Erill Castell-Estac Basin in the most unknown basin, only Besly and Collinson (1991) studied in a concrete sector (ErillCastell) the sedimentology. The aim of this chapter is study in detail more outcrops and sectors to cover all of this basin and provide an overall view of the sedimentology of the basin. From this point 10 detailed stratigraphic sections have been studied (Fig. 5.1.1) across the studied sector.

The sedimentological information allow to understand the paleoenvironmental conditions occurred in the Upper Carboniferous-Lower Triassic times and their evolution in the time. Moreover, the sedimentology and stratigraphy will be the basis of the following approaches of this thesis. The precise situation in the stratigraphy and the depositional environment information couple the pedogenesis study (Chapter 6) and the sampling of isotopes and clay mineralogy samples.

Further more of a classical sedimentological study, he interaction between the sediments and the syn-sedimentary tectonics is other goal of the study of Erill Castell Basin. These aspects are deal in the discussion chapter.
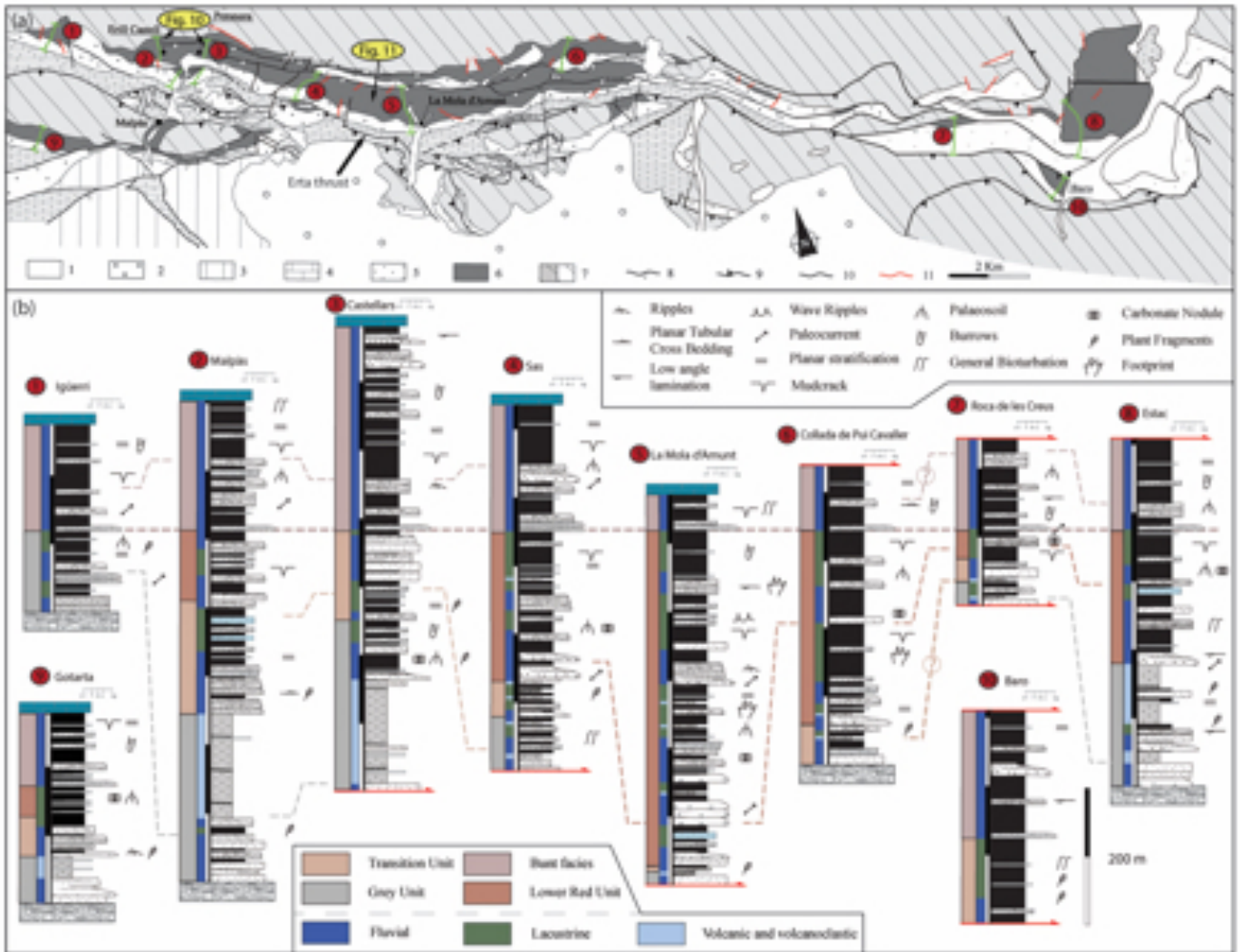
Figure 5.1.1. (a) Geological map of the Erill Castell-Estac Basin based on Saura (2004) and Saura and Texiell (2006). (1) Quaternary (2) Cenozoic cover (3) Jurassic-Cretaceous (4) Marine Triassic (5) Lower-Middle continental Triassic (Bunt.) (6) Late Carboniferous-Permian (7) Variscan Basament (8) Back-thrust (9) Inverse fault (10) Normal fault (11) Late Carboniferous-Lower Triassic synsedimentary faults. (b) Stratigraphic sections measured with the principal sedimentary structures in the Erill Castell-Estac Basin. The position and distribution of the reference levels are shown in dash lines. c-l: Clay-Limestone. f: fine sandstone. m: medium sandstone. c: coarse sandstone. cg: Conglomerate. Gotarta and Baro sections are not correlated due are placed in different thrust sheet (Erdo-Gotarta slice and Arcalís-Espaén slice, Saura and Teixell, 2006). The sections boundaries are marked by basement (chaotic representation), faults (red lines) and Triassic Marine deposits (top blue carbonates). From Lloret et al. (2018).

5.2 Facies and architectural elements

The sedimentary analysis is based on facies description and their vertical and lateral stacking pattern, in order to identify facies associations and architectural elements. These associations and elements will form the basis for the definition and interpretation of the sedimentary record of the three differentiated fluvial, lacustrine and volcaniclastic genetic groups. The descriptions in this chapter include Carboniferous, Permian, and Triassic rocks.

5.2.1 Fluvial deposits

Fluvial deposits have been observed as channels and overbank (levees, crevasse splays) sub-environments in Carboniferous, Permian, and Triassic units. Their description and interpretation is based here on six differentiated architectural elements, which are, in turn, obtained from the characterization of eleven lithofacies, as shown in Table 5.2.1 and Figure 5.2.1. In this work, we have basically followed the Miall's (1996, 2014) classification codes, adding some newer ones. The vertical and lateral stacking patterns of these facies in the constitution of architectural elements are shown in Figures 6, 8 and 9. These figures also show the occurrence of these elements in the stratigraphical units

Fluvial channel elements (Fig. 5.2.2)

Gravel Bar deposits (GB): This element is composed of interbedded sequence of coarse conglomerates made up of matrix-supported planar cross-stratified conglomerate (Gmp; Fig. 4c), matrix-supported trough cross-bedded conglomerates (Gmt) and clast-

Fluvial

	Code	Facies description	Interpretation	G.U.	T.U.	L.R.U.	BUNT.	Graphic representation
coarse-grained lithofacies	**Gh**	Clast-supported coarse-grained conglomerates with rounded to sub-rounded 3-10 cm-sized cobbles. Crudely horizontal bedding.	Longitudinal bedforms, lag deposits		•	•	•	1.5m
	Gmt	Matrix-supported trough cross-bedded conglomerates and sandstones, up to 6 cm-sized sub-rounded pebbles. Locally weak graded, beds have commonly non-channelized erosive bases.	Minor channel fills		•	•	•	0.5 m
	Gm	Matrix-supported massive or crudely bedded conglomerates. Clasts (6 cm of maximum size) are sub-rounded and commonly imbricated.	Longitudinal bars		•	•	•	0.5 m
	Gmp	Matrix-supported planar cross-stratified conglomerates and sandstones. Sub-rounded to rounded up to 4 cm-sized pebbles. Tabular to wedge-shaped sets reach 20 cm in thickness.	Planar bedflow from traction by a unidirectional current		•	•	•	0.7 m
medium-grained lithofacies	**St**	Fine to medium trough-cross-bedded sandstones. Fining upwards sets make up thicknesses of several tens of centimetres.	Dune migration	•	•	•	•	0.2 m
	Sp	Fine to coarse sandstones with planar cross-stratification. Cross-bedding is typically at or near the angle of repose, with sharp and angular terminations.	Transverse bar migration	•	•	•	•	0.5 m
	Sr	Fine to medium sandstones with ripple cross-laminations. Sets are rarely larger than 10 cm in thickness. Cosets form thicknesses of few decimetres.	Ripple migration by unconfined tractional flows in lower regime	•	•	•	•	0.2 m
	Ss	Sandstone, medium to coarse. Solitary (20 cm) or grouped beds with epsilon cross-bedding.	Isolated meandering fluvial channels	•	•	•	•	0.4 m
	Sh	Fine to medium horizontally-stratified sandstones. Single beds are about 50 cm thick. Colour: red and grey/greenish.	Horizontal laminations in planar bedflow (upper flow regime)	•	•	•	•	0.5 m
	Se	Fine to medium sandstones with erosional scours surfaces and intraclasts. Basal well-rounded pebbles of several cm sizes, are followed by fining-up sandstones with cross-laminated sets.	Scour - and - fill deposits	•	•	•	•	0.75 m
fine-grained lithofacies	**Fl**	Massive or fine laminated sandstones and siltstones in a fining upward trend. Bioturbation traces, both burrows and rhizoliths, commonly appear into sandstones and siltstones respectively.	Overbank, abandoned channels or drape deposits	•	•	•	•	~ 1 m
	Fr	Massive bioturbated mudstones and siltstones with greenish/greyish root marks. Beds with any primary sedimentary structures.	Abandoned channel or near channel deposits	•	•		•	2.5 m
	C	Coal stringers and mudstones with high organic content and plant accumulation (leaves and stalks). Colours: black, grey, green.	Vegetated swamp deposits	•	•		•	1 m
	P	Mudstones and siltstones with carbonate nodules, as the results of the gradual coalescence of carbonate cements; these, locally, can constitute more or less continuous carbonate levels.	Soil with chemical precipitation	•		•	•	1.5 m

Table 5.2.1. Summary of sedimentary facies classification and interpretation (modified after Miall, 1996, 2014) recognized in the field. The facies codes are generally made up of a capital letter, which abbreviates the grain size, followed by one or two lower-case letters summarizing the facies' main characteristics.

72

supported coarse-grained conglomerates (Gh) facies, and it may present fine-grained laminated sandstone facies (Fl) on top. The single sequence thickness is 1-2 m, and the vertical repetition of GB sequences (up to 7) reaches 10 m in the basal parts of the TU and the LRU (Fig. 5.3.1). The conglomerates are composed of quartzitic-pebbles up to 6 cm in size, which are commonly sub-rounded and weakly-graded with horizontal and imbricated alignments (Gh). Parallel lamination and bioturbation traces are the main characteristics of the fine sediments at the top of the sequences. The basal contact of this element is strongly erosive and its lateral continuity is up to 30 m.

Interpretation: The coarse massive framework-less elements are related to mesoforms and amalgamated mesoforms constituting longitudinal and transverse gravel bars (Ramos et al., 1986; Ashmore, 1991; Miall, 1996). The clast size suggest a highly energetic system, which could be related to the proximal-middle zones of a fluvial distributary system. The gradational transition from gravel to fine sands indicates a single event characterized by abrupt deposition that triggers channel obstruction and subsequent filling (Fl) in a single event (Rust et al., 1985; Owen et al., 2017). Mesoform development in gravel-bed rivers is strongly affected by the nature of gravel transport, which is normally not regular at any point in a braided system but operates as a series of pulses (Hoey, 1992).

Channel deposits (CH): This element is characterized by conglomerates and sandstones forming packages up to 2 m thick. Incisional concave-upward bases are generally marked by undulating fourth-order bounding surfaces (Miall, 1996, 2014) and well-defined lateral morphology uninterrupted by other elements. The overall vertical stacking pattern results from the association of several main bottom-to-top facies
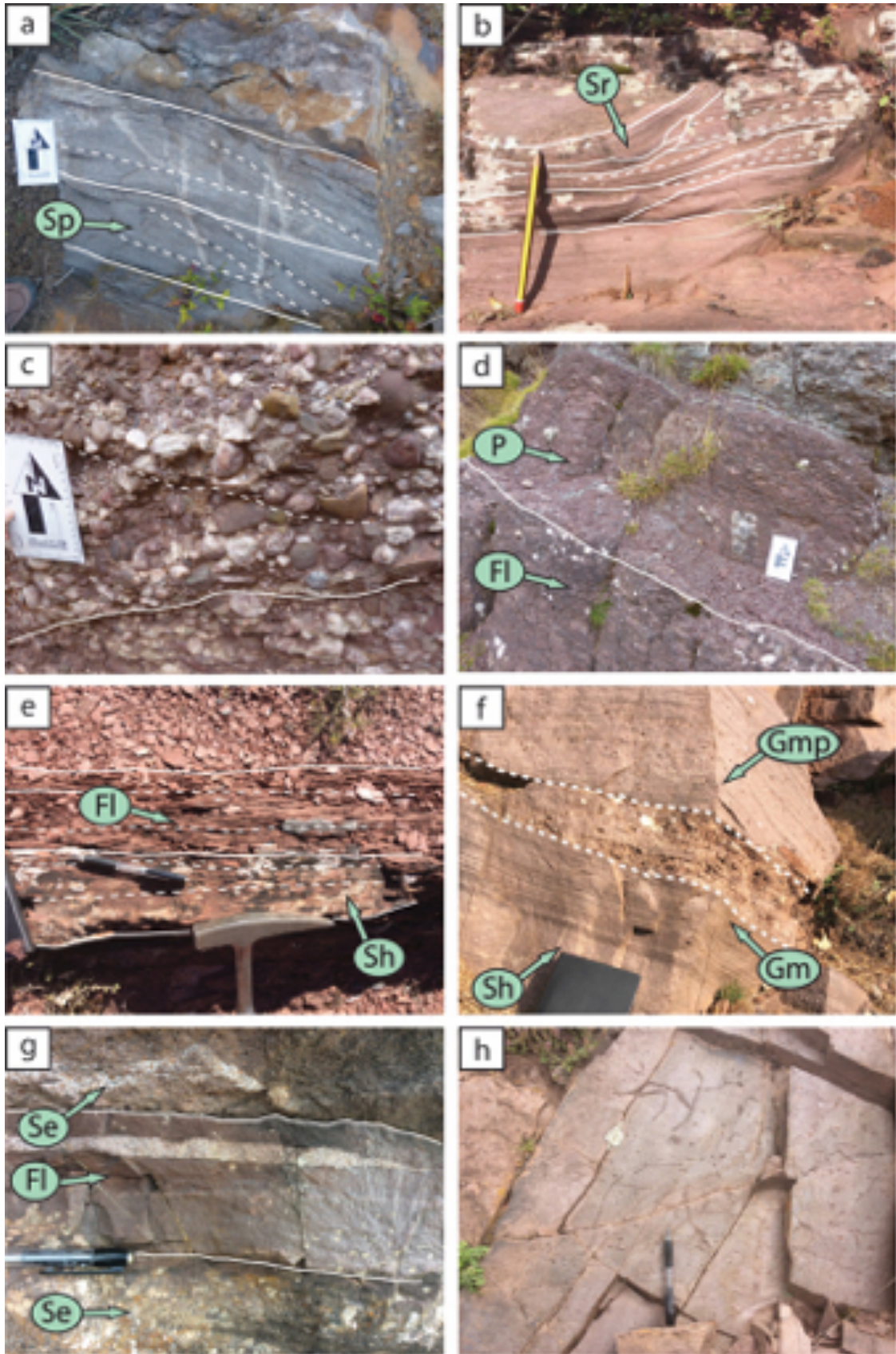
Figure 5.2.1. Representative fluvial lithofacies and sedimentary structures recognized in the field. (a) Sp sandstone with cross-bedding structure (TU). (b) Buntsandstein Sr lithofacies with ripple cross-laminations. (c) Coarse-grained conglomerate corresponding to the Gh facies, basal Buntsandstein. (d) Fl and P lithofacies with massive aspect and carbonate nodules, respectively (LRU). (e) Sh lithofacies with horizontal stratification and Fl with fine lamination (Bunt.). (f) Sh, Gm and Gmp lithofacies of the middle Buntsandstein facies. (g) Se with erosional surface and Fl with horizontal laminations (LRU). (h) Fl lithofacies with intense bioturbation (Bunt.).

successions: coarse basal lag, matrix-supported planar cross-stratified conglomerates and sandstones (Gmp, Fig. 5.2.1f) and fine- to medium-grained horizontally stratified sandstones (Sh, Fig. 5.2.1e), occasionally with bioturbation and ripples (Fl and Fr) but mostly presenting erosion surfaces

Interpretation: This element usually represents the infill of an active fluvial channel form. The presence of multiple internal levels of erosive contacts together with multiple filled channel facies represents lateral refill and vertical stacking of amalgamated fluvial channel facies over time. Fine sand facies at the top indicate the refill of minor channels, including abandoned channel and chute channel facies generated during falling water stages (Hopkins, 1985; Owen et al., 2017).

Sandy Bedforms (SB): This element is mostly made up of fine/medium-grained sandstones with cross-bedded facies (St), tabular beds (Sp facies) and small-ripple cross-beds or climbing-ripple laminations (Sr facies, Fig. 5.2.1b). Overlying these facies is the finest part of the sequence, characterized by silty laminated facies (Fl), siltstone facies (Fr) with common carbonate nodules and bioturbation (P facies). This architectural element reaches a thickness of up to 3 m and constitutes clear fining-upward sequences when finer sediments (Fl, Fr and P) are preserved in the upper part. Vertical stacking of these elements may reach up to 15 m in thickness and are separated by internal erosive surfaces.

Interpretation: This element represents flow-regime bedforms that form in mid-channel sand dominated river systems that actively migrate during floods (e.g., Coleman, 1969; Colombi et al., 2017). Vertical stacking of different bedform types indicates long- or short-term changes in flow regime (Godin, 1991). The finer sediments with small-scale structures at the top were deposited during falling water stages.

Lateral Accretion deposits (LA): This element is characterized by sharp and often erosional bases, on which the associated facies assemblages are generally composed of basal lags of crudely bedded conglomerates (Gh) of a few centimeters thick, overlain by medium-to-coarse sands with epsilon cross-bedding (Ss), small-scale planar and trough-cross bedded sandstones (Sp and St, Fig. 5.2.1a), with fine-grained facies (Fl, Fig. 5.2.1g, h) at the top. In the sandy part wedge-like sheets (0.20 m thick) are commonly characterized by minor internal erosional surfaces. Individual basal coarse bodies are 0.10 – 0.20 m thick.

Interpretation: This architectural element is interpreted as the depositional product of active channel-belts by lateral bar growth. The accretion surfaces testify to the lateral migration of meander point bars (e.g., Stear, 1983; Sambrook Smith et al., 2016; Wu et al., 2016).

Fluvial overbank elements (Fig. 5.2.2)

Floodplain Fines deposits (FF): This element is exclusively composed of fine-grained facies associations and its basal surface is not channelized. Sheets have large lateral continuity and consist of fine-laminated siltstones and sandstones (facies Fl, Fig. 5.2.1g*)* interbedded with thin lenses of sandstones (up to 0.10 – 0.30 m thick), sometimes with ripples. Massive bioturbated siltstones (Fr) may also occur as thin intercalated layers. Coal levels (facies C, Fig. 5.2.3b) may occur only in the Grey and Transition Units. Individual elements are generally 0.30-0.40 m thick. The pedogenic alteration (facies P, Fig. 5.2.1d) commonly occurs as multi-horizon paleosols, with root relicts and very distinct calcrete levels.

Interpretation: This element constitutes the sedimentary product deposited during overbank flow; the dominant process is generally the non-channelized fluxes (e.g.,

Wakelin-King and Webb, 2001; Müller et al., 2004; North and Davidson, 2012). This element is characteristic of flooded areas away from channel belts and located in distal zones of alluvial plains with development of floodplain paleosols (Smith et al., 1989; Platt and Keller, 1992; Ghazi and Mountney, 2009). Coal beds commonly appear interbedded with fine-grained overbank sediments, sometimes overlying or underlying crevasse-splay deposits (e.g., Hacquebard and Donaldson, 1969).

Crevasse splay Channel (CC): Siltstones and sandstones settled in horizontally stratified/laminated facies (Sh, Fl) and tabular/planar stratified facies (Sp) with associated ripple cross-laminated sandstones (Sr) and bioturbation. This element may extend from a few decimeters to several meters in thickness when this element is repeated in vertical successions. This element usually grades upward into the coarser terms.

Interpretation: These fine siltstones, sandstones and related sequences represent crevasse-splay and natural levee elements, with interbedded overbank fines (Donselaar and Schmidt, 2005; Simon and Gibling, 2017). Cumulative crevasse-splay successions are common in the sedimentary record (Bown and Kraus, 1987), and they may extend some km away from the channel margins.
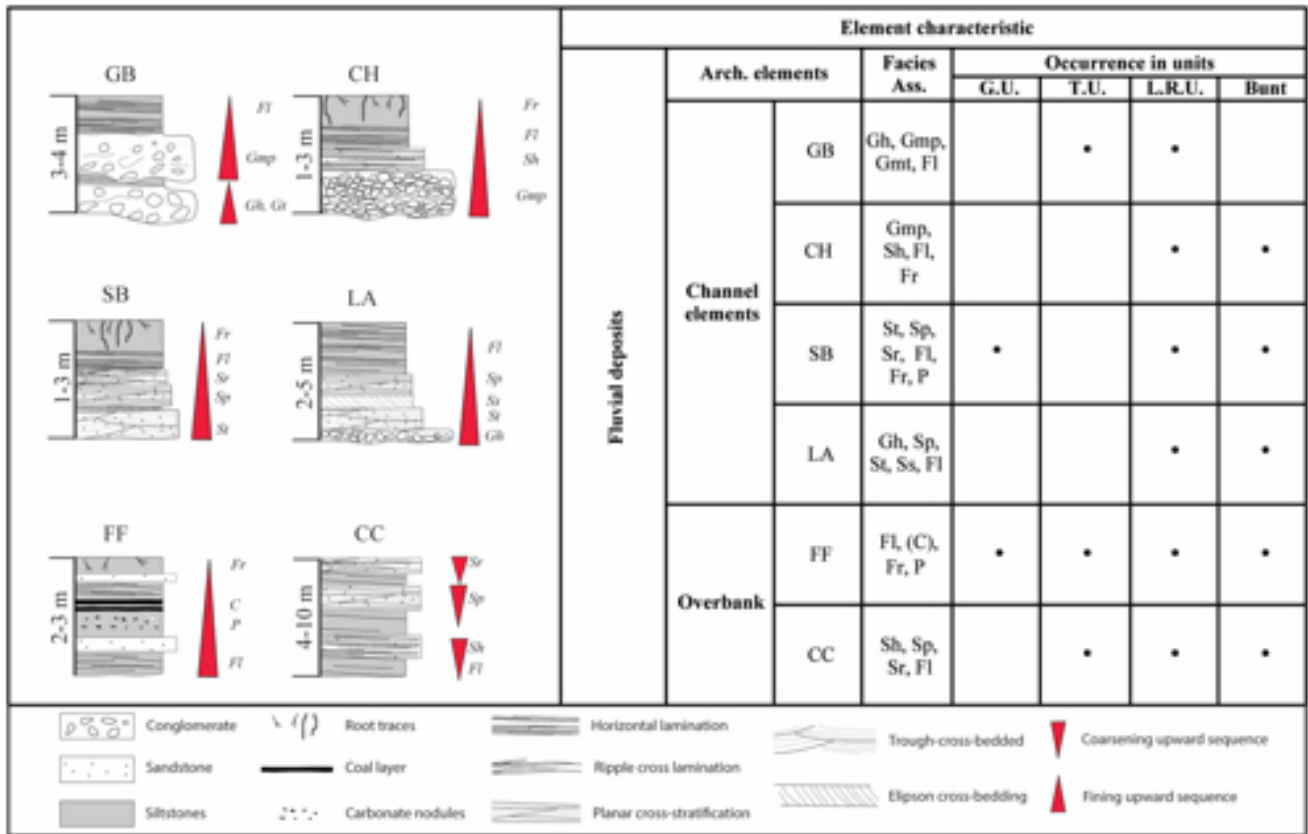
Figure 5.2.2. Representative facies associations and architectural elements of fluvial and alluvial deposits. Fluvial codes are taken from Miall (1978, 2014).

5.2.2 Lacustrine deposits

The description and interpretation of these deposits is here based on the differentiation of five facies and their vertical and lateral combinations, in order to constitute four facies associations, L1 to L4 (Fig. 5.2.4). The description and interpretation of these facies is shown in Table 5.2.2, and their representative field pictures in Figure 5.2.3. Lacustrine facies are separated into marginal and shallow water facies associations. These associations and their occurrence in the different stratigraphical units are shown in figure 5.2.4.

| Code | | Facies description | Interpretation | Stratigraphic units (Gisbert, 1981) | | | | Graphic representation |
				G.U.	T.U.	L.R.U.	BUNT.	
Gm_L	marginal / Lacustrine	Matrix-supported conglomerates with erosive. Clast range size is 5-15 cm, usually subangular-subrounded, poorly selected. Carbonate clasts may occur.	Proximal lag deposits of shallow water	•				1.5m
Sm_L	marginal / Lacustrine	Fine-medium size sandstone matrix-supported, greyish-reddish coloration in 0.2 to 1 m thick. Alternate with finest fractions. Poor horizontal lamination and also bioturbation and root traces occurs.	Marginal lake deposits		•	•	•	0.5 m
Fm_L	shallow water / Lacustrine	Mud-cracked mudstone with limestones 0.3 m thick as maximum. Alternation with red-dark siltstone might occur. Laminated structures not present, otherwise nodular aspect is common.	Playa-lake mud-flat deposits with disecation precesses	•	•	•		0.5 m
Fh_L	shallow water / Lacustrine	Siltstone with massive and laminated structure. Not over 0.1 m layers of very-fine sandstones. Coloration is variable among reddish to greyish. Carbonate nodules could be present.	Playa-lake mud-flat deposit	•	•	•	•	0.7 m
M_L	shallow water / Lacustrine	Massive red siltstone and claystone with weak horizontal lamination. Intense vertical root bioturbation and densely packed carbonate nadules.	Shallow lacustrine with fluctuant water level	•	•	•	•	0.2 m
dslBr	Volcanic-volcaniclastic	Matrix-supported fine grain with phanerocrysts of plagioclase (<1cm) and lithics. Fiames and plagioclase are strongly lined up with flow direction. Positive gradiation and lightly horizontal lineation.	Hydro-plastic flow, ignimbrite	•	•			0.5 m
mLTi	Volcanic-volcaniclastic	Massive lapilli-tuff matrix-supported facies. Isotropic organization and poorly sorted volcanic fragments. Non-stratified structures, thickness may reach 10 m. Very high matrix/clast ratio.	Fluid escape-dominated flow-boundary zone with pyroclast flow.		•	•		0.2 m
cA	Volcanic-volcaniclastic	Massive andesite with interbedded minor tuffs. Massive aspect, nevertheless 3-30 cm layers with flow surface discontinuities. Quarz and feldspar crystals are well preserved as well as vesicular features. Fine particles at the topmost.	Subaerial lava flow within ash deposits		•	•		0.5 m
//sT	Volcanic-volcaniclastic	Very fine grain tuffs with greyscale coloration within black millimetre levels. Centimetre parallel lamination in 5-10 cm bodies thick. Usually up-fining trend from fine to very-fine.	Ash fall deposits product of effusive volcanic activity.		•	•		2.5 m
mLBr	Volcanic-volcaniclastic	Massive lithic-rich matrix-supported breccia with mid-size matrix of volcanic fragments. Clasts presents vitreous with polygonal morphology.	High density debris flow proximal to effusive hydro-magmatic activity.		•			1 m
Ss_V	Volcanic-volcaniclastic	Fine to medium sandstone composed of re-worked volcanoclastic sediments with horizontal laminatons and low cross-beds. Occasionally presents weak channelized base.	Reworked deposit during inter-erupt period		•	•		1.5 m

Table 5.2.2. Summary of lacustrine and volcaniclastic facies codes recognized in the field; the fundamental diagnostic characteristics and interpretations have been modified following Branney and Kokelaar (2002), Aziz et al. (2003), Schnurrenberger et al. (2003) and D'Elia et al. (2012, 2018).

79

Lake margin facies associations (Fig. 5.2.4)

Lacustrine association 1 (L1): This association is broadly arranged in a fining upward sequence with an erosive base. It is represented by beds up to 0.25-0.30 m thick at the base, constituted by matrix-supported coarse-grained conglomerates with clasts generally less than 15 cm in diameter (Gm$_L$ facies, Fig. 5.2.3c). The upper part consists of laminated siltstone facies (Fh$_L$ facies, Fig. 5a), normally arranged in beds up to 1.5 m thick.

Interpretation: The presence of coarser basal "lag" in this association is interpreted as a marginal deposit (Valero-Garcés et al., 2014). This association is also interpreted as low-gradient margins of lacustrine zones under a subaerial environment. The fine water-saturated sediment remains were controlled by fluctuating lake levels (Calvo et al., 1995; Aziz et al., 2003).

Shallow-water facies associations (Fig. 5.2.4)

Lacustrine association 2 (L2): This association constitutes a coarsening-upward sequence of siltstones and sandstones, with Fh$_L$ and Sm$_L$ (Fig. 5.2.3a) as the main associated facies. Facies Fh$_L$ may be finely laminated and is mostly composed of siltstones that may contain carbonate nodules up to 0.10 cm thick, as well as mud cracks. Poorly structured sandstones commonly form thin laminated intervals several decimeters thick (Fm$_L$, Fig. 5.2.3b) at their base. Well-developed bioturbations appear in both facies. The whole succession may reach 0.8 m in thicknesses and its base is weakly erosive.

The succession may accrue several times vertically, reaching up to 2.6 m in thickness.

Interpretation: The presence of carbonate nodules suggests shallow water conditions with vegetation (Smooth and Olsen, 1988), and mud cracks indicate that deposits underwent subaerial conditions after deposition (Aziz et al., 2003). Therefore, we interpret this element as originating in a shallow-water lacustrine environment as a result of the filling of small ponds (Talbot et al., 1994).

Lacustrine association 3 (L3): This association is represented by centimetre-thick red siltstones and claystones characterized by variable amounts of carbonate nodules (M_L facies, Fig. 5.2.3d) alternating with massive or laminated siltstones beds (Fh_L facies). Massive and locally laminated sandstones (Sm_L facies) are characteristic of the topmost part of the sequence. This succession shows a coarsening upward trend and an overall thickness of 3 m. The base surface is sharp on the underlying deposits.

Interpretation: This association is interpreted as the sedimentary product of a palustrine fluctuating water level environment (Aziz et al., 2003). The Sm_L facies placed in the topmost suggest marginal conditions for this association, formed under low-energy conditions at the margin of a shallow lake subject to frequent changes in water level (Freytet and Plaziat, 1982).

Lacustrine association 4 (L4): This association is represented by a fine-grained association of facies essentially dominated by dark laminated siltstones (Fh_L facies) and tabular carbonate beds (Fm_L facies). The Fm_L facies occur mainly as a layer $0.10 - 0.20$ m thick. Carbonate beds cyclically follow the fine-grained siliciclastic levels and the cycles may reach up to 2 m. The overall thickness of this association reaches up to 4 m, in thinning and fining-upwards trends at outcrop-scale. The lateral continuity of this association may reach hundreds of meters. The basal surface is normally sharp.

Interpretation: This element is interpreted as a shallow lacustrine deposit with episodic flood discharges leading to rapid decantation of fine particles (Vandervoort, 1997). The darkness of the facies suggests reducing conditions after deposition (Aziz et al., 2003).

5.2.3 Volcanic-volcaniclastic deposits

For the volcanic and volcaniclastic deposits, we have followed the Branney and Kokelaar's (2002) facies classification (Table 5.2.2). The facies association (Fig. 5.2.4) observed have been related to Martí's works (1986, 1988). This elementary subdivision and its occurrence in the stratigraphical units are shown in Figure 5.2.4.

Volcanic element 1 (V1): This element is represented by a fining upward succession that starts with diffuse coarse-grained micro-breccia (dslBr, Fig. 5.2.3h) with an erosive surface at the base. Briefly, micro-breccias facies decrease in grain-size up to a diffuse boundary where tuff facies (mLTi, Fig. 5.2.3f) starts. The tuffs are bad classified and stratified. In the topmost part of this sequence, re-worked sandstones (Ssv) appear to erode the tuff facies. Lithics and flames-structures of 2-3 cm appear in the middle part of this bodies. The thickness of this element is variable. The basal (dslBr) lithofacies may reach a thickness of 50 cm, while tuff facies represent most of the succession and may reach a thickness of 5 m. The topmost sandstones bodies are restricted to 20-30 cm in thickness.
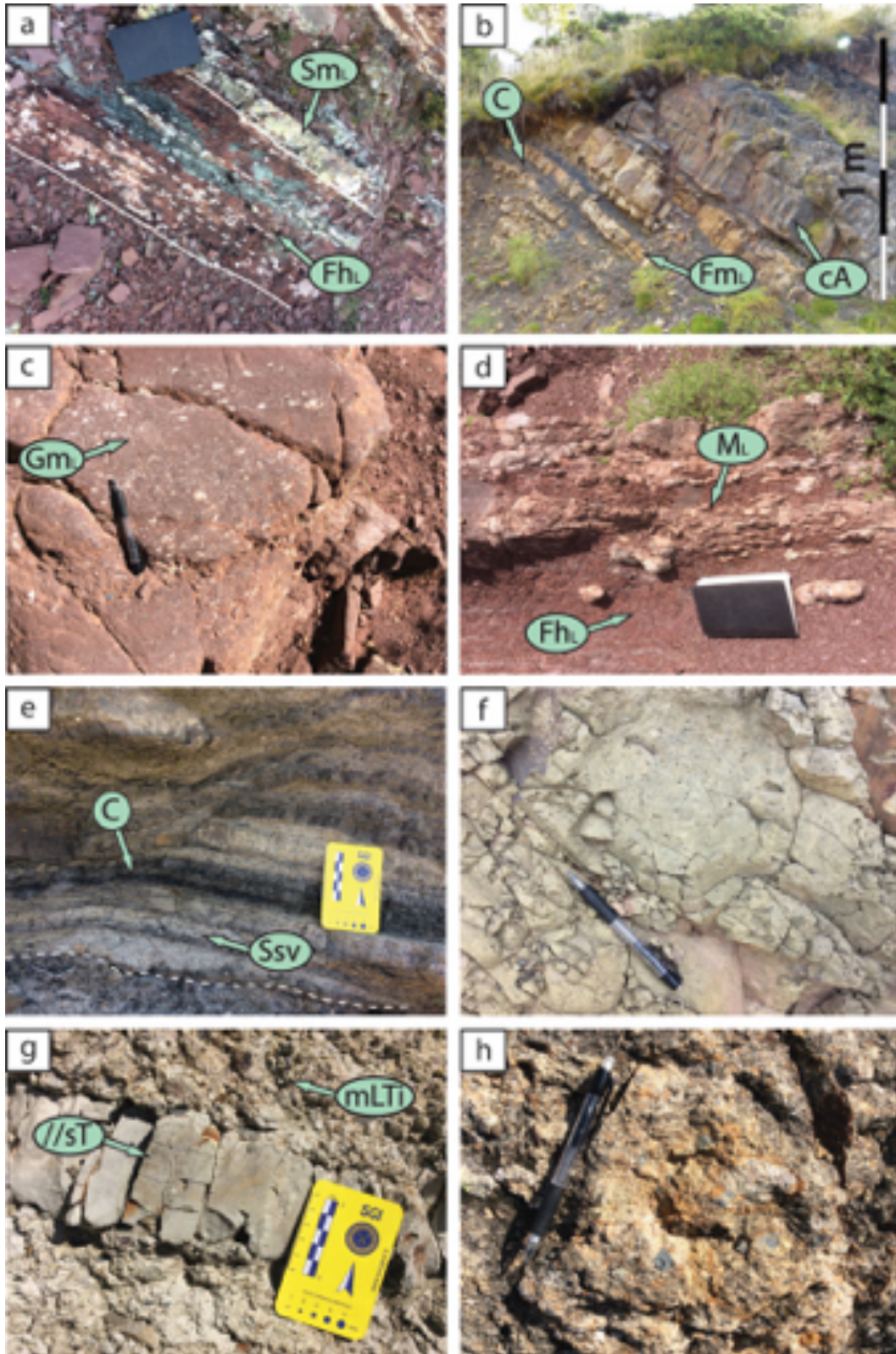
Figure 5.2.3. Representative lacustrine and volcanic lithofacies and sedimentary structures recognized in the field. (a) Lacustrine Fh_L lithofacies with horizontal laminations and greyish colorations corresponding to flooding episodes. Sm_L lithofacies with massive aspect (LRU). (b) Alternation of C and Fm_L lithofacies corresponding to lacustrine deposits, with a volcanic (cA) sheet layer (TU) set upward. (c) Gm_L facies corresponding to proximal lag deposits (LRU). (d) Fh_L and M_L deposits with laminar structures and concentrations of packed carbonates nodules. (e) Re-worked volcanic sandstones (Ss_V) with slightly erosive surface and carbon interstratified (lithofacies C), GU. (f) Massive lapilli deposits (mLTi) from the GU. (g) Medium-coarse volcanic tuffs (mLTi) with intercalation of ash fall deposits (//sT). (h) Coarse volcanic deposits (dslBr) from the GU. From Lloret et al. (2018)

Interpretation: This element presents a fining-upward trend followed by 20-30 cm thick sandstone beds at the top. The element is interpreted as an ignimbrite deposit related to the collapse of the vertical eruptive column (Martí, 1986; Martí and Mitjavila, 1988). The presence of lithics fragments and flames structures indicate hidromagmatic eruptions.

Volcanic element 2 (V2): This element is represented by a chaotic association heterometric and heterolitic tuffs (mLTi) reaching 3-4 m in thickness with interbedded reworked sandstones (Ssv, Fig. 5.2.3e). The coarser bodies present weak erosive surfaces and poor internal organization. The thickness of the Ssv facies is less than 30 cm but the lateral continuity of these bodies may reach tens or hundreds of meters.

Interpretation: This association is interpreted as pyroclastic "debris flow" deposit related with hidromagmatic eruptions or rain (Martí, 1986; Martí and Mitjavila, 1988). This element is defined as a lahar deposit, which are linked to volcanic eruptions or the remobilization of other pyroclastic deposits.

Volcanic element 3 (V3): Volcanic association of andesite layers (cA) of variable thicknesses (0.2 to 1 m). It mostly consists of a fining upward deposit succession of //sT volcanic facies (Fig. 5g) interbedded into cA facies. The thickness of this element may reach 200 m, and are usually located in the bottom parts of the stratigraphic column.

Interpretation: The interpretation of this association is the intermittent sub-aerial effusive lava episodes (Martí, 1986). The preservation of tuff deposits indicate a rapid cooling of andesite lava. The very fine //sT lava are interpreted by Martí (1986, 1988) as cinerites (pyroclastic fall deposits). The absence of any reworked deposit indicates a short

time lapse between lava flow and tuff deposits. In the LRU this element is not associated with lava deposits, and only cinerites appear in 20-30 cm thick levels.
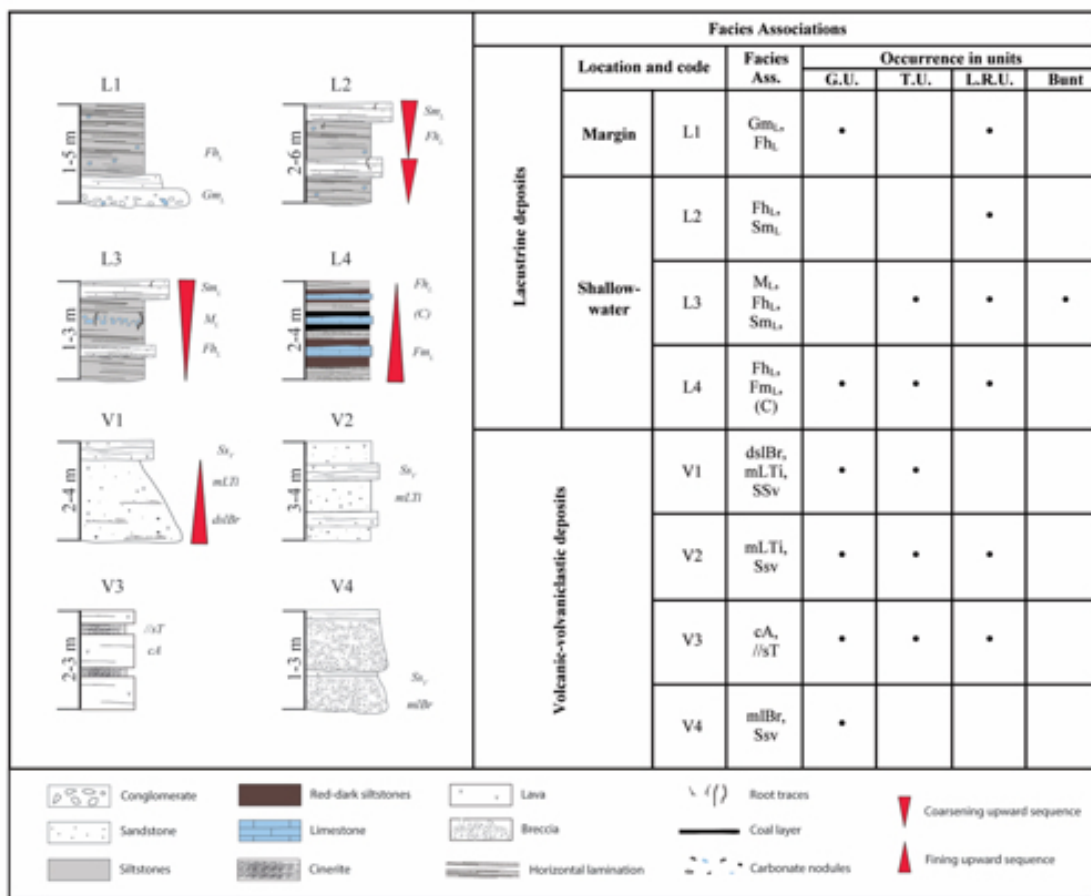
Figure 5.2.4. Representative facies associations and architectural elements of lacustrine and volcanic-volcaniclastic deposits. The lithofacies codes corresponds from Miall (1978, 2014) for lacustrine faces and for the volcanic and volcaniclastic lithofacies from Branney and Kokelaar (2002). From Lloret et al. (2018).

Volcanic element 4 (V4): This element is represented by matrix-supported breccias (mlBr) of poorly-organized volcanic clasts. Clasts are angular and up to 0.3 m in diameter. These facies reach up to 0.5 m in thickness and their base may be sharp or erosive. At the top, interbedded cross-bed sandstones (Ssv) with horizontal laminations (10-20 cm thick) appear. This association may reach 10-20 m in thickness. This element is normally associated with the element *V3*.

Interpretation: This facies association is present in the basal part of the stratigraphic section of the GU. Their lateral extension may reach 50 m long and are characteristic in many areas (e.g., Erill Castell, Estac, Gotarta). This association is interpreted as a co-ignimbrite lag fall deposits (Martí, 1986; Martí and Mitjavila, 1988). The interbedded sand (Ssv) deposits are interpreted as intermittent reworking time (Martí, 1986, 1996; Mujal et al., 2018).

5.3 Depositional evolution

The interpretation of the differentiated facies associations, their lateral and vertical successions and their occurrence in the stratigraphical units, make it possible to define the depositional evolution for each unit and the general vertical evolution in the whole sedimentary record.

Grey Unit (Fig. 5.3.1): This unit is constituted by volcaniclastics and fluviolacustrine sedimentary environments (V1 to V4; L1 and L4) with a smaller proportion of fine sediments of fluvial overbank (SB, FF) origin (Fig. 6). In general terms, the GU consists of a fining upward succession together with a decrease in volcanic influence over time. This unit usually starts with breccia deposits (V4, Fig. 5.3.1), interpreted as proximal fan product triggered by abrupt slopes. Its poor rounding and clast size suggest a short transport distance from the basin margins. The lowermost surface boundary represents the major erosion surface of the studied sedimentary record, separating the basement from the upper Palaeozoic and lower Mesozoic, the so-called "Variscan unconformity".

Upwards, a succession of andesitic volcanic bodies (V3), ignimbritic (V1) and ash fall deposits (//sT) may reach 200 m in thickness. The ignimbritic bodies extend for all the Erill Castell area, as indicated by Martí and Mitjavila (1988), while the andesite lava flows and lens-shaped tuff layers (V2) are more restricted. In the upper part of the GU, pure volcanic deposits yield reworked sandstones (Ssv lithofacies), associated incipient fluvial deposits (FF) and shallow-water lacustrine deposits with thick coal deposits (L4). The latter sedimentary setting is developed in most parts of the basin, presenting deposits ranging from shallow-water lacustrine to marginal lake deposits (L1). The presence of significant coal levels in the upper part of the GU indicates an environment with rich

vegetation in a humid climate context (Gascón-Cuello and Gisbert, 1987; Talbot, 1988; Mujal et al., 2018).

Transition Unit (Fig. 5.3.1): The basal boundary of this unit lies conformably on the GU (Fig. 2). This unit is composed of fluvial (GB, FF, CC) and lacustrine deposits (L3, L4) with volcanic and volcaniclastic deposits interbedded (V1, V2, V3) in a general fining upward trend. The basal deposits usually start with a Palaeozoic clastic breccia that evolves upward to ephemeral fluvial systems, mostly represented by poorly- organized gravel-channelized deposits and various associated overbank deposits (Fig. 5.3.1). As in
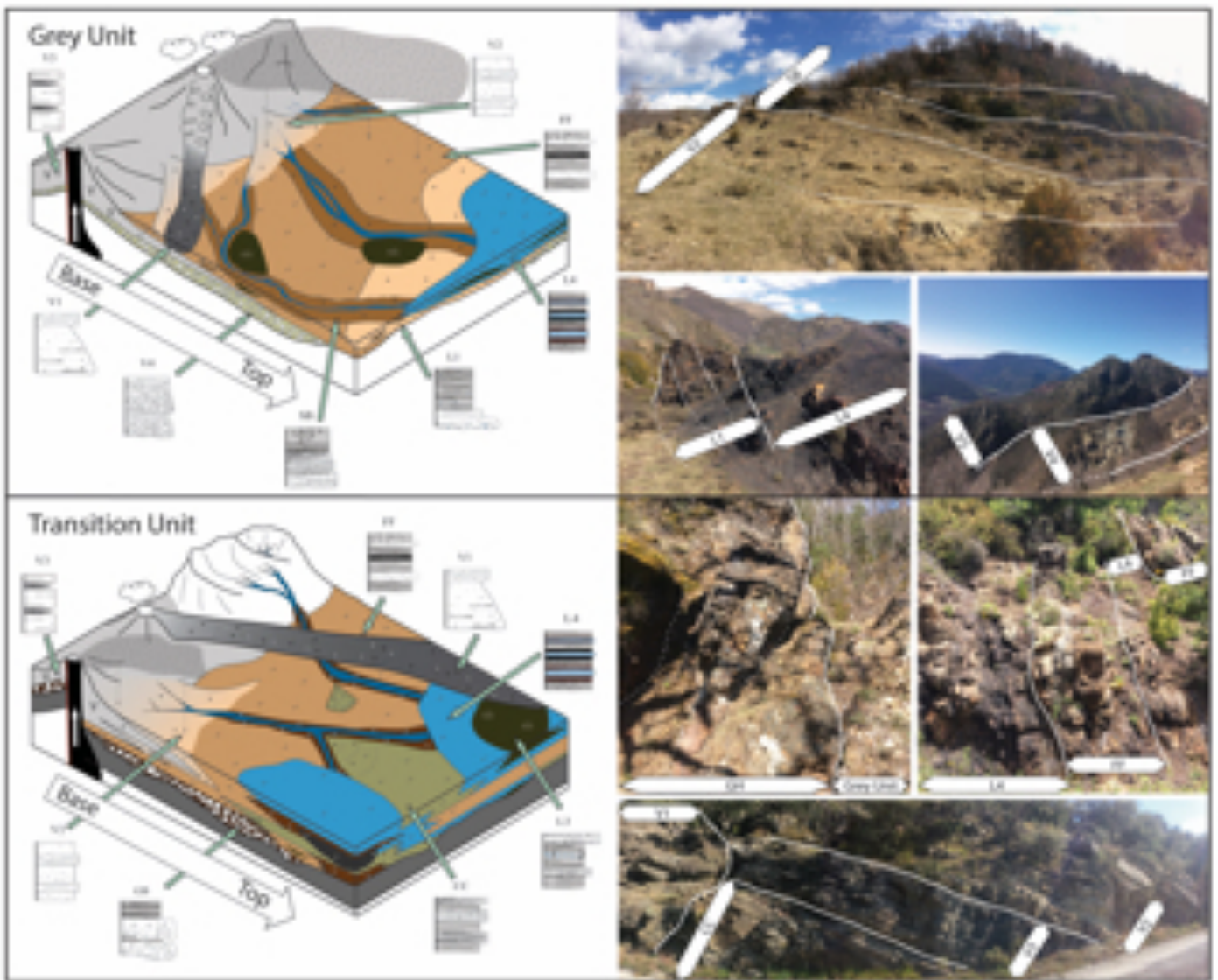
Figure 5.3.1. Paleoenvironmental reconstructions for the Grey Unit and Transition Unit related to the facies associations observed. From Lloret et al. (2018). Grey Unit photos: Malpàs and Gotarta sections; Transition Unit photos: Malpàs, Gotarta and Estac sections.

88

the GU, lacustrine sediments may present associated coal deposits, indicative of humid climates. However, the presence of palustrine carbonate levels with episodic flood discharges alternating with playa-lake carbonates, probably precipitating undersubaerial exposition (Janaway and Parnell, 1989), would indicate alternating wet and dry climates. The volcanic deposits are represented by pyroclastic flows (V1) that may reach a thickness of 10 m (Gotarta sector, Fig. 5.1.1b) and thin (1-2 m) andesite lavas (V3) set in the base of the TU, which also suggest syn-volcanic activity during the deposition of the unit. Also, tuff deposits (V2) are very common in this unit.

Lower Red Unit (Fig. 5.3.2): This unit lies unconformably on top of the TU and its presence is clear by a change in facies and by its red colour. The LRU is characterized by frequent sedimentary changes: fluvial (GB, CH, SB, LA, FF, CC), lacustrine (L1 to L4) and volcanic to volcaniclastic (V2, V3). The red-colored basal deposits are composed of fluvial channelized elements (GB and CH) and overbank elements (CC). Some channelized bodies represent meandering fluvial deposits. In the middle part, depositional environments correspond to lacustrine marginal elements (L1) and shallow-water elements (L2, L3 and L4). They are mostly represented by shallow-water lakes with episodic flood discharges (L4) and palustrine environments (L3) with about 200 m of lateral extention. In these facies there is no sign of any development of coal levels (C facies), with only a few plant fossils imprint being reported (Mujal et al., 2018). The vertical pattern of this middle part provides, however, an alternating succession of lacustrine and fine-grained fluvial elements corresponding to floodplains (FF and CC) (Fig. 9). In the areas where the LRU shows its largest stratigraphical thickness, an increase in channelized sand-body (SB and LA) elements is noted (at La Mola d'Aumunt and Sas; Fig. 5.1.1b). These are usually tabular and isolated by floodplain fines (FF and CC) and characterized by little lateral migration of the sand bodies. It is important to

highlight the absence of well-developed massive carbonate beds in the lower parts of the lacustrine deposits.

On the whole, these findings reflect wet and dry-to-semiarid conditions, in contrast to the humid conditions assigned to GU and TU (tropical to peritropical climate of Broutin and Gisbert, 1985; Gascón-Cuello and Gisbert, 1987). Tuffs (V2), cinerites,
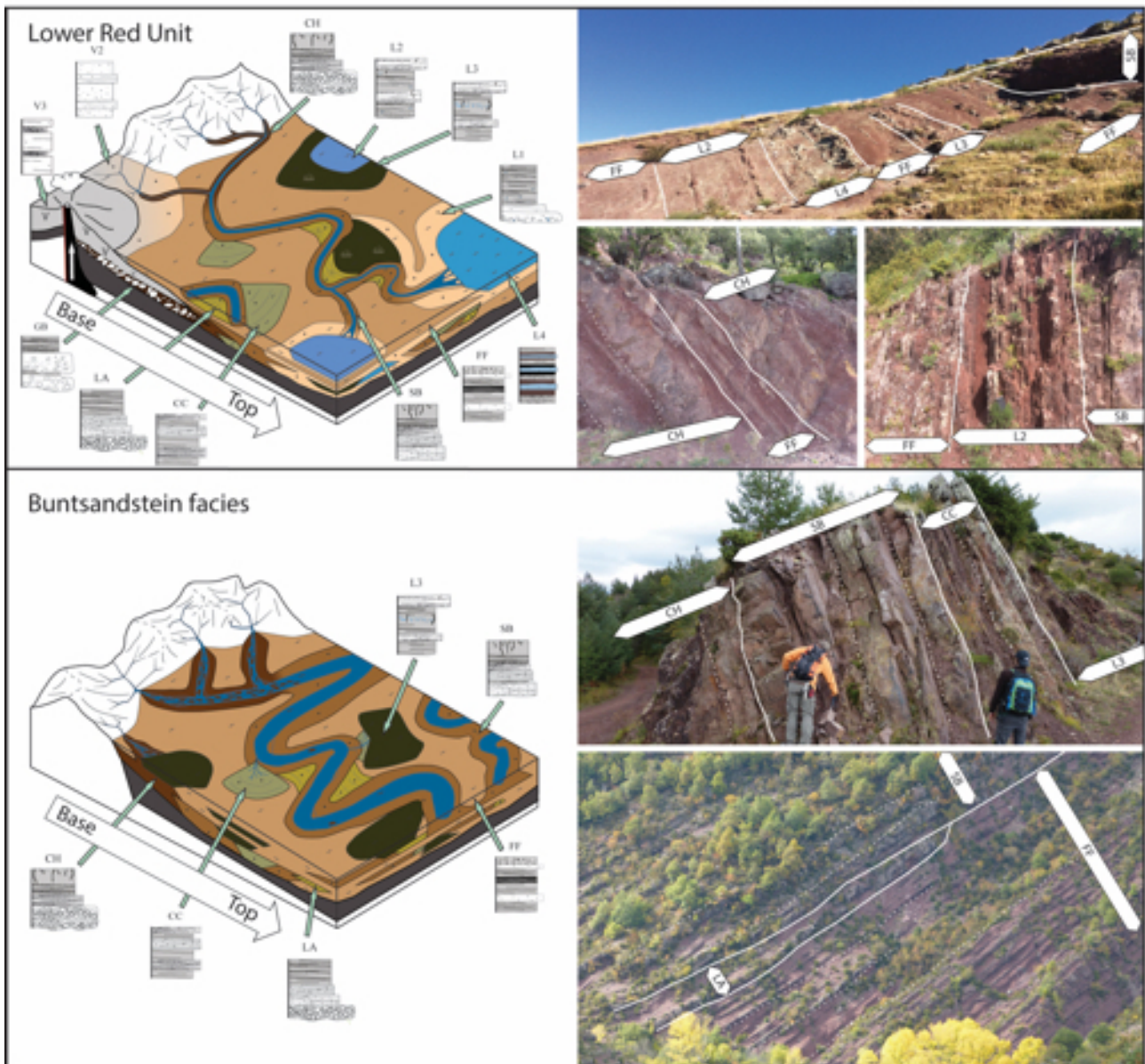
Figure 5.3.2. Paleoenvironmental reconstructions for the Lower Red Unit and Buntsandstein related to the facies associations observed. From Lloret et al. (2018). LRU photos: La Mola d'Amunt, Sas and Collada de Pui Cavaller sections; Buntsandstein facies photos: Sas section.

small andesitic and ignimbritic layers (V3) are the volcanic elements distinguished in the LRU. They are concentrated in the basal parts of the succession and decrease in

importance upwards. The general trend of this unit is clearly fining-upward, but where thicknesses are greater two fining-upward sequences have been identified.

Buntsandstein (facies) Unit (Fig. 5.3.2): This last unit shows a high rank unconformity on the underlying units, or even on the basement. The deposits of this unit lack any volcanic influence and their depositional environment is fluvial in its lowermost parts and lacustrine-floodplain in the rest of the unit. The basal conglomerates (CH) are represented and laterally persistent throughout the Erill Castell-Estac Basin. They are characterized by clast-supported to matrix-supported conglomerates related to gravel braided fluvial systems. Above them, sandy braided fluvial systems developed for most Buntsandstein deposition sedimentation (Fig. 5.3.2). This upper part is composed by orange-red sandstones and siltstones. An unconformable contact separates the two parts of the Buntsandstein deposits, indicating an important change in the upper part of this unit. Amalgamated sandbars with lateral accretion (LA, SB) and overbank (FF, CC), including playa lake deposits (L3), are characteristic of these fluvial systems. The general trend is fining-upward, but in sectors in which the thicknesses are greater (e.g., Malpàs, Castellars, Sas and Roca de les Creus) two upward fining sequences are recognizable. In the topmost part of the unit, a succession of green marls and fine evaporite beds (mm scale) indicates a progressive transition to the marine sediments in Muschelkalk facies (Borruel-Abadía et al., 2015). The contact between the upper fine deposits and the dolomites of the first Triassic marine incursion probably represents a hiatus that lasted until the Anisian (Escudero-Mozo et al., 2014).

6. Permian and Triassic paleopedology

6.1 Introduction

The paleosol study is an interesting tool, traditionally used to interpret the paleoenvironments where those soils were developed (Freytet and Plaziat, 1982; Retallack, 1984, 1994; Plat, 1989; Kraus, 1999; Tabor and Montañez, 2002; Müller et al., 2004; Li et al., 2016; Morelli et al., 2017). The development of soils is directly related to tectonics, parental material, climate and vegetation. Understanding how these elements affected the fossil soils provides information of great value for the reconstruction of the geological past.

Several classifications have been defined to provide an accurate taxonomy (Terzaghi Karl, 1924; Cline, 1949, 1963; Butler, 1980; Retallack, 1988; FAO, 1998). The most cited and most widely used in the scientific community is the USA Soil Survey Staff (Fig. 6.1), which has been adapted to paleosols by Retallack (1984, 1988, 1994). This classification provides a number of the current pedotypes identified. Each pedotype implies a generic climatic category, such as wet, semi-wet, arid and semi-arid. The climatic implications of each pedotype can be induced from the current soils, using the actualism principle.

Many scientific publications have described and analyzed the paleoclimatic and palaeoenvironmental conditions on the basis of paleosols. Several publications have discussed this topic (Tabor and Montañez, 2004; Yakimenko et al., 2004; Sheldon, 2005, 2006; Retallack et al., 2006; De la Horra et al., 2008; Bourquin et al., 2011; Thomas et al., 2011; Newell et al., 2012; Gastaldo et al., 2014; Tanner and Lucas, 2017). Broadly speaking, these articles describe how the paleosols changed during the Paleozoic-Mesozoic transition, confirming most of the climatic and environmental observations obtained by other methods.
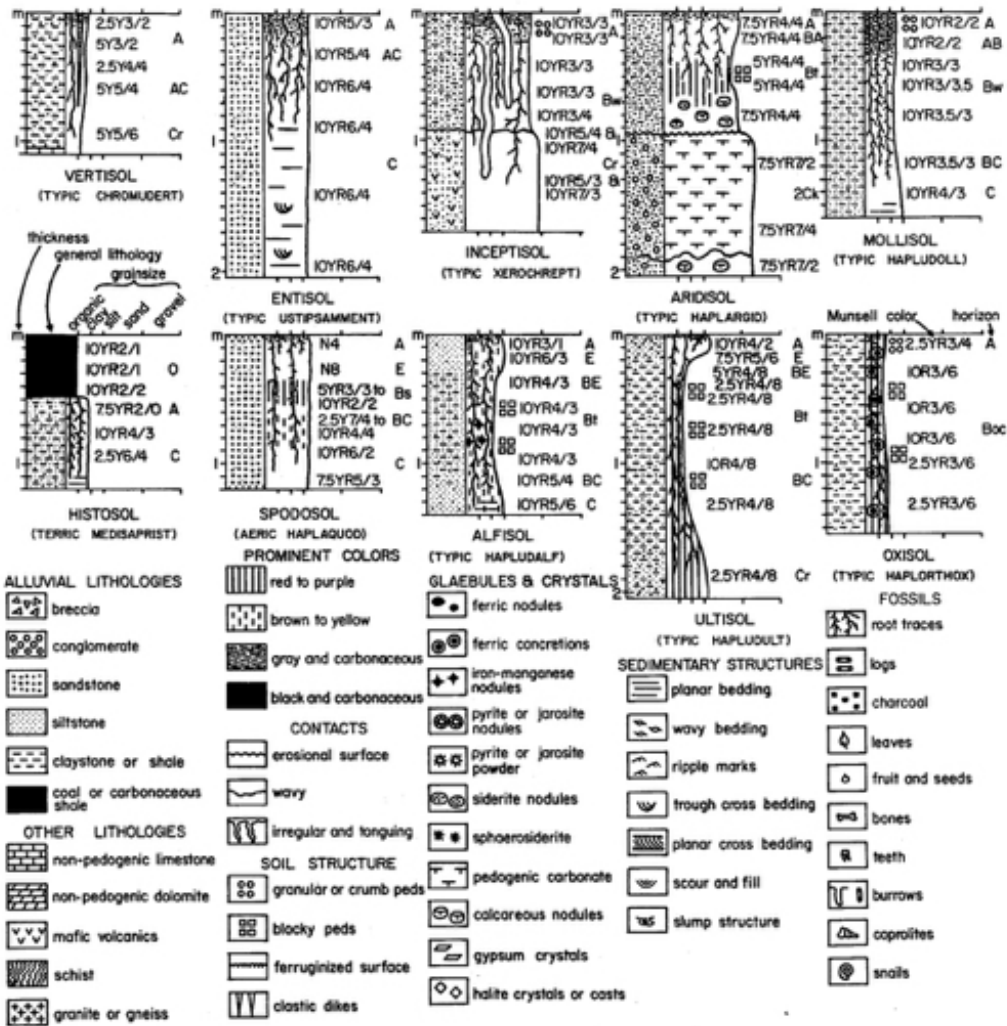
Figure 6.1. USDA modern soil classification from Retallack (1988).

The general idea about the arid and semi-arid conditions of red bed deposits was discussed in Sheldon (2005), who questioned t it using paleosols data from the Cala del Vino Formation in Sardinia (Italy). Based on the depth of the Bk horizon in the paleosols and the geochemical data from the whole rock, Sheldon (2005) demonstrated the presence of humid conditions in Sardinia (Italy) red bed deposits. The paleoprecipitation was calculated using the Bk horizon depth and trace element geochemistry. Furthermore, Sheldon (2005) indicated a major chemical weathering of the earliest Triassic soils even though the formation time for an otherwise genetically similar phenomenon was an order of magnitude shorter. Shifts between Permian and Triassic pedotypes have been detected

93

in Antartic terrains, under the influence of climate change (Retallack et al., 2005), and these data matched the plant remains, carbon isotope chemostratigraphy and total organic carbon analyses.

In the SE Iberian Peninsula De la Horra et al. (2012) identified paleoecological and paleoenvironmental changes during the Middle-Late Permian. Based on field and petrological evidences, they described paleoclimatic changes from arid-semiarid to humid conditions during that period of time, which coincided with the absence of any macro- and micro- paleontological data in the whole SE Iberian Ranges. These authors describe this fact as a biotic crises, and linked these alterations to the mid-Capitanian mass extinction.

6.1.1 Paleosol framework in the Southern Pyrenees

The paleosols of Permian and Triassic deposits in the Southern Pyrenees have only been studied in detail by Gascón-Cuello and Gisbert (1987). This publication used old-fashioned terminology but made some interesting observations and interpretations. Ferric and hydromorphic soils were distinguished for the Grey and Transition units, and. the authors suggested that these soils were formed with more than 1,000-1,200 mm y^{-1} of mean annual precipitation (MAP), in altitudes below 1.200 m and temperatures above 25ºC (see Strahler, 1970; Fitzpatrick, 1980). They describe Vertic soils for all the Permian and Triassic deposits, interpreted as having less than 1,000 mm y^{-1} precipitations, with a marked seasonally separating wet and arid conditions. They also noted the presence of "caliches" or calcretes in Permian and Triassic deposits that have historically been interpreted as arid conditions subject to long aerial exposure. The presence of early syn-diagenetic cements with replacements and alternant mineralogy showing contradictory environmental significance indicates a high seasonallity for the Lower Permian deposits. Finally, these authors proposed that the Lower Red Unit was the drier unit because the

hydrolyzing intensity during the Lower Permian was minimal (Gascón-Cuello and Gisbert, 1987).

UNIDAD	EDAD	PALEOSUELOS PRESENTES	PRECIPITACION MEDIA ANUAL (MAX. Y MIN.)	PALEOCLIMA SEGUN NOMENCL. STRAHLER (1970)
UFB	TRIASICO BUNTSANDSTEIN	CALCRETAS INCIP. VERTISOLES ESTADIOS HIDROMORFOS		ESTEPA TROPICAL
URS	PERMICO MEDIO. SUP.	CALCRETAS VERTISOLES ESTADIOS HIDROMORFOS		ESTEPA TROPICAL
URI	AUTUNIENSE	CALCRETAS VERTISOLES		ESTEPA TROPICAL
UT	STEPHANO--AUTUNIENSE	VERTISOLES GLEYSOLES / FERRALSOLES GLEYSOLES		SUBTROPICAL HUMEDO / TROPICAL WET-DRY
UG	STEPHANIENSE B	FERRALSOLES GLEYSOLES GLEYSOLES PLINTICOS		TROPICAL WET-DRY A TROPICAL HUMEDO

Figure 6.1.1. Pedotypes and climatic evolution from the Stephanian-B to the Lower Triassic in the Catalan Pyrenees, from Gascón-Cuello and Gisbert (1987).

Figure 6.1.1 shows the climatic evolution that can be inferred from the paleosols study. A tropical wet-dry climate was hypothesized for the Stephanian B (Upper Carboniferous). After the Carboniferous-Permian transition, the inferred climate moved toward less precipitation and warmer temperatures. Later on, the precipitations increased but steppe environments were interpreted for the middle-late Permian and Lower Triassic times.

More recently, Mujal et al. (2018) named the presence of paleosols in the Late Carboniferous-Lower Permian deposits (Fig. 6.1.2). Their work focused on the Carboniferous-Permian transition, which involve the Grey and Transition units. They identified Histosols and ferric horizons in the Grey Unit, interpreting them as humid and sub-humid climatic conditions, and they identified gleyed and calcic Vertisols in the Transition Unit. According to Mujal et al. (2018), the climate switched in the Asselian times (TU) towards semi-humid and semi-arid conditions; this concurred with the interpretations of Gascón-Cuello and Gisbert (1987).
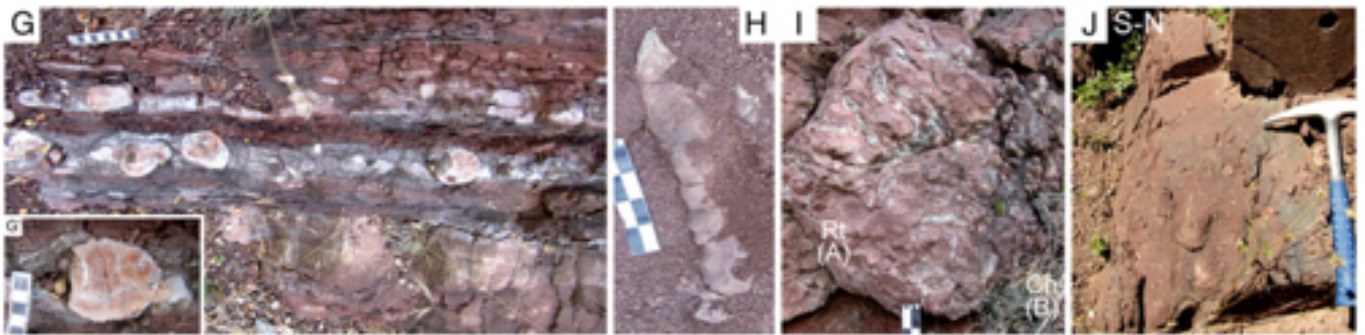
Figure 6.1.2. Pedogenic features identified by Mujal et al. (2018). G: Carbonate septarian nodules (detail in G') defining stratification and interbedded with mudstones. H: Large rhizolith. I: Greenish root traces (Rt, horizon A) above carbonate nodules (Cn, horizon Bkk). J: Tiny carbonate nodules (Protosol) in a silty mudstone.

6.2 Parental material constrains and mineralogical composition

The original parental material from the Permian-Triassic paleosols in the Central-Eastern Southern Pyrenees is varied. Several deposits were able to develop pedogenic features, according to our field work, microscopic observations and bulk mineralogy analysis (Fig. 6.2.1).

In the successions there was a notable the influence of volcanic deposits in the lower parts of the Permian, with very fine-grain tuffs and thick sheet-lava (20-30 cm) being the most representative materials. The composition of the volcanism is calc-alkaline andesite for the lowest Permian and alkaline rhyolite for the lower-middle Permian (Bixel, 1984, 1987). The petrographic study of the tuff deposits showed very-fine sandstone with numerous dull volcanic fragments (50-60%), while the other components are mainly quarz (25-30%), feldspars (10-15%) and detrital biotite (<5%). In the Lower Triassic there were not tuffs deposits, and consequently volcanic parental
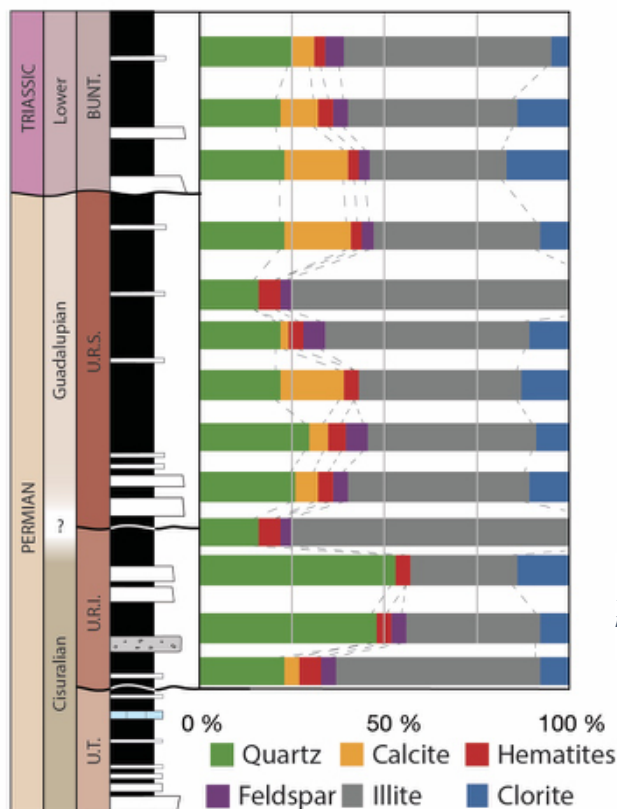
Figure 6.2.1. Schematic stratigraphic log of Permian and Triassic deposits with clay mineral semi-quantitative percentages of minerals associated.

materials were restricted to the Permian. In the absence of any volcanic influence the depositional environment was completely different; in these caseses, the parental materials were deposited on the channels and flood-plains of rivers. The distal parts of alluvial systems and playa-lake settings were the other fine-deposits in which paleosols developed.

The petrological study did not show any significant differences between these depositional environments and the mineralogical composition. In these kinds of deposits, the main components are quartz (40-60%), feldspar (10-15%), rock fragments (5%) and clay minerals (20-30%). Nevertheless, the mineralogy contained in fine-grain materials (<2 μm) did change during the Permian-Triassic times. In the Lower Permian red beds the mineralogy mainly consisted of quartz, illite, calcite, chlorite and kaolinite. In the upper part of the succession all these components decreased in importance, apart from calcite, which increased substantially. Moreover, in the Lower Triassic red beds the fine-grained clay minerals compositions changes again to become predominantly quarts-illite (even more than in the lower Permian deposits), with a near total absence of calcite. All the Permian-Triassic paleosols studied were involved in monotonous red bed successions; the characteristic reddish coloration is due mainly due to red iron oxide, which is probably not original. The shallow burial could produce this colour as a result of dehydration and recrystallization of ferric hydroxides (Blodgett, 1988; Retallack, 1997).

6.3 Description and classification of pedotypes

Seven different pedotypes have been identified and exacly situated in the Permian-Triassic red bed successions, base on the criterion of the presence of distinctive soil structures, as defined in the methodology chapter. The paleosol profiles were subdivided into horizons on the basis of changes observed in the macro- and micro-morphological features (Fig. 6.3.1). A general description of each pedotype is included and summarized in Table 6.3.1, and examples of characteristic macro- and micro-morphologies are presented in figures (Figs. 6.3.2, 6.3.3, 6.3.4 and 6.3.5). Each of the pedotypes is classified, giving rise to paleoenvironmental interpretations (Table 6.4.1).

6.3.1 Derana pedotype

Description

The Derana pedotype shows three distinct horizons and the profile is usually about of 50 cm thick (Fig. 8.4.2a). The uppermost horizon (20-25 cm) is a massive mudstone with small spherical nodules (≤1 cm) and an intense reddish coloration (10R5/6). The soil peds are granular and weakly calcareous with HCl (dissolution 10% concentrate). The bottom boundary is clear and the surface has a wavy morphology, although there are small transition areas between the horizons (2-3 cm). The middle horizon is build of massive reddish (10R4/6) mudstones (30-35 cm thick) with slightly sub-angular blocky peds, easily confused with intense horizontal mudstone lamination. The main characteristic is the presence of vertical structures no longer than 10 cm; we interpret these structures as being root casts (Fig. 6.3.2c). Their greyish-greenish (GLEY 2, 6/5BG) haloes coloration clearly distinguishes these structures from parental material. Carbonate content is calcareous, according to Birkeland (1984) and Retallack (1988), and gradually (2-3 cm) this horizon passes through a wavy surface to the underlying level. The lowest horizon presents varying thicknesses, but it usually reaches 10 cm thick. Original sedimentary
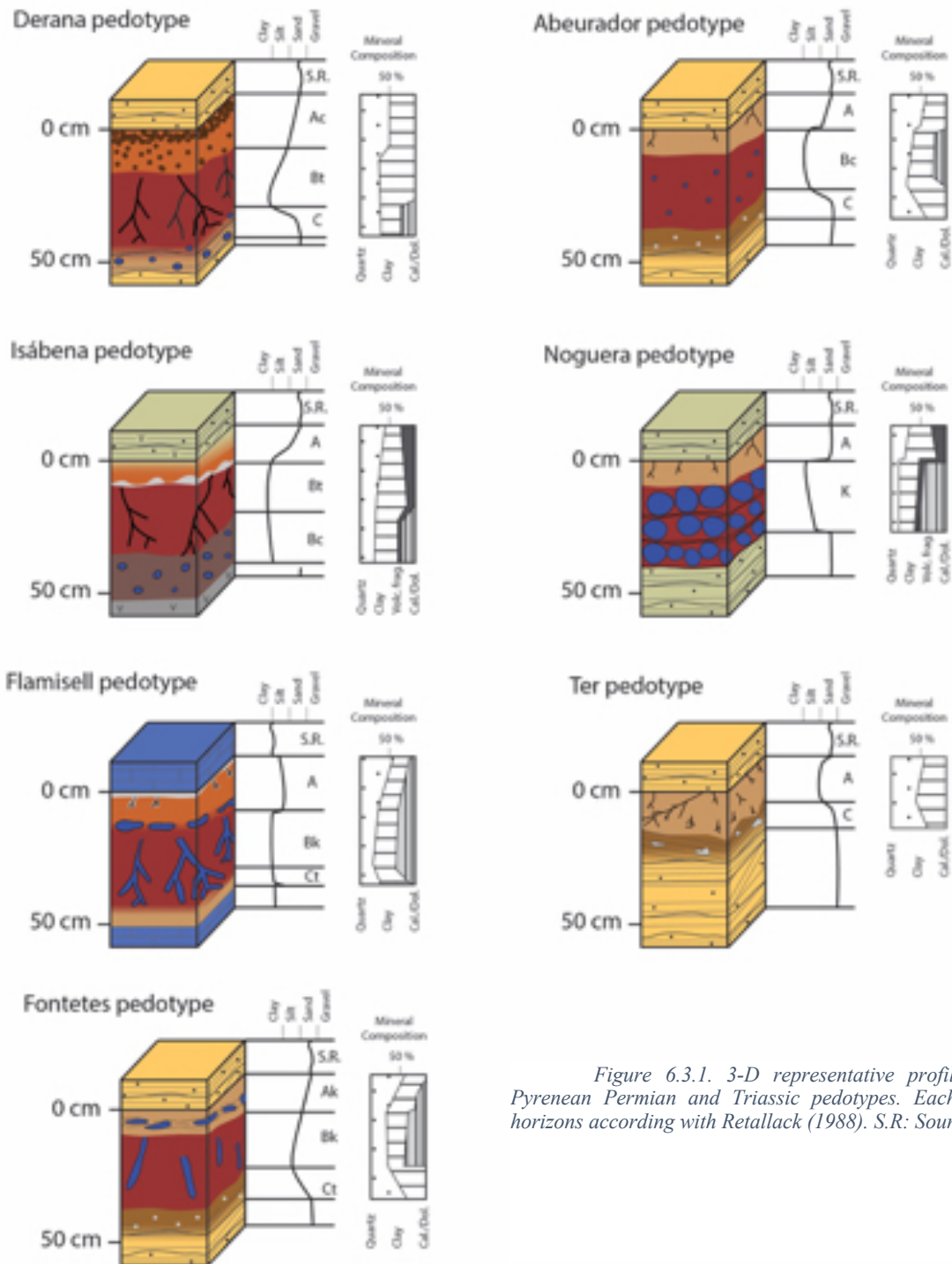
Figure 6.3.1. 3-D representative profiles of the Southern Pyrenean Permian and Triassic pedotypes. Each type is divided in horizons according with Retallack (1988). S.R: Source Rock.

structures are common, although where pedogenic processes were stronger the parental material lost its primary features and platy peds could be distinguished. The reddish (10R5/1) coloration is common in both cases, although spherical greyish (GLEY 1, 6/1) halos exists in such peds, albeit without any evidence of the root casts found in the middle horizon (Fig. 6.4.3c). Another important

Pedotype	A horizon	B horizon	C horizon
Derana	20-25 cm, red (10R 5/6) mudstone, granular peds, weakly calcareous, small spherical nodules	30-35 cm, red (10R 4/6) mudstone, sub-angular peds, calcareous, vertical root traces (10 cm), greyish-greenish halos (GLEY2 6/5BG)	10 cm, weak red (10R 5/1) fine sandstone, platy peds, non-calcareous, primary sedimentary structures, greyish halos (GLEY1 6/1)
Abeurador	5-10 cm, brownish (7.5YR 5/2) siltstone, platy peds, very weak calcareous	10-20 cm, red (2.5YR 5/8) mudstone, granular peds, weakly carbonaceous, numerous well-rounded carbonaceous nodules (1 cm) with strongly carbonaceous reaction	5-10 cm, dark red (2.5YR 4/6) mudstone, granular peds, non-carbonaceous, light bluish grey (GLEY2 8/10GB) halos, corss-primary sedimentary structures
Isábena	10-15 cm, dark reddish brown (2.5YR 3/3) fine sandstone, granular peds, non-calcareous, light greenish grey (GLEY1 8/5G) halos	20-30 cm, greish brown (10YR 5/2) mudstone, granular peds, non-calcareous, very calcareous roots (10 cm), light greenish grey (GLEY1 8/5G) halos	10-25 cm, light reddish brown (2.5YR 7/3), sub-angular blocky peds, very-weak calcareous, spherical nodules (1-2 cm) with high carbonaceous content
Noguera	10 cm, brown (10YR 4/3) fine sandstone, granular peds, very-weak calcareous, small root casts (1-2 mm wide, 3-5 cm long)	20-30 cm, light yellowish brown (10YR 6/4) siltstone, subangular blocky peds, calcareous, big concentrated carbonate nodules (1-10 cm), fine root traces (1 cm)	Not present
Flamisell	5-10 cm, bluish grey (GLEY2 5/10BG) mudstone, angular blocky peds, strongly calcareous, drab-haloed root traces, petrocalcic horizon	20-30 cm, dark greenish grey (GLEY1 3/10Y) claystone, granular peds, strongly calcareous, vertical rhizoconcretions (1-2 cm wide, 10 cm long), 1 cm spherical rhizoconcretions in the base	10 cm, reddish brown (5YR 4/3) siltstone, subangular blocky peds, non-calcareous, primary sedimentary structures, small slickensides
Ter	20-25 cm, yellowish red (5YR 4/6) very fine sandstone, granular peds, very-weak calcareous, small (5 mm wide, 10 cm long) drab root traces (10GY 7/1)	Not present	20 cm, dark reddish brown (5YR 3/4) medium sandstone, platy peds, non-calcareous, primary sedimentary strctures
Fontetes	10 cm, weak red (10R 5/2) fine sandstone, platy peds, very-weak calcareous, pole green (GLEY1 7/5G) carbonate nodules (1 cm), small root traces (2-3 mm wide, 1-2 cm long)	20-30 cm, dark greyish grey (10R 3/1) siltstone, granular peds, strongly calcareous, vertical rhizoconcretions (5-10 cm long) very calcareous	10 cm, very dark red siltstone, granular peds, non-calcareous, small carbonate nodules (1.5 cm), primary sedimentary structures

Table 6.3.1. Summary of main pedogenic features of the pedotypes identified in the Permian and Triassic deposits.

aspect is the absence of carbonate, due to the non-calcareous reaction with HCl. The transition to the below parental material is gradual and irregular. The lateral extension of Derana pedotype can reach several meters (5-10 meters), disposed on top of alluvial and original fluvial deposits.

Classification

The fine material from the first horizon of the Derana pedotype was interpreted as being a zone of physical alteration and classified as a B horizon. The presence of spherical nodules can endow this horizon with the "c" subordination, according to Retallack (1988). The middle horizon is fine-composed and the vertical root casts are filled by fine material, and it is therefore interpreted as a Bt horizon. The bottommost horizon is composed of spherical haloes and maintains primary sedimentary structures. The haloes could correspond to the occurrence of roots, even though those have not been preserved. The relict sedimentary structures indicate poor development in this horizon and so it was classified as a C horizon. On the whole, this pedotype is interpreted as being an Alfisol, despite its non-well clay accumulations.

The weak and non-calcareous reactions indicate a stage I of carbonate accumulations (Machette, 1985). The clear differentiation between the horizons and the low carbonate content indicates weakly to very weakly developed stages of paleosol development.
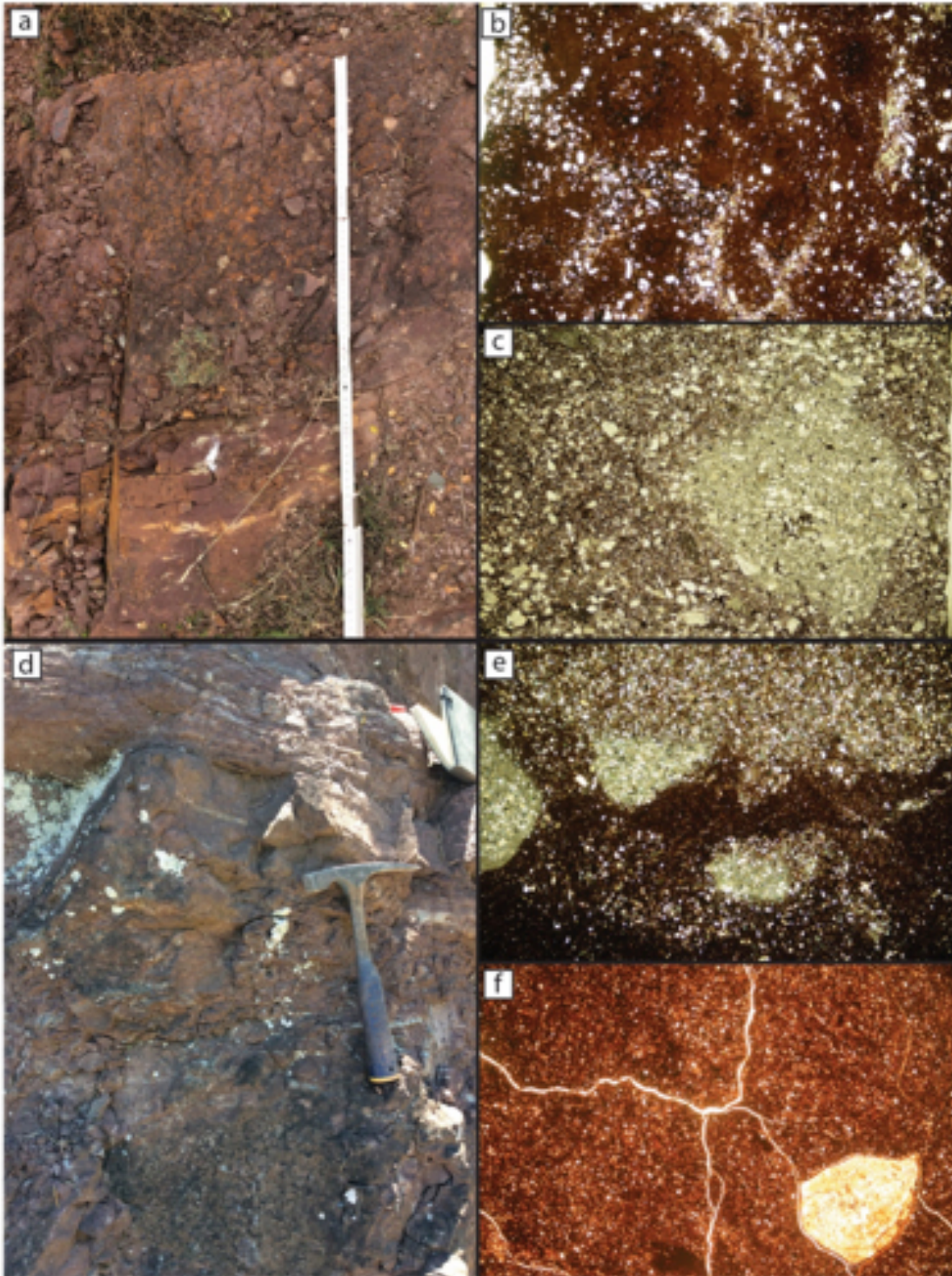
Figure 6.3.2. (a) Field example of Derana pedotype, the rule is 50 cm long. (b) Derana (Suils-P1A). F1 2xNP. Loamy sand in an open porphiric distribution with very abundant worm-like features or crescent striated structures. Probably, these features are related to excremental infilling and indicative of high biological activity. (c) Derana (Suils-P1C). F4 2xNx. Sand in a monic distribution with a clearer depletion pedofeature around a center of amorphous material (in dark red colour). Probably, the depletion zone is related to a root channel. (d) Field example of Abeurador pedotype. (e) Abeurador (P2-2). F5 2xNx. Micro loadcast structures of sand on red silty material. In the lower part of the picture a crescent striated structure is appreciated. (f) Abeurador (P2-B1). F6 2xNx. Sandy loam well sorted and distributed in subangular blocky peds separated by cracks. A calcitic nodule with concentric structure and micritic texture occurs in the lower right part of the photograph

103

6.3.2 Abeurador pedotype

Description

The Abeurador pedotype is organized into three different horizons, with total thicknesses of 25 cm to 50 cm (Fig. 6.3.2d). The top horizon is brownish (7.5YR5/2) in color and corresponds to well-developed platy peds in siltstones. Very weak carbonaceous reactions were recorded in the uppermost levels (5-10 cm approx.). Only the intense horizontal platy shape remains, and thus no sedimentary structures are recognizable. An abrupt and smooth boundary separates the upper horizon from the middle horizon, which is reddish and 10-20 cm thick. Fine materials compose this horizon and ped structures are organized with granular features. Loadcast structures of sand on red silty material have been identified (Fig. 6.3.2e). Inside the fines of this horizon a significant amount of carbonate nodules is present, and organized in "matrix-supported" rock fabric. The nodules size is small (not bigger than 1 centimeter) and very well rounded. The carbonate content diverges strongly from granular-matrix to nodules; in the first case, very weak carbonaceous reactions have been noted, and in the second strongly carbonaceous reactions have been described. The transition to the bottommost horizon (5-10 cm) is clear, with nodules disappearing gradually in a wavy surface and giving way to semi-consolidate red (2.5YR4/6) mudstone with a granular shape (Fig. 6.3.2f). Unlike the previous horizon, the carbonate is completely absent, no nodules are identified and there is no reaction with HCl. Only small light bluish grey (GREY 2, 8/10GB) halos of 1-2 cm^2 are recorded. Such structures have been interprete as small root traces. Normally original sedimentary structures such as cross-bedding and horizontal laminations can be recognized in this last horizon. The lateral continuity of the Abeurador pedotype reaches 20-30 meters in length.

Classification

104

The first horizon is composed of brown siltstones with very small root traces in the topmost layer. This horizon is interpreted as a horizon A with no subordinate descriptors. The second horizon is characterized by small rounded carbonaceous nodules and is interpreted as a horizon Bc. The main difference from the Derana Bt horizon is the absence of vertical root traces in the Abeurador pedotype. The third and last horizon is composed of fines with several grey halos, interpreted as the remains of root traces (horizon C). This horizon gradually loses its pedogenic features as sedimentary structures appear.

The presence of small carbonate nodules and their reaction with acid indicate discrete soil development, and this is therefore assigned to stage II (Machette, 1985). The presence of roots in horizon A and the lateral continuity (20-30 m) indicate weakly development. This pedotype is interpreted as being an Inceptisol, due to its moderate development.

6.3.3 Isábena pedotype

Description

Three horizons characterizes this pedotype, which has thicknesses between 50 cm and 70 cm (Fig. 6.3.3a). The topmost horizon is dark reddish brown (2.5YR 3/3) and composed of fine sandstones. The upper boundary is diffuse and merges with the beds above, with medium-fine sandstone gradation. The peds have a granular shape and are medium in size (2-5 mm). The calcareous content is absent in the reddish part of this horizon, while in the greenish grey (GLEY1 8/5G) part of the halos are weak. These are located in the bottom part of the horizon and have rounded morphologies 2-5 cm in size. The boundary with the bottom horizon is irregular and often unclear. The second horizon is composed of grayish brown (10YR5/2) mudstone 20-30 cm thick.

The peds are granular with medium sizes and a non-calcareous reaction. The main feature of this horizon is the presence of very-well ramificated traces of root casts with very calcareous reactions. These casts are 1-2 cm wide and 5-10 cm long, and they are associated with light greenish colorations (GLEY1 8/5G), small halos and fine (5 mm) root traces. The second horizon passes gradually downward into light reddish-brown (2.5YR 7/3) and very fine sandstone with sub-angular blocky peds and very weak calcareous content. The last horizon is 10-25 cm thick and is characterized by the presence of spherical (1-2 cm) carbonate nodules (Fig. 6.3.3b) with higher concentrations, that never become "clast-supported", in the lower parts of the horizon. The relationship with the parental material is clearly sharp. The boundary surface is wavy, but the separation between it and the next is evident in the field. The parental material of the Isábena pedotype is made up of medium-size sandstones which are volcanic-associated. Under the microscope the presence of volcanic fragments represents up to 70% of the sub-angular clasts (Fig. 6.3.3c).

Classification

The main characteristic of this pedotype is the volcanic parental material. The quartz and plagioclase sandy volcanic material indicates an Andisol classification, according to the USA Soil Classification (Retallack, 1988).

The characteristics of this pedotype give rise to further interpretation and classification. The first identified horizon is characterized by a weak development and the presence of grey halos in the topmost part. These features indicate the assignation of an A horizon. The next horizon contains very well developed root ramifications. The carbonate content of such a structure is well developed in a horizons 30-40 cm thick and there are also smaller grey-haloed root casts. The assignation here is a B horizon, with the subdivision Bt. The lower horizon is also identified as a B horizon, but with the Bc subdivision. This

is supported by the presence of spherical nodules. Due to the organization and the presence of the horizon identified, the most probable classification is as an Alfisol, but the volcanic parent material assigns this pedotype to the Andisols order. The suborder classification of the US Soil Service is an Udand paleosol, with an udic soil moisture regime.

The presence of important carbonate roots and nodules and their reaction with acid, indicates significant soil development, and therefore stage III-IV is assigned (Machette, 1985). The presence of roots in horizon Bt, which is interpreted as being an incipient calcic, indicates strong development (Retallack, 1984).

6.3.4 Noguera

Description

The Noguera pedotype is composed of two horizons, whit a total thickness of 30 to 40 cm (Fig. 6.3.3d). The parental material for this pedotype is composed of volcanic and volcano-clastic deposits consisting of tuffs and reworked sandstones. The top boundary with the parental material is clear and horizontal. The first horizon is about 10 cm thick and composed of grown (10YR 4/3) fine sandstone. The internal structure is defined by medium-coarse (0.5 cm) granular peds with very-weak-calcareous reactions. Small root casts (1-2 mm wide, 3-5 cm long) are sometimes present in the bottom parts of the first horizon of some of the studied Noguera paleosols. The contact with the underlying horizon is gradual, with wavy morphologies. The bottom horizon is composed by pale red (10R 6/4) siltstones with sub-angular, blocky, coarse (0.3 cm) peds. The distinctive characteristic of this horizon is the presence of numerous large (5-10 cm) carbonate nodules with a spherical morphology. The nodules are set in a pseudolayer (10-15 cm thick) separated by a fine layer (2-5 cm thick) with wavy laminations. B-fabrics (Fig. 6.3.3e) and orange colorations can be distinguished under a microscope, and this

horizon's carbonate content can be distinguished as ferric calcites (Fig. 6.3.3f). This feature indicates the presence of iron products. This nodular horizon is usually repeated 3-4 times an reaches up to 4 meters (e.g., the Gotarta section). The lateral extension of the Noguera pedotype is 20-30 meters.

Classification

As in the previous pedotype, the presence of volcanic fragments in the parental material could serve to directly classify this pedotype as an Andisol, but other features provide further criteria for its accurate identification and classification.

The topmost horizon contains small root traces in 5-10 cm thin layers, without any other important features. Usually these kinds of horizons are classified as an A horizon due to the presence of root traces, despite the absence of organic material. The lower horizon is characterized by pseudolayers of large carbonate nodules. These horizons reach 30-40 cm and are usually indicative of a long-term development of paleosols. This horizon is assigned to K horizon due to the carbonate pseudolayer formed by the nodules. The characteristic K horizon is related to arid and semi-arid paleosol conditions that are represented by Aridisols.

The continuous carbonate layer indicates a III-IV stage of carbonate development, according to the classification of Machette (1985). On the basis of this classification Retallack (1984, 1988) indicate a strong development of this pedotype.
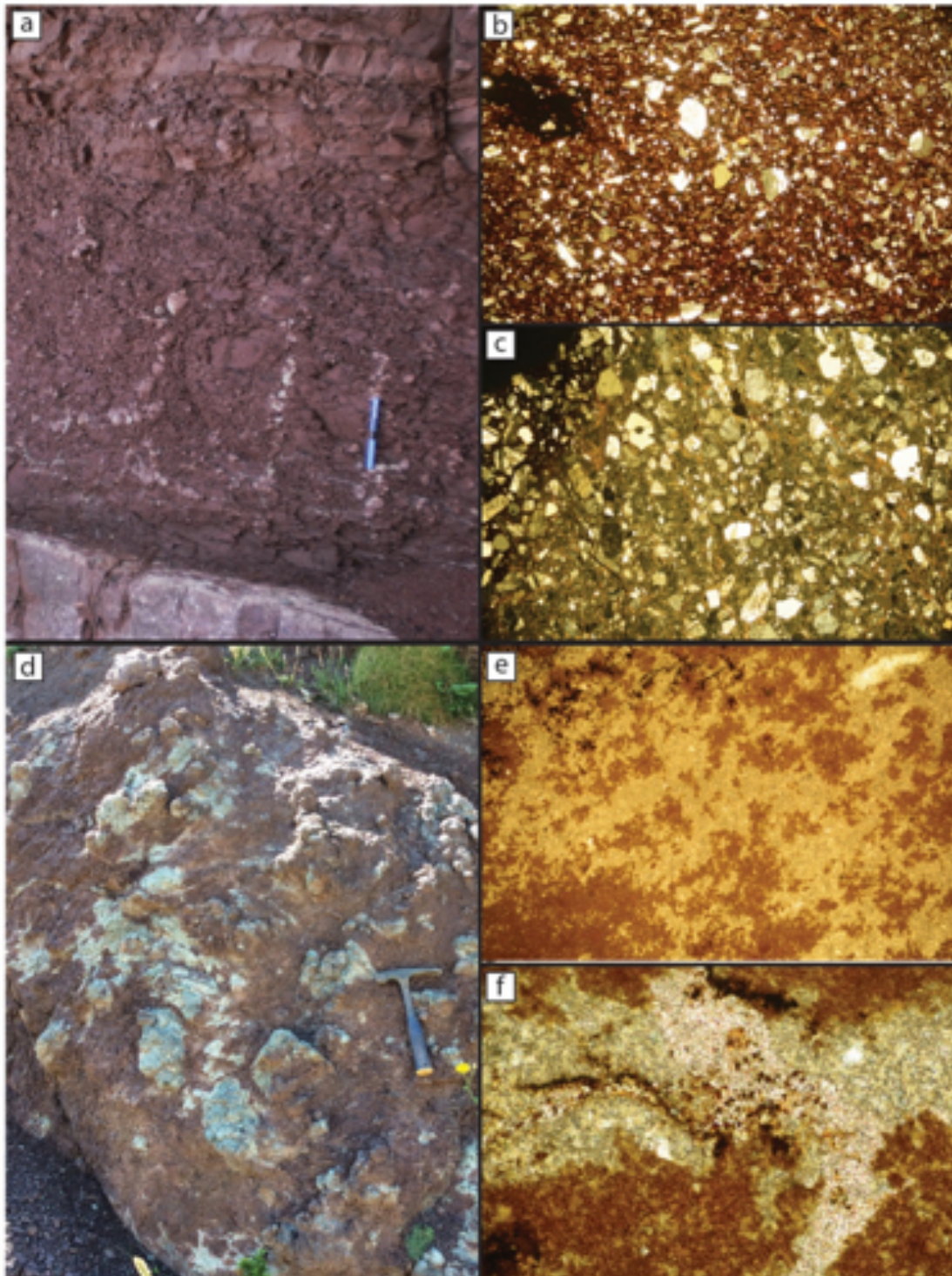
Figure 6.3.3. (a) Field example of Isábena pedotype. (b) Isábena (Mola-S4A). F11 2xNx. Enaulic distribution of sandy volcanic material composed of quarzt and plagiclase. A dark red and opaque pedofeature can be observed in the upper left part of the microphotography. It is a compound impregnative ferruginous nodule. Probably, the presence of these nodules was related to poor soil drainage and excess of water for some periods. (c) Isábena (Mola-S4B). F14 2xNx. Open porphiric distribution of sandy volcanic material in a clayey birefringent matrix. Note the sand size grains are floating in red silty material oriented in the vetical axis of the picture, probably reflecting the original sedimentation of the subvolcanic deposit. (d) Field example of Noguera pedotype. (e) Noguera (Got-S2A). F18 5xNx. Cristallitic b-fabric of fine particles of calcite and clay in yellow colour. The presence of iron produces an orange colour. Some amorphous iron/manganese impregnations can be seen in the upper part of the microphotograph. (f) Noguera (GotS2B). F21 20xNx. Sparite crystals of ferric calcite (red tinted), green clayey and calcitic material, and brown ferroginous spariteand some impregnations of black and opaque amorphous material.

6.3.5 Flamisell pedotype

Description

This pedotype is composed of three horizons 50 cm thicks (Fig. 6.3.4a). The topmost one is composed of fine sandstone 5-10 cm thick with bluish-grey coloration (GLEY 2/5BG). The peds have an angular blocky shape and fine size (0.5-1 cm). The carbonate content in this first horizon is strong. Moreover, a fine (1-2 cm) grey layer occur in the bed rock and small drab haloed root traces (2-3 cm) are visible immediately below this level. After that, there are several cm of mudstone without any root traces. The boundary with the second horizon is characterized by a continuous 5 cm layer of horizontal carbonate with a nodular apperance. The second horizon is 20-30 cm thick and dark greenish-grey-colored (GLEY1 3/10Y) claystone with very fine (1mm) granular peds. Very well developed vertical rhizoconcretions (1-2 cm wide, 10 cm long) are located below the carbonate horizontal layer. The middle horizon finishes with 1 cm spherical rhizoconcretions in the base. Finally, the bottommost horizon is composed of 10 cm of reddish brown (5YR 4/3) siltstones with sub-angular blocky peds (1 to 2 cm). This horizon presents primary sedimentary structures with clay accumulation and slickensides.

Classification

The topmost horizon is composed of small root traces with bluish colorations, and it is interpreted as being an A horizon. The intermediate horizon contains significant carbonated root traces in a very-well developed horizon, which is interpreted as being a Bk horizon. The lower horizon does not usually appear and it contains an accumulation of clay, indicative of relict parental material mixed with sand. This horizon is interpreted as being a Ct, according to Retallack (1988).

Although it is described as a pedotype because of the root traces and the presence of horizons, the microphotography and other characteristics indicate palustrine features. These are evidenced by the presence of micrite and microsparite mosaics, detrital grains and gastropod remains in the parental material (Figs. 8.4.4b,c). In the field, tabular limestones were identified above and below the Flamisell pedotype. Accordingly, it can be interpreted a mixed system in which pedogenic processes occurred into a palustrine environment. In this case, no classification has been proposed by Retallack (1984, 1988) and the proposal, in this case, is to define this pedotype as a palustrine soil from a transitional environment between lacustrine and fluvial systems in which periods of flooding alternated with no-flood periods. The flood periods could generate the parental horizons of limestones and the Bk horizon, which presents long root traces. The A horizon non-flood period is inferred from the small roots (1-3 cm). The horizontal carbonate layer between the A and Bk horizons is interpreted as marking the beginning of the flooding period.

6.3.6 Ter pedotype

Description

The Ter pedotype is composed of two different horizons with a thickness of 30-40 cm (Fig. 6.3.4d). The parental material is composed of alluvial medium-fine sandstones. The first horizon is characterized by yellowish-red (5YR 4/6) very fine sandstones with granular peds. Broadly speaking, this horizon has weak-calcareous content with small (5 mm wide, 10 cm long) drab root traces with grey coloration (10GY 7/1; Fig. 6.3.4e). Furthermore, long (10 cm) diagonal root traces are present through out this horizon (Fig. 6.3.4f). The second horizon has medium sandstone lithology, with thicknesses recorded between 10 to 25 cm. The color of this horizon is dark reddish-

brown (5YR 3/4), characterized by platy peds with no calcareous content. Cross-bedds laminations are still present, as a relic of primary sedimentary structures.

Classification

The Ter pedotype is composed of two horizons and both are poorly developed. The presence of small root traces with very weak-calcareous reactions indicate an A horizon. The absence of clay and organic concentrations and non-excessive development rule out a B horizon assignation. The lower horizon consists of parental material (sandstones) with pedogenic alteration. Original sedimentary structures remain, with the presence of small haloes and root traces. These features indicate a C horizon, according to the classification followed. The poor development of these paleosols and the slight separation between horizons indicate an Entisol order (Retallack, 1988).

The carbonate development consists of dispersed carbonates that correspond with stage I of Machette (1985). The stage development for the Entisols studied in the field indicates a weak-very weak development, according to Retallack (1984).
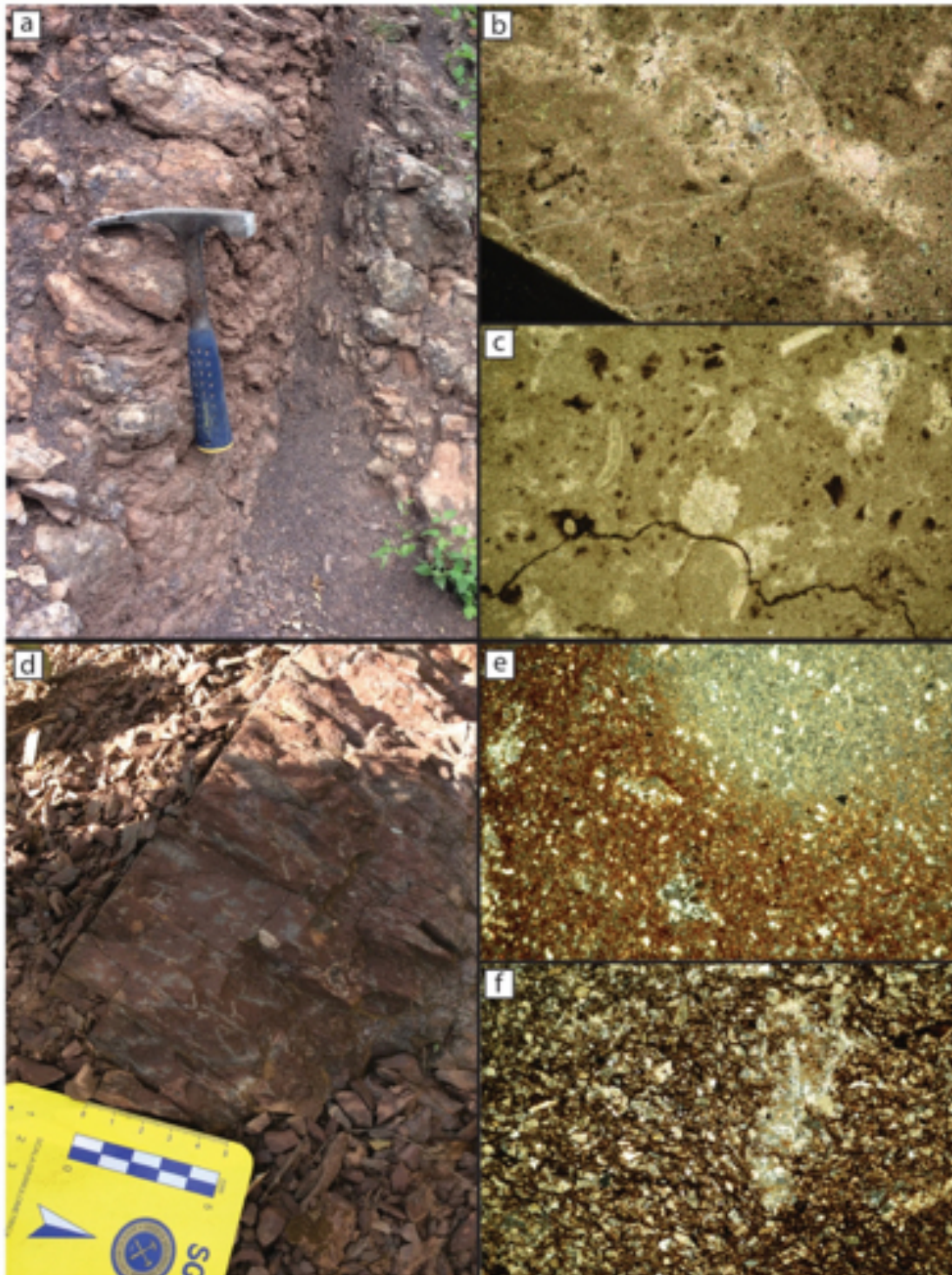
Figure 6.3.4. (a) Field example of Flamisell pedotype. (b) Flamisell (Mola 2A). F23 5xNx. Micrite and microsparite mosaic with some areas of irion remobilisation (in dark opaque colous). Detrital grains are common.(c) Flamisell (Mola S1B). F26 10xNx. Micrite with dark ferroginous mottles, patches of sparite and gasteropods remains. (d)Field example of Ter pedotype. (e) (i): Ter (Mola S5A). F29 5xNx. Pale green depletion pedofeature in red sandy loam material. These zones are common in soils subjected to periodic waterlogging. (f) Ter (Mola S5B). F32 10xNx. Vertical void infilled with sparite deforming a sandy material.

6.3.7 Fontetes pedotype

Description

The Fontetes pedotype shows three distinct horizons that define a profile of 40-50 cm (6.3.5a). The uppermost horizon is a 10-15 cm layer of weak red (10R 5/2) fine sandstone. The peds have a medium (2-5 mm) platy shape with very weak carbonate content. In the middle part of this horizon there are pale green (Gley1 7/5G) carbonate nodules 1 cm in diameter (Fig. 6.3.5b); when these occur, the horizontal laminations become wavy. The boundary with the horizon below is clear. The middle horizon is characterized by 20-30 cm of dark greyish (10R 3/1) siltstone with fine (1-2 mm) granular peds. The main pedogenic element is the presence of rhizoconcretions 5 to 10 cm long. The carbonate content differs from very weak in the "matrix" to very calcareous in the rhizoconcretions. Desiccation cracks were identified; these originated before the precipitation of carbonates (Fig. 6.3.5c). The Fontetes pedotype finishes with a horizon 10 cm thick. This is ~10 cm of very dark red siltstone composed of granular peds. Carbonate nodules (1.5 cm in diameter) occur with greyish haloed mottling. In the bottommost horizon, few primary sedimentary cross-bedding structures can be recognized.

Classification

The topmost horizon is interpreted as an Ak horizon because it is the surface with the parental material and contains a carbonate layer. The next horizon is composed of rhizoconcretions which indicate a B horizon with a Bk subdivision because of the high carbonate content. The bottom horizon is characterized by carbonate nodules in a material with relict sedimentary structures, indicating a C horizon and a Ct subdivision, because of the presence of clay accumulation. Microphotography has identified several cracks,

which are usually linked to arid and semi-arid conditions, as well as some micritic and sparite carbonate, which probably indicates semi-palustrine environments. In the case of the Ter pedotype, the macroscopic evidence in the field does not indicate any clear palustrine system. These considerations will be further discussed in this chapter. The classification for this pedotype is as Alfisol, because of the presence of a differentiated A, B and C horizons, indicating a strong development of paleosols.

According to the Machette (1985) classification, the Fontetes pedotype is classified as being at stage II-III of carbonate content, while Retallack (1984) classifies it as presenting a moderate stage of soil development.
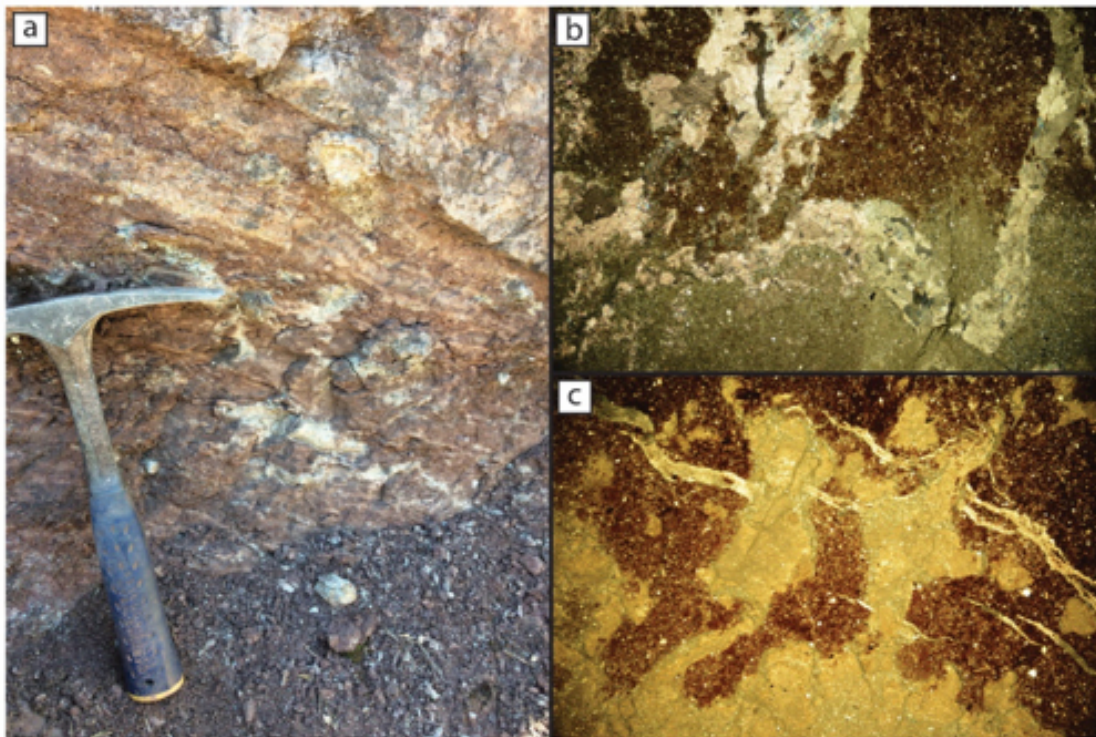
Figure 6.3.5. (b) Fontetes (Villarua P6B). F35 2xNx. Part of calcitic nodules. Micrite, microsparite and sparite crystals can be differentiated. (c) Fontetes (Villarua P6D). F40 2xNx. Precipitation of carbonate was after the formation of the cracks infilled now with calcite. These cracks were probably dessication cracks, implying water table oscilations.

6.4 Vertical and horizontal distribution

The recognition of each pedotype in the field allows to discern the distribution of paleosols during the studied timespan (Fig. 6.4.1). The study of paleosols is focused on the Permian and Triassic red beds including the LRU, URU and Buntsandstein facies. In addition to the paleoenvironmental and climatic considerations, the systematic study presented herein is crucial to the recognition of the red beds units in the Late Paleozoic-Lower Mesozoic deposits in the Southern Pyrenees.

The Lower Red Unit (Artinskian) is characterized by the presence of the Noguera, Flamisell, Isábena and Ter pedotypes. Their distribution is heterogenic in age and in their paleogeographic situation on the basin. The Noguera pedotype is lacated in sections where the LRU thickness is small (i.e., Gotarta; 100-200 m) and rarely appears where stratigraphic units are thick. Its situation in the stratigraphic logs is usually in the middle-upper part and it is strongly linked to sectors with major volcano-clastic deposits occur (lahars and remobilized sandstones, V2 architectural element). The Flamisell pedotype is well represented in the sectors where thicknesses are greater (e.g., La Mola d'Amunt, Castellar de N'Hug, Estac). In the sectors with less thicknesses it does not appear, in keeping with the non-appearance of palustrine deposits (L2 and L3 architectural elements). The main incidence of the Flamisell pedotype occurs in the lower deposits of the LRU. The Isábena pedotype is linked with volcanic processes (V2 architectural element). Its distribution is widely spread along all the studied sectors with moderate and large thicknesses: La Mola d'Amunt, Castella de N'Hug, La Trava. The vertical distribution is homogeneous, so it occurs in all the stratigraphic logs. Finally, the Ter pedotype is represented in almost all the studied sectors. Its vertical distribution is not restricted to any specific situation in the stratigraphic logs.

The Upper Red Unit (Kungurian-Wordian) has similar characteristics to the Lower Red Unit. The paleosols identified in this unit are the following: Flamisell, Isábena, Fontetes and Ter. The most significant changes are the appearance of the Fontetes pedotype and the disappearance of the Noguera pedotype. This finding will be discussed in the corresponding chapter. The new pedotype is represented in all the URU studied sectors, which are situated in the Eastern part of the Southern Pyrenees (Gramós and Castellar-Camprodón basins). It is usually are distributed in the upper part of the unit, some 20-30 meters below the Permian-Triassic boundary. It is important to indicate that the sedimentary situation of this pedotype correspond with the finest architectural elements (FF and CC). Consequently, several examples of this pedotype were identified in the lower deposits of the Castellar de N'Hug sector, in keeping with the trend towards finer material at the top of the Castellar-Camprodón basin. The Isábena pedotype is definitely scarce in this unit. A few examples were located in the basal fine deposits where thick (20-30 cm) volcanic layers appear (V2 and V3 architectural elements). Nonetheless, the development of the Isábena paleosols is substantial as in the Lower Red Unit ones. The Flamisell pedotype is set in the sectors with greater thicknesses and is related to the development of the Fontetes pedotype. These are usually found in alternation and where the strong deformation allows to observe horizontal changes these pedotypes seem to be related. The last pedotype to appear is the Ter pedotype. As in the LRU, these paleosols appear in all the units and sectors.

The Buntsandstein facies unit (Anisian) is also composed of red beds and several paleosols were developed here. In the Lower Triassic deposits more restricted pedotypes were recognized. In the field work undertaken, it was verified that there was no pedogenic development in the basal facies (CH and SB architectural elements), which means that
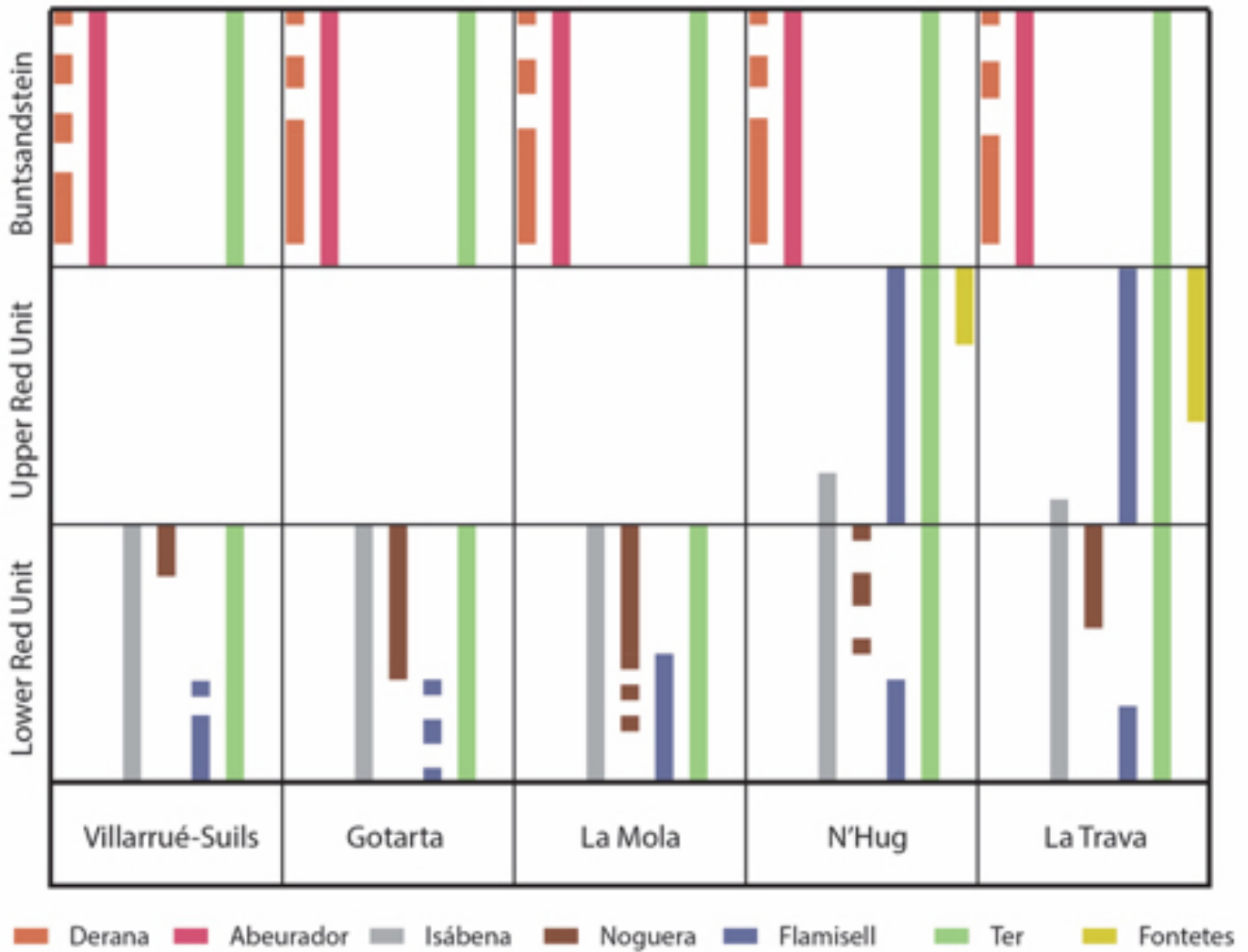
Figure 6.4.1. Vertical and horizontal distribution of the pedotypes in the Lower Red Unit, Upper Red Unit and Buntsandstein facies unit.

this occurred in the middle part of the stratigraphic sections. Another characteristic of this unit is the fact that the first pedotype to appear is the Derana. This finings is evident in all the studied sectors. This pedotype therefore represents a key level to stratigraphic correlations. Furthermore, it gives rise to a relief in the current topography that makes it easy to recognize. It usually reappears several meters upwards, but with a lower development and less thickness. It is found in the fines deposits of fluvial floodplains (FF architectural element). The other pedotypes that outcrop in the Lower Triassic deposits are the Abeurador and Ter pedotypes. As in the case of the previous units, Ter paleosols appear equally in all the sectors and in the whole stratigraphic record after the first appearance of Derana. In contrast, the Abeurador pedotype presents a heterogeneous

distribution. It is set in the middle-upper part of the sections and is poorly distributed., despite being present in almost all the sectors. Abeurador soils are associated with crevasse splay and palustrine water fluctuant environments (CC and L3 architectural elements).

7. Isotopic analysis of paleosols

7.1 Introduction

Soils are the node in which atmosphere, biosphere and geosphere coexist. Pedology was restricted to qualitative interpretations until the emergence of the latest geochemistry techniques. Carbon isotopic ratios in soil carbonates are now determined by the fraction of vegetation respiration in the local ecosystem and by the influence of atmospheric CO_2 in soil gas by temperature (Cerling, 1984, 1992, 2009; Cerling and Quade, 2013). The carbon isotopic composition of soils was first modelled using the model for carbonate formation resulting from CO_2 degassing that was developed by Hendy (1971):

$$CaCOC_3 + H_2O + CO_2 = Ca^{+2} + 2HCO^{-3}$$
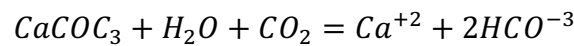
The carbon is derived from the rock and from biological CO_2, with the solubility product:

$$K_{Calcite} = \frac{\alpha_{Ca^{+2}}\ \alpha^2_{HCO^{-3}}}{\rho_{CO_2}}$$

Where $K_{Calcite}$, $\alpha_{Ca^{+2}}$, $\alpha^2_{HCO^{-3}}$ and ρ_{CO_2} are the solubility product of calcite, the activity of the Ca^{+2} ion, the activity of the HCO^{-3} ion and the ρCO_2, respectively.

Cerling (2009) considered that the diffusion theory for CO_2 transport in soils had become well established (Baver et al., 1972; Kirkham and Powers, 1972) and that the diffusion model had been extended to include transport of $^{12}CO_2$ and $^{13}CO_2$ in the soil's atmosphere. Accordingly, he established that carbonate in the soil can form in four ways:

(1) Degassing from soil solution. Soil ρCO_2 profiles generally increase with depth, so that downward movements of soil solutions increases rather than

solubility decrease solubility. Upward movement of soil solutions is important in groundwater discharge zones. Degassing also occurs as soils decrease their respiration rates seasonally as a result of decreasing temperature or soil humidity.

(2) Increasing ion activity as a result of evaporation or evapotranspiration. Direct evaporation of soil solution is important in soils where uncovered ground is exposed. Soils totally covered with vegetation do not always show evaporation enrichment of stable oxygen isotopes in soil waters (Hsieh et al., 1998). Evapotranspiration is the predominant form of water loss at depth in most soils. Therefore, an increase in ion activity of Ca^{+2} and HCO^{-3} leads to carbonate formation.

(3) Increase in ion activity as a result of ion exclusion during freezing. Ion exclusion of salts is a well-known property of water during freezing, but it does not appear to be a major contributor to soil carbonate.

(4) Retrograde solubility of calcite. Calcite is more soluble at low temperatures than high temperatures. So, changes in temperature result in changes in solubility.

Furthermore, Cerling (2009) maintains that the evapotranspiration is the most important contributor to soil carbonate formation, so the isotopic signature is in equilibrium with species respiration. The isotopic signature is more negative at grater depths due to the abovementioned considerations (Fig. 1.2.2). This theory was thoroughly demonstrated for paleosoils in different geological ages (Takeuchi et al., 2010; Golubtsov et al., 2014; Andrews et al., 2017). Therefore, the isotopic signature of paleosoils reflects atmospheric concentrations and could be used as a paleoclimatic indicator (Fig. 7.1.1;

Ekart, et al., 1999; Mortazavi et al., 2013; Heilbronn et al., 2015; Ghosh et al., 2016; Li et al., 2016; Andrews et al., 2017; Schobben et al., 2017; Richard et al., 2018).
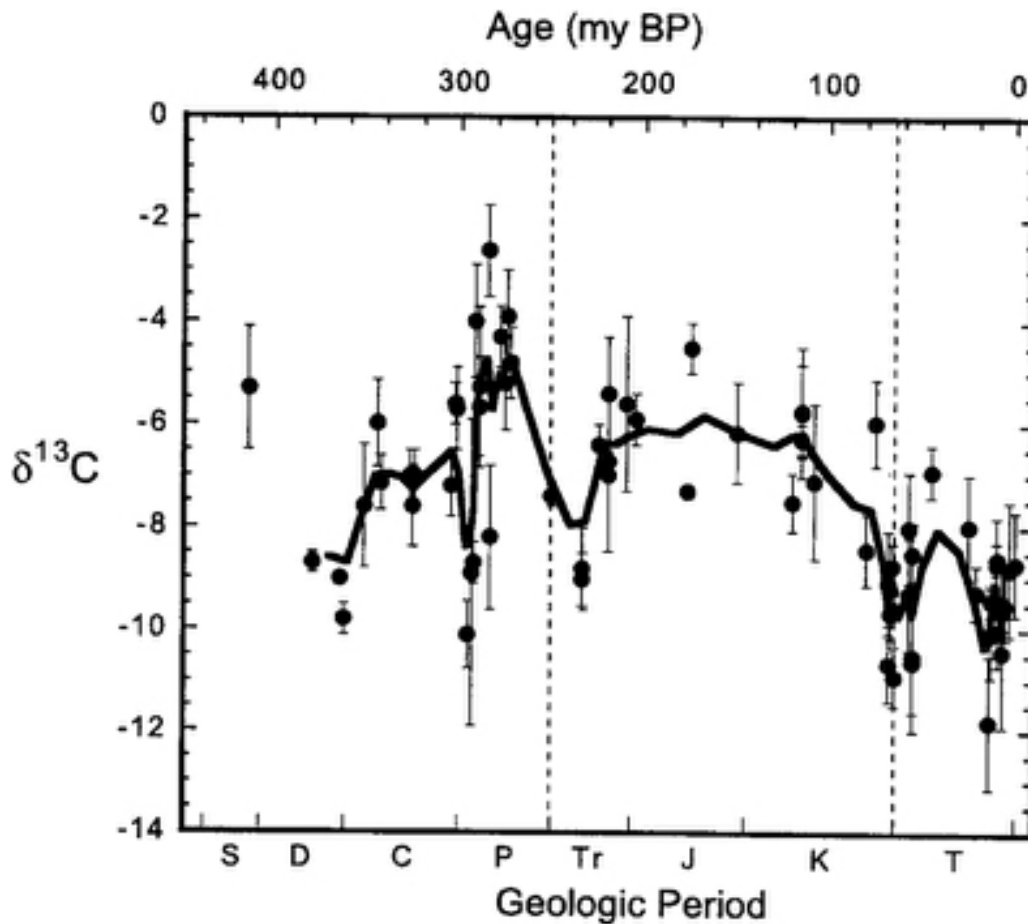
Figure 7.1.1. Isotopic composition of pedogenic carbonates. Averages for each formation are plotted with standard deviation bars. The curve represents a 5 point weighted running average for the data points. From Ekart et al. (1999).

Vegetation plays an important role in the isotopic signature of the paleosols. The signature depends on the respiration process during the absorption of the CO_2. Plants have three types of metabolism, C3, C4 and CAM. In the C3 type the CO_2 is directly fixed in the Calvin cycle, with no previous fixations. The first stable product, in which the carbon is fixed, is composed of three carbon compost (C3). In the C4 metabolism the first fixation of CO_2 is driven by a product with four carbon composts (C4). Finally, the CAM respiration consists of two different processes. Whereas in the C3 and C4 they absorb and fix carbon during the day, in the CAM these processes are separated: CO_2 is absorbed during the night and eliminated during the day. This differentiated carbon cycle in plants

led to a different signature in the isotopic signature. In C3 plants, the $\delta^{13}C$ is between -24 and -30‰ (Deines, 1980; Badeck et al., 2005), while in C4 plants the $\delta^{13}C$ is between -11 and -13‰ (Deines, 1980; Badeck et al., 2005) and in CAM plants respiration presents intermediate values. As C4 respiration is an evolution of C3 respiration, C4 first appears in the Neogene (Cerling et al., 1993) and it therefore did not exist in Permian and Triassic times.

No isotopic analyses had ever previously been conucted on Central-Eastern Southern Pyrenees Permian-Triassic terrains, so the isotopic data presented in this thesis are completely new. The objectives of these analyses are to:

- Observe variations in the isotopic values of pedotypes established by using field and microscopic techniques. This analysis will back up the observations and pedogenic diagnosis that are made.

- Identify variation in the isotopic signature in the different horizons of each pedotype.

- Corroborate whether the carbonate composition in paleosols presented any variations in different periods of time.

7.2 Results

The 40 samples studied (Fig. 7.2.1) have been represented in a $\delta^{13}C$-$\delta^{18}O$ diagram. This diagram allows to understand the isotopic signature of the stable isotopes studied in a representational form. The $\delta^{13}C$ values range from -9 $\delta^{13}C$ to -0,5 $\delta^{13}C$. The $\delta^{18}O$ values range from -2 $\delta^{18}O$ to -13 $\delta^{18}O$. In comparison with previous studies, these values are acceptable. Andrews et al. (2017) obtained between carbonate -10 $\delta^{13}C$ and -5 $\delta^{13}C$ for pedogenic carbonate in Argentinian Cenozoic paleosols. Cerling (2009) obtained values of $\delta^{13}C$ between -10 $\delta^{13}C$ and 0 $\delta^{13}C$ for pedogenic carbonate in Holocene paleosols. Fewer works have examined $\delta^{18}O$ values but Golubtsov et al. (2014) obtained values between -7 $\delta^{18}O$ and -15 $\delta^{18}O$ and Cerling (2009) identified isotopic compositions of $\delta^{18}O$ between 0 $\delta^{18}O$ and -20 $\delta^{18}O$. In conclusion, the results can be accepted as they fall within the ranges established by previous studies.
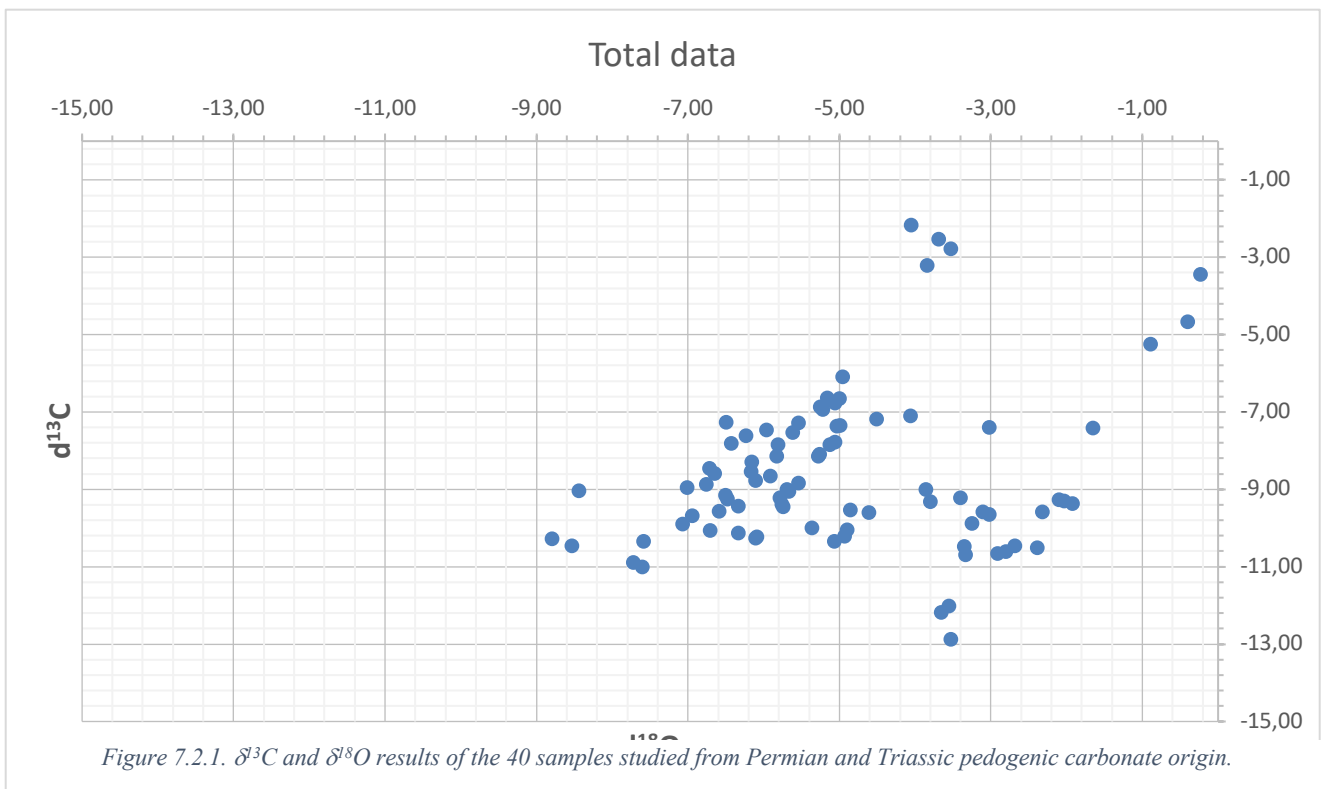
Figure 7.2.1. $\delta^{13}C$ and $\delta^{18}O$ results of the 40 samples studied from Permian and Triassic pedogenic carbonate origin.

7.2.1 Pedotype identification via the isotopic signature

One of the objectives proposed is corroborate the pedogenic diagnosis carried out with hand-samples in the field, and with petrological observations made under the microscope. In Figure 7.2.1, the values have been separated for each of the pedotypes established.

The values used to identify variations between pedotypes were the B-horizon data (Fig. 7.2.2). The B-horizon is the horizon that presents most pedogenic carbonate, as well as being the horizon in which the vegetation and the atmosphere are most closely related (Cerling, 2009; Sheldon and Tabor, 2009). There could therefore be greater differences between the isotopic composition of pedotypes in this horizon.
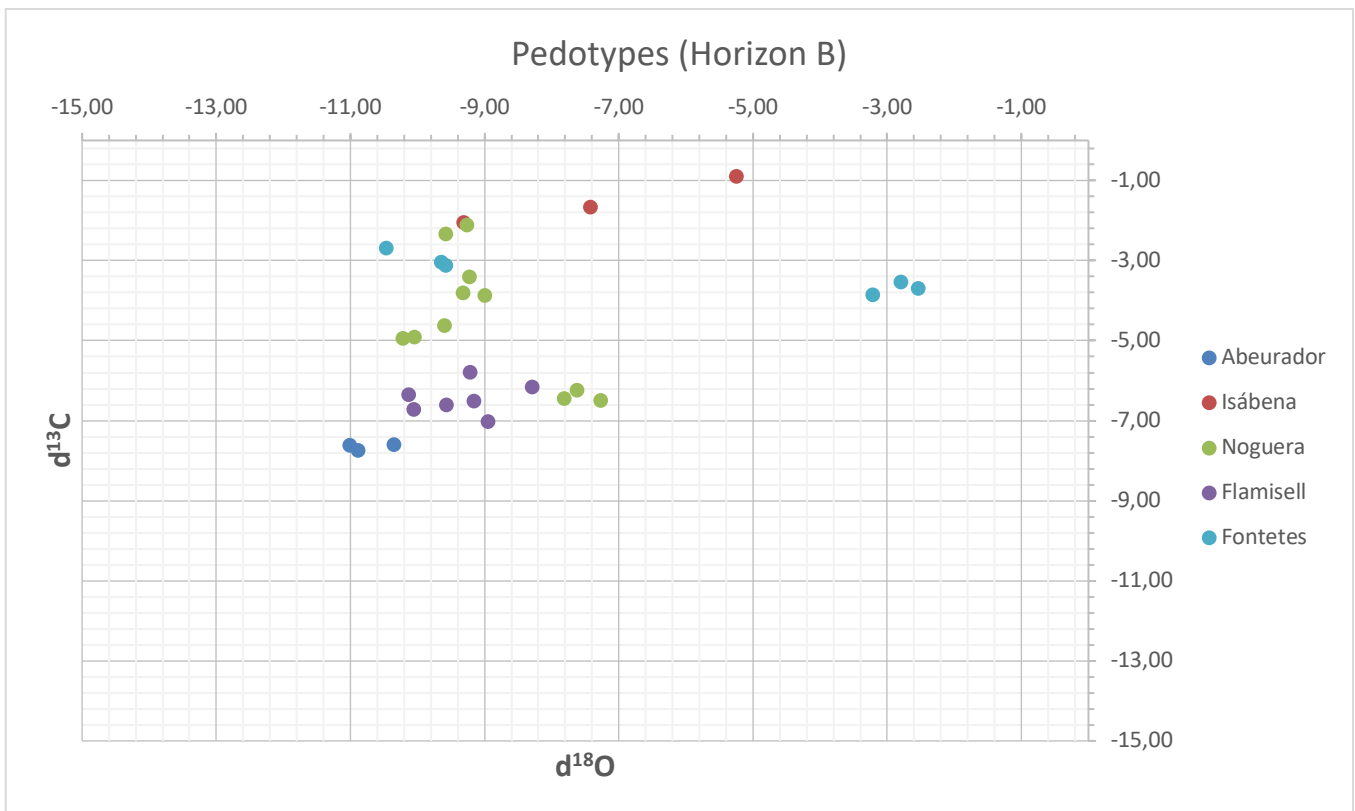
Figure 7.2.2. Isotopic composition of the B horizon of the Permian and Triassic paleosols. The data is separated by the pedotypes identified in the field and under the microscope.

In general terms, it is possible to observe in Figure 7.2.2 that the isotopic composition of each pedotype is different, while their values are grouped togheter and situated within specific ranges.

The Abeurador pedotype data (Figure 7.2.3) indicate a range of $\delta^{13}C$ between -11,01 and -10,36. The separation between the highest and the lowest values is 0,65. On the $\delta^{18}O$ axis the values lie between -7,59 and -7,73 and so the difference is almost non-existent (0,14) in this case. As a first consideration, the Abeurador samples are well constrained. The Isábena pedotype data relative to the B horizon (Fig. 7.2.3) show $\delta^{13}C$ values of between -2,04 and -0,89, with a difference of -1,15. With respecto to the $\delta^{18}O$ values, the range lies between -9,32 and -5,26, with a difference of 4,06 between the values. In the case of the Isábena pedotype the $\delta^{13}C$ seems well constrained, but the $\delta^{18}O$ show dispersion in their results.
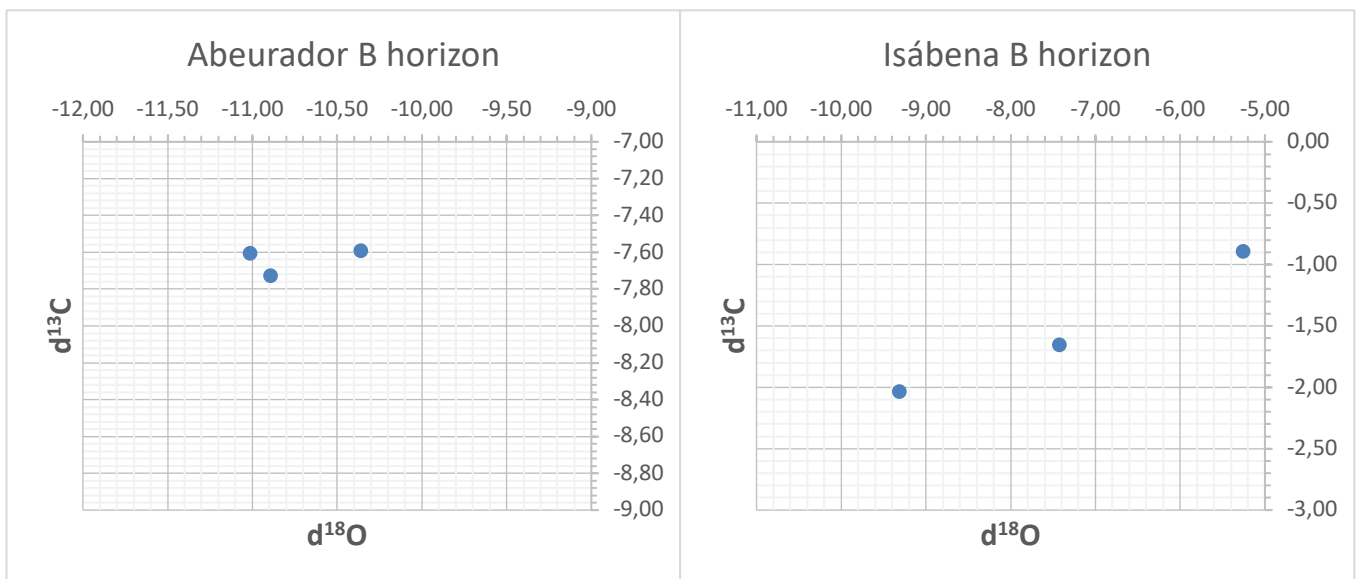
Figure 7.2.3. Abeurador and Isábena B horizon compositions. Note that the horizontal and vertical scale are modified.

The Noguera pedotype's isotopic composition in the B horizon is shown in the Figure 7.2.4. The range of the $\delta^{13}C$ values lies between -2,11 and -6,50, the distance

126

between the maximum and minimum being 4,39. The $\delta^{18}O$ values fall between -7,28 and -10,22, with a difference of 2,94. If Figure 7.2.3 is observed in detail, the isotopic compositions are seen in groups, and the values are well constrained for each group. As for the Flamisell pedotype, the results obtained lie between -5,79 and -6,71 for the $\delta^{13}C$. The differences between the extremes is 0,92. The $\delta^{18}O$ are situated between -8,30 and -10,14, with a difference of 1,84. The Flamisell pedotype data seems to be well constrained and poorly dispersed.
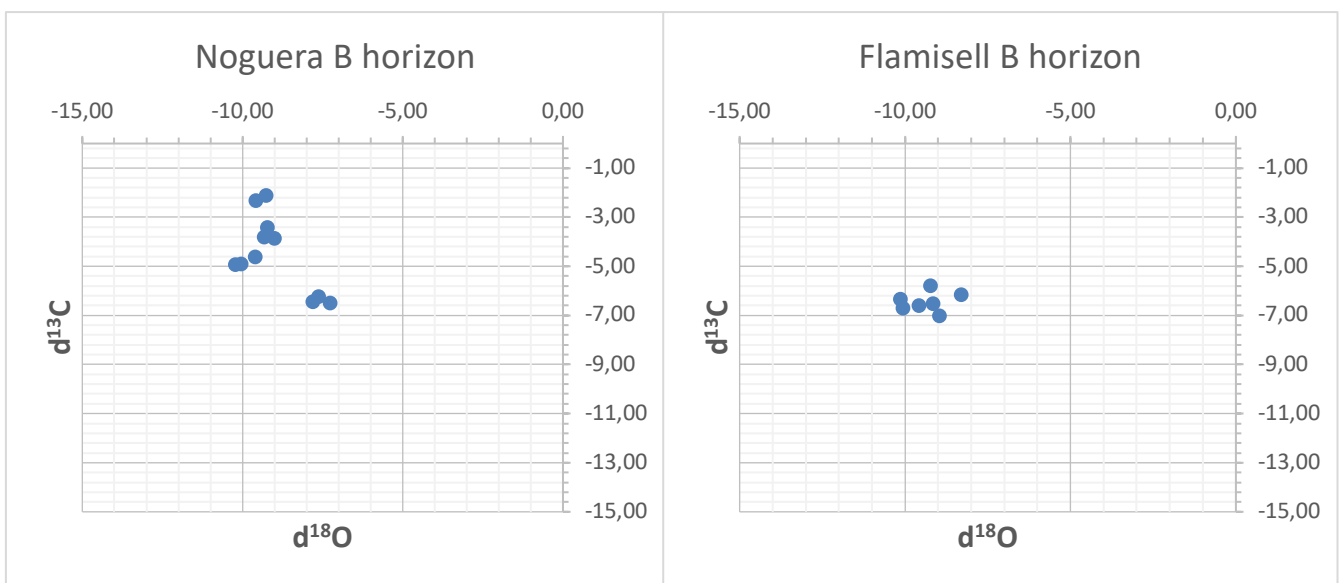
Figure 7.2.4. Noguera and Flamisell B horizon compositions.

Finally, the last B horizon isotopic compositions analyzed was that of the Fontetes pedotype (Fig. 7.2.5). This is characterized by $\delta^{13}C$ values between -2,68 and -3,84, with a difference of 1,16. As for the $\delta^{18}O$, the values range between -2,54 and -10,48, showing the greatest dispersion of all the pedotype (7,94). In conclusion, the $\delta^{13}C$ values are grouped in the same range and the $\delta^{18}O$ are extremely scattered overall, but a closer examination reveals two identifiable subgroups, as in the case of Noguera pedotype. It is generally accepted that the $\delta^{18}O$ isotopic values of calcite are related to the crystallization

temperature (Sheldon and Tabor, 2009). Therefore, diagenesis can affect the $\delta^{18}O$ isotopic composition more strongly than in the case of the $\delta^{13}C$ composition, which is more stable during burial.
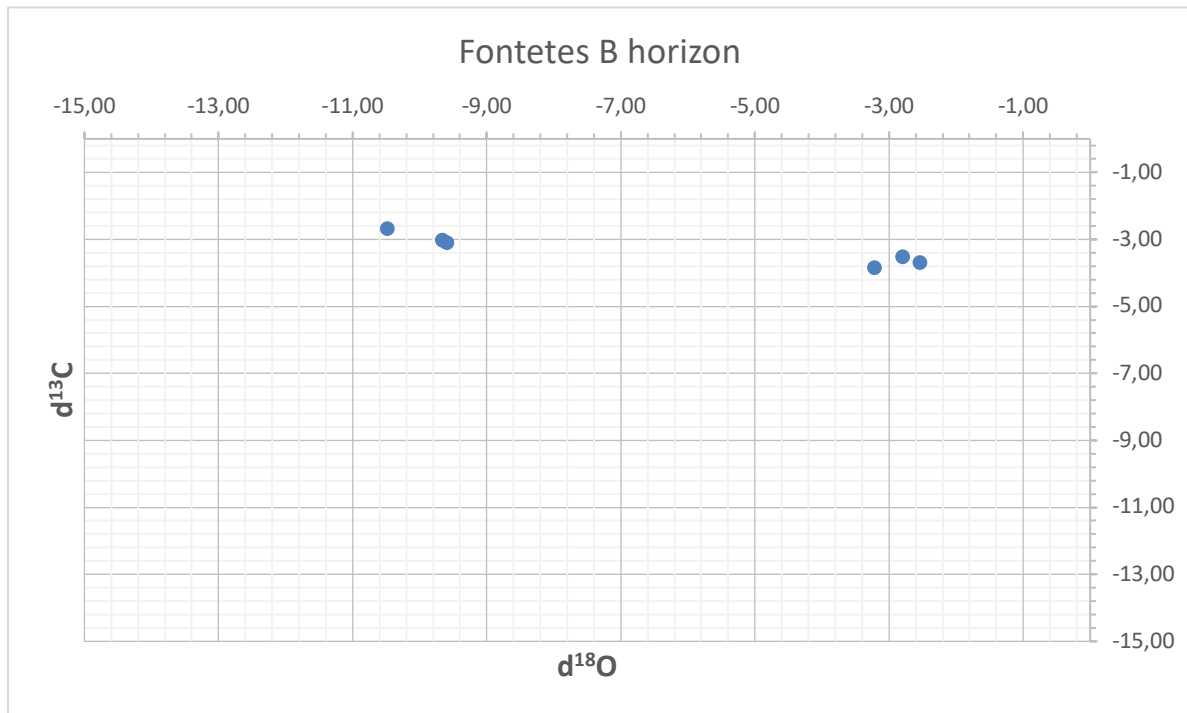
Figure 7.2.5. Fontetes B horizon compositions.

7.2.2 Horizon identification via the isotopic signature

The second objective of the study was to establish wether the different horizons of the paleosols have the same isotopic composition. In order to reach this objective, the results obtained were separated according to the horizons. The comparison between the values was undertaken using the same paleosols, to avoid any possible variations in vegetation or climatic.

The first example is the paleosol called Mola S3, which is situated in the La Mola d'Amunt sector. Its stratigraphic position is the Lower Red Unit. In the field, this example was identified as a Noguera pedotype. In Figure 7.2.6, the values are separated according

128

to the horizons. It can be seen from this representation that each horizons has a different isotopic signature. The $\delta^{13}C$ presented the most significant changes. The B horizon had values of between -3,25 and -5,54, and the A horizon had values of between -2,11 and -3,41, although the $\delta^{18}O$ fell within the same range for both the A and the B horizons.
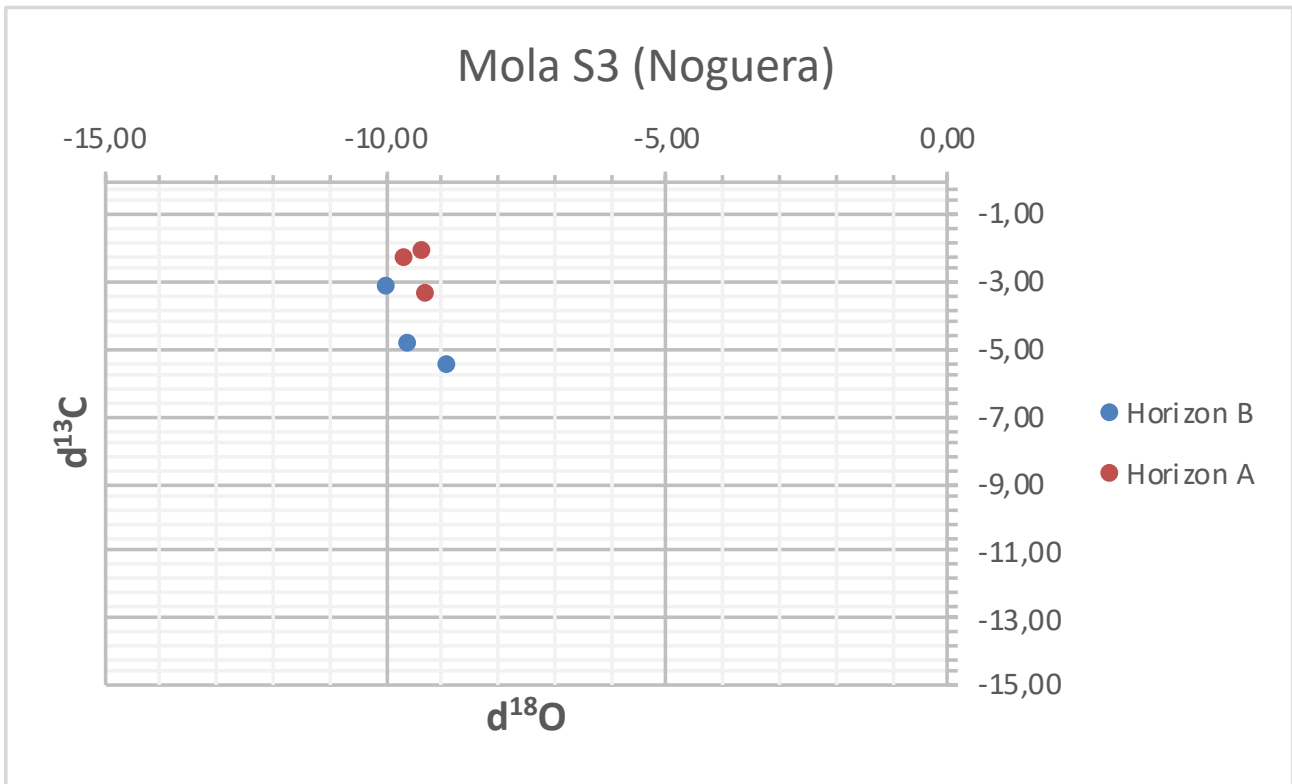
Figure 7.2.6. Isotopic compositions of the Noguera pedotype example Mola S3.

The next example is the Suils P2 paleosol, which is interpreted as an Abeurador pedotype. The stratigraphic position of the samples is the Buntsandstein faces unit. In this case the differentiation between the horizons analyzed was the same as in the previous example. The values of the $\delta^{13}C$ (Fig. 7.2.7) shows a distinctive signature, with horizon B having more negative values (-8,44 to -8,79). The A horizon has a more positive signature (-7,59 to -7,73) for the $\delta^{13}C$. The $\delta^{18}O$ in Suils P2 shows more dispersion than in Mola S3 but there was no distinction between the horizons.
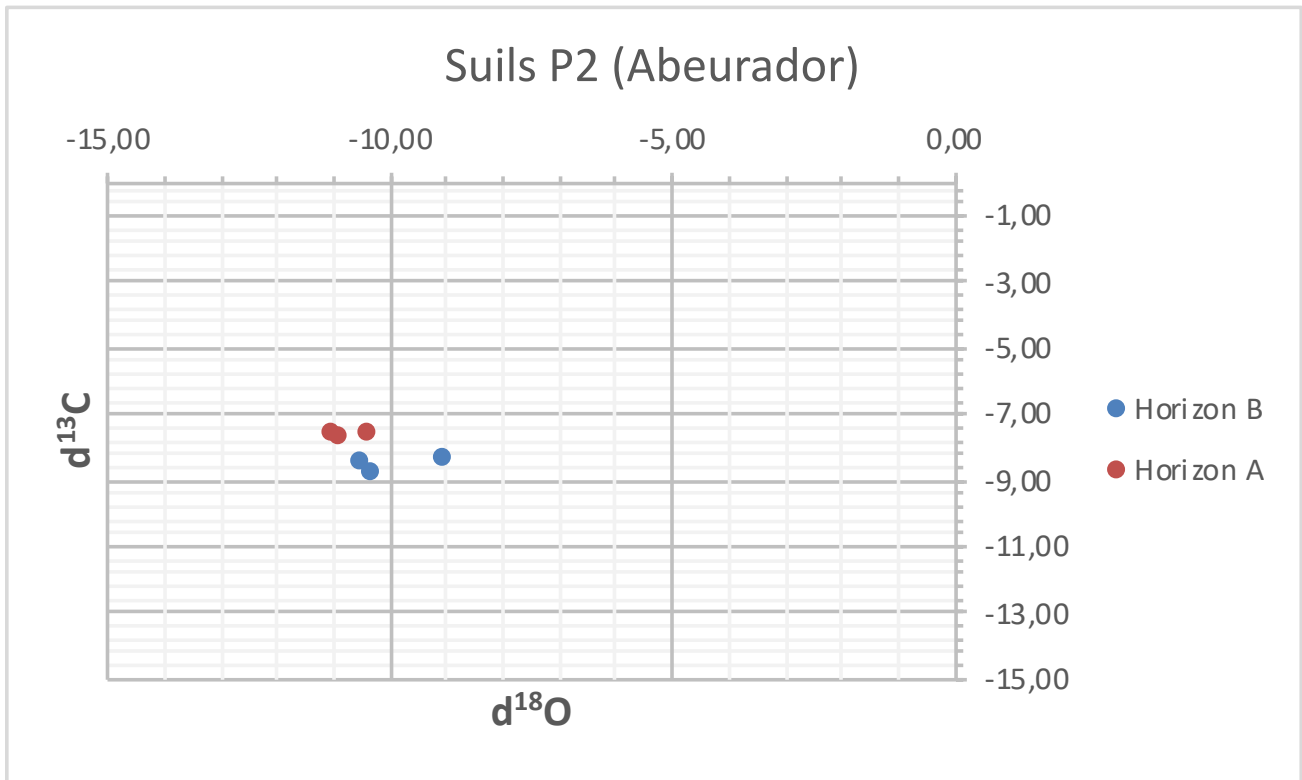
Figure 7.2.7. Isotopic compositions of the Abeurador pedotype example Suils P2.

In the case of the Flamisell pedotype, the individual signature of each horizon was studied as well (Fig. 7.2.8). This example is from the La Mola d'Aumnt sector, in the Lower Red Unit stratigraphic position. In this case the trend observed in the other two examples was maintained. The δ^{13}C of the B horizon are more negative (-6,51 to -7,01) and the A horizon values are more positive (-6,09 to -6,48). The δ^{18}O presented differences between the horizons but these were not marked. The B horizon is more positive and the A horizon values are more negative. Despite this, some values overlap, probably due to subsequent alteration of the rocks during burial.
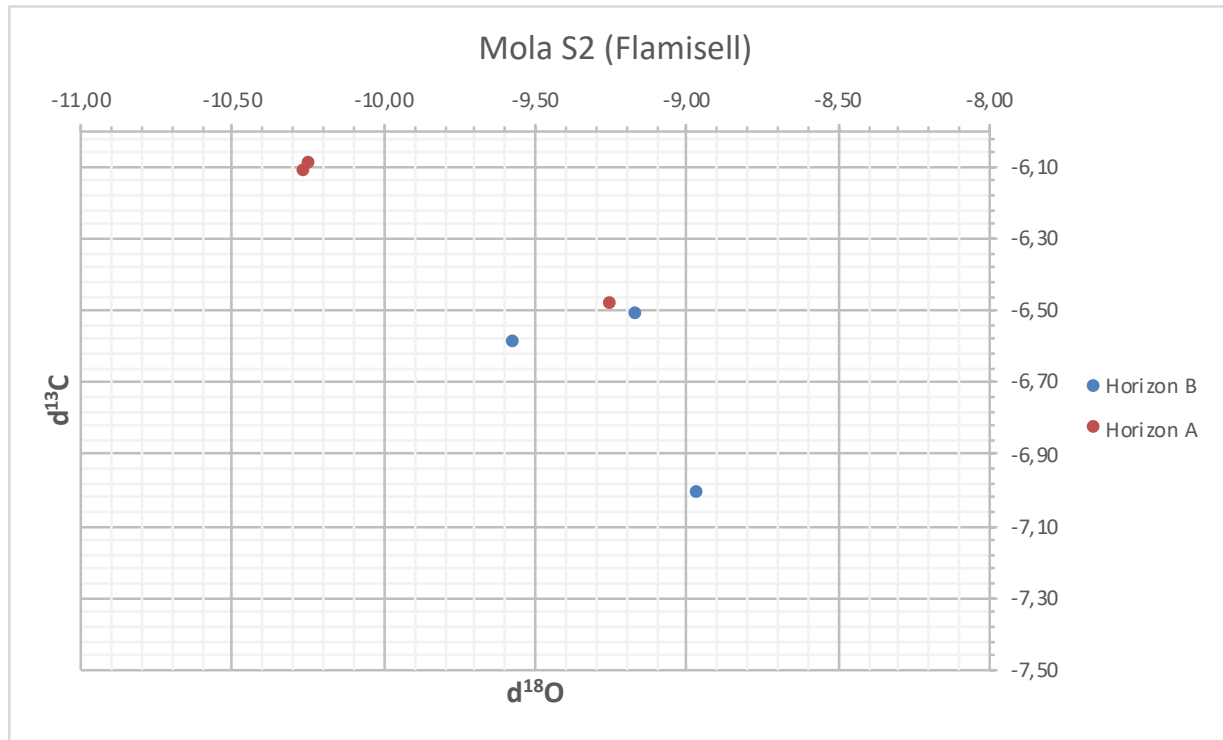
Figure 7.2.8. Isotopic compositions of the Flamisell pedotype example Mola S2.

The last example presented herein corresponds to the Fontetes pedotype. The location of VIP6 6 is in the Villarrué section, on the Lower Red Unit. The δ^{13}C values fall between -1,93 and -3,36 (Fig. 7.2.9). It is possible to see distinctions between the horizons; horizon B is more negative than the horizon A, as in all the preceding examples. The horizon B has values of between -2,91 and -3.36, and the horizon A of between -1,93 and -3,11. The δ^{18}O values do not show any significant difference between the two horizons.

Figure 7.2.9. Isotopic compositions of the Fontetes pedotype example VIP6.

7.2.3 Variation of the isotopic signature in the stratigraphic units

The final objective of this chapter is to corroborate whether differences between values exist across the geological time, in the samel way as there are changes in the isotopic signature between pedotypes and horizons, as described in the last sub-chapters. The data was obtained from the Lower Red Unit, Upper Red Unit and the Buntsandstein facies Unit. With the total data available (Fig. 7.2.10), it is possible to see the main differences between the three stratigraphic units sampled. The Lower Red Unit (Lower Permian, Artinskian) presents the most positive values of $\delta^{13}C$ but they are highly dispersed. The Upper Red Unit (middle Permian) shows intermediate values in comparison with the other two units. The Lower Triassic (Buntsandstein facies Unit) values are clearly more negative than the Permian units.

Figure 7.2.10. Isotopic composition of the total data separated by the Permian and Triassic stratigraphic units.

In order to make our data more precise, Figure 7.2.11 shows the B horizon values classified by stratigraphic units. This should confirm or refute the differences observed in Figure 7.2.10, where the data was not filtered. The results for the B horizon indicate the same differences as with the unfiltered data. Therefore, the pedogenic carbonate in the Central-Eastern Southern Pyrenees indicates significant differences between the Permian and Triassic isotopic signatures.
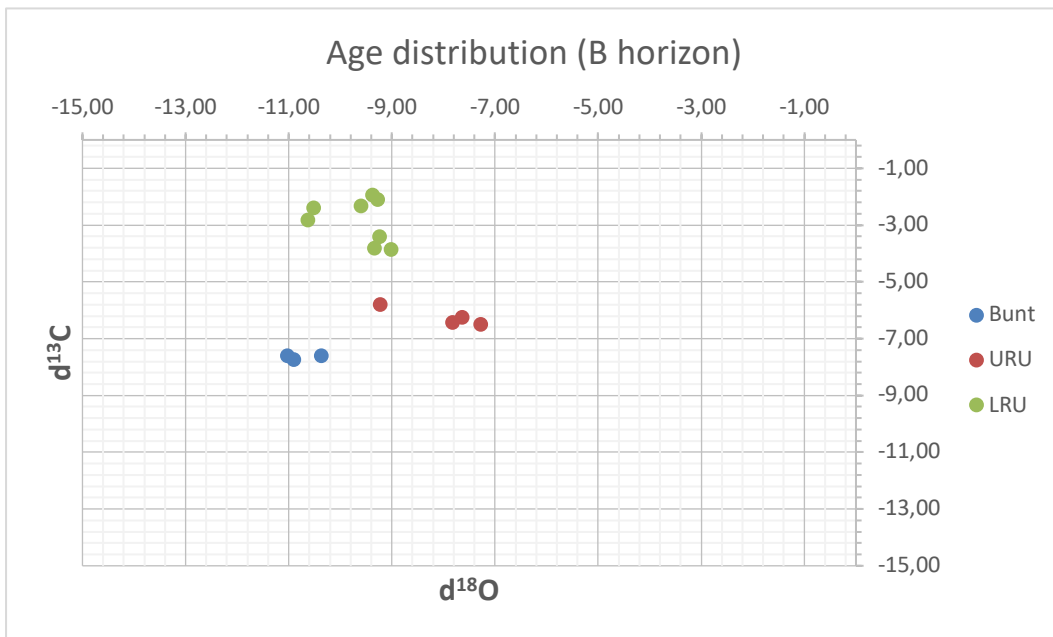
Figure 7.2.11. Isotopic composition of the B horizon data separated by the Permian and Triassic stratigraphic units.

133

8. Clay Mineralogy

8.1 Introduction

Clay minerals have been studied in continental deposits to interpret paleoenvironmental factors for many years (Keller, 1970; Singer, 1980, 1984; Ingles and Anadon, 1991; Benito et al., 2005; Xu et al., 2017). Primary-stage clay minerals are considered to be those clay minerals which originate directly from parent materials. This is because the mineral phase formed possess the lowest free energy attainable in the environment at the time when the genesis of clay minerals occurs. Any of the clay minerals families -kaolin, smectite-montmorillonite, illite, chlorite-vermiculite, and other less common varieties- can be produced in the weathering environment. The genesis of each clay mineral can be inter-related with certain distinguishing materials or energies, which are indicators of the genetic environment.

The identification of paleoenvironmental and paleoclimatic conditions using clay mineralogy data in continental deposits is a matter of discussion, especially in the Permian and Triassic materials (Alonso-Azcárate et al., 1997; Körner et al., 2003; Hong et al., 2008; Marfil et al., 2015; Xu et al., 2017). The paleontological content in non-marine terrains is usually poor, and geochemical approaches such as clay mineralogy analyses have been usefully for filling this information gap. The interpretation of minerals over the course of the stratigraphic record is based on Keller's work (1970), which established the main guidelines. Kaolinization occurs when the geological environment removes Ca^{2+}, Mg^{2+}, Fe^{2+}, Na^+ and K^+. The processes which can made this happen are precipitation, fresh water availability and high Al/Si ratio. These kinds of environments are linked to humid and vegetated scenarios. Montmorillonitzation represents a process in which evaportation is higher than the precipitation, and so semi-arid conditions are inferred. Moreover, the presence of montmorillonite minerals is related to igneous-type

minerals. Kaolinite is typical of low-temperatures conditions for low-gradient diagenetic processes, and so ahumid tropical climate with good drainage conditions is traditionally inferre (Singer, 1984; Ehrenberg, 1993).

One of the factors that restrict paleoenvironmental discussion is the metamorphism that occurred after the genesis of clay minerals. Thermal maturity studies in the Sichuan basin (China; Xu et al., 2017) demonstrated that the clay mineral transformative illitization of smectitic clays corresponding to the early-middle diagenetic stage (the %illite contents in I/S in K–bentonites lies mostly in the range of 50–80%; Xu et al., 2017). Lindgreen and Surlyk (2000) stated that low-moderate diagenesis mainly influences mixed-layer minerals while discrete minerals are not significantly affected and still carry valuable primary signals of the sedimentary environment. Tectonic effects on deposits is another issue that needs to be considered. Intense tectonics could generate distortion in the data obtained, so it is not advisable to draw any major conclusion solely on the basis of data from clay mineralogy. The illite crystallinity index (IC) is used to indicate the degree of diagenesis or metamorphism (Árkai et al., 1995, 2004; Jiang et al., 1997). An IC index higher than 1 indicates early diagenesis, between 1 and 0,425 late diagenesis, and under 0,425 indicate an Anchizone metamorphism. Therefore, if the values of the IC index are above 0,425 subsequent paleoenvironmental interpretations will be consistent.

8.1.1 Clay mineralogy framework in the Southern Pyrenees

Studies of the Permian-Triassic transition have been carried out in various parts of the world (Fisher and Jeans, 1982; Alonso-Azcárate et al., 1997; Hong et al., 2008; Xu et al., 2017) and recently in the Catalan (Central-Eastern) Pyrenees by Mujal et al. (2017b), with subsequent comments by Ronchi et al. (2018). Mujal et al. (2017b) argued

that the mineralogical and geochemical composition of Permian and Triassic rocks supports a humid-semiarid-humid climatic trend and that these data, combined with sedimentological features, are indicative of sedimentary continuity. They based their interpretations on claims that small variations in clay mineralogy (and in other phases like albite and analcime) are indicative of climatic variations and they use the inferred climatic change to support the continuity of the sedimentary record. However, Ronchi et al. (2018) disagreed with Mujal's interpretations because the degree of diagenesis is not discussed and no oriented aggregates of clay concentrates were made. Furthermore, Ronchi et al. (2018) claimed controversial results from their studies of samples collected in a nearby zone.

8.2 Results

The IC index obtained from the studied samples variates according to the area (Fig. 8.2.1).
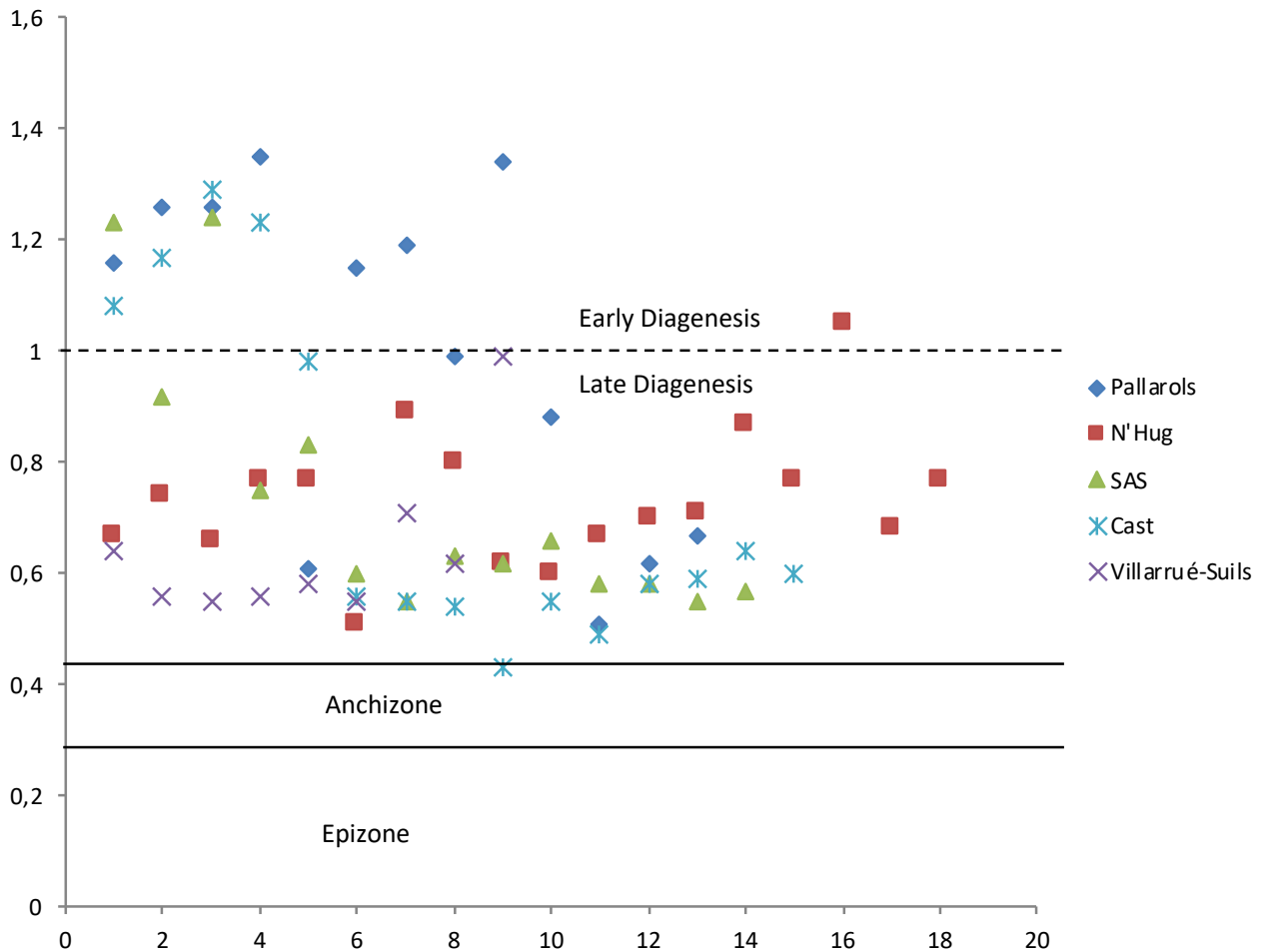
Figure 8.2.1. IC index diagram of the samples studied.

All the samples were taken from the diagenesis area, so their mineralogical composition was not altered by metamorphism. This fact allowed to interpret the data obtained as a consequence of paleoclimatic conditions and not of any other processes.

8.2.1 Samples

The clay mineralogy results obtained are organized in accordance with the division into stratigraphic units. Stratigraphic and tectonic issues made it impossible to sample all the units in all the sectors but, nevertheless, a complete sampling is presented here for each unit (Fig. 8.2.2). The total number of samples analyzed was 79.
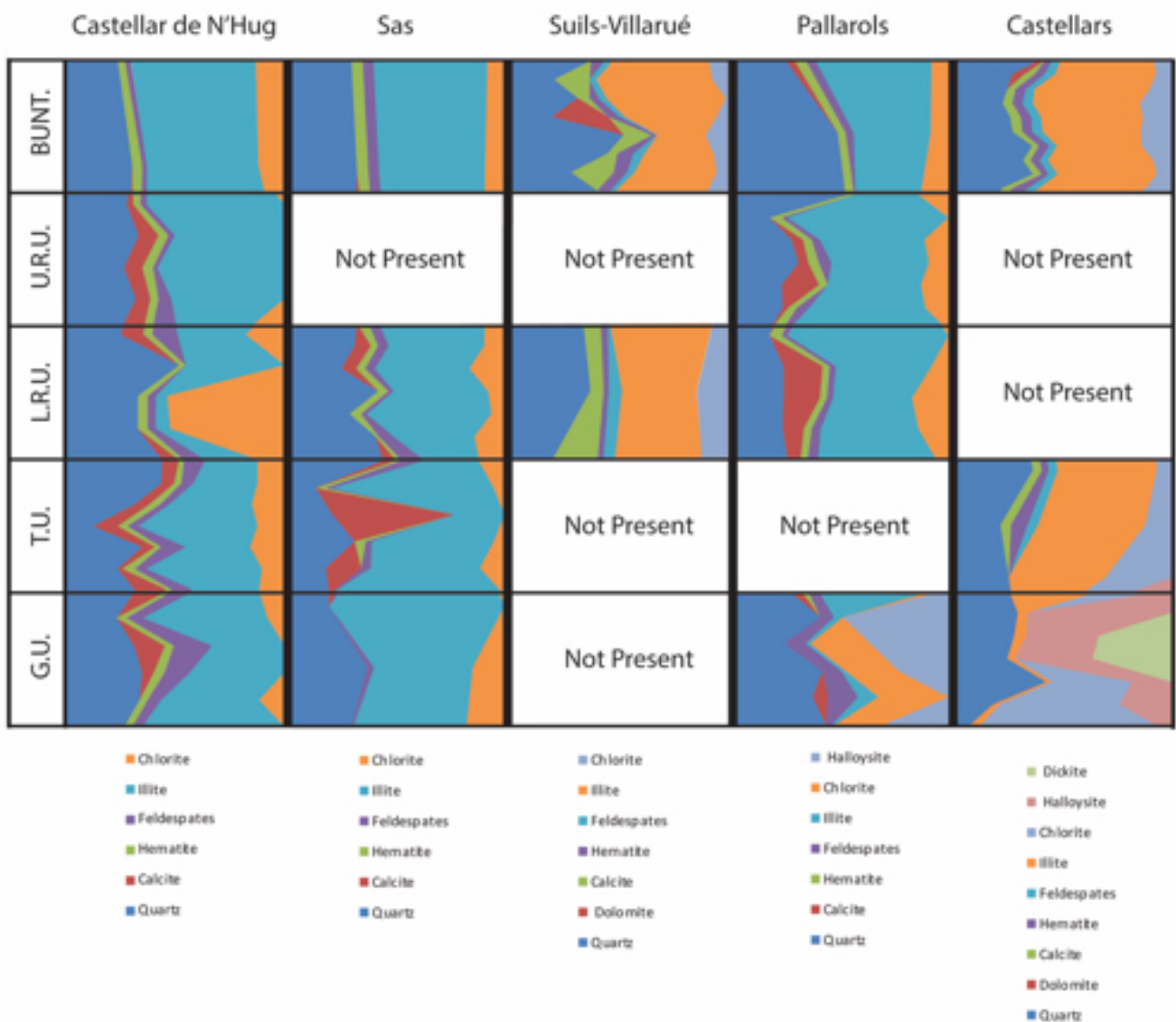
Figure 8.2.2. Overall results of the clay mineral analysis done in the Southern Pyrenees. In each sector is represented the stratigraphic units outcropping.

8.2.2. Grey Unit characterization

The Grey Unit was sampled in four sections: Castellar de N'Hug, Sas, Pallarols and Castellars. In the Suils-Villarrué section the Late Carboniferous unit is lacking due to tectonics and depositional configurations. The study of the four sections sampled makes it possible to characterize the clay mineralogy of the Grey Unit.

In general terms the Grey Unit is characterized by the presence of chlorite, illite, feldspates, hematite, calcite, quartz, halloysite and dickite (Fig. 8.2.2). Some differences in clay mineralogy were recorded between the Late Carboniferous deposits (Fig. 8.2.2). The Castellar de N'Hug sector was characterized by the following percentages: 24-35% of quartz; 0-14% of calcite, but only two samples with calcite content (NH7-8 and NH8); 4-5% of hematite; 4-17% of feldspates; 33-65% of illite and 0-11% of chlorite, but only two samples with chlorite content (NH7 and NH9). The Sas sector contained: 18-36% of quartz; 0% of calcite; 0% of hematite; 1-3% of feldspars; 46-82% of illite and 0-18% of chlorite. The percentatges of the clay mineralogy in the Pallarols sector are: 23-42% of quartz; 0-7% of calcite, but only one sample containing calcite (PAL-GU2); 3-14% of feldespates; 2-10% of illite; 0-33% of chlorite, but only the sample PAL-GU5 did not contain this mineral and 0-49% of halloysite, but only the sample PAL-GU2 did not contain this mineral. Finally, clay mineralogy of the Castellars section was as follows (Fig. 8.2.3): 5-42% of quartz; 0% of calcite; 0% of hematites; 0% of feldspars; 2-6% of illite; 0-85% of illite; 5-36% of halloysite and 0-37 of dickite. In this last sector it is notable that in the basal samples the chlorite was the most representative mineral while moving upwards it was replaced by halloysite and dickite (Table 8.2.1).

Figure 8.2.3. Synthetic stratigraphic column of Castellar sector with the clay mineralogy percentages. The total thickness of the Grey Unit is 225 meters.

	Quartz	Calcite	Hematite	Feldespates	Illite	Chlorite	Halloysite	Dickite
CAST11	5	0	0	0	5	85	5	0
CAST12	17	0	0	0	3	56	24	0
CAST13	42	0	0	0	2	37	19	0
CAST14	24	0	0	0	3	0	36	37
CAST15	26	0	0	0	6	0	34	34
CAST16	28	0	0	0	5	0	67	0

Table 7.2.1. Clay mineral content of Castellars sectors in the Grey Unit deposits. CAST11 sample corresponds to the bottommost deposits and CAST16 for the topmost.

8.2.3 Transition Unit characterization

In the sampled sectors the Transition Units is represented in Castellar de N'Hug, Sas and Castellars. In the other two sections TU is lacking is due to a stratigraphic unconformity in Pallarols and for tectonic reasons in Suils-Villarrué.

The clay mineralogy in this unit was represented by chlorite, illite, feldspates, hematite, calcite and quartz. The main difference with from the previous unit was the absence of halloysite and dickite. The percentages of the Castellar de N'Hug sector were as followsg: 13-35% of quartz; 2-14% of calcite; 2-6% of hematite; 4-11% of feldspars; 29-53% of illite and 10-16% of chlorite. The Sas sector was characterized by 12-43% of quartz; 0-57% of calcite, with two samples without any calcite content (SAS5 and SAS8); 0-10% of feldspars; 23-75% of illite and 0-12% of chlorite. The clay mineralogy results from the Castellars sector were: 20-35% of quartz; 0-5% of calcite; 0-8% of hematite; 0-5% of feldspar; 45-50% of illite and 7-31% of chlorite.

The contents are quite similar with respect the previous unit, but there are some small differences. The presence of hematite minerals is the most evident change. The shift is poor but the content switch from many 0% (Table 8.2.2) to 2-6% in the Castellar de N'Hug area (Table 8.2.4). Other mineral that increased in their presence were the calcite, with an increase in both Castellars and Castellar de N'Hug. In contrast, dickite and halloysite completely disappeared.

	Quartz	Calcite	Hematite	Feldespate	Illite	Chlorite
NH14	32	7	5	4	37	15
NH13	13	11	5	5	54	12
NH12	35	6	3	11	29	16
NH11	24	2	6	5	53	10
NH10	32	14	2	10	30	12

Table 8.2.2. Clay mineral content of Castellar de N'Hug sector in the Transition Unit deposits. NH10 sample corresponds to the bottommost deposits and NH 14 for the topmost.
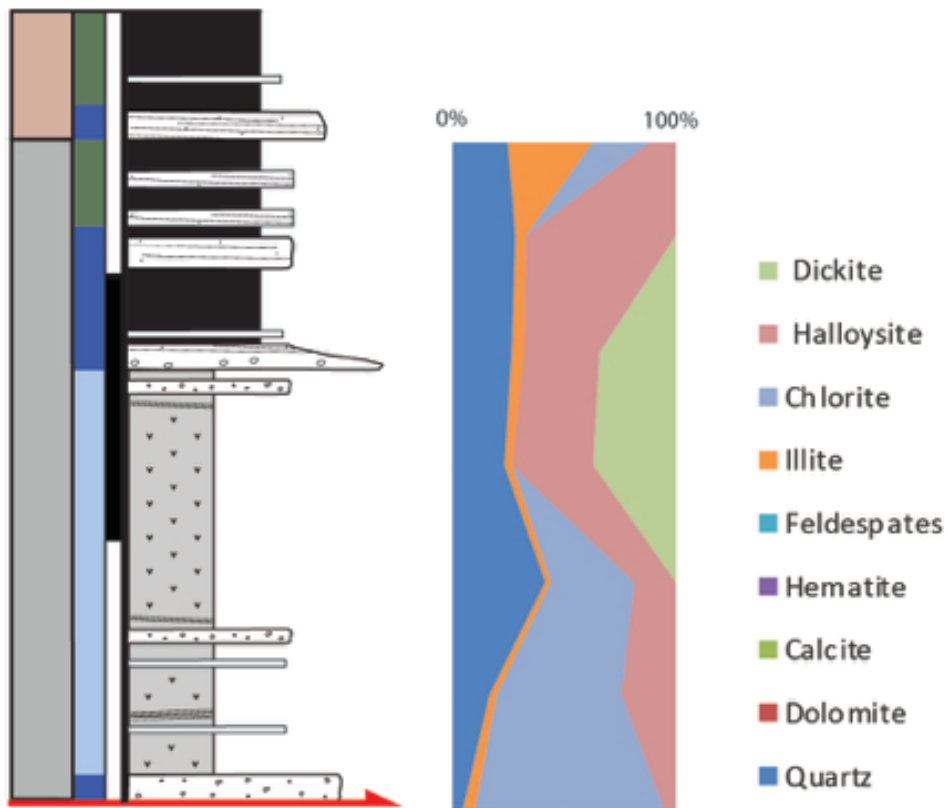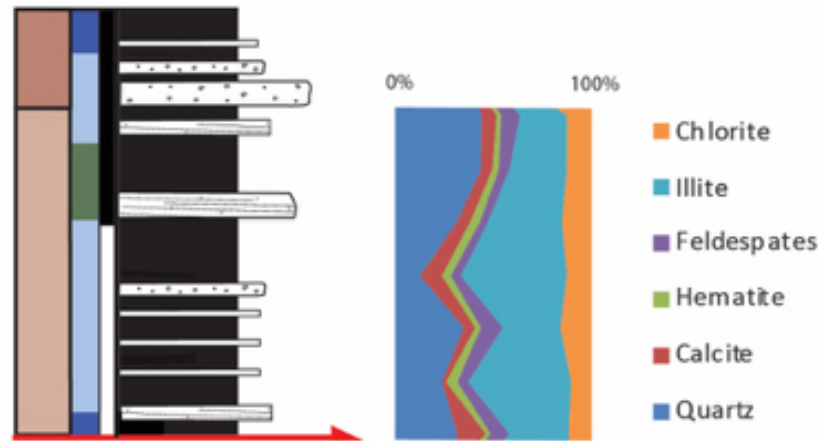
Figure 8.2.4. Synthetic stratigraphic column of Castellar de N'Hug sector with the clay mineralogy percentages. The total thickness of the Transition Unit is 150 meters.

8.2.4 Lower Red Unit characterization

This unit represents the oldest red bed deposits in the Southern Pyrenees stratigraphy. Clay mineralogy sampling undertaken in the Castellar de N'Hug, Sas, Suils-Villarué and Pallarols sectors. In the case of the Castellar sector, this unit did not outcrop because high-angular unconformity occurs between the TU and Buntsandstein facies unit.

The mineralogy that characterizes this unit is the following: chlorite, illite, feldespates, hematite, calcite and quartz. The Castellar de N'Hug sector is characterized by: 33-52% of quartz; 0-7% of calcite, only present in two samples (NH15 and NH16); 3-4% of hematite; 5-45% of illite and 0-53% of chlorite. The Sas sector was represented by (Table 8.2.3 and Fig. 8.2.5): 24-41% of quartz; 0-7% of calcite, but only two samples with calcite content (SAS14 and SAS16); 1-5% of hematite; 2-7% of feldspars; 38-58% of illite and 6-14% of chlorite. The Suils-Villarué sector presented: 20-37% of quartz; 6-20% of calcite; 3% of hematite; 1-6% of feldspars; 34-47% of illite and 7-14% of chlorite. The Pallarols sector contained the following percentages: 16-25% of quartz; 0-18% of

142

calcite, the PAL-LRU5 sample with no calcite content; 3-6% of hematite; 37-75% of illite and 0-17% of chlorite.

It is possible to see that the mineralogy is similar in the Transition Unit, as the percentages did not change substantially. Despite some non-significant changes, a slight increase in calcite can be inferred. Another increase was the percentage of illite with respect to the Grey Unit content.

	Quartz	Calcite	Hematite	Felspars	Illite	Chlorite
SAS10	40	0	1	7	38	14
SAS11	28	0	5	3	58	6
SAS12	41	0	5	2	44	8
SAS14	24	7	4	4	44	16
SAS16	30	7	3	5	45	9

Table 7.2.3. Clay mineral content of Sas sector in the Lower Red Unit deposits. SAS10 sample corresponds to the bottommost deposits and SAS16 for the topmost.

The most significant variation occurred in the same unit. The chlorite percentages in Castellar de N'Hug present huge variations in comparison with the other sectors. There is a clear relationship between illite and chlorite: whenever there is a high propostion of illite, there is a low proportion of chlorite. This phenomenon was also observed in the Transition Unit.

Figure 8.2.5. Synthetic stratigraphic column of Sas sector with the clay mineralogy percentages. The total thickness of the Lower Red Unit is 225 meters.

8.2.5 Upper Red Unit characterization

This unit represents the third red bed unit, and is the last Permian unit. The sectors sampled were: Castellar de N'Hug and Pallarols. Is important to note that this unit only appear in the two Easternmost basins (Gramós and Camrpodón-Castellar). This situation is explored in the Discussion chapter.

The clay mineralogy obtained from the Lower Red Unit is: quartz, calcite, hematite, feldspar, illite and chlorite. The Castellar de N'Hug sector contained this composition: 25-34% of quartz; 3-10% of calcite; 3-5% of hematite; 2-12% of feldpars; 31-63% of illite and 0-18% of chlorite, but only the bottommost sample (NHURU1) has chlorite content. The Pallarols sector percentages were: 16-30% of quartz; 0-17% of calcite; 4-6% of hematite; 0-6% of feldspars; 44-75% of illite and 0-13% of chlorite.

144

	Quartz	Calcite	Hematite	Feldespates	Illite	Chlorite
NHURU5	28	3	3	3	63	0
NHURU4	34	9	5	3	50	0
NHURU3	27	8	5	2	58	0
NHURU2	33	6	4	6	51	0
NHURU1	25	10	4	12	31	18

Table 8.2.4. Clay mineral content of Castellar de N'Hug sector in the Upper Red Unit deposits. NHURU1 sample corresponds to the bottommost deposits and NHURU5 for the topmost.

The content of the two sectors had similar compositions. In Castellar de N'Hug an increase of illite content was observed going upwards, while there was also a decrease in the feldspars content towards the top deposits (Table 8.2.4 and Fig. 8.2.6). As in the Lower Red Unit, the mineralogy presents similitudes with the other two Permian units. The dickite and halloysite minerals were not been recorded in this unit. The illite percentages seem to be higher than in the oldest units, and the chlorite content is reduced as a result.
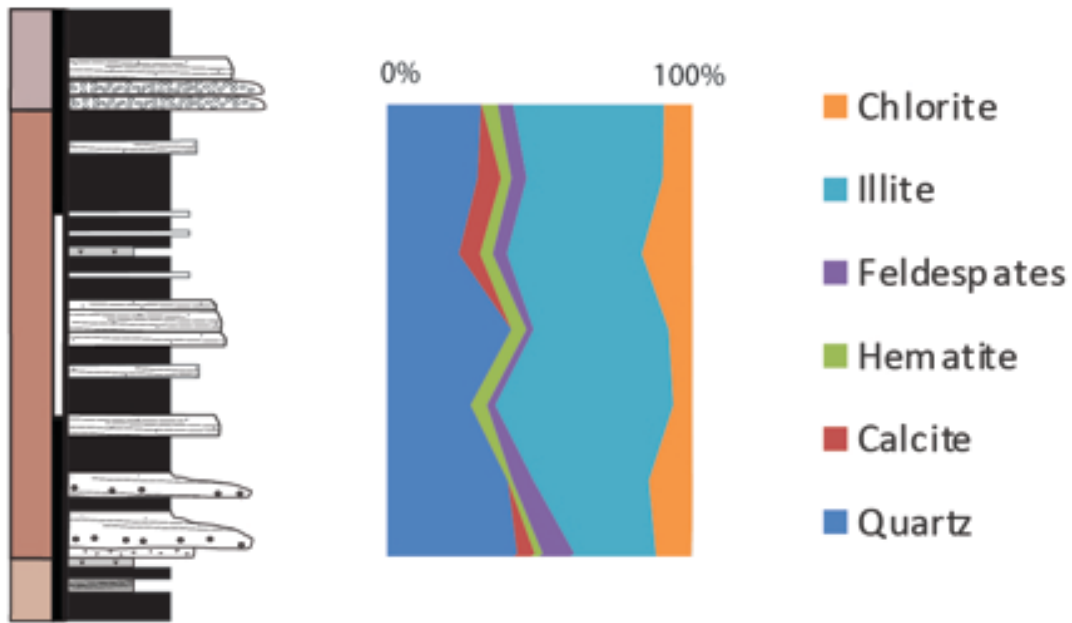

Figure 8.2.6. Synthetic stratigraphic column of Castellar de N'Hug sector with the clay mineralogy percentages. The total thickness of the Upper Red Unit is 170 meters.

8.3.6 Buntsandstein facies "unit" characterization

The Lower Triassic unit represents the last continental deposits in the Southern Pyrenean basins studied. These deposits mainly consist of siltstones, sandstones and conglomerates. The outcrop of this unit is good and the sampling was performed in all five studied sectors: Castellar de N'Hug, Sas, Suils-Villarrué, Pallarols and Castellars.

The clay mineralogy detected in this unit was: quartz, dolomite, calcite, hematite, feldspars, illite and chlorite. In the Castellar de N'Hug area the percentages obtained were: 24-31% of quartz; 0% of dolomite; 0% of calcite; 3-5% of hematite; 2-3% of feldspars; 51-57% of illite and 12-13% of chlorite. In the Sas sector: 28-31% of quartz; 0% of dolomite; 0% of calcite; 5% of hematite; 5% of feldspars; 50-53% of illite and 8-9% of chlorite. In the Suils-Villarrué sector (Table 8.2.5): 19-52% of quartz; 0-26% of dolomite, only in sample SUILS5; 0-16% of calcite; 0-7% of hematite; 1-5% of feldspars; 22-55% of illite and 1-10% of chlorite. In Pallarols the results were: 23-53% of quartz; 0% of dolomite; 0-4% of calcite; 4-6% of hematite; 0-4% of feldspars; 29-55% of illite and 8-14% of chlorite. Finally, in the Castellars sector (Table 8.2.6 and Fig. 8.2.6): 21-38 of quartz; 0-6% of dolomite; 0-5% of calcite; 4-5% of hematite; 3-5% of feldspars; 39-54% of illite and 8-15% of chlorite.

The most notable difference between the sectors is the variability in the calcite content, ranging from 16% in some samples (SUILS7) to 0% in many others. The hematite and feldspars content were constant throughout the studied sectors, as was the case in the previous units.

	Quartz	Dolomite	Calcite	Hematite	Feldespars	Illite	Chlorite
SUILS2	40	0	0	6	3	42	9
SUILS2P	28	0	19	6	4	38	5
SUILS3	45	0	5	7	5	32	7
SUILS4	52	0	13	2	1	22	10
SUILS5	19	26	0	5	3	42	5
SUILS6	31	0	5	4	3	55	1
SUILS7	20	0	16	0	3	53	7
SUILS8	37	0	0	6	4	44	8

Table 8.2.5. Clay mineral content of Suils sector in Buntsandstein facies unit deposits. SUILS2 sample corresponds to the bottommost deposits and SUILS8 for the topmost.

	Quartz	Dolomite	Calcite	Hematite	Feldespars	Illite	Chlorite
CAST20	31	0	4	4	4	49	8
CAST21	35	0	3	5	3	39	14
CAST22	26	0	5	5	5	46	15
CAST23	25	0	5	5	5	47	13
CAST24	21	0	5	4	5	50	15
CAST25	23	0	4	5	4	54	10
CAST26	26	6	5	4	5	47	8
CAST27	38	3	0	4	4	43	8

Table 7.2.6. Clay mineral content of Castellar sector in Buntsandstein facies unit deposits. CAST20 sample corresponds to the bottommost deposits and CAST27 for the topmost.

The most striking difference from the Carboniferous and Permian units is the appearance of dolomite. This mineral is usually located in the upwards samples (Table 8.2.7). Chlorite presented low values with respect the oldest Permian units, as it did in the Upper Red Unit. No dickite or halloysite minerals were noted in this unit.
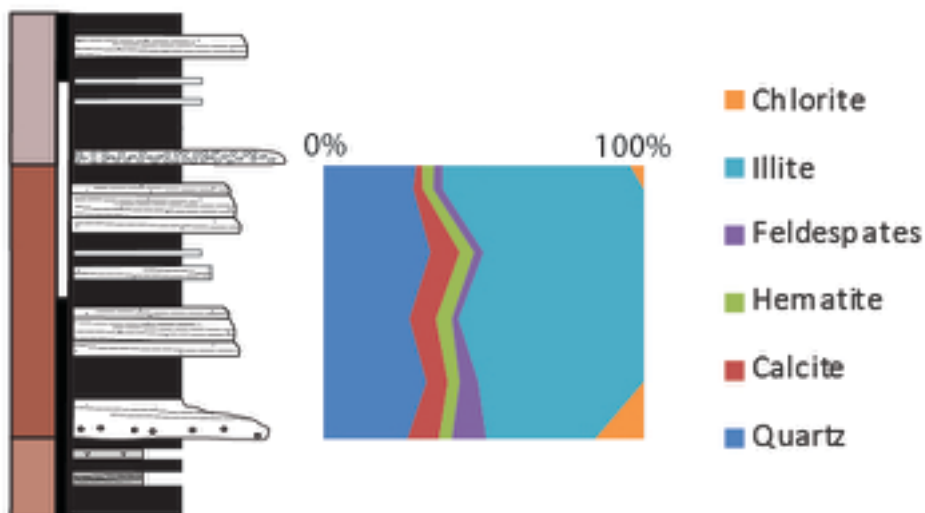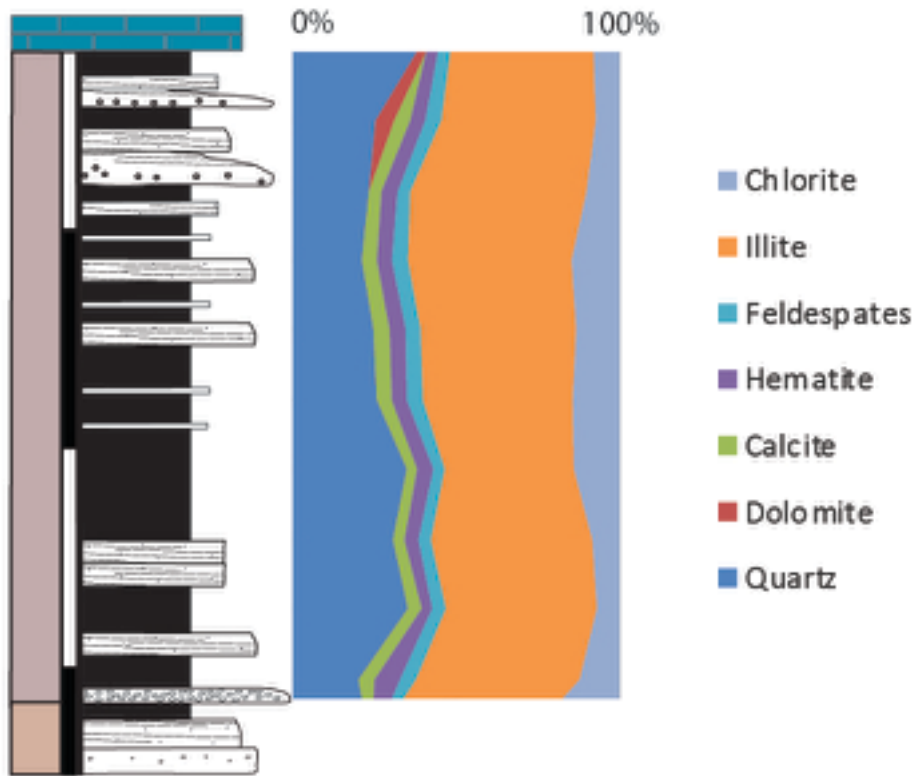

Figure 8.2.7. Synthetic stratigraphic column of Castellars sector with the clay mineralogy percentages. The total thickness of the Upper Red Unit is 260 meters.

9. Tectonic and sedimentation of Erill Castell-Estac Basin

9.1 Introduction

The Erill Castell-Estac Basin is a ESE–WNW basin, approximately 20 km long, in the Pont de Suert-Sort area, Central Southern Pyrenees (Fig. 9.1.1). A complex network of foreland-directed thrusts characterizes its current structure; these thrusts and backthrusts resulted from marked rotation and overturning during the Alpine shortening (late Cretaceous–early Miocene; Vergés and Martínez, 1988). The Erill Castell-Estac Basin is part of the Erta domain, one of the southward-facing thrust sheets forming the Pyrenean Axial Zone (e.g., Poblet, 1991; Muñoz, 1992; Saura, 2004). Several internal backthrusts affect the Erta thrust sheet but, according to tectonic reconstructions, these sheets are part of the original Erill Castell-Estac Basin. The stacking of these sheets involved the Variscan basement and the Upper Carboniferous-to-Triassic cover producing an imbricate fan of backthrusts that internally deformed the basin.
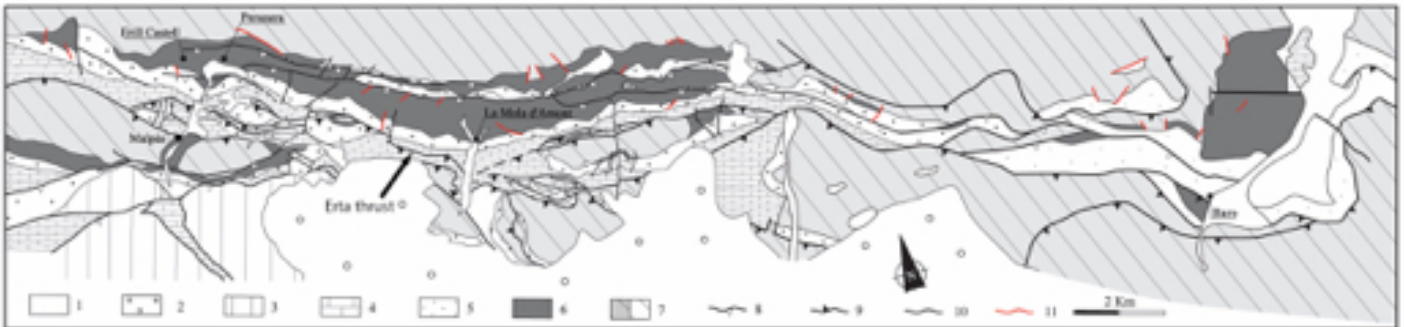
Figure 9.1.1. Geological map of the Erill Castell-Estac Basin based on Saura (2004) and Saura and Texiell (2006). (1) Quaternary (2) Cenozoic cover (3) Jurassic-Cretaceous (4) Marine Triassic (5) Lower-Middle continental Triassic (Bunt.) (6) Late Carboniferous-Permian (7) Variscan Basament (8) Back-thrust (9) Inverse fault (10) Normal fault (11) Late Carboniferous-Lower Triassic synsedimentary faults. Modified from Lloret et al. (2018).

Palinspastic restorations clearly indicate that the Erill Castell- Estac Basin was initially formed as a half-graben trough, produced by continental transtension from the Late Carboniferous-Early Permian (e.g., Poblet, 1991; Saura and Teixell, 2006; Fig.

9.1.2); moreover, the future Erta fault acted as the main southern basin-bordering fault, during the onset and evolution of this basin. Soriano et al. (1996) and Saura (2004) included the Estac sector in the same thrust (Erta) as the Erill Castell sector, stablishing the Erill Castell-Estac Basin. The Late Palaeozoic continental succession reflects the interplay of tectonism, volcanism, clastic sedimentation and climatic evolution. Deposition and erosion processes are controlled by alternating periods of tectonic activity, culminating with extended erosive events marked by angular unconformities. The entire basin infill reaches a considerable thickness (up to 1000 m).
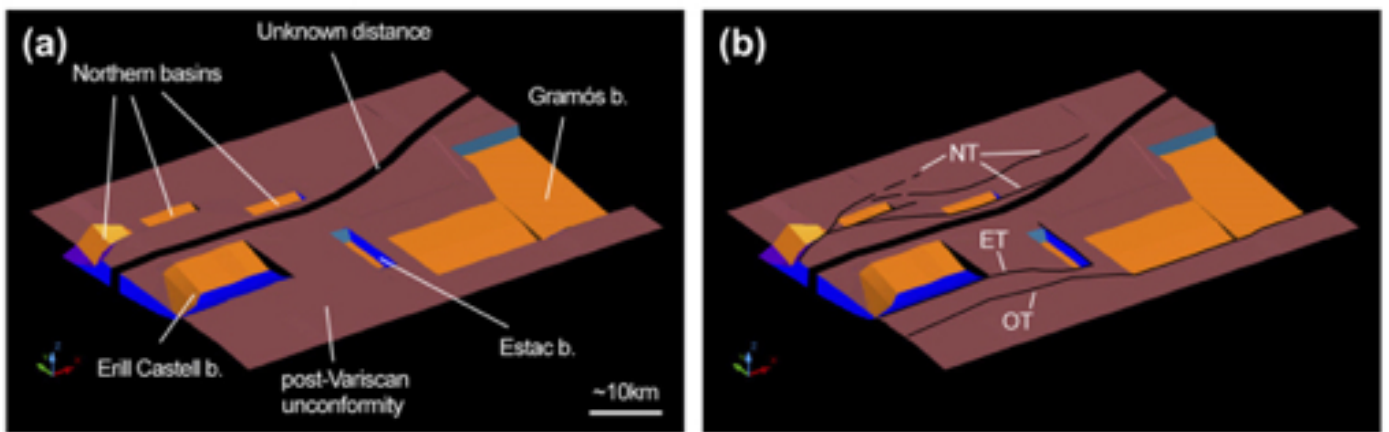
Figure 9.1.2. Simplified palinspastic model of the Stephanian-Permian basins of the Southern border of the Pyrenean Axial zone, based on several restored sections (Saura, 2004). a) Cartoon showing location of main Stephanian-Permian basins. Black gap between the Northern basins and the Erill Castell, Estac and Gramo's basins indicates that the original separation is unknown due to unconstrained displacement of the Nogueres thrust sheet. b) Trace of the future Pyrenean thrusts inverting the basin system. OT: Orri thrust, ET: Erta thrust, NT: Basal and internal Nogueres thrusts. From Saura and Teixell (2006).

9.2 Syn-sedimentary faulting analysis

The coupling of detailed field mapping and digital image analysis revealed significant syn-depositional tectonic activity during the basin's development (Figs. 9.2.1 and 9.2.2). The Late Carboniferous-Early Triassic succession generally dips to the S-SW. The stratal dip and strike variability above and below the main unconformities indicate tectonic pulses between depositional periods. The units are affected by numerous faults showing changes in thickness in both walls (Fig. 9.2.2). Only the faults that were active until the Buntsandstein sedimentation were studied. The restoration of the original position of the successions made it possible to observe the faulting geometry. The tectonic evolution of the basin was therefore revealed by the analysis of the major unconformities and faults with respect to the stacking pattern of stratigraphic units.

9.2.1 Unconformities

From base to top, three main unconformities have been recognized in the study area, illustrated by dash lines on panoramic photos and maps (Fig. 9.2.1). The first major unconformity marks the contact between the GU sediments on the deformed Palaeozoic basement rocks. In the Eric Castell-Estac Basin, the angular relationship between the sedimentary infill changes from 0º to 50º in a few meters due to basement folding.

The second angular unconformity is situated between the TU and the LRU (Fig. 9.2.1). The angle between these two units, lowermost and lower Cisuralian respectively, ranges from 5º to 17º. The strike and dip of GU and TU strata have been rotated back to the LRU horizontal depositional position. Therefore, we have interpreted that, before the sedimentation of the lower Cisuralian LRU, the Upper Carboniferous-Lower Permian deposits were tilted to the W (182/17W) in the Erill Castell-Castellars (ECC) sectors and to the S (067/11S) in La Mola d'Aumunt (LMA) sector (Fig. 9.2.1).

The third angular unconformity occurs at the base of the Buntsandstein and reflects a hiatus or gap of several million years. The Lower Triassic deposits, deeply erosive, overlie all of the Late Carboniferous-Permian units and the basement rocks. The angle between the Buntsandstein deposits and LRU is variable, ranging from 6º to 35º (Fig. 9.2.1). The strike and dip of the LRU have been rotated back to the Lower Triassic horizontal depositional position. The back-tilting shows that the Upper Carboniferous-lower Permian deposits were tilted to the SE with a 051/35SE in the ECC sector and 062/22S orientation in the LMA sector before Lower Triassic deposition.

9.2.2 Analysis of faulting

In this section, we describe the presence of syn-sedimentary faults for each of the studied units. The syn-sedimentary character has been interpreted when stratigraphic thickness variation is observed between the foot wall and the hanging wall. A fault affects older rocks and if there is also variation in the thickness, the fault is interpreted as syn-sedimentary. If not, the syn-sedimentary activity cannot be inferred despite its presence. The kinematics of the fault has been interpreted in the basis on the relative movement between the hanging wall and the footwall, and the angle of the fault plane (Figs.9.2.1 and 9.2.2). The faults have been grouped in families by its structural similarities and represented in figure 9.2.2.
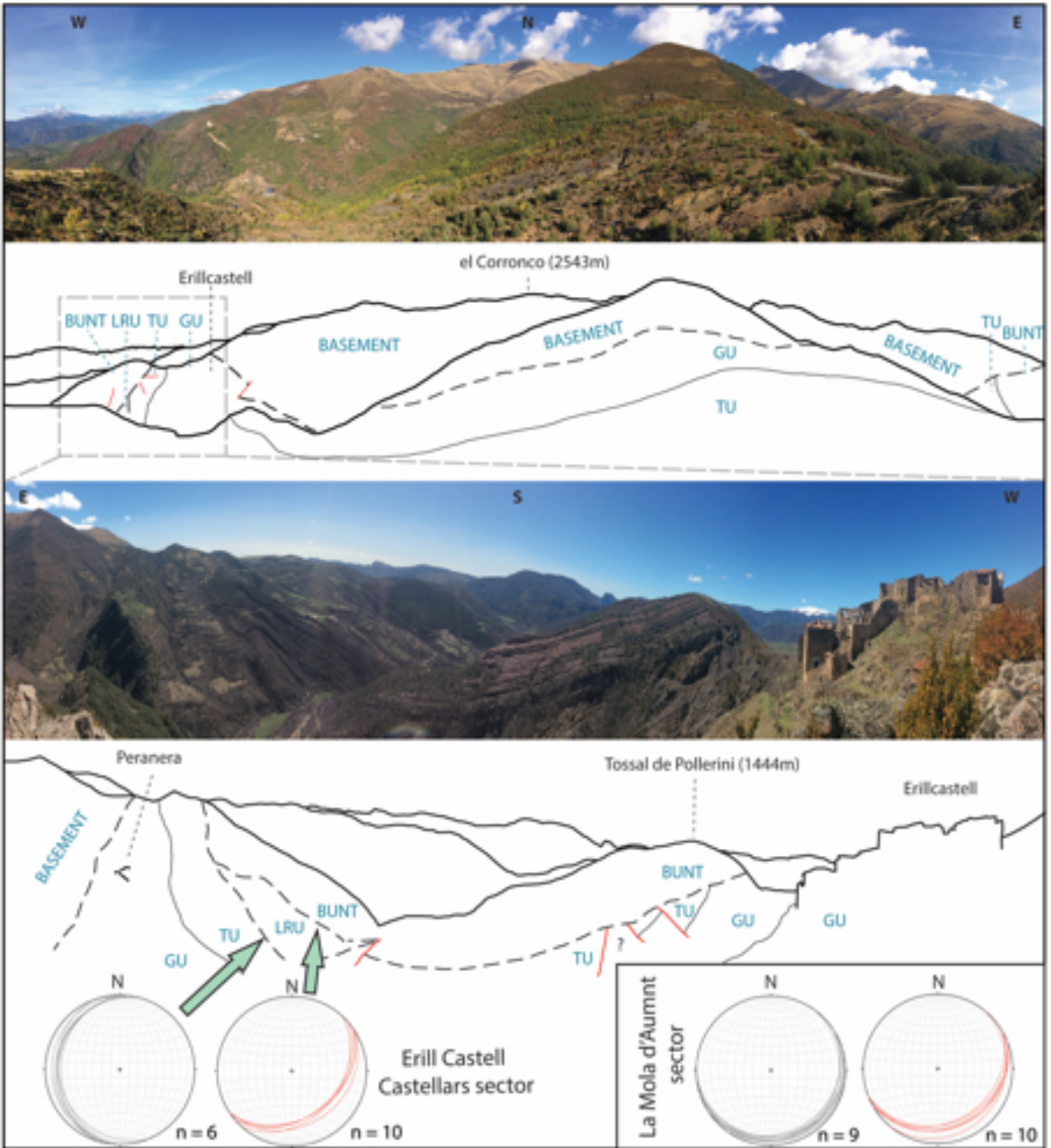
Figure 9.2.1. Panoramic view and line drawing of the stratigraphic boundaries in the area of Erill Castell village. Dashed lines are interpreted unconformities, and continuous lines are concordant stratigraphic contacts. In red are represented synsedimentary faults. The stereographic equal area projection plots represent the back-tilted stratifications in relationship with the overlying stratigraphic unit. The overlying unit is not represented in the stereographic projections. In grey: the Grey Unit and Transition Unit strike and dip strata directions; in red: the Lower Red Unit strike and dip strata directions.From Lloret et al. (2018).

All the GU is affected by syn-sedimentary faults. After restoration to the horizontal, three main families of faults have been recognized (Fig. 9.2.2). The N-S faulting has high- (80-90º) and low- (15-20º) inclination angle and the dip slips are to the W and E. The NW-SE faults dips to the NE with a moderate angle (~30º) and the NE-SW faults generally show higher angles (75-88º), which are NW-SE trending, despite a few
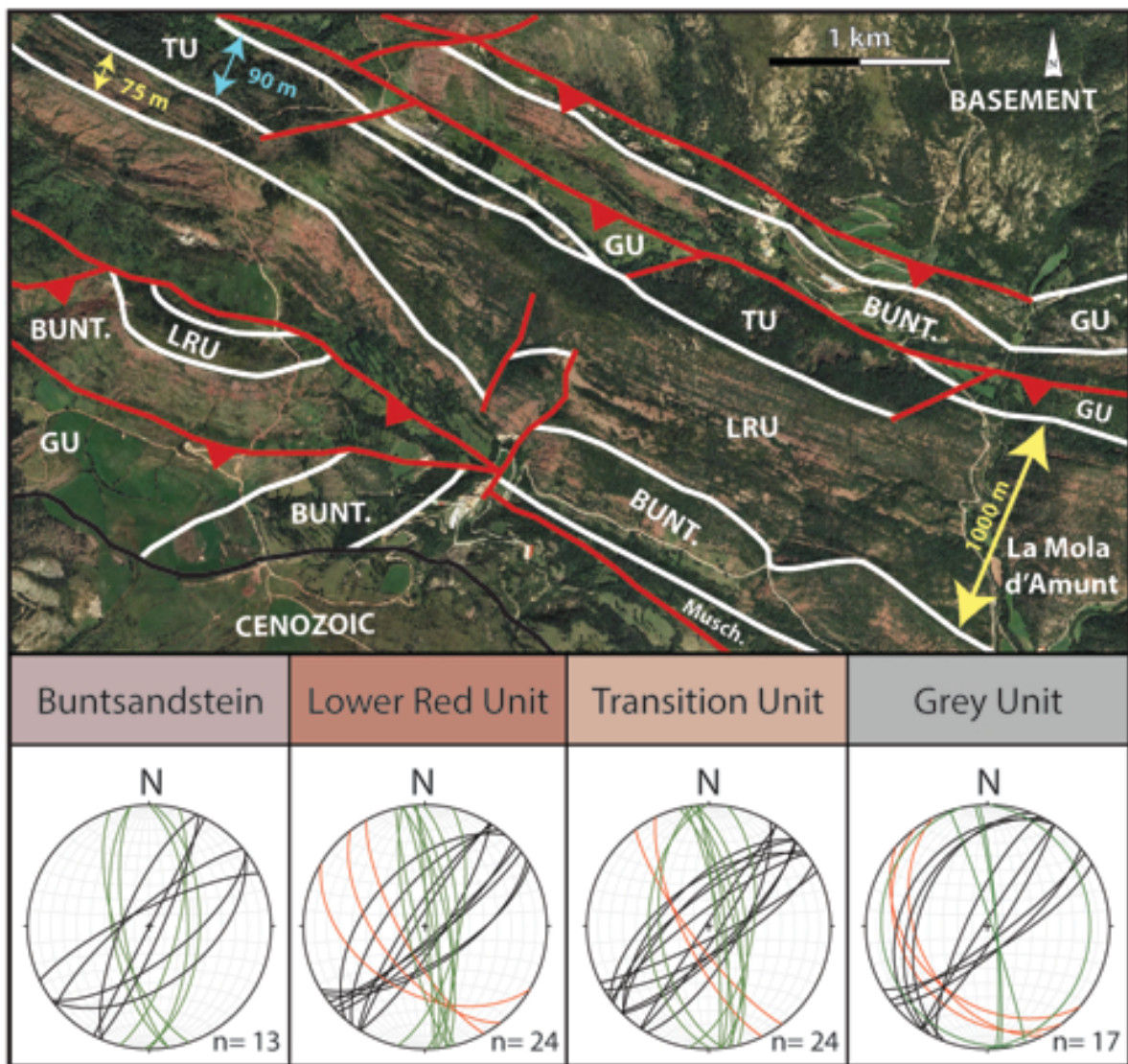
Figure 9.2.2. Interpreted aerial photo of the stratigraphy and syn-tectonic situation in the Western zone of La Mola d'Amunt. The arrows highlights the thickness variation in the Transition Unit and the Lower Red Unit in a short distance due to syn-tectonic faulting and the unconformities among the stratigraphic units. At the bottom, the stereographic in equal area projection of the synsedimentary faults sets recognized and back-tilted in the basin. Buntsandstein: black NE-SW; green N-S. Lower Red Unit: black NE-SW; green N-S; red NW-SE. Transition unit: black NE-SW; green N-S; red NW-SE. Grey Unit: black NE-SW; green N-S; red NW-SE. Orthophoto source: http://www.icgc.cat. From Lloret et al. (2018).

fractures with moderate dipping (45º) to the SE. In the field, some stratigraphic normal dip-slips have been recognized with 9 to 20 m of vertical displacements between the footwall and the hanging wall. Vertical displacements of ~80-90 m have been inferred by cartography.

Both the TU and LRU are affected by the same families of faults (Figs. 9.2.1, 9.2.2). Probably, the tectonic setting was the same for the two units. Three main families have been measured: The N-S set presents conjugate faulting with very high dipping angles (80-90º) to the W and E. The NE-SW set also presents conjugate fractures but with a high verticality. Finally, the NW-SE set is characterized by a moderate-high angle dip (65-80º) only to the NE. The vertical displacements (2-5m) observed in the field for these two units correspond to normal faulting. From the cartography, several meters of vertical displacement have been inferred (20-30 m; Figs. 9.2.1 and 9.2.2).

The faulting affecting the Buntsandstein deposits is characterized by two normal fault sets separated in their dip strike by 30º. The directions are N-S and NE-SW, with dip strikes to the W-E and NW-SE, respectively (Fig. 9.2.2). The faults affecting the Bunsandstein presentdips between 60 to 75º. Therefore, the Triassic is characterized by lower dip angles in comparison with the Permian faults. The vertical displacements observed are not bigger than 20 m (Fig. 11).

10. Discussion

10.1 Central-Eastern Southern Pyrenean tectono-stratigraphic context

Basins characterized by syn-depositional tectonics create complex infills and usually develop an intricate tectono-stratigraphic system (Allen and Allen, 2005). In the case of the Erill Castell-Estac Basin, the vertical and lateral variability of facies is further complicated by the Alpine deformation and inversion of previous structures. As a result, this basin was involved in a complex geological setting. Hereafter we describe its tectono-stratigraphic context from the point of view of an incipient continental basin that evolved to a phase of widespread terrestrial sedimentation. The phase of continental evolution ends with the Middle Triassic marine deposition of carbonatic sediments. Based on field data, facies analysis and tectonic reconstruction, we can depict a step-by-step evolution of the Erill Castell-Estac Basin and, at the same time, define three sedimentary cycles coupled with three main tectonic phases. Based on the tendencies showed by the deposits in each unit, minor tectonic pulses have been also identified. Major tectonic pulses are defined here by the presence of angular unconformities between sedimentary cycles. The evolution of the Eric Castell-Estac Basin allows us to frame our results in a regional context.

The substantial concordance and temporal continuity between the GU and TU units, and their sedimentary similarities, allow to define a first sedimentary cycle (SC1) corresponding to the latest Carboniferous-earliest Permian time-interval. The SC1 comprises the volcanic-volcaniclastic and reduced lacustrine deposits of the GU and the TU fluvio-lacustrine deposits and can be related to initial crustal transtensional and transpressional tectonic movements (GU) and a more active transtensional phase (TU). The syn-depositional set faulting during the initial phase (Fig. 9.2.2) shows a NW-SE
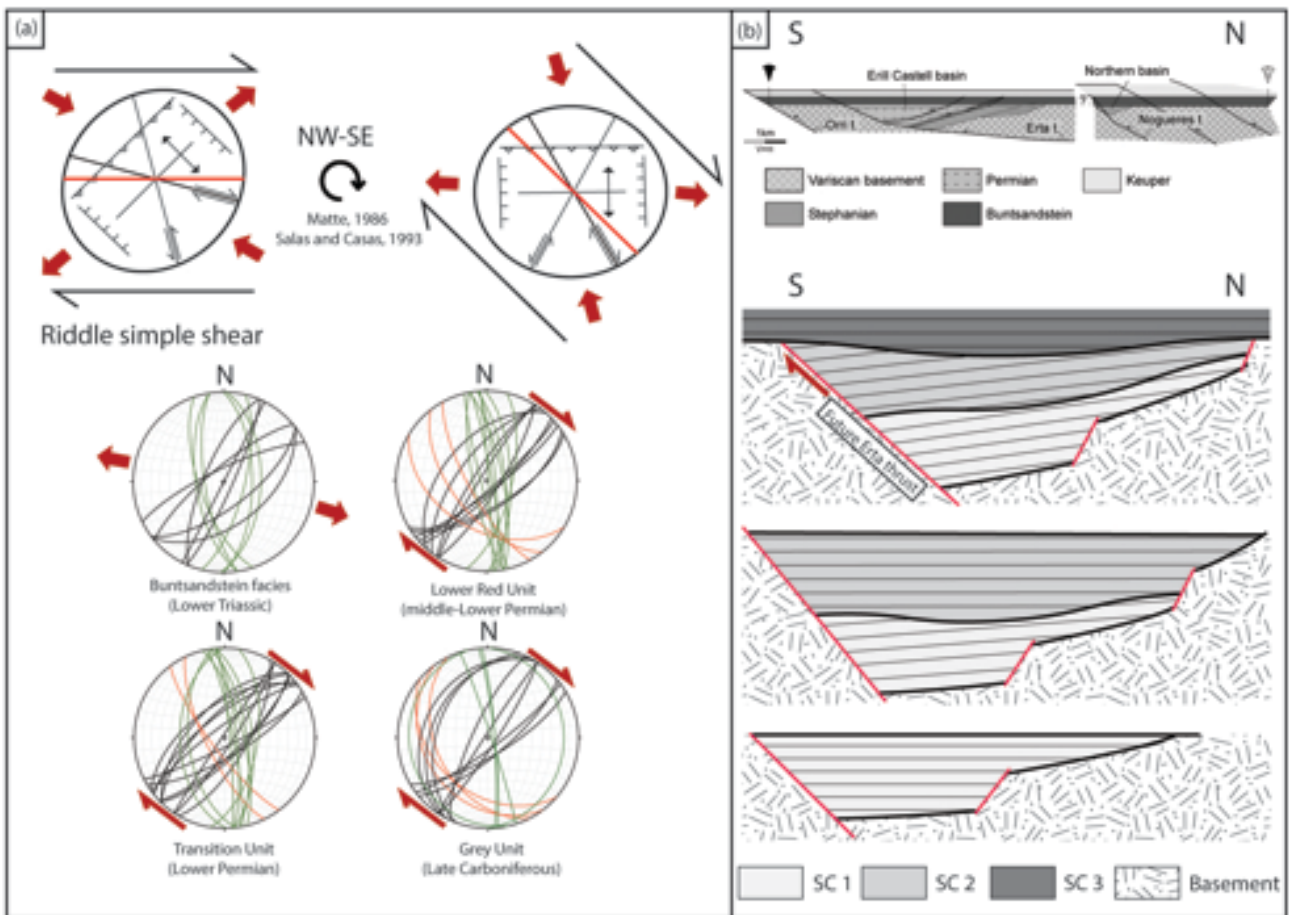
Figure 10.1.1. (a) Interpretation of the faults set for each unit, taking into account the rotation proposed by Matte (1986) and Salas and Casas (1993) in SW Europe and the Riddle simple shear fault association. (b) Simplified sketch of the basin Sedimentary Cycles filling according to the back-tilted stratification data presented in this work and the palinspastic restorations of the Erill Castell-Estac Basin provided by Saura and Teixell (2006). From Lloret et al. (2018).

dextral simple shear fault disposition (Fig. 10.1.1a), characterized by three families with low-moderate dips (Fig. 9.2.2) indicating compressive structures (Anderson, 1905, 1951). The NW-SE set corresponds to the main set faults, according to Riddle's simple shear model (Fig. 10.1.1a). The current Erta thrust (Poblet, 1991; Saura, 2004; Saura and Texiell, 2006) (Fig. 10.1.1b) would result from the inversion of this system. The NE-SW set corresponds to the secondary strike-slip faulting, according with Riddle simple shear model (Fig. 10.1.1), and the N-S structures to the extensive (high angle) and compressive (low angle) faulting, according to Anderson's models (1905, 1951).

The sedimentary response to this context gives rise to basal GU breccias generated along a pronounced slope, indicating a strong initial tectonic pulse in which the sediment

157

supply was higher than the basin's accommodation. After deposition of this lower coarse-grained part of GU, the main part of the unit is represented by large effusive volcanic deposits, with interbedded lake and marsh deposits at the top (Fig. 5.1.1b), indicating a shift to less accommodation space in the basin. The scarce presence of proximal fluvial systems (SB element, Fig. 5.3.1) in the topmost GU could be also explained by a rapid and widespread emplacement of volcanic rocks, filling most of the accommodation space and preventing the development of alluvial environments. Under this regime, two isolated sub-basins were created (Fig. 10.1.1) in the Malpàs and Estac areas. According to previous interpretations (Martí, 1986; Martí and Mitjavila, 1988), the correspondence between thicker volcanic rocks and main depositional zones suggests that subsidence was also strongly linked to volcanic processes.

The conformable boundary between the GU-TU indicates a gradual change in the tectonic frame: notwithstanding, we observed in the stereographic plots higher dipping faults (Fig. 9.2.2) indicating extensional faulting involved in the transtensional setting (Fig. 10.1.1a) and ascribed to the transition phase. The set directions of faults in this case do not show any significant change, thus endorsing the continuity of the sedimentary infill. Nevertheless, the TU is mostly represented at its base by ephemeral fluvial systems (Fig. 5.3.1) and related to minor tectonic pulses (Fig. 10.1.3). The upper part of this unit resembles the lacustrine setting in the topmost GU deposits. In the TU, the tectonic control triggered thickness variations of tens of meters over 1-2 km (Fig. 9.2.2). The direction of the extension was W-E strike linked to the N-S normal faulting, generating an elongated basin. Despite of this, the previous sub-basins were still disconnected between them (Fig. 10.1.2). The fining upward trend of the TU (Fig. 5.1.1) is directly linked to sediment supply and accommodation space, and shows the same characteristics evidenced in the GU tectonic phase. An initial tectonic pulse (Fig. 10.1.3) made available a significant proximal sediment supply at the base of the TU, and fluvial systems

developed simultaneously (Fig. 5.3.1). Upwards, the accommodation space and sediment supply are balanced and this triggered widespread deposition of lacustrine deposits. The horizontal restoration of the overlying LRU indicates slight changes in the angularity between the Erill Castell-Castellars and La Mola d'Amunt sectors (Fig. 9.2.1). No large volcanic deposits were recorded in La Mola d'Amunt and the strata orientation concurred with that of the LRU, suggesting a non-volcanic control. However, the ECC sector presents thick volcanic deposits and dips to the W. This scenario fits better with a volcanic subsidence and not with tectonics, as showed by Martí and Mitjavilla (1988).

The LRU overlies the TU through a high rank unconformity (Figs. 9.2.1 and 10.1.1b). Although in some areas a sedimentary continuity has been observed between the TU and LRU (Broutin and Gisbert, 1985; Mujal et al., 2018), this angular unconformity has been observed in our study area between the two units, and that relationship should be similar in all the Central-Eastern Southern Pyrenean Basins (Gretter et al., 2015; Ronchi et al., 2018). The facies and colour of the LRU unit mark an important change in the sedimentary succession of the basin. This tone change could be related to the climatic shift described between the precedents units, deposited under humid conditions, and the LRU deposited under semi-arid climate (Nagtegaal, 1969; Gascón-Cuello and Gisbert, 1987; Mujal et al., 2018). We therefore ascribed the LRU to the second Sedimentary Cycle (SC2) of the Erill Castell-Estac Basin (Fig. 10.1.2). The basal angular unconformity (Fig. 9.2.1) evidences a tectonic tilting. This angular unconformity has been described in all the Permian basins of the Central-Eastern Southern Pyrenees and is related to the beginning of a major tectonic pulse but under the same tectonic transtensional regime. This pulse likely generated topographic highs that triggered the fluvial channelized elements at the base of SC2 (LRU). The presence of locally thick lacustrine deposits, with massive carbonates, occurs in the La Mola d'Amunt area, which represented the depocentre of the basin during this time.
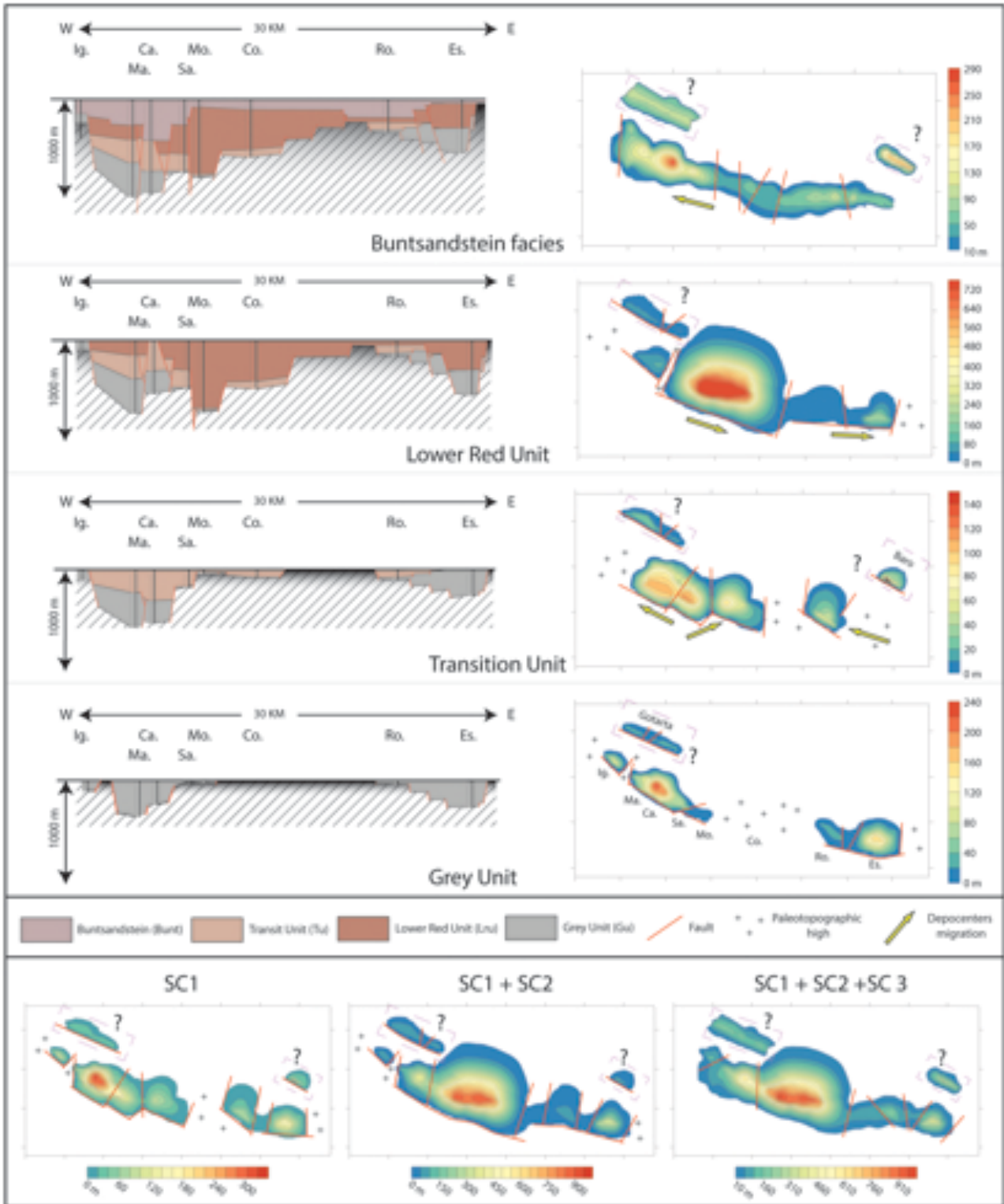
Figure 10.1.2. 2-D section of Erill Castell-Estac basin and isopach maps and syn-depositional faulting of the Erill Castell-Estac Basin. Thickness values derived from the stratigraphic successions and cartography undertaken in this work and previous works (Soriano et al., 1996; Saura, 2004; Saura and Teixell, 2006; Mujal et al., 2018). Ig.: Igüerri, Ma.: Malpàs, Ca.: Castellars, Sa.: Sas, Mo.: La Mola d'Amunt, Co.: Collada de Pui Cavaller, Ro.: Roca de les Creus, Es.: Estac. Arrows shows depocenters migrations. Buntsandstein Facies isopachs lower boundary is 10 m thick due to the reginal extension of these deposits. The paleo-distances between Erill Castell-Estac Basin with Gotarta and Baro sub-basins are unknown. From Lloret et al. (2018).

160

The general fining-upward trend of the LRU also suggests a general reduction in tectonic activity during the final stages of the SC2. Short-living tectonic pulses represented by minor fining-upwards sequences occur in the LRU (Figs. 5.1.1 and 10.1.3). This unit shows similar transtensional tectonic setting as the TU, but with a higher W-E extension of the basins than in previous stages (Fig. 10.1.2), that can be related to the extensional N-S faults. The depocentral areas acquired progressively an elongated morphology and migrated eastward, following the main fault direction (NW-SE). The horizontal restoration of the Buntsandstein record succession shows a clear tilting of the LRU to the SE (Fig. 9.2.1) in a perpendicular orientation to the NW-SE transtensive faulting. This finding reflects the extensional component of the strike-slip main fault during the Early Permian, and this concurs with the half-graben model for the Erill Castell-Estac Basin proposed by Saura (2004) and Saura and Teixell (2006).

Finally, the Buntsandstain Unit represents the third sedimentary cycle (SC3) and the last extensional phase with continental deposits in the basin. Its base is marked by a high-rank unconformity (Fig. 10.1.1b) with erosive features. The first Triassic deposits above the unconformity are represented by coarse braided fluvial deposits (Fig. 5.3.2). These coarse basal facies occur in the whole basin and are represented by CH element with Gh- and Gmp-dominant lithofacies (see also Gretter et al., 2015; Mujal et al., 2016a; Ronchi et al., 2018). The extension of these elements over the basin represents a dramatic sedimentological and tectonic change in the development of Erill Castell-Estac Basin. As regards the sedimentology, the main feature of the Buntsandstein facies is the evolution from braided rivers to meandering systems and playa-lake environments (also suggested by Mujal et al., 2017a), which was not observed in the Permian underlying units within the study area. Aeolian deposits also occur in the middle part of the Buntsandstein basal facies in the neighboring Gramós Basin (Borruel-Abadia et al., 2015; Gretter et al., 2015). Another remarkable aspect of the Triassic deposition is the absence of lacustrine

architectural elements, and the cessation of all volcanic activity. At the top of the Lower Triassic clastics, the first green marls and evaporates testify the Muschelkalk marine trangression. During the time of Buntsandstein facies sedimentation, the tectonic setting also changed, and the strike-slip faulting activity change to normal N-S and NE-SW conjugate faulting controlled by extensional tectonic regime (Fig. 10.1.1). The isopach maps (Fig. 10.1.2) shows an homogeneous sedimentation pattern across the basin. Furthermore, Lower Triassic Buntsandstein facies were related to regional extension over Western Europe (Bourquin et al., 2011). The phases, here described for sedimentary fill of all the basin represents a good example of tectono-sedimentary model for small continental basins.
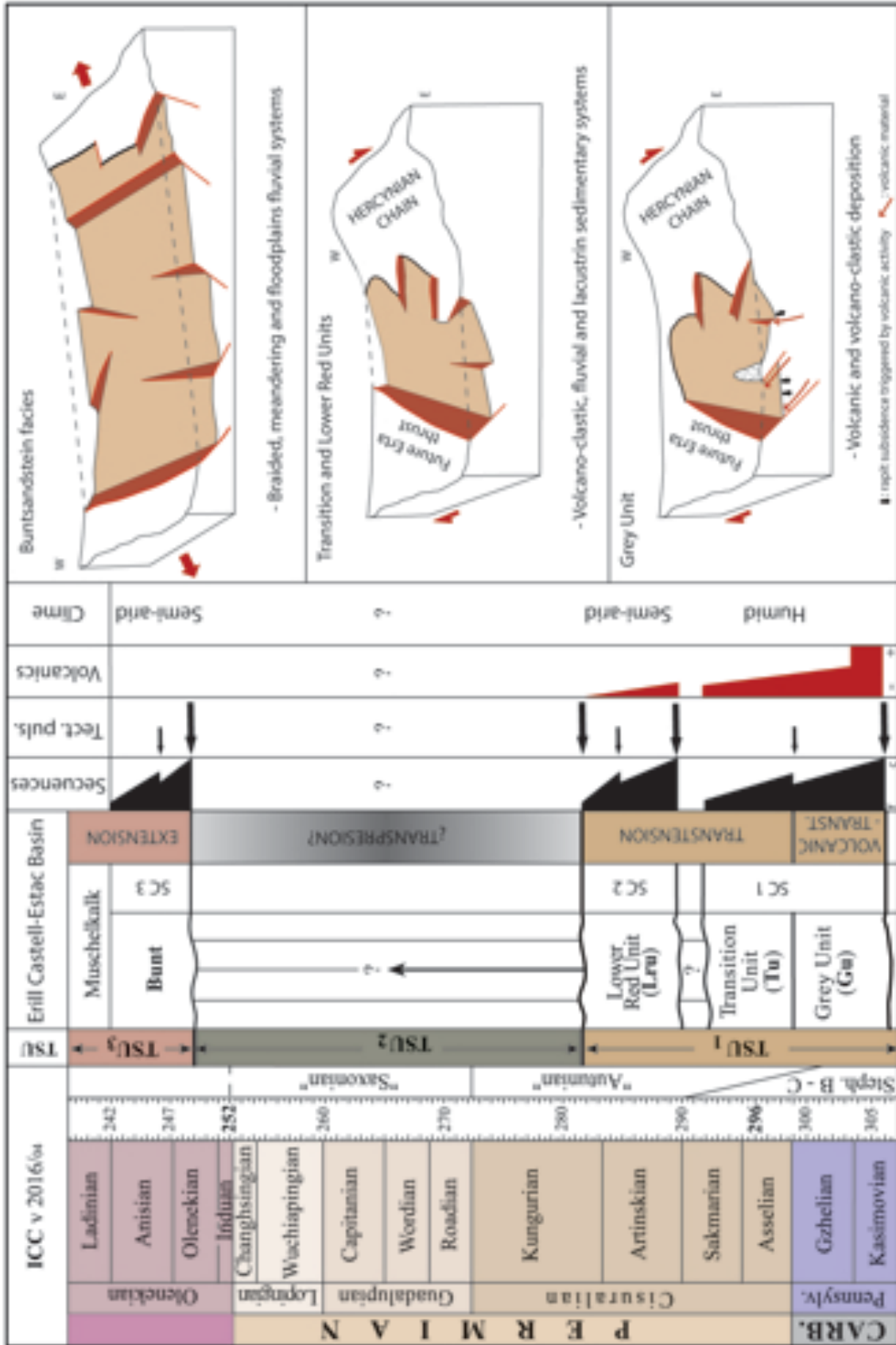
Figure 10.1.3. General diagram of the organization of the stratigraphic record, the sedimentary cycles and the Tectono-stratigraphic Units in the Erill Castell-Estac Basin. Sequence columns indicate the fining-upward trends identified (c: coarse deposits; f: fine deposits). Tectonic pulses situate the position of the tectonic events inferred from the stratigraphic record; the big arrows indicate major tectonic events inferred from stratigraphic unconformities and small arrows indicate minor tectonic events inferred from the

10.2 Paleosols

Several observations can be made as a result of the classification of the pedotypes and their distribution. The first piece of evidence is the variability of pedotypes across the stratigraphic unit record, as seen in the sedimentology record. The numerous kinds of pedotypes is a response to the variables that influence their formation: paleotopography, climate, vegetation and depositional environment (Retallack, 1988, 1998; Kraus, 1999; Alonso-Zarza, 2003). The role of these variables is not always clear, but nevertheless some aspects of their influence can be discerned for each stratigraphic unit. The Pyrenean basins during the Permian and Early Triassic were pretty far away from the influence of the Palaeotethys (Bourquin et al., 2011; Gretter et al., 2015), so eustatic control can be ruled out.

The Lower Red Unit is characterized by a major tectonic pulse at the beginning and a minor tectonic pulse in the middle part (Lloret et al., 2018). The subsidence can be assumed to be continuous except for the initial and middle pulses (10.1.3). The depositional systems were mainly fluvial, lacustrine and volcanic in the lower portion. Moving upwards, the fluvial and lacustrine systems were the most representative depositional systems. The Flamisell pedotypes (Fig. 10.2.1) were located in the basal parts and linked to lacustrine deposits corresponding to the depocenters. The pedotypes related to an active volcanic setting (Isábena) were located along all sectors, indicating a widespread volcanic activity in all the basins. Their controls seem to be mainly linked to the presence of volcanics products, and likely not to other factors. The Noguera pedotype is present in the topmost part of the stratigraphic sections and its stratigraphic position indicates that flooded areas were its parental material. This finding is in keeping with the scarce tectonic activity in the upper part of the LRU (Lloret et al., 2018). The calm environments and shallow-water deposits indicate that the accommodation space was

164

small. Its well-development implies periods maked by a slow sedimentation rate relative with respect to the pedogenesis rates. The high concentration of carbonates has been associated with periods of arid and semi-arid conditions. The large thicknesses of the Bk
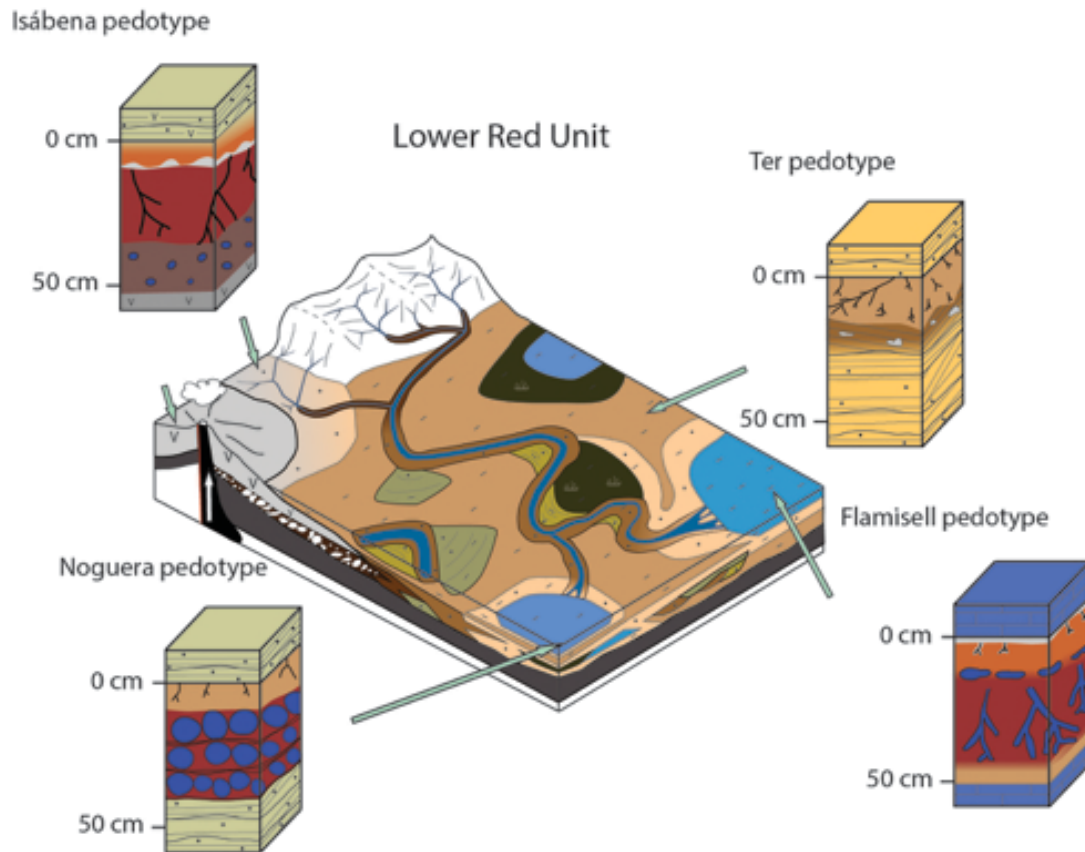
Figure 10.2.1. Lower Red Unit pedotype localization in the depositional systems. Modified from Lloret et al. (2018)

horizon (usually more than 0,5 meter) are usually related to big changes in the paleoprecipitation, with a high seasonability between wet and dry periods (Retallack, 2001). The overlapping of paleosols in the Lower Red Unit is frequent. Episodic sedimentation with intervals of different duration (Yakimenko et al., 2004) produced meters of paleosols, as founds in the Gotarta section. However, differences in soil development could be caused by variations in environmental aridity. While the Isábena pedotype is linked to semi-humid conditions, the Alfisols were formed under vegetation that permits the maintenance of reserves of mineral nutrients (Retallack, 2001). The vegetation associated with Alfisols ranges from grassy woodland to open forests. Their

topographic setting is variable, but those paleosols are not found in high mountains (Buol et al., 1997).

The Upper Red Unit paleosols (Fig. 10.2.2), found in different basins but not in the Erill Castell-Estac Basin, consist of pedotypes similar to those of the Lower Red Unit, probably as the result of similar paleoclimatic conditions, paleoecologically features, and tectonics. The Flamisell pedotype occurs everywhere in the URU, probably due to more moderate tectonic activity. The tectonic pulses generate relief preventing lacustrine development; in fact, a slow subsidence favours calcretes and lake formation (Newell et al., 2012; de Wet et al., 2015). The carbonate nodules of the URU pedotypes (Flamisell, Fontetes and Ter) indicate good oxygenation of the soil under arid to semiarid climatic conditions (Retallack, 2001). Furthermore, this unit also presents the root traces in exceed of 40 centimetres, which could indicate a low phreatic level. As in the Lower Red Unit, the presence of the Flamisell pedotype indicates periods of waterlogging of the soil, but
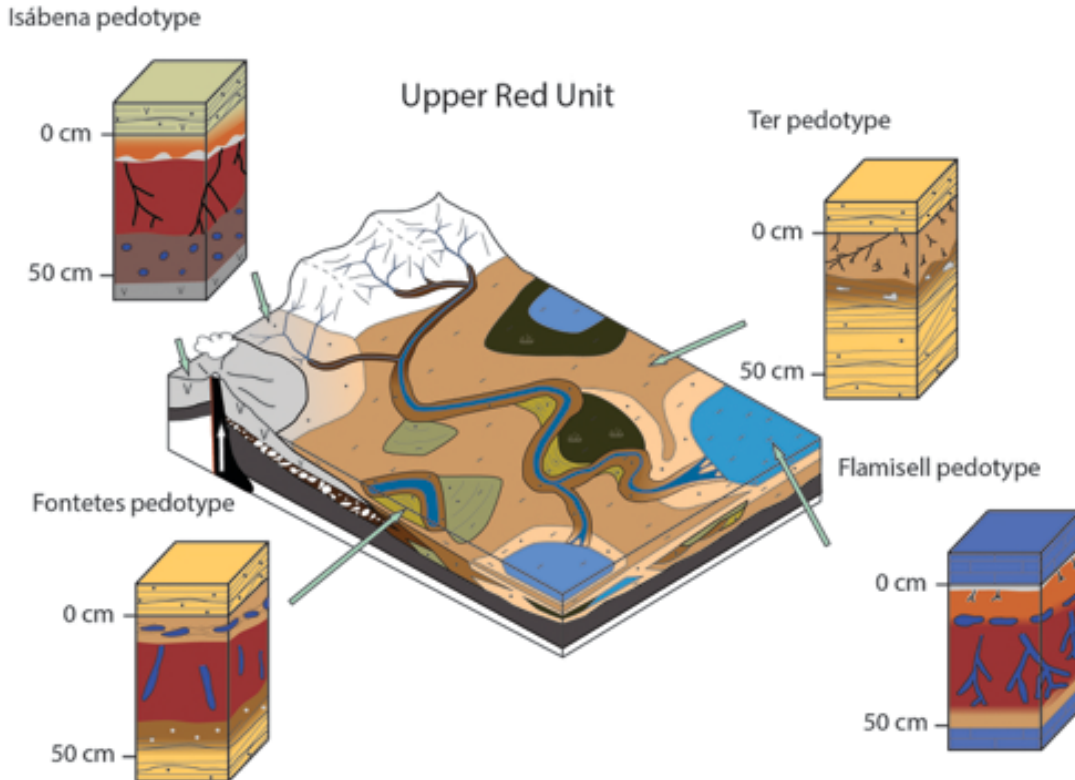
Figure 10.2.2. Upper Red Unit pedotype localization in the depositional systems. Modified from Lloret et al. (2018)

166

the presence of the Ter pedotype (Inceptisol) indicates a poor development, typically of semi-arid conditions (Reinhardt and Wayne, 1988). The depth of the preserved calcareous subsurface indicates the duration of soil development (Retallack, 1998, 2001). In the case of the URU paleosols, these horizons were between only a few centimetres and 40-50 cm in depth, and so the estimate of soil development is about 10^3 years. All these considerations have led to interpret these units as a monsoonal climate that could be relate to today's climate in India or the (drier) Mediterranean.

Lower Triassic paleosols (10.2.3) are markedly different from their Permian equivalents (Fig. 6.4.1), particulary as their poor development of them. The main conclusion to be drawn from this is that the climate and sedimentation/tectonics conditions were unfavourable. The second important issue is the almost total absence of pedogenic carbonate, as well as the very small and disseminated root traces. These evidences indicate a low structured vegetation and climatic conditions unfavourable to soil development. The scarcity of abundant water generated non-carbonaceous paleosols (Retallack, 2001). Moreover, if the sedimentation is slow and steady, a cumulative-truncated profile can result, but if sedimentation is too rapid and unsteady, truncated soils occur and become buried (Marriott and Wright, 1993). Thus, a rapid and unsteady sedimentation can be inferred from the truncated profiles observed in the Lower-Middle Triassic soils (Table 6.3.1 and Fig. 6.3.1).

In the Triassic, the Derana pedotype is the most characteristic pedotype studied. The Derana pedotype is not only widespread in all the stratigraphic logs, but it is always the first paleosol represented in the Triassic. Bourquin et al. (2011) indicate that no paleosols have been identified before the Spathian (late Early Triassic). This fits well with the palynological data from the Middle Triassic ascribed to the Pelsonian, and the stratigraphic position of the first paleosol in the Buntsandstein facies Unit. The spread of the Derana pedotype in the basin could represent at least a basin event, as the ferruginous

Ac horizon indicates a well-drained soil (Retallack, 2001). The basin event could be tectonic, but no relevant tectonic phase has been identified. The sedimentation change substantially to finer deposits (Fig. 5.1.1) after the first occurrence of the Derana pedotype. It is therefore probable that the formation of this key level represents a period with a low sedimentation rate due to a calm tectonic phase. Another factor that could influence the absence of paleosols in the Early-Middle Triassic deposits is the low presence of vegetation, due to the Permian-Triassic extinction (Erwin, 1994; Benton and Twitchett, 2003; Benton and Newell, 2014). The absence of macro-paleobotanic content in the Buntsandstein facies Unit supports this idea.

The isotopic composition of the different pedotypes indicates changes in the carbonate formation. Each pedotype has its own diagnosis and particular factors pertaining to its formation (Retallack, 2001). The factors that influenced in the $\delta^{13}C$ signature were the vegetation, water and the atmospheric CO_2 Cerling, 1984, 2009; Sikes and Ashley, 2007; Andrews et al., 2017).

Only a few publications have clearly indicated the isotopic signatures of the different pedotypes (Krull and Retallck, 2000; Sikes and Ashley, 2007) and most of publications related to pedogenic carbonate isotopes have not even classified the pedotypes (Takeuchi et al., 2000; Badeck et al., 2005; Andrews et al., 2017). In the Central-Eastern Southern Pyrenees the Andisols and Aridisols (Noguera and Isábena pedotypes) present the lowest values of the $\delta^{13}C$ (Fig. 7.2.2). Their development was moderate to well-developed, and they both shared the same parental material, derived from volcanic processes. The volcanic materials are mostly andesitic. Szymanski and Szkaradek (2018) have pointe to acid soil condition, as a result of the weathering of andesitic rocks. Kolasinski et al. (2008) demonstrated that the acidification decreases (1 to 2) the $\delta^{13}C$ signature, indicating that the original composition was more positive. The

Andisols therefore had values between 0 and -3 $\delta^{13}C$, probably due to the influence from vegetation, and in fact neither of these two pedotypes were characterized by significant root traces (Table 6.3.1, Figs. 6.3.3a and 6.3.3d).
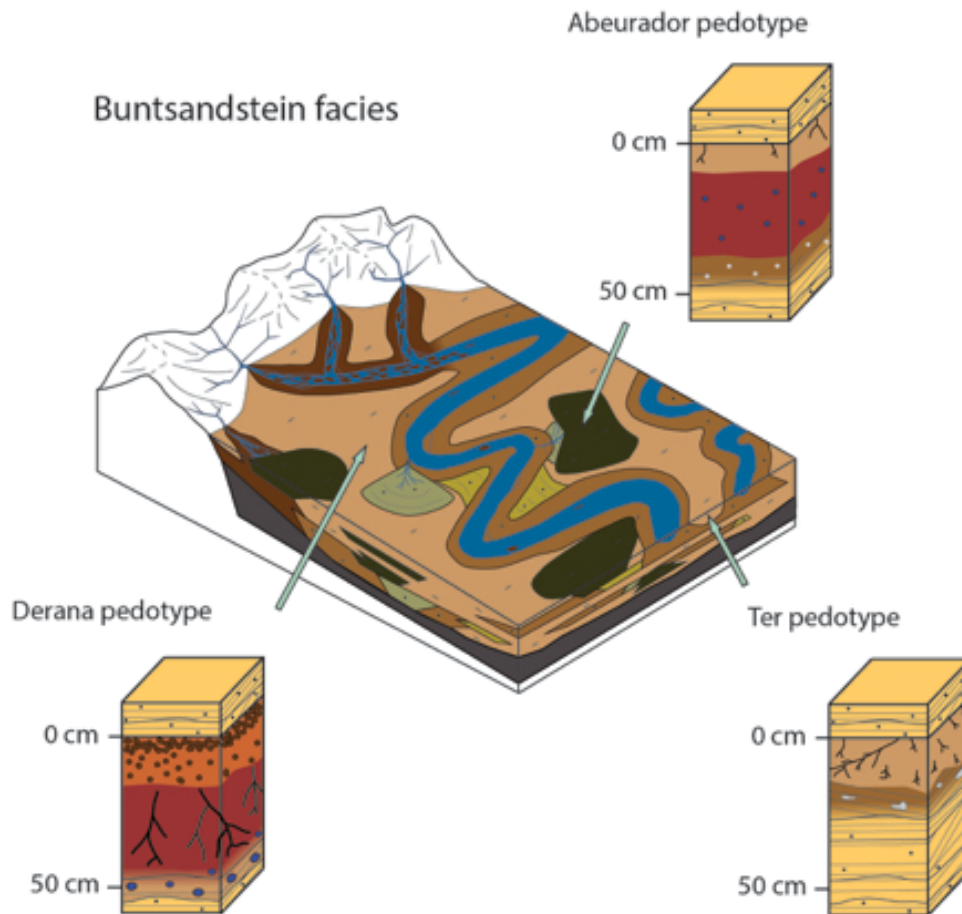

Figure 10.2.3. Buntsanstein facies Unit pedotype localization in the depositional systems. Modified from Lloret et al. (2018).

The Noguera pedotype presents two groups of isotopic compositions, the higher probably being more closely related to volcanics and the other one group to Aridisol features. The Isábena pedotype is also characterized by a subsurface horizon of clay accumulation (like the Fontetes pedotype), which is classified as an Alfisol feature. Both share the same isotopic range ($\delta^{13}C$ values from -2 to -4). The Abeurador pedotype has the most negative signature and represents a poorly developed soil (Inceptisol), and the values of the horizons A and B (Fig. 7.2.7) are similar (Fig. 10.3.4). The distribution of

the Fontetes A-B horizons indicates a similar pattern (Fig. 7.2.9), and its development is moderate. The timespan of soil development seems to be a key aspect in the fraction of $\delta^{13}C$.
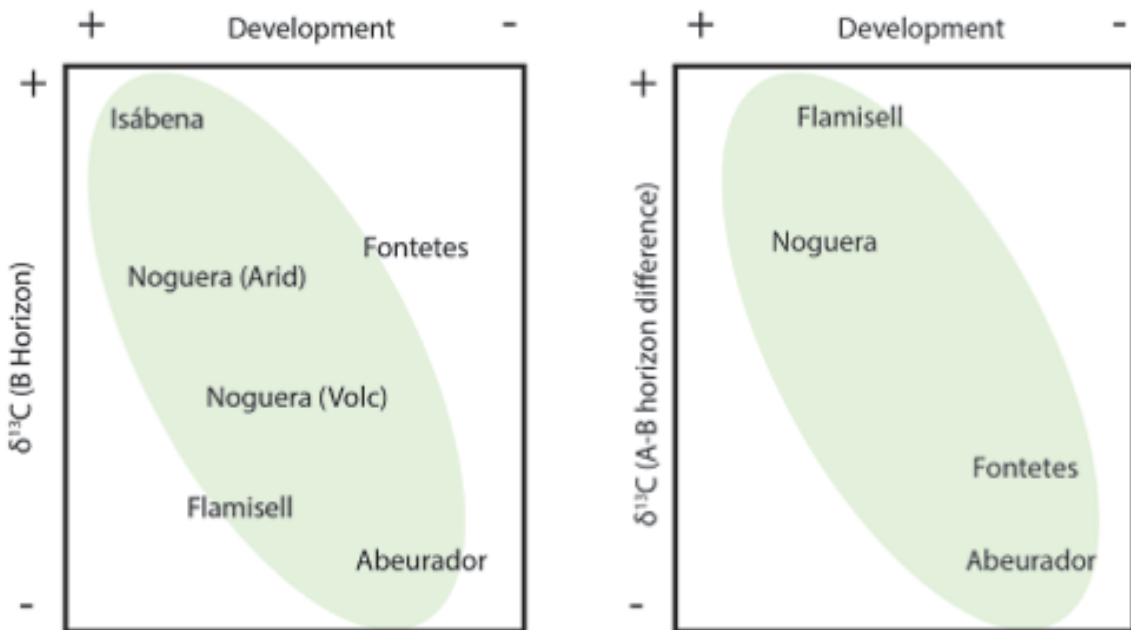
Figure 10.2.4. Correlation between the $\delta^{13}C$ of the B horizon and their grade of development and correlation of the difference between A-B horizon and their grade of development.

From the vegetation point of view, the $\delta^{13}C$ signature of the C3 plants is between -24 and -30‰ (Deines, 1980; Badeck et al., 2005) and that of the C4 is between -11 and -13‰ (Deines, 1980; Badeck et al., 2005). As C4 respiration appears in the Neogene (Cerling et al., 1993) the C3 respiration is the response of the isotopic vegetation signature. More positive values occur because the respiration is not the only response of the carbonate isotopic signature. The mixing of biological ^{13}C and atmospheric ^{13}C explains the intermediate values obtained and this confirms the trustworthiness of these values. Furthermore, some lacustrine samples were analyzed; as this depositional system is not strongly influences by vegetation, it can be used as a control for the $\delta^{13}C$ isotopic

signature of an abiotic environment. The values obtained were close to -2 to 0 $\delta^{13}C$, and thus a basic average gives the paleosols carbonate signature. The Flamisell pedotype is linked to palustrine environments but even so its $\delta^{13}C$ values were more negative than the expected, probably due to the pedogenic development, and this meant that a large fraction of the isotopic signature presented a great difference between the parental material and the pedogenic product.

As observed in this study, the horizons have different $\delta^{13}C$ signature, and in the data presented, the B horizon is mostly more negative than the A horizon. The variation in the $\delta^{13}C$ is usually close to 1-2. Krull and Retallack (2000) observed this same trend in the Permian and Triassic soils of Antartica. Cerling (2009) has suggested that evapotranspiration is the mechanism underlying this differentiation. From the observations presented in this thesis (Fig. 6.3.1 and Table 6.3.1), the B horizon is generally characterized by the presence of roots, which are the responsible for respiration and CO_2 extraction. The lower values in the B horizon are consistent with the soil dynamics and the degree of development (Fig. 10.2.4). Although roots are more present in the B horizon, the A horizon values indicate a moderate respiration of vegetation. If this were not the case, the isotopic values would be closer to the lacustrine values. The sedimentology of paleosols is a key factor in other approaches, such as isotopic analysis, although the sampling of A horizons instead of B horizons could produce significant misinterpretations.

10.3 Paleoclimatic considerations

<u>Grey Unit (Gzhelian, Late Carboniferous)</u>

From the sedimentological point of view, some paleoclimatic can be found in the Grey Unit. The presence of coal deposits with moderate-well development indicates wet conditions (Retallack, 1996), while the hydromagmatic volcanism in the Erill Castell-Estac Basin indicates a high water content in the depositional system. This interpretation is supported by the findings of previous studies (Martí, 1986, 1991; Martí and Mitjavila, 1988).

The palynological study of samples in the GU of Rio Pallarols and Gotarta, indicates the presence of fern spores such as *Acanthotriletes*, *Deltoidospora*, *Granulatisporites*, *Lophotriletes* and *Microreticulatisporites*. These taxons are linked to the Carboniferous hygrophilous microflora, and they are indicative of a humid period.

Halloysite and dickite minerals were found in the Grey Unit (Fig. 8.2.2). The ratio of kaolinite (including halloysite, dickite and nacrite) to illite is a suitable proxy for paleoclimatic reconstruction, because kaolinite is normally formed by intense chemical weathering in a warm and humid climate, whereas illite is usually formed by physical weathering in a cool and dry climate. However, illite may have also been derived from the alteration of micas under warmer and wetter conditions (Birkeland 1984). Halloysite is formed at low temperatures (4-200ºC, Gorbachev, 1977) and is typically an indicator of good drainage in humid tropics (Parham, 1969) with moderate rain falls (Chadwick et al., 2003). In volcanic or ash soils, tubular halloysite crystals with relatively low iron concentrations and platy halloysite crystals with higher iron concentrations have been described by Hart et al. (2002). Dudas and Harward (1975) have identified halloysite and some allophane, and Delvaux et al. (1992) have describe the coexistence of halloysite and kaolinite in volcanic soils. They suggested a sequence whereby kaolinite content

172

progressively increases at the expense of hydrated halloysite as the result of increased soil weathering. In the clay mineralogy study, kaolinite was not present, so moderate-to-low paleosols development was supposed the Grey Unit. The dickite mineral forms part of the kaolin clay groups, as does the halloysite. The formation of dickite has the same paleoclimatic implications as that of halloysite.

In conclusion, the Grey Unit was deposited under wet-humid conditions, and probably in warm temperatures. A tropical or equatorial palaeolatitudinal position can be inferred from these paleoclimatic conditions. We therefore agree with Broutin and Gisbert (1985) and Gascón-Cuello and Gisbert (1987), who suggested a tropical wet-dry to tropical humid climate for the Grey Unit.

Transition Unit (Asselian-Sakmarian, lower Cisuralian)

The first (Lower) Permian unit presents a stratigraphic continuity with the Upper Carboniferous unit. The facies analysis show similar depositional paleoenvironments (Fig. 5.3.1), with fluvio-lacustrine deposits with intense volcanic influences. The lacustrine deposits were more representative in the topmost part of this unit, indicating a lower subsidence in that stratigraphic part (Lloret el al., 2018). Lake carbonates layers were present in many sections, although their were generally not very thick, but in any case their presence suggest abundant water availability. In the Transition Unit the coal layers almost disappear, only being preserved in small layers only in the basal part of the unit. On this basis, wet conditions can be inferred for the lower part of the Transition Unit. The absence coal does not prove any aridification in the TU but it is indicative of a climatic variation, particulary as lacustrine deposits are more present in the upper part of the unit. Gascón-Cuello and Gisbert (1987) have similarly hypothesized a change from tropical wet-dry to a tropical sub-humid climate in the TU.

The palynological content of the Transition Unit shows a depletion of "Stephanian" microflora in favor of "Autunian" microflora. According to Broutin (1986), the absence of the genera *Thymospora, Punctatosporites* or *Densosporites* is probably due to the incapacity of the relative-producer to resist the first manifestations of climate change, i.e. instability and gradual evolution to drier conditions. In fact, *Punctatosporites* genus does not appear in the Transition Unit.

The clay mineralogy in the TU presents great variations with respect the Grey Unit: the absence of halloysite and dickite indicates that soils from the erosion of volcanic deposits were formed under different conditions. The volcanic activity during the early Lower Permian has been described by various authors (Martí, 1986; Martí and Mitjavila 1988; Gretter et al., 2015; Mujal et al., 2018; Lloret et al., 2018). Another implication that can be derived from these mineral findings is that there was a climatic change between the Gu and the TU, because in the latter case drier conditions could have prevented the genesis of such minerals. Halloysite formation occurs in humid tropical areas (1200 mm/yr), and so lower precipitation rates can be inferred for the Transition Unit.

The possible aridification registered in the Central-Eastern Southern Pyrenees during the Carboniferous-Permian has been studied in detail by Mujal et al. (2018). These authors support their case with paleobotanic, ichnological and paleosols data. Paleomagnetic data are also provided herein, but with inconclusive results.

Lower Red Unit (Artinksian-Kungurian, middle-late Cisuralian)

The Lower Red Unit is characterized by fluvial and playa-lake deposits with little volcanic influence (Fig. 5.3.2; Lloret et al., 2018). The most evident feature is the change in coloration of the red bed deposits. This colour change could be related to a climatic shift similar to that described above in the underlaying units: i.e., a change from sediments

174

deposited under humid/semi-humid conditions (TU) to the LRU semi-arid climate (Nagtegaal, 1969; Gascón-Cuello and Gisbert, 1987; Mujal et al., 2018). Coal deposits are entirely absent and the most valuable climate information is provided by paleosols.

The pedotypes present in this unit are: Isábena (Andisol), Noguera (Aridisol), Flamisell (Palustrine) and Ter (Entisol). The Isábena Andisol has a subsurface Bt horizon formed under fertile vegetation, like modern Alfisols, which are found in semi-humid to semi-arid climatic conditions and not present in high mountains, or at high latitudes, such us the Poles (Retallack, 2001). Entisols present substantial variation in their climatic conditions, as they can be developed under both humid and dry and warm and cold conditions, but Aridisols have mainly been assigned to arid to semi-arid conditions (Retallack, 2001). Finally, palustrine deposition are very common in suitable semi-arid to sub-humid climates (Alonso-Zarza, 2003). Soils forming under dry monsoonal conditions are most often Vertisols or Aridisols, but rarely Mollisols (FAO, 1971–1981). In contrast, the soils formed under wet monsoonal conditions are most often Ultisols or Vertisols (FAO, 1971–1981). Thus, dry monsoonal conditions are the best approximation for this unit. Gascón-Cuello and Gisbert (1987) interpreted the LRU climate as being similar to a tropical steppe and Broutin and Gisbert (1985) suggested a climate passing from a peritropical savannah to a semi-arid environments.

In this unit, the palynological data do not further any particular paleoclimatic interpretation. Nevertheless, the well constrained paleoclimatic considerations deriving from other approaches could allow to interpret the palynological assemblages as a dry monsoonal microflora. The clay mineralogy indicates a relative high percentage of carbonates related to the Bk horizons of paleosols. Any further interpretations from the clay mineralogy relative to paleoclimate in this thesis would to be speculative because no conclusive results have been obtained for the red beds deposits.

In comparison to the Transition Unit the Lower Red Unit presents clues of more aridity. There was probably no clear change between the climate conditions of the upper TU and the LRU, but a general aridification can be inferred during the Asselian-early Kungurian trend. The aridification that occurred during the Cisuralian has been described in USA terrains via paleosols interpretation by Fielding et al. (2008). In the Northern peri-Tethys area, aridification during the Permian (Schneider et al., 2006). Furthermore, Roscher and Schneider (2006) have reported the presence of several wet periods during the Permian, within a general trend towards aridization.

Upper Red Unit (Kungurian-?Roadian, late Cisuralian-early Guadalupian)

The sedimentary facies of the Upper Red Unit are not significantly different from those of the Lower Red Unit, so there is no evidence from the sedimentological features for any different paleoclimatic interpretations. Moreover, no palynological data have been obtained and the clay mineralogy data are inconclusive. Paleopedogenesis is therefore the best approach to interpreting paleoclimate during the Kungurian-Roadian, as there are very few reliable fossils from this period in the Central-Eastern Southern Pyrenees (see Mujal et al., 2016a; Ronchi et al., 2018).

The pedotypes identified in this unit were Flamisell (Palustrine), Ter (Entisol) and Fontetes (Alfisol). As in the LRU, the presence of palustrine paleosols indicates moderate humid-dry conditions. The frequency of paleosols at the top of the unit could indicate greater availability of water but, as discussed above, this could be triggered more by tectonic features than by climate. In any case, extreme aridification can be ruled out, due to the presence of fluvial facies. The Ter pedotype is not a good climatic indicator, on account of its poor development. Alfisols are found under semi-humid to semi-arid conditions. The absence of Aridisols could indicate less aridification than in the Lower

176

Red Unit, but this fact would be local, in the light the overall aridification of the Permian (Schneider et al., 2006; Roscher and Schneider, 2006; Fielding et al., 2008). There have been no reports to date, according to the authors cited above, of any more humid period in the Western peri-Tethys after the Artinskian. The most plausible climate for the URU would be monsoonal with semi-arid to semi-humid periods. Broutin and Gisbert (1985) ascribed the climate of a peritropical savannah to this unit.

Buntsandstein facies Unit (upper Olenekian to Anisian, ?Lower-Middle Triassic)

From the sedimentological point of view, the Buntsandstein facies Unit shows some clear differences with the Permian Units. The most significant is the absence of lacustrine deposits, indicating low water availability. Aeolian deposits also occur inside the Buntsandstein lower facies in the Gramós Basin (Gretter et al., 2015; Mujal et al., 2016b), indicating arid conditions. Further, ventifacts have been found in the basal coarse-grained continental Triassic deposits in many places of the SW Europe (Bourquin et al., 2011). There were no coal deposited at all.

The carbonate content is very low and only small amounts were found in some paleosols. This is evident in the clay mineralogy analysis (Fig. 8.2.2), were calcite was present in only a few samples. The dolomite found in some sections was located in the upper part of the logs and is probably related to the first marine incursion in the ?Middle Triassic (Muschelkalk). The deposits which contain dolomite have a greyish coloration and are related to the Röt facies. The sporomorphs collected in this unit allowed to date these deposits with great precision but gave no clear paleoclimatic indicators.

The pedotypes characteristic of the middle-upper part of the Buntsandstein (i.e., the finer facies above the conglomerate) were Derana (Alfisol), Abeurador (Inceptisol) and Ter (Entisol). Inceptisols are linked with forest to tundra-type vegetation, and in a

dry climate their development exceed tens of thousand years (Retallack, 2001). The effervescence of Lower Triassic paleosols is very poor when hydrochloric acid is applied, and there is nothing that would qualify as Bk horizons (Soil Survey Staff, 1998). The carbonate in the paleosols studied was not deep, and according to Royer (1999) and Retallack (2001), this indicates low paleoprecipitations.

Arid (semi-arid) conditions can be inferred for the Buntsanstein facies Unit with the data obtained. Although Mujal et al. (2018) suggested humid conditions here, based on clay mineralogy data, Ronchi et al. (2018) have refuted that interpretation. Many other authors have indicated arid or semi-arid paleoclimatic conditions for the Lower-Middle Triassic in the Western peri-Tethys area (Gisbert, 1981; Gascón-Cuello and Gisbert, 1987; Cassinis et al., 2003; Durand et al., 2007; Bourquin et al., 2011; López-Gómez et al., 2012; Gretter et al., 2015; Lloret et al., 2018).

10.4 Regional context and correlation

The depositional units described by Gisbert (1981) are, in the author opinion, still valid and can be correlated along the main Pyrenean basins, from W to E: Anayet, Aragón Bearn, Castejón-Laspaúles, Erill Castell, Gramós and Castellar-Camprodón (Fig. 10.4.1).
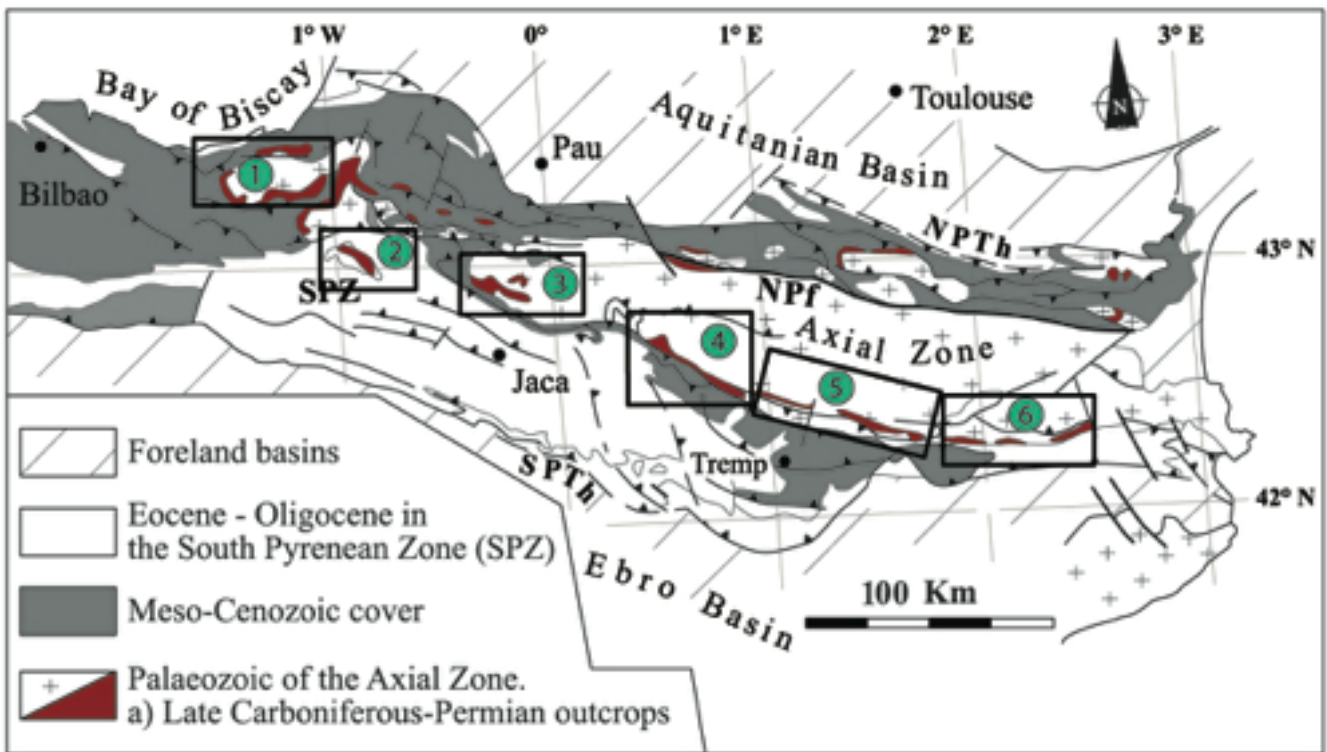
Figure 10.4.1. Situation of the six main basins in the Southern Pyrnees. 1: Anayet Basin; 2: Aragón-Bearn Basin; 3: Castejón-Laspaúles Basin; 4: Erill Castell-Estac Basin; 5: Gramós Basin; 6: Castellar-Camprodón Basin. Modified from Lloret et al. (2018).

The characteristics of the Erill Castell-Estac Basin described in this thesis present features similar to the rest of the basins, albeit with some notable differences. The volcanites and ignimbrites related to GU and TU are present in all Pyrenean basins, and usually can be followed at kilometric scale inside each basin (Gisbert, 1981; Mitjavila and Martí, 1988; Martí, 1996; Galé, 2005; Izquierdo-Lavall, 2013, 2014; Gretter et al., 2015). The coal levels of the GU are also found throughout all these basins (Gisbert, 1981; Talens and Wagner, 1995; Gretter et al., 2015; Mujal et al., 2018) and they yield a rich macroflora and microflora (Dalloni, 1930; Álvarez-Ramis and Doubinger, 1987;

Talens and Wagner, 1995; Mujal et al., 2018). From palaeoenvironmental and sedimentological viewpoints, there are no major differences between the various basins: similar fluvial and lacustrine environments have been described for the LRU and Buntsandstein facies in the Gramós and Castellar de n'Hug areas (Gisbert, 1981; Gretter et al., 2015; Mujal et al., 2017a, b, 2018). The absence of the Upper Red Unit (Middle-?Late Permian) in the Castejón-Laspaúles and Erill Castell-Estac basins (García-Senz et al., 2009a,b; Izquiero-Lavall et al., 2013) (Figs. 10.4.1, 10.4.2 and 5.1.1) is in fact the trait that distinguishes these basins from both the more eastward Gramós and Castellar-Camprodón basins and the western Anayet and Aragón Bearn basins (near Jaca in Fig. 10.4.1; Cantarelli et al., 2013).

Three geological scenarios could explain the complete absence of the URU in the studied Erill Castell-Estac Basin and in the more westward Castejón-Laspaúles area: a) non-deposition of the youngest Permian unit due to the presence of a topographic high; b) a deep erosion after the deposition in the cited sectors during the Late Permian; or c) tectonic pinch-out that located the URU below the current topography.

All three hypotheses are plausible and there is no conclusive evidence in favor of any of them, although some points need to be taken into consideration. The absence of Late Carboniferous-Permian basins to the West of Castejón-Laspaúles up to the outcropping of the Anayet basin located 90 km to the West (Valero-Garcés and Gisbert, 1992; García-Senz et al., 2009a, b) seems to indicate a westward thinning of the strata and increased thickness to the E. We have no clear evidence to date, but a topographic high during the Middle-?Late Permian in the western Castejón de Sos and Erill Castell-Estac basins would better explain non-deposition, with respect to an erosion event.

In this thesis it is also suggested that the tectono-stratigraphic phases described in the Erill Castell-Estac Basin shows many similarities to classic continental rifting

evolution (Schlische and Olsen, 1990; Carroll and Bohacs, 1999), even though the scale is much smaller. These models did not consider main tectonic pulses during their evolution, whereas in Erill Castell-Estac Basin we showed that intermediate pulses triggered some repetitions in their phases. Nevertheless, similar trends can be considered (Fig. 10.1.3): (1) an incipient phase where numerous small faults created isolated depocentres, in accordance with the described Sedimentary Cycle 1; (2) a phase where tectonic subsidence exceeds sediment supply, which corresponds to the basal part of Sedimentary Cycle 2; (3) a progressive balancing of sedimentation rates and tectonic subsidence relative to the upper part of the same SC2; and (4) sedimentary supply exceeding the accommodation space, corresponding to the Sedimentary Cycle 3 with the first Triassic Tethys marine trangression.

Tectono-stratigraphic units (TSU) were described in the neighboring Eastern Pyrenean basins with the aim of proposing large-scale correlations across Western Europe (Gretter et al., 2015). This subdivision was previously used by other authors in continental basins of the same time interval throughout Europe (e.g., Cassinis et al., 1995, 2012; Virgili et al., 2006; Gretter et al., 2015). In the case of the Erill Castell-Estac Basin, the GU, TU and LRU would correspond to TSU1 because these units are all related to a general transtensive phase (Fig. 10.1.3). As mentioned above, the URU is not recorded in Erill Castell and therefore a major tectonic event occurred, and so we propose assigning the URU to TSU2. This assignation is in concordance with Speksnijder (1985) and Gretter et al. (2015), which showed that the URU overlies the LRU (or even the pre-Variscan basement, Mujal et al., 2017a) through a high rank unconformity. TSU3 corresponds to the Buntsandstein Unit, following Gretter et al. (2015). The Erill Castell-Estac Basin was involved in the regional transtensive tectonic regime already proposed for the Early Permian in Western Europe by the Variscan chain shearing and dismantling scenario (Arthaud and Matte, 1977; Soula et al., 1979; Echtler and Malavieille, 1990; Scotese,

2003; Edel et al., 2015, 2018). The continental sedimentary record of the Pyrenean basins is therefore closely related to other European basins that evolved from a post-collisional frame to the first marine incursion during the Middle Triassic (e.g., Edel et al., 2015, 2018; Rodríguez-Méndez et al., 2016).

However, as is in this thesis was described, the Upper Red Unit and the Lower Red Unit present similitudes. Their differentiation is usually difficult and their sedimentological, pedological and clay mineralogical contents are similar. Their differentiation have been proposed by Gisbert (1981) based on supposed and never pictured angular unconformity. The internal unconformities in basins under active tectonic regime are common, and the unconformity between the Lower and the Upper Red Unit could represent one of them. The ichnological data from Mujal's works represents an interesting tool to calibrate the age of this two units. Nevertheless, tetrapod's footprints are not well constrained in the SW Europe, and their recognition is usually uncertain. In this thesis is not shown determinant data supporting the absence of this age gap. But the option to go back to an unique Red Unit (Fm. Peranera *Auctt*) could simplify further interpretations.

<u>Southern Pyrenees and SW Europe correlation</u>

In the Cantabrian Mountains the Stephanian B-C (Upper Carboniferous) is post-tectonic, but not post-orogenic. These deposits cover the Variscan structures of the internal zones unconformably. This is because there was still some orogenic activity within this time-frame in the Eastern part of the Cantabrian Zone (Picos de Europa Unit). The continental Stephanian B-C basins are extensional and are related to the volcanic and
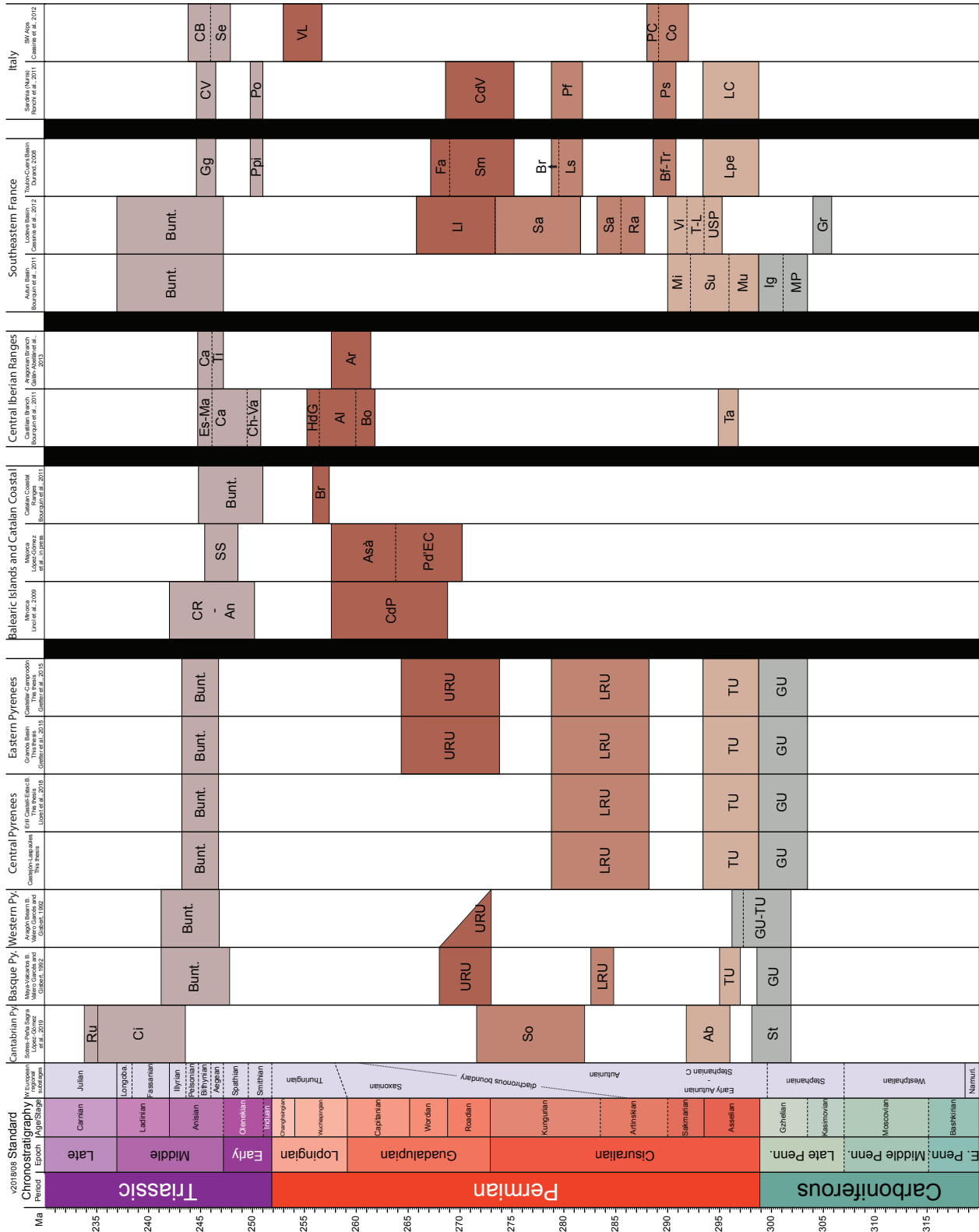
Figure 10.4.2. Stratigraphic correlation of the Upper Carboniferous-Middle Triassic basins in the SW Europe. St: San Tirso, Ab: Acebal, So: Sotres, Ci: Cicera, Ru:Rueda; CdP: Cala del Pilar, An: Antechristo, CR: Cala Rotja, Pd'EC: Port d'Es Canonge, SS: Son Serralta, Br: Brugers; Ta: Tabarreña, Bo: Boniches, Al: Alcotas, HdG: Hollos de Gallo, Ch-Va: Chequilla-Valdemeca, Ca: Cañizar, Es-Ma: Eslida-Marines; Ar: Araviana, Ti: Tierga, Ca:Calcena; MP: Mont Pelé, Ig: Igornay, Mu: Muse, Su: Surmoulin, Mi:, Gr: Graissessac, USP: Usclas St. Privat, T-L: Tuilières-Loiras, Vi: Viala, Ra: Rabejac, Sa: Salagou, Ll: La Lieude, Lpe: Les Pellegrins, Bf: Bron, Tr: Transy, Ls: Les Salettes, Br: Calc. du Bau Rouge, Sm: St. Mandrier, Fa: Fabregas, Ppi: Port-Isol Conglomerate, Gg: Gonfaron; LC: Lu Caparoni, Ps: Pedro Siligu, Pf: Porto Ferro, CdV: Cala del Vino, Po: Porticciolo, CV: Cala Viola, Co: Collio Fm., PC: Ponternica Conglomerate, VL: Verrucano Lombardo, Se: Servino, CB: Carniola di Bovegno.

183

subvolcanic extension (Merino-Tomé et al., 2017). Therefore, the westernmost Cantabrian zone show some similarities with the Pyrenean sector in terms of tectonic context (Fig. 10.4.2). Moreover, López-Gómez et al. (2019) have proposed for the first time a stratigraphic correlation between the Cantabrian and the Centra-Eastern Pyrnees: the Tirso (St) unit could correspond to the Grey Unit. Unit, (2) the Acebal (Ab) unit to the Transition Unit and (3) the Sotres unit (So) to the Lower and Upper Red units. The Middle Triassic continental deposits in the Cantabrian zone (Cicera Unit, Ci) are slightly younger (Anisian-Carnian; López-Gómez et al., 2019) with respect to the Pyrenean ones (Anisian; Clavet et al., 1993; this work). This finding seems to indicate that the Lower-Middle Triassic continental basins along the Central-Eastern Southern Pyrenees could be diachronous.

In the Basque and Western Pyrenees the stratigraphic units were divided with the same nomenclature as in the Central-Eastern Pyrenees. The Grey and Transition units corresponds to the same range of age (Gzhelian-Asselian). In the Basque zone these two units are separated by a hiatus (Valero-Garcés and Gisbert, 1992). The Lower and Upper Red units have a lower temporary range, for the LRU was indicated the Asselian-Sakmarian transit, and for the URU the upper part of the Artinskian and the lower part of the Kungurian (Fig. 10.4.2). The URU completely disappears in the Western-Central Southern Pyrenees. The Buntsandstein facies Unit has the same age (Anisian) in all the Pyrenees, to date.

In the Balearic and Catalan Coastal Ranges no Upper Carboniferous-Lower Permian deposits have been found (Fig. 10.4.2). The URU from the Pyrenees could be equivalent with the Cala del Pilar Fm. (CdP) in Minorca, and Asà and Port d'Es Canonge (Pd'EC) formations in Majorca. The Brugers (Br) Fm. in the Catalan Coastal Ranges has

a Wuchiapingian age (Bourquin et al., 2011), so this unit is out of range in comparison with the URU (Rodian-Worian). The palynofloras of the Buntsandstein facies (Antechristo, An; Cala Roja, CR; Son Serrata, SS) in the Balearic Islands indicated younger ages for the first continental Triassic deposits (Smithian, Olenekian). In the Catalan Coastal Ranges this deposits has been dated as Early-lower Middle Triassic (Díez et al., 2010).

The Central Iberian Ranges and the Pyrenees have great differences in their stratigraphic organization (Fig. 10.4.2). The Transition Unit could be equivalent with the Tabarreña Formation (Ta), but the rest of the Permian units pertains to the Middle Permian, so no stratigraphic correlations can be done.

The Southeastern basins of France have similitudes with the Pyrenean stratigraphy (Fig. 10.4.2). The Upper Carboniferous-Early Permian deposits have correlative ages: (1) the Grey Unit with the Mont Pelé (MP) and Igornay (Ig) formations in the Autun basin, and with the Graissessac (Gr) formation in the Lodeve basin. (2) the Transition Unit with the Muse (Mu), Surmoulin (Su) and Millery (Mi) formations in the Autun basin, with the Usclas St. Privat (USP), Tuilières-Loiras (T-L) and Viala (Vi) formations in the Lodeve basin, and with the Les Pellegrins (Lpe) Formation in Toulon-Cuers basin. (3) the Lower Red Unit with the Rabejac (Ra) and Salagou (Sa) formations in the Lodeve basin, and with the Les Salettes (Ls) and Calc. du Bau Rouge (Br) in Toulon-Cuers basin. (4) the Upper Red Unit with the La Lieude (Ll) Formation in the Lodeve basin, and with the St. Mandrier (SM) and Fabregas (Fa) formations in the Toulon-Cuers basin. (5) the Buntsandstein facies Unit with the same unit (Bunt.) in the Autun and Lodeve basins, and with the Gonfaron (Gg) Formation in the Toulon-Cuers basin. The Port-Isol Conglomerate (Ppi, Early Triassic) from this last basin has not correlation with any Pyrenean unit.

In Italy exists Upper Carboniferous sediments in isolated outcrops (Ronchi et al., 2008), these units can be correlated to the Grey Unit (see Juncal et al., 2018). The Permian and Triassic correlations are: (1) the Transition Unit with the Lu Caparoni (LC) Formation in the Nurra (Sardinia). (2) the Lower Red Unit with the Pedro Siligu (PS) and Porto Ferro (Pf) formations in Sardinia, and with the Collio Formation (Co) and Ponternica Conglomerate (PC) in the SW Alps. (3) the Upper Red Unit with the Cala del Vino (CdV) Formation in the Nurra. (3) the Buntsandstein facies Unit with the Cala Viola (CV) Formation in the Nurra, and with the Servino (Se) and Carniola di Bovegno (CB) formations in the SW Alps. In Sardinia exists a conglomerate (Porticciolo, Po) similar in age with the Port-Isol Conglomerate from Toulon-Cuers (Cassinis et al., 2003). The Verrucano Lombardo (VL) formation does not match with any Pyrenean stratigraphic unit, but could fit well with the Central Iberian Ranges Middle Permian.

Isotopic correlation

Some global correlation can be drawn for the Permian-Triassic times from the isotopic data obtained. Figure 7.2.11 shows a clear decrease during the Permian and Triassic of the $\delta^{13}C$ in the pedeogenic carbonate. This trend can be strongly correlated with the global curve (Fig. 10.4.3) and shows a decrease during the Permian to the Middle Triassic. This is generally related to the Siberian Traps activity, which lasted for several million years (Benton and Twitchett, 2003; Benton and Newell, 2014). For the first time, this decrease has been detected in the Southern Pyrenees, and the isotopic data obtained in this study can probably be directly related to the worldwide climatic change that occurred during these times. The study of pedogenic carbonate is a very good tool in continental desposits for unravelling past atmpospheric conditions. The resulting data

supports the aridification described in the Permian as being related to the activity of the Siberian Traps.
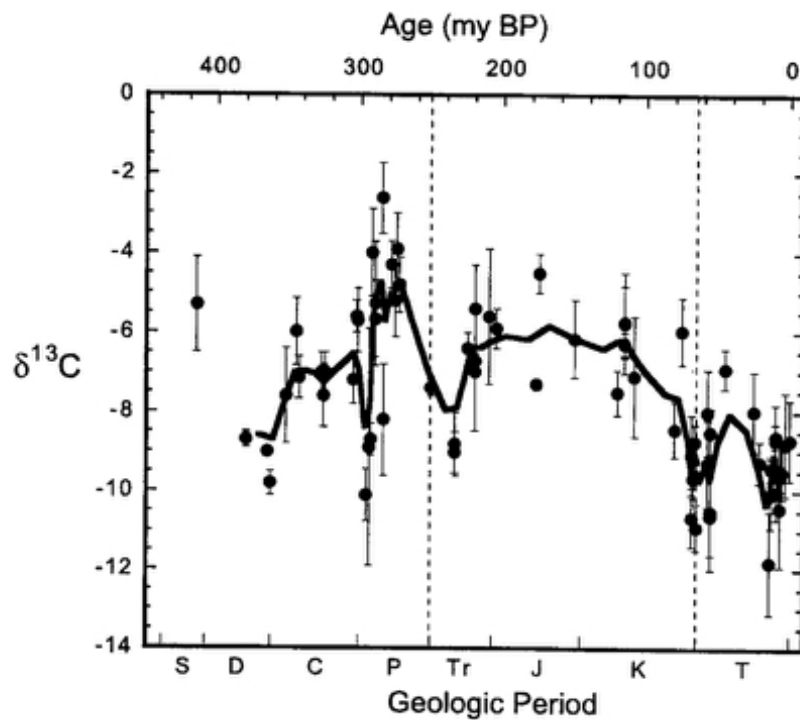
Figure 10.4.3. Isotopic composition of pedogenic carbonates. Averages for each formation are plotted with standard deviation bars. The curve represents a 5 point weighted running average for the data points. From Ekart et al. (1999).

The $\delta^{13}C$ isotopic trends of the paleosols obtained can be related to non-pedogenic $\delta^{13}C$ recorded in other parts of the world (Fig. 10.4.4). For instance, the Permian-Triassic negative shift has been observed by many studies (Clarkson et al., 2013; Buggisch et al., 2015; Cheng et al., 2019; Maaleki-Moghadam et al., 2019).

The recent study of Buggisch et al. (2015) in the Austrian and Italian Alps indicate a period of high variability during the Gzhelian-Asselian periods. During the Artinskian-Kungurian the isotopic values had smaller ranges and tende toward more negative values. This trend can be correlated with the isotopic values obtained in the studied zone for the same period (Fig. 10.4.4). The isotopic values of the LRU (Artinskian-Kungurian) show a negative tendency going upwards the stratigraphic record, seeming to indicate that the age proposed is in agreement with the isotopic variations recorded in the Alps for the
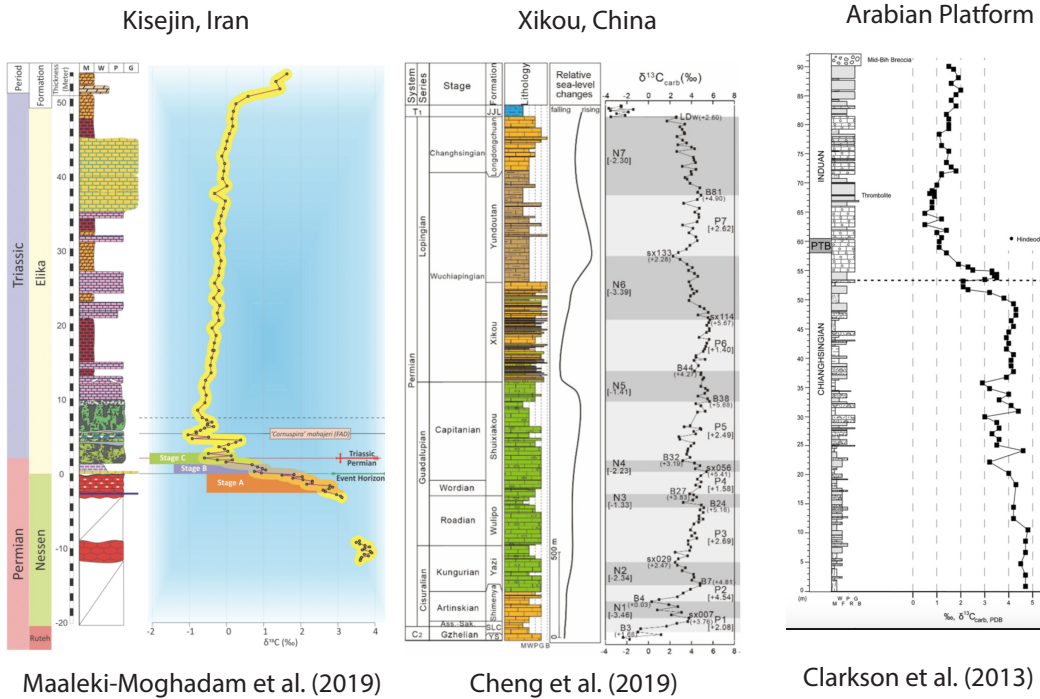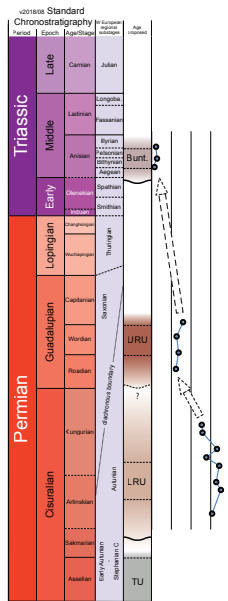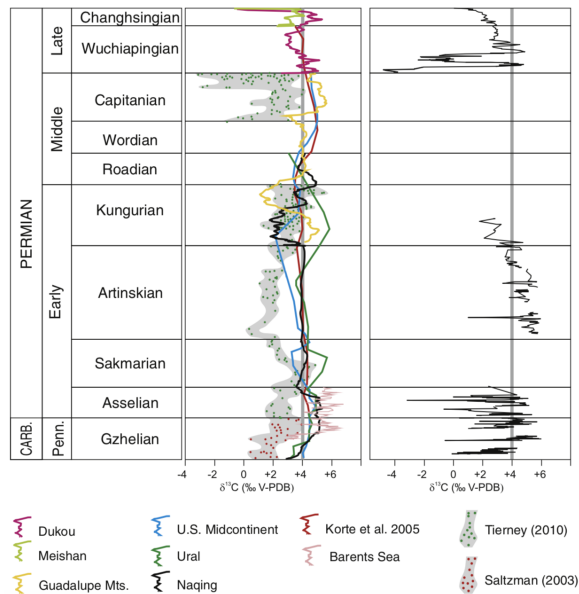
Figure 10.4.4. Examples of other isotopes curves from over the world and from the Pyrenees.

same period. This trend has also been observed in Xikou (China) for marine deposits during the Kungurian, so this isotopic shift probably corresponds with a global process. In the SW European basins, this trend may be related to the closure of the Ural gateway, which may have triggered an upwelling of cold, nutrient-rich deep waters along the

Northwestern Pangean margin (Beauchamp, 1994; Mii et al., 1997; Blomeier et al., 2011; Buggisch et al., 2015; Beauchamp and Grasby, 2012). The Rodian-Wordian isotopic data from China, the USA (Guadalupe Mountains) and the Urals show low δ^{13}C variations, in keeping with the results obtained in the Central-Eastern Southern Pyrenees. The discontinuity of the sedimentary record in the studied area rules out any subsequent correlation with the Late Permian age.

11. Conclusions

A multidisciplinary approach that included the analysis of stratigraphic, sedimentological, pedogenic, isotopic, mineralogic and tectonic data allowed us to understand the evolution of a key basin in the Central-Eastern Southern Pyreneean and in all the surrounding basins of the chain as well. Based on this understanding, several conclusions can be remarked from different points of view:

Erill Castell-Estac Basin depositional evolution:

(1) The infill of Erill Castell-Estac Basin consists of three different sedimentary cycles with a general fining upward trend. The first one (SC 1) corresponds to the GU and TU lithostratigraphic units mostly constitute by volcanic and volcaniclastic deposits at the base and fluvial-lacustrine at the top, developed under humid conditions. The SC 2 corresponds to the LRU and mostly consists of fluvial and playa-lake fine deposits deposited under semi-arid conditions. The third (SC 3) corresponds to the Buntsandstein clastic deposits occurred during the Early-early Middle Triassic; these fluvial deposits are mainly braided and meandering systems in an alternating arid to semi-arid climatic conitions.

(2) Sedimentological, stratigraphic and tectonic features indicate that the Erill Castell-Estac Basin's history developed under different phases of evolution subject to distinct triggering mechanisms. In the initial phase (latest Carboniferous) a volcano-tectonic subsidence gave rise to isolated sub-basins. In the second phase (early-to-late Cisuralian) the volcanic influence diminished in favor of greater tectonic control associated with a transtensive regional context. The sub-basins started to be interconnected and depocenters migrated next to the main southern basin boundary fault (future Erta thrust). Moreover, during the late Early-Middle Permian the basin infill balanced the generated accommodation space generated. Later on, in the Early Triassic,

190

the deposition was more widespread and exceeded the accommodation space generated in the Permian. This last episode occurred under a more extensional regime. This evolution mirrors the classical continental rifting models, albeit at a different scale.

(3) The Erill Castell-Estac Basin is a key area for understanding the evolution of Central-Eastern Southern Pyrenean Late Carboniferous-Early Triassic basins. The complete absence of the URU is an important stratigraphic event, peculiar only to this area and the Castejón-Laspaúles basins (Central Southern Pyrenees). It is considered here to be related to the presence of a topographic high separating the Eastern Pyrenean basins from the Western ones, which would explain the non-deposition of this unit in those areas.

(4) According to the new tectono-stratigraphic evolution described in this work, we propose, in the Erill Castell-Estac Basin, the following regional organization of TSUs: a first TSU1 made up of the Grey Unit, Transition Unit and Lower Red Unit; a TSU2 (missing) relative to the Upper Red Unit; and a TSU3 represented by the Buntsandstein facies.

(5) The evolution of the Erill Castell-Estac Basin provides a good and new example of the sedimentary filling of strike-slip basins and offers new stratigraphic, tectonic, and paleoclimatic data on the continental Carboniferous to Triassic rocks of the Western Tethys during the preceeing stages of Pangea break-up.

(6) The palynological data obtained and identified provide new chronostratigraphic information. Some of the new palynological assemblages presented are very significant and exceptional. The Grey Unit provided good bio-chronostratigraphic dated for the first time, calibrating perfectly with the radiometric data. The age obtained (Gzhelian) from the pollen association discovered is the most precise reported to date. In other Southern Western Europe basins, these data represent a key to

correlating microflora assemblages in the latest Carboniferous- earliest Permian timespan. These data shed greater light on the problematic issue of mixed flora assemblages and the old terminology (Stephanian-Autunian) used by the authors. The Lower Red Unit has been dated for the first time with palynological assemblages, and also this time constraint correlates very well with the previous radiometric dating. The sporomorph content in the upper part of the Buntsandstein facies Unit allows to date these deposits with great precision as Pelsonian in age (middle Anisian).

(7) The pedogenic record shows significant changes along the stratigraphic Permian-Triassic succession. This allows to interpreting paleoclimate variations over time: (a) semi-arid conditions for the Artinskian (b) semi-arid conditions for the Kungurian and (c) arid to semi-arid conditions for the Early-Lower-Middle Triassic. A detailed pedogenic study represents a good stratigraphic tool for identifing different units with very similar facies.

(8) The stable isotopes of the pedogenic carbonates underlined the different signature for each pedotype. The vegetation and atmospheric composition were the responsible for such variations, and the pedogenic carbonate is therefore a good proxy for obtaining paleoclimatic values. The results show a tendency to more negative values with the younger deposits of the succession; and this could be explanied by the Permian-Triassic extinction and the increase in volcanic gases from the Siberian Traps volcanism.

(9) Based on the presence of halloysite and dickite, the clay mineralogy analysis indicates that the Late Carboniferous was under humid conditions. Slight changes were found in the clay composition of the Permian and Triassic units, and the very low carbonate content in the Lower Triassic could indicate arid to semi-arid conditions. In this thesis, clay mineralogy has not in itself pointed to any major climatic changes but it has an been a useful back-up to all the other methodologies used.

(10) The Upper and Lower Red units do not present any major lithological differences, and the supposed angular unconformity reported by some authors may only be a tectonic-induced internal unconformity of little rank significance. The rest of the data obtained could show variations between these two units, but most of them could be produced by a normal basin evolution of clogging and climate variations. Unfortunately, no paleontological content has been found to date the Upper Red Unit with greater precision, apart frome some doubtful vertebrate remains (Mujal et al., 2016b).

(11) The combination of all the approaches followed -all requiring a detailed basilar knowledge of the stratigraphy- has allowed to reconstruct the Upper Carboniferous-Lower Triassic basins of the Central-Eastern Southern Pyrenees. The climate variations were derived from humid conditions in the Late Carboniferous-Early Permian, a monsoonal period in the Artinskian-Kungurian represented by the Lower and Upper Red Units and, finally, an arid to semi-arid regime in the Early Triassic.

11.1 Further research:

This thesis contributes to enlarge the geological knowledge of the studied zone, but it also leaves some questions. The dating of the Upper Red Unit is one of the most urgent aspects, essential to any resolution of the stratigraphy organization of the Southern Pyrenees record. Once this chronostratigraphic problem has been elucidated in more detail, the researches would have a more detailed correlation of all the Permo-Triassic Pyrenean successions, from the Cantabrian Zone to the Easternmost Catalan Pyrenees. More detailed knowledge of the whole sector would surely help to unravel fundamental paleogeographical issues, such as the relationship between the Southern (Spanish) and Northern (French) Pyrenean basins, and the great differences between the Iberian Permian record and the Pyrenean record.

The Triassic deposits also open up many questions: the first is the possibility tof precisely dating the marine transgression in this part of the Iberian plate. The precision of the palynological data on Triassic ages could allow to date places the first marine-influenced deposits in many in the Pyrenees. The Tethys opening occurred from East to West, and the Southern Pyrenees represents a good outcrop to confirm and date such event. Still with respect to the Lower Triassic deposits, the Derana pedotype has been found in all the studied sectors. In these three years of the PhD project, I have seen very similar paleosols in the Triassic record in Sardinia, and an interesting future project could be to correlate the Permian and Triassic paleosols of other Southwestern Europe sectors such as this. Once the isotopic signatures have been verified, a complete isotopic curve for all the continental Permian deposits in the SW Europe could be a very interesting goal.

12. Refrencees

Algeo, T.J., Chen, Z.Q., Fraiser, M.L., Twitchett, R.J., 2011. Terrestrial–marine teleconnections in the collapse and rebuilding of Early Triassic marine ecosystems. Palaeogeography, Palaeoclimatology, Palaeoecology 308, 1–11. https://doi.org/10.1016/j.palaeo.2011.01.011

Allen, J.R.L., 1963. The Classification of Cross-Stratified Units. With Notes on Their Origin. Sedimentology 2, 93–114. https://doi.org/10.1111/j.1365-3091.1963.tb01204.x

Allen, P.A., Allen, J.R., 2005. Basin Analysis: Principles and applications. Blackwell Publishing, Oxford, UK.

Alonso-Azcárate, J., Arche, A., Barrenechea, J., López-Gómez, J., Luque, F.J., Rodas, M., 1997. Palaeogeographical significance of clay mineral assemblages in the Permian and Triassic sediments of the SE Iberian Ranges, eastern Spain. Palaeogeography, Palaeoclimatology, Palaeoecology 136, 309–330. https://doi.org/10.1016/S0031-0182(97)00044-8

Alonso-Zarza, A.M., 2003. Palaeoenvironmental significance of palustrine carbonates and calcretes in the geological record. Earth-Science Reviews 60, 261–298. https://doi.org/10.1016/S0012-8252(02)00106-X

Alonso-Zarza, A.M., Meléndez, A., Martín-García, R., Herrero, M.J., Martín-Pérez, A., 2012. Discriminating between tectonism and climate signatures in palustrine deposits: Lessons from the Miocene of the Teruel Graben, NE Spain. Earth-Science Reviews 113, 141–160. https://doi.org/10.1016/j.earscirev.2012.03.011

Álvarez-Ramis, C., Piradondy, M., Doubinger, J., 1969. Sur la flore fossile du Carbonifère de Surroca (Gerona, Espagne). Comptes rendus de l'Académie des Sciences de Paris 268, 2559–2561

Álvarez-Ramis, C., Doubinger, J., Diéguez Jiménez, M.C., 1971. Estudio paleobotánico de la flora de Ogassa (Gerona). Estudios Geológicos XXVII (3), 267–277.

Álvarez-Ramis, C., 1985. Sobre la presencia de flora autuniense en las series carboníferas del Pirineo leridano (España). Compte Rendu 10e Congrès International de Stratigraphie et Géologie du Carbonifère, Madrid 1983, 2, 181–189.

Álvarez-Ramis, C., Doubinger, J., 1987. Microflora de Estac (Lérida). Cuadernos de Geología Ibérica 11, 131-137

Anadón, P., Marzo, M., 1977. Evolución y características sedimentológicas de las facies fluviales basales del Buntsandstein de Olesa de Montserrat (Provincia de Barcelona). Cuadernos de Geología Ibérica 4, 211–222.

Anderson, E.M., 1905. The dynamics of faulting. Transactions of the Edinburgh Geological Society 8, 387–402.

Anderson, E.M., 1951. The Dynamics of Faulting and Dyke Formation with Application to Britain. Oliver & Boyd, Edinburgh, UK.

Andrews, E., White, T., del Papa, C., 2017. Paleosol-based paleoclimate reconstruction of the Paleocene-Eocene Thermal Maximum, northern Argentina. Palaeogeography, Palaeoclimatology, Palaeoecology 471, 181–195. https://doi.org/10.1016/j.palaeo.2017.01.042

Arche, A., López-Gómez, J., 1996. Origin of the Permian-Triassic Iberian Basin, central-eastern Spain. Tectonophysics 266, 443–464.

Arche, A., López-Gómez, J., 2005. Sudden changes in fluvial style across the Permian−Triassic boundary in the eastern Iberian Ranges, Spain: Analysis of possible causes. Palaeogeography, Palaeoclimatology, Palaeoecology 229, 104–126. https://doi.org/10.1016/j.palaeo.2005.06.033

Árkai, P., Sassi, F.P., Sassi, R., 1995. Simultaneous measurements of chlorite and illite crystallinity a more reliable tool for monitoring low to very low grade metmorphism in metapelites. A case study from the Southern Alps (NE Italy). Eur. J. Mineral. 7, 1115–1128.

Árkai, P., Brime, C., Kisch, H.J., 2004. On the calibration of the illite Kübler index (illite "crystallinity"). https://doi.org/10.5169/seals-63752

Arthaud, F., Matte, P., 1977. Late Paleozoic strike-slip faulting in southern Europe and northern Africa: Result of a right-lateral shear zone between the Appalachians and the Urals. Geological Society of America Bulletin 88, 1305–1320.

Ashauer, A., 1934. Die östliche eudigung der Pyrenean. Publicación extraordinaria sobre la Geologia de España 2, 210–336.

Ashmore, P.E., 1991. How do gravel-bed river braid? Canadian Journal of Earth Sciences 28, 326-341.

Avanzini, M., Bargossi, G., Borsato, A., Castiglioni, G.B., Cucato, M., Morelli, C., Prosser, G., Sapelza, A., 2007. Note illustrative della Carta Geologica d'Italia alla scala 1:50.000, Foglio 026 Appiano. Servizio Geologico d'Italia APAT, Dipartimento Difesa del Suolo, Roma. pp 184.

Aziz, H.A., Sanz-Rubio, E, Calvo, J.P., Hilgen, F.J., Krijgsman, W., 2003. Palaeoenvironmental reconstruction of a middle Miocene alluvial fan to cyclic shallow lacustrine depositional system in the Calatayud Basin (NE Spain). Sedimentology 50, 211–236.

Badeck F.W. Tcherkez G. Nogues S. Piel C. and Ghashghaie J., 2005. Post-photosynthetic fractionation of stable carbon isotopes between plant organsa widespread phenomenon. Rapid Commun. Mass Spectrometry 19, 1381–1391.

Baver L.B., Gardner W.H., Gardner W.R., 1972. Soil Physics. 4th Issue, John Wiley & Sons, Inc., New York.

Beauchamp, B., 1994. Permian climatic cooling in the Canadian Arctic, in: Klein, G.D. (Ed.), Pangea: Paleoclimate, Tectonics and Sedimentation During Accretion, Zenith

and Break-up of a Supercontinent. Geological Society of America, 229–246. https://doi.org/10.1130/SPE288-p229

Beauchamp, B., Grasby, S.E., 2012. Permian lysocline shoaling and ocean acidification along NW Pangea led to carbonate eradication and chert expansion. Palaeogeography, Palaeoclimatology, Palaeoecology 350–352, 73–90. https://doi.org/10.1016/j.palaeo.2012.06.014

Benito, M.I., de la Horra, R., Barrenechea, J.F., López-Gómez, J., Rodas, M., Alonso-Azcárate, J., Arche, A., Luque, J., 2005. Late Permian continental sediments in the SE Iberian Ranges, eastern Spain: Petrological and mineralogical characteristics and palaeoenvironmental significance. Palaeogeography, Palaeoclimatology, Palaeoecology 229, 24–39. https://doi.org/10.1016/j.palaeo.2004.12.030

Benton, M.J., 1995. Diversification and extinction in the history of life. Science 268, 52–58. https://doi.org/10.1126/science.7701342

Benton, M.J., Twitchett, R.J., 2003. How to kill (almost) all life: the end-Permian extinction event. Trends in Ecology & Evolution 18, 358–365. https://doi.org/10.1016/S0169-5347(03)00093-4

Benton, M.J., Newell, A.J., 2014. Impacts of global warming on Permo-Triassic terrestrial ecosystems. Gondwana Research 25, 1308–1337. https://doi.org/10.1016/j.gr.2012.12.010.

Berthelin, M., Broutin, J., Kerp, H., Crasquin-Soleau S., Platel J.P., Roger J., 2003. The Oman Gharif mixed paleoflora: a useful tool for testing Permian Pangea reconstructions. Palaeogeography, Palaeoclimatology, Palaeoecology 196, 85–98.

Berthelin, M., Stolle, E., Kerp, H., Broutin, J., 2006. Glossopteris anatolica Archangelsky and Wagner 1983, in a mixed middle Permian flora from the Sultanate of Oman: comments on the geographical and stratigraphical distribution. Review of Palaeobotany and Palynology 141, 313–317.

Besly, B.M., Collinson, J.D., 1991. Volcanic and tectonic controls of lacustrine and alluvial sedimentation in the Stephanian coal-bearing sequence of the Malpàs-Sort Basin, Catalonian Pyrenees. Sedimentology 38, 3-26.

Birkeland, P.W., 1984. Soils and Geomorphology, 2nd Edition, Oxford University Press, New York, Oxford. 372 pp.

Bixel, F., Lucas, C., 1983. Magmatisme, tectonique et sédimentation dans les fossés stéphano-permiens des Pyrénées occidentals. Revue de Géographie Physique et de Géologie Dynamique 24, 329–324.

Bixel, F., 1984. Le magmatism stéphano-permien des Pyrénées. University of Toulouse, Toulouse, France.

Bixel, F., 1987. Le volcanisme Stephano-Permien des Pyrenees petrographie, mineralogie, geochimie. Cuadernos Geología Ibérica 11, 41–55.

Blakey, R. C. (2012). Rectangular global maps.

Blake, B.M., Cross, A.T., Eble, C.F., Gillespie, W.H., Pfefferkorn, H.W., 2002. Selected plant megafossils from the Carboniferous of the Appalachian region, United States, in: Hills, L.V., Henderson, C.M., Bamber, E.W. (Eds.), Carboniferous and Permian of the World, Canadian Society of Petroleum Geologists, Memoir 19, 259–335.

Blodgett, R.H., 1988. Calcareous paleosols in the Triassic Dolores Formation, southwestern Colorado, in: Geological Society of America Special Papers. Geological Society of America, pp. 103–122. https://doi.org/10.1130/SPE216-p103

Blomeier, D., Dustira, A., Forke, H., Scheibner, C., 2011. Environmental change in the Early Permian of NE Svalbard: from a warm-water carbonate platform (Gipshuken Formation) to a temperate, mixed siliciclastic-carbonate ramp (Kapp Starostin Formation). Facies 57, 493–523. https://doi.org/10.1007/s10347-010-0243-z

Borruel-Abadía, V., López-Gómez, J., De la Horra, R., Galán-Abellán, B., Barrenechea, J.F., Arche, A., Ronchi, A., Gretter, N., Marzo, M., 2015. Climate changes during the Early–Middle Triassic transition in the E. Iberian plate and their palaeogeographic significance in the western Tethys continental domain. Palaeogeography, Palaeoclimatology, Palaeoecology 440, 671–689.

Bouroz, A., Doubinger, J., 1977. Report on the Stephanian–Autunian boundary and on the contents of Upper Stephanian and Autunian in their stratotypes, in: Holub, V.M., Wagner, R.H. (Eds), Symposium on Carboniferous Stratigraphy. Prague: Geological Survey, 147–169.

Bourquin, S., Durand, M., Díez, J., Broutin, F., Fluteau, 2007. The Permian-Triassic boundary and lower Triassic sedimentation in western European basins: an overview. Journal of Iberian Geology 33, 221–236.

Bourquin, S., Bercovici, A., López-Gómez, J., Diez, J.B., Broutin, J., Ronchi, A., Durand, M., Arché, A., Linol, B., Amour, F., 2011. The Permian–Triassic transition and the onset of Mesozoic sedimentation at the northwestern peri-Tethyan domain scale: Palaeogeographic maps and geodynamic implications. Palaeogeography, Palaeoclimatology, Palaeoecology 299, 265–280.

Bown, T.M., Kraus, M.J., 1987. Integration of Channel and Floodplain Suites, I. Developmental Sequence and Lateral Relations of Alluvial Paleosols. Journal of Sedimentary Research 57, 587-601.

Branney, M.J., Kokelaar, P., 2002. Pyroclastic Density Currents and the Sedimentation of Ignimbrites. Geological Society of London, Memoirs 27, Geological Society, London.

Broutin, J., Gisbert, J., 1985. Entorno paleoclimático y ambiental de la flora stephano-autuniense del Pirineo catalán. Compte rendux Dixième International de Stratigraphie et de Géologie du Carbonifère, Madrid 53–66.

Broutin, J., 1986. Étude paléobotanique et palynologique du passage Carbonifère Permien dans le sud-ouest de la Péninsule Ibérique: Cahiers de Paléontologie, Éditions du Centre National de la Recherche Scientifique, Paris, 165 pp.

Broutin, J., Doubinger, J., Langiaux, J., Primey, D., 1986. Conséquences de la coexistence de flores à caractères stéphaniens et autuniens dans les bassins limniques d'Europe occidentale. Mémoires Société Géologique de France 149, 15–25.

Broutin, J., Doubinger, J., Gisbert, J., Satta-Pasini, S., 1988. Permières datations palynologiques dans les faciès Buntsandstein des Pyrénées catalanes espagnoles. Comptes Rendus de l'Académie des Sciences du Paris 2, 159–163.

Broutin, J., Doubinger, J., Farjanel, G., Freytet, P., Kerp, H., Langiaux, J., Lebreton, M.L., Sebban, S., Satta, S., 1990a. Le renouvellement des flores au passage Carbonifère-Permien: approche stratigraphique, biologique, sédimentologique. Comptes Rendus de l'Académie des Sciences 311 (2), 1563–1569.

Broutin, J., Doubinger, J., El Hamet, M.O., Lang, J., 1990b. Palynologie comparée du Permien nigérien (Afrique occidentale) et Péritéthysien. Implications stratigraphiques et phytogéographiques. Review of Paleobotany and Palynology 66, 243-261.

Broutin, J., Châteauneuf, J., Mathis, V., 1992. The Lodève Basin, in: Châteauneuf, J., Broutin, J., Farjanel, G., Mathis, V., Pacaud, G. (Eds.), Permian Basins in the French Massif Central, Cahiers de Micropaléontologie. Éditions du CNRS, Paris.

Broutin, J., Cabanis, B., Châteauneuf, J., Beroin, J., 1994. Évolution biostratigraphique magmatique et tctonique du domaine Palététhysien occidental (SW de l'Europe): implications palégéographiques au Permien inférieur. Bulletin de la Société Géologique de France 165, 163–179.

Broutin, J., Berthelin, M., 2005. Dynamic of settlement of mixed floras during the Permian in the Peri-Tethyan domain: paleogeographic and paleoclimatic significance, in: Lucas, S.G., Zeigler, K.E. (Eds.), The Nonmarine Permian. New Mexico Museum of Natural History and Science Bulletin 30, 24–25.

Brugman WA, 1986. A Palynological Characterization of the Upper Scythian and Anisian of the Transdanubian Central Range (Hungary) and the Vincentinian Alps (ltaly). Ph.D Thesis, University de Utrecht, pp. 95.

Buggisch, W., Krainer, K., Schaffhauser, M., Joachimski, M., Korte, C., 2015. Late Carboniferous to Late Permian carbon isotope stratigraphy: A new record from post-Variscan carbonates from the Southern Alps (Austria and Italy). Palaeogeography, Palaeoclimatology, Palaeoecology 433, 174–190. https://doi.org/10.1016/j.palaeo.2015.05.012

Bullock, P., Fedoroff, N., Jongerius, A., Stoops, G., Tursina, T., 1985. Handbook for Soil Thin Section Description. Waine Research Publications, Wolverhampton (UK).

Buol, S.W., Hole, F.D., McCracken, R.J., Southard, R.J., 1997. Soil Genesis and Classification, 4th edn. Iowa State Univ. Press, Ames.

Burg, J.P., Van Den Driessceh, J., Brun, J., 1994. Syn- to post-thickening extension in the Variscan belt of Western Europe: models and structural consequences. Géologie de la France 3, 33–51.

Butler, B. E., 1980. Soil classification for soil survey. Oxford: Oxford Science Publications. Science, 96.

Calvet, F., Solé De Porta, N., Salvany, J.M., 1993. Cronoestratigrafía (Palinología) del Triásico sudpirenaico y del Pirineo Vasco-Cantábrico. Acta Geológica Hispánica 28, 33–48.

Calvo, J.P., Jones, B., Bustillo, M., Fort, R., Alonso-Zarza, A.M., Kendall, C., 1995. Sedimentology and geochemistry of carbonates from lacustrine sequences in the Madrid Basin, central Spain. Chemical Geology 123, 173–191.

Cantarelli, V., Aldega, L., Corrado, S., Invernizzi, C., Casas-Sainz, A., 2013. Thermal history of the Aragón-Béarn basin (Late Paleozoic, western Pyrenees, Spain); insights into basin tectonic evolution. Italian Journal of Geosciences 132, 443–462.

Carroll, A.R., Bohacs, K.M., 1999. Stratigraphic classification of ancient lakes: Balancing tectonic and climatic controls. Geology 27, 99–102.

Casas, J.M., Domingo, F., Poblet, J., Soler, A., 1989. On the role of Hercynian and Alpine thrusts in the Upper Paleozoic rocks of the Central and Eastern Pyrenees. Geodinamica Acta 3, 135–147.

Cascales-Miñana, B., Cleal, C.J., 2014. The plant fossil record reflects just two great extinction events. Terra Nova 26, 195–200.

Casini, L., Oggiano, G., 2008. Late orogenic collapse and thermal doming in the northern Gondwana margin incorporated in the Variscan Chain: A case study from the Ozieri Metamorphic Complex, northern Sardinia, Italy. Gondwana Research 13, 396–406.

Cassinis, G., Doubinger, J., 1992. Artinskian to Ufimian palynomorphs assemblages from the Central Southern Alps, Italy and their regional stratigraphic implications. In: Nairn, A.E.M., Koroteev, V. (Eds.), Contributions to Eurasian Geology, Papers Presented at the International Congress Permian System of the World, Part I. University of South Carolina, Columbia, 9–18.

Cassinis, G., Toutin-Morin, N., Virgili, C., 1995. A General Outline of the Permian Continental Basins in Southwestern Europe. In: Scholle, P.A., Peryt, T.M., Ulmer-Scholle, D.S. (Eds), The Permian of Northern Pangea. Springer, Berlin, Heidelberg, 137–157.

Cassinis, G., Di Stefano, P., Massari, F., Neri, C., Venturini, C., 2000. Permian of South Europe and its interregional correlation, in: Yin, H., Dickins, J.M., Shi, G.R., Tong, J. (Eds.), Developments in Palaeontology and Stratigraphy, Permian-Triassic Evolution of Tethys and Western Circum-Pacific. Elsevier, 37–70. https://doi.org/10.1016/S0920-5446(00)80005-9

Cassinis, G., Durand, M., Ronchi, A., 2003. Permian-Triassic continental sequences of Northwest Sardinia and South Provence: stratigraphic correlations ans palaeogeographical implications. Bollettino Società Geologica Italiana Volume speciale, 119–129.

Cassinis, G., Perotti, C.R., Ronchi, A., 2012. Permian continental basins in the Southern Alps (Italy) and peri-mediterranean correlations. International Journal of Earth Science (Geologische Rundschau) 101, 129–157.

Cerling, T.E., 1984. The stable isotopic composition of modern soil carbonate and its relationship to climate. Earth and Planetary Science Letters 71, 229–240. https://doi.org/10.1016/0012-821X(84)90089-X

Cerling, T.E., 1992. Use of Carbon isotopes in paleosols as an indicator of the P(CO2) of the paleoatmosphere. Global Biogeochemical Cycles 6, 307–314.

Cerling, T.E., 2009. Stable Carbon Isotopes in Palaeosol Carbonates, in: Palaeoweathering, Palaeosurfaces and Related Continental Deposits. Wiley-Blackwell, pp. 43–60. https://doi.org/10.1002/9781444304190.ch2

Cerling, T.E., Quade, J., 2013. Stable Carbon and Oxygen Isotopes in Soil Carbonates, in: Climate Change in Continental Isotopic Records. American Geophysical Union (AGU), pp. 217–231. https://doi.org/10.1029/GM078p0217

Chadwick, O.A., Gavenda, R.T., Kelly, E.F., Ziegler, K., Olson, C.G., Elliot, W.C., Hendricks, D.M., 2003. The impact of climate on the biogeocjemical functioning of volcanic soils. Chemical Geology 202, 195–223.

Cheng, C., Li, S., Xie, X., Cao, T., Manger, W.L., Busbey, A.B., 2019. Permian carbon isotope and clay mineral records from the Xikou section, Zhen'an, Shaanxi Province, central China: Climatological implications for the easternmost Paleo-Tethys. Palaeogeography, Palaeoclimatology, Palaeoecology 514, 407–422. https://doi.org/10.1016/j.palaeo.2018.10.023

Clarkson, M.O., Richoz, S., Wood, R.A., Maurer, F., Krystyn, L., McGurty, D.J., Astratti, D., 2013. A new high-resolution δ13C record for the Early Triassic: Insights from the Arabian Platform. Gondwana Research 24, 233–242. https://doi.org/10.1016/j.gr.2012.10.002

Clayton, G., Coquel, R., Doubinger, J., Gueinn, K.J., Loboziak, S., Owens, B., Streel, M., 1977. Carboniferous miospores of Western Europe: illustration and zonation. Mededelingen rijks Geologische dienst 29, 1–71.

Cleal, C.J., Opluštil, S., Thomas, B.A., Tenchov, Y., 2010. Late Moscovian terrestrial biotas and palaeoenvironments of Variscan Euramerica. Netherlands Journal of Geosciences 88, 181–278.

Cleal, C.J., Opluštil, S., Thomas, B.A., Tenchov, Y., 2011. Pennsylvanian vegetation and climate in tropical Variscan Euramerica. Episodes 34, 3–12.

Cleal, C.J., 2016. A global review of Permian macrofloral biostratigraphical schemes, in: Lucas, S.G., Shen, S.Z. (Eds.), The Permian timescale. London: Geological Society, Special Publications 450, 1-15.

Cline, M. G., 1949. Basic principles of soil classification. Soil Science, 67(2), 81-91.

Cline, M. G., 1963. Logic of the new system of soil classification. Soil 17-22.

Coleman, J.M., 1969. Brahmaputra river: Channel processes and sedimentation. Sedimentary Geology 3, 129–239.

Colombi, C.E., Limarino, C.O., Alcober, O.A., 2017. Allogenic controls on the fluvial architecture and fossil preservation of the Upper Triassic Ischigualasto Formation, NW Argentina. Sedimentary Geology 362, 1–16.

Cortesogno, L., Cassinis, G., Dallagiovanna, G., Gaggero, L., Oggiano, G., Ronchi, A., Seno, S., Vanossi, M., 1998. The Variscan post-collisional volcanism in Late Carboniferous–Permian sequences of Ligurian Alps, Southern Alps and Sardinia (Italy): a synthesis. Lithos 45, 305–328.

Dalloni, M., 1930. Étude géologique des Pyrénées catalanes. Annales Faculté des Sciences de Marseille XXVI (3), 1–373.

De La Horra, R., Benito, M.I., López-Gómez, J., Arche, A., Barrenechea, J.F., Luque, J., 2008. Palaeoenvironmental significance of Late Permian palaeosols in the South-Eastern Iberian Ranges, Spain. Sedimentology 55, 1849–1873. https://doi.org/10.1111/j.1365-3091.2008.00969.x

De la Horra, R., Galán-Abellán, A.B., López-Gómez, J., Sheldon, N.D., Barrenechea, J.F., Luque, F.J., Arche, A., Benito, M.I., 2012. Paleoecological and paleoenvironmental changes during the continental Middle–Late Permian transition at the SE Iberian Ranges, Spain. Global and Planetary Change 94–95, 46–61. https://doi.org/10.1016/j.gloplacha.2012.06.008

de Wet, C.B., Godfrey, L., de Wet, A.P., 2015. Sedimentology and stable isotopes from a lacustrine-to-palustrine limestone deposited in an arid setting, climatic and tectonic factors: Miocene–Pliocene Opache Formation, Atacama Desert, Chile. Palaeogeography, Palaeoclimatology, Palaeoecology 426, 46–67. https://doi.org/10.1016/j.palaeo.2015.02.039

Deines, P., 1980. The isotope composition of reduced organic carbon. Handbook of Environmental Isotope Geochemistry, The Terrestrial Environment, A (Fritz, P. and Fontes, J. Ch., eds.), 329–406, Elsevier, Amsterdam, Oxford, New York.

Delvaux, B., Teissier, D., Herbillon, A.J., Burtin, G., Jaunet, A.M., Vielvoye, L., 1992. Morphology, texture, and microstructure of halloysitic soil clays as related to weathering and exchangeable cations. Clays and Clay Minerals 40, 446–456.

Díez, J.B., 2000. Geología y Paleobotánica de la Facies Buntsandstein en la Rama Aragonesa de la Cordillera Ibérica. Implicaciones bioestratigráficas en el Peritethys Occidental. Univ. de Zaragoza and Univ. Paris, Zaragoza, Spain; Paris, France.

Diez, J.B., Broutin, J., Ferrer, J., 2005. Difficulties encountered in defining the Permian–Triassic boundary in Buntsandstein facies of the western Peritethyan domain based on palynological data. Palaeogeography, Palaeoclimatology, Palaeoecology 229, 40–53. https://doi.org/10.1016/j.palaeo.2005.06.029

Diez, J.B., Broutin, J., Grauvogel-Stamm, L., Bourquin, S., Bercovici, A., Ferrer, J., 2010. Anisian floras from the NE Iberian Peninsula and Balearic Islands: A synthesis. Review of Palaeobotany and Palynology 162, 522–542. https://doi.org/10.1016/j.revpalbo.2010.09.003

DiMichele, W.A., Aronson, R.B., 1992. The Pennsylvanian–Permian vegetational transition: a terrestrial analogue of the onshore–offshore hypothesis. Evolution 46, 807–824.

DiMichele, W., Mamay, S., Chaney, D., Hook, R., Nelson, W., 2001a. An Early Permian flora with Late Permian and Mesozoic affinities from north-central Texas. Journal of Paleontology 75(2), 449-460.

DiMichele, W.A., Pfefferkorn, H.W., Gastaldo, R.A., 2001b. Response of late Carboniferous and early Permian plant communities to climate change. Annual Review of Earth and Planetary Sciences 29, 461–487.

DiMichele, W.A., Tabor, N.J., Chaney, D.S., Nelson, W.J., 2006. From wetland to wet spots: environmental tracking and the fate of Carboniferous elements in Early Permian tropical floras, in: Greb, S.F., DiMichele, W.A. (Eds.), Wetlands Through Time. Geological Society of America, Special Papers, 399, 223–248.

DiMichele, W.A., Montañez, I.P., Poulsen, C.J., Tabor, N.J., 2009. Vegetation–climate feedbacks and regime shifts in the Late Paleozoic ice age earth. Geobiology 7, 200–226.

Donselaar, M.E., Schmidt, J.M., 2005. Integration of outcrop and borehole image logs for high-resolution facies interpretation: example from a fluvial fan in the Ebro Basin, Spain. Sedimentology 52, 1021–1042.

Doubinger, J., 1968. Études palynologiques dans le Permo-Carbonifère de l'Autunois les schistes de Muse. Bulletin de la Société d'Histoire Naturelle de Autun, 50: 14-19.

Doubinger, J., 1971. Contribution a la palynologie de l'Autunien: les schistes de Charmoy, Bassin de Blanzy (Saône-s-Loire). Bull. Soc. Hist. Nat. Autun 58, 15–18.

Doubinger, J., 1974. Études palynologiques dans l'Autunian. Review of Palaeobotany and Palynology 17, 21–38.

Doubinger, J., Robert, J.F., Broutin, J., 1978. Données complémentaires sur la flore Permo-Carbonifère de Surroca-Ogassa (province de Gérone, Espagne). 103e Congrès national des Sociétés savantes, Nancy 1978: Sciences II, 39-45.

Doubinger, J., Álvarez-Ramis, C., 1984. Flores de quelques bassins stéphaniens d'Espagne: corrélations avec les flores du stratotype de Saint-Etienne (France). Compte Rendu 9e Congrès International de Stratigraphie et Géologie du Carbonifère, Washington and Champaign-Urbana 1979, 2, 515–522.

Doubinger, J., Roy-Dias, C., 1985. La paléoflore du Stéphanien de l'Oued Zat (Haut Atlas de Marrakech-versant Nord – Maroc). Geobios 18, 573–586.

Doubinger, J., Odin, B., Conrad, G., 1987. Les associations sporopolliniques du Permien Continentaldu basin de Lodève (Hérault, France): caractérisationde l'Autunien superior, du "Saxonien" et du Thuringien. Extrait des Annales de la Societe Géologique du Nord CVI, 103-109.

Dudas, M.J., Harward, M.E., 1975. Weathering and authigenic halloysite in soil developed in Mazama ash. Soil Sci. Soc. Amer. Jour. 39, 561–566.

Durand, M., 2006. The problem of the transition from the Permian to the Triassic Series in southeastern France: comparison with other Peritethyan regions. Geological Society, London, Special Publications 265, 281–296. https://doi.org/10.1144/GSL.SP.2006.265.01.13

Durand, M., Bourquin, S., 2013. Criteria for the identification of ventifacts in the geological record: A review and new insights. Comptes Rendus Geoscience 345, 111–125. https://doi.org/10.1016/j.crte.2013.02.004

Echtler, H., Malavieille, J., 1990. Extensional tectonics, basement uplift and Stephano-Permian collapse basin in a late Variscan metamorphic core complex (Montagne Noire, Southern Massif Central). Tectonophysics, 177, 125–138.

Edel, J.B., Schulmann, K., Lexa, O., Diraison, M., Géraud, Y., 2015. Permian clockwise rotations of the Ebro and Corso-Sardinia blocks during Iberian-Armorican oroclinal bending: Preliminary paleomagnetic data from Catalan Coastal Range (NE Spain). Tectonophysics 657, 172-186.

Edel, J.B., Schulmann, K., Lexa, O., Lardeaux, J.M., 2018. Late Palaeozoic palaeomagnetic and tectonic constrains for amalgation of Pangea supercontinent in the European Variscan belt. Earth-Science Reviews 177, 589-612.

Ehrenberg, S.N., Aagaard, P., Wilson, M.J., Fraser, A.R., Duthie, D.M.L., 1993. Depth-dependent transformation of kaolinite to dickite in sandstones of the Norweigian continental shelf. Clay Minerals 325–352.

Ekart, D.D., Cerling, T.E., Montañez, I.P., Tabor, N.J., 1999. A 400 Million year carbon isotope record of pedogenic carbonate: Implications for paleoatmospheric carbon dioxide. American Journal of Science 299, 805–827.

Erwin, D.H., 1994. The Permo–Triassic extinction. Nature 367, 231–236. https://doi.org/10.1038/367231a0

Escudero-Mozo, M.J., Martín-Chivelet, J., Goy, A., López-Gómez, J., 2014. Middle-Upper Triassic carbonate platforms in Minorca (Balearic islands): Implications for Western Tethys correlations. Sedimentary Geology 310, 41–58.

FAO, 1998. World Reference Base for Soil Resources. Food and Agriculture Organization of the United Nations (FAO), International Society of Soil Science (ISSS), International Soil Reference and Information Centre (ISRIC), Vol. 84. World Soil Resources Reports, Rome, 84, 91 pp.

Faura, M., 1913. Síntesis estratigráfica de los terrenos primarios de la Cataluña, con una descripción de los yacimientos fosilíferos más principales. Memorias de la Real Sociedad Española de Historia Natural 9, 5-202.

Faura, M., 1914. Dictamen sobre las formaciones petrolíferas de San Juan de las Abadesas (Provincia de Gerona), que trata de explotar la "Compañía Española de Aceites de Esquisto, (S.A.)". Barcelona: Tip. A. Febrer. Pp. 12.

Fielding, C.R., Frank, T.D., Isbell, J.L., 2008. Resolving the Late Paleozoic Ice Age in Time and Space. Geological Society of America.

Fisher, M.J., Jeans, C.V., 1982. Clay mineral stratigraphy in the Permo-Triassic red bed sequences of BNOC 72/10-1A, Western Approaches, and the south Devon Coast. Clay Minerals 17, 79–89. https://doi.org/10.1180/claymin.1982.017.1.08

Fitzpatrick, E.A., 1980. Soils. Their formation, classification and distribution. Longman, London, UK.

Fortuny, J., Sellés, A.G., Valdiserri, D., Bolet, A., 2010. New tetrapod footprints from the Permian of the Pyrenees (Catalonia, Spain): preliminary results. Cidaris 30, 121–124.

Fortuny, J., Bolet, A., Sellés, A.G., Cartanyà, J., Galobart, À., 2011. New insights on the Permian and Triassic vertebrates from the Iberian Peninsula with emphasis on the Pyrenean and Catalonian basins. Journal of Iberian Geology 37, 65-86.

Franke, W., 2000. The mid-European segment of the Variscides: tectonostratigraphic units, terrane boundaries and plate tectonic evolution. In: Franke, W., Haak, V., Oncken, O., Tanner, D. (Eds.), Orogenic Processes: Quantification and Modelling in the Variscan Belt. Geological Society, London, Special Publications 179, 35–61.

Freytet, P., Plaziat, J.-C., 1982. Continental Carbonate Sedimentation and Pedogenesis - Late Cretaceous and Early Tertiary of Southern France. Schweizerbart Science Publishers, Stuttgart, Germany.

Gaggero, L., Oggiano, G., Buzzi, L., Slejko, F.F., Cortesogno, L., 2007. Post-variscan mafic dikes from the late orogenic collapse to the Tethyan rift: evidence from Sardinia. Ofioliti 32, 15–37.

Gaggero, L., Gretter, N., Langone, A., Ronchi, A., 2017. U–Pb geochronology and geochemistry of late Palaeozoic volcanism in Sardinia (southern Variscides). Geoscience Frontiers 8, 1263–1284.

Galán-Abellán, B., López-Gómez, J., Barrenechea, J.F., Marzo, M., De la Horra, R., Arche, A., 2013. The beginning of the Buntsandstein cycle (Early–Middle Triassic) in the Catalan Ranges, NE Spain: Sedimentary and palaeogeographic implications. Sedimentary Geology 296, 86–102. https://doi.org/10.1016/j.sedgeo.2013.08.006

Galé, C., 2005. Evolución geoquímica, petrogenética y de condiciones geodinámicas de los magmatismos pérmicos en los sectores central y occidental del Pirineo. Ph.D. thesis, Universidad de Zaragoza, Zaragoza, Spain.

Galtier, J., Broutin, J., 1995. La flore de la Zone de transition de l'Autunien supérieur de Lodève. Sciences Géologiques Bulletin Strasbourg 48, 83–93.

Gand, G., Galtier, J., Garric, J., Teboul, P-A., Pellenard, P., 2013. Discovery of an Autunian macroflora and lithostratigraphic re-investigation on the western border of the Lodève Permian basin (Mont Sénégra, Hérault, France). Paleoenvironmental implications. Comptes Rendus Palevol 12, 69–79.

Gandin, A., Tongiorgi, M., Rau, A., Virgili, C., 1982. Some examples of the Middle-Triassic Marine transgression in South-Western Mediterranean Europe. Geologische Rundschau 71, 881–894. https://doi.org/10.1007/BF01821109

García-Senz, J., Ramirez-Merino, J., Navarro-Juli, J.J., Rodríguez-Santiesteban, R., Castaño, R.M., Leyva, F., Garcia-Sansegundo, J., Ramirez Del Pozo, J., 2009a. Memoria Explicativa de la Hoja 213 (Pont de Suert). Institutio Geológico y Minero de España (IGME), Madrid, Spain.

García-Senz, J., Ramirez-Merino, J., Navarro-Juli, J.J., Rodríguez-Santiesteban, R., Castaño, R.M., Leyva, F., Garcia-Sansegundo, J., Ramirez Del Pozo, J., 2009b. Hoja 213 (Pont de Suert) del Mapa Geológico de España a Escala 1:50000.

Garrido-Megías, A. (1973): Estudio geológico y relación entre tectónica y sedimentación del Secundario y Terciario de lavertiente meridional pirenaica en su zona central (Provincias de Huesca y Lérida). Tesis Doctoral Universidad Granada, 395p.

Gascón-Cuello, F., Gisbert, J., 1987. La evolución climática del Stephaniense, Pérmico y Buntsandstein del Pirineo catalán en base al estudio de paleosuelos. Cuadernos de Geología Ibérica 11, 97–114.

Gastaldo, R.A., Knight, C.L., Neveling, J., Tabor, N.J., 2014. Latest Permian paleosols from Wapadsberg Pass, South Africa: Implications for Changhsingian climate. Geological Society of America Bulletin 126, 665–679.

Ghazi, S., Mountney, N.P., 2009. Facies and architectural element analysis of a meandering fluvial succession: The Permian Warchha Sandstone, Salt Range, Pakistan. Sedimentary Geology 221, 99–126.

Ghosh, N., Basu, A.R., Bhargava, O.N., Shukla, U.K., Ghatak, A., Garzione, C.N., Ahluwalia, A.D., 2016. Catastrophic environmental transition at the Permian-Triassic Neo-Tethyan margin of Gondwanaland: Geochemical, isotopic and sedimentological evidence in the Spiti Valley, India. Gondwana Research 34, 324–345. https://doi.org/10.1016/j.gr.2015.04.006

Gisbert, J., 1981. Estudio geológico–petrológico del Stephaniense-Pérmico de la sierra del Cadí. Diagénesis y Sedimentología. Ph.D. thesis, Universidad de Zaragoza, Zaragoza, Spain.

Gisbert, J., 1983. El Pémico de los Pirineos españoles, in: Martínez-Díaz, C. (Ed.), Carbonífero y Pérmico de España. Publicaciones del Instituto Geológico y Minero de España, pp. 405–420.

Glennie, K.W., 1990. Rotliegend sediment distribution: a result of late Carboniferous movements. In: Hardman, R.F.P., Brooks, J. (Eds), Tectonic Events Responsible for Britain's Oil and Gas Reserves. Geological Society, London, Special Publications 55, 127–138.

Godin, P., 1991. Finning-upward cycles in the sandy-braided river deposits of the Westwater Canyon Member (Upper Jurassic, Morrison Formation, New Mexico. Sedimentary Geology 70, 61-82.

Golubtsov, V.A., Cherkashina, A.A., Pustovoytov, K.E., Stahr, K., 2014. Stable carbon and oxygen isotopes in pedogenic carbonate coatings of chernozems in the Southern Cis-Baikalia as indicators of local environmental changes. Eurasian Soil Sc. 47, 1015–1026. https://doi.org/10.1134/S1064229314100032

Gómez-Alba, J., 2007. La cuenca carbonífera de Surroca–Ogassa (Ripollès, Cataluña, España). Historia económica, minera y geológica y catálogo de la flora carbonífera catalana del Museu de Ciències Naturals de Barcelona. Monografies del Museu de Ciències Naturals 4, 1–263.

Gorbachev, B.F., 1977. Comparative stability and formation conditions of kaolinite and halloysite. Lithology Min- Resour. 12, 700–707.

Gretter, N., Ronchi, A., López-Gómez, J., Arche, A., De la Horra, R., Barrenechea, J., Lago, M., 2015. The Late Palaeozoic-Early Mesozoic from the Catalan Pyrenees (Spain): 60Myr of environmental evolution in the frame of the western peri-Tethyan palaeogeography. Earth-Science Reviews 150, 679–708.

Gulbranson, E.L., Montañez, I.P., Tabor, N.J., Limarino, C.O., 2015. Late Pennsylvanian aridification on the southwestern margin of Gondwana (Paganzo Basin, NW Argentina): A regional expression of a global climate perturbation. Palaeogeography, Palaeoclimatology, Palaeoecology 417, 220–235.

Hacquebard, P.A., and Donaldson, J.R., 1969. Carboniferous coal deposition associated with flood-plain and limmic environments in Nova Scotia. In: Dapples, E.C., Hopkins, M.E. (Eds), Environments of Coal Deposition. Geological Society of America Special Papers 114, pp. 143-191.

Harris, N.B., Freeman, K.H., Pancost, R.D., White, T.S., Mitchell, G.D., 2004. The character and origin of lacustrine source rocks in the Lower Cretaceous synrift section, Congo Basin, west Africa. American Association of Petroleum Geologists Bulletin 88, 1163–1184.

Hart, R.D., Gilkes, R.J., Siradz, S., Singh, B., 2002. The nature of soil kaolins from Indonesia and Western Australia. Clays Clay Minerals 50, 198–207.

Hartevelt, J.J.A., 1970. Geology of the upper Segre and Valira valleys, Central Pyrenees, Andorra, Spain. Leidse Geologische Mededelingen 45, 167–236.

Heilbronn, G., Boulvais, P., Marchand, E., Robin, C., Bourquin, S., Barrier, L., Jia, Y., Fu, B., Jolivet, M., 2015. Stable isotope characterization of pedogenic and lacustrine carbonates from the Chinese Tian Shan: Constraints on the Mesozoic–Lower Cenozoic palaeoenvironmental evolution. Chemie der Erde - Geochemistry 75, 133–141. https://doi.org/10.1016/j.chemer.2014.11.004.

Hendy, C.H., 1971. The isotopic geochemistry of speleothems-I: The calculations of the effects of different modes of formation on the isotopic composition of speleothems and their applicability as paleoclimate indicators: Geochimica et Cosmochimica Acta, v. 35, p. 801–824.

Henk, A., 1992. Michtigkeit und Alter der erodierten Sedimente im Saar-Nahe-Becken (SW-Deutschland). Geol Rundsch 81: 323- 331

Henk, A., 1993. Subsidenz und tektonik des Saar-Nahe-Beckens (SW-Deutschland). Geologische Rundschau 82, 3–19. https://doi.org/10.1007/BF00563266

Hoey, T.B., 1992. Temporal variations in bedload transport rates and sediment storage in gravel-bed rivers. Progress in Physical Geography 16, 319-338.

Hong, H., Zhang, N., Zhaohui, L., Xue, H., Xia, W., Yu, N., 2008. Clay mineralogy across the P-T Boundary of the Xiakou section, China: evidence of clay provenance and environment. Clays and Clay Minerals 56, 131–143. https://doi.org/info:doi/10.1346/CCMN.2008.0560201

Hopkins, J.C., 1985. Channel-fill deposits formed by aggradation in deeply scoure, superimposed distributaries of the Lower Kootenai Formation. Journal of Sedimentary Petrology 55, 42-52.

Hsieh, F.Y., Bloch, D. A., and Larsen, M.D., 1998. A simple method of sample size calculation for linear and logistic regression. Statistics in Medicine, 17, 1623-1634.

Hyland, E.G., Sheldon, N.D., 2016. Examining the spatial consistency of palaeosol proxies: Implications for palaeoclimatic and palaeoenvironmental reconstructions in terrestrial sedimentary basins. Sedimentology 63, 959–971. https://doi.org/10.1111/sed.12245

Ingles, M., Anadon, P., 1991. Relationship of clay minerals to depositional environment in the non-marine Eocene Pontils Group, SE Ebro Basin (Spain). Journal of Sedimentary Research 61, 926–939. https://doi.org/10.1306/D426780C-2B26-11D7-8648000102C1865D

Isozaki, Y., Aljinović, D., 2009. End-Guadalupian extinction of the Permian gigantic bivalve Alatoconchidae: End of gigantism in tropical seas by cooling. Palaeogeography, Palaeoclimatology, Palaeoecology, Extinction, dwarfing and the Lilliput effect 284, 11–21. https://doi.org/10.1016/j.palaeo.2009.08.022

Isozaki, Y., Aljinović, D., Kawahata, H., 2011. The Guadalupian (Permian) Kamura event in European Tethys. Palaeogeography, Palaeoclimatology, Palaeoecology 308, 12–21. https://doi.org/10.1016/j.palaeo.2010.09.034

Izquierdo-Llavall, E., Casas-Sainz, A., Oliva-Urcia, B., Scholger, R., 2014. Palaeomagnetism and magnetic fabrics of the Late Palaeozoic volcanism in the Castejón-Laspaúles basin (Central Pyrenees). Implications for palaeoflow directions and basin configuration. Geological Magazine 151, 777–797. https://doi.org/10.1017/S0016756813000769

Izquierdo-Llavall, E., Casas-Sainz, A.M., Oliva-Urcia, B., 2013. Heterogeneous deformation recorded by magnetic fabrics in the Pyrenean Axial Zone. Journal of Structural Geology 57, 97–113. https://doi.org/10.1016/j.jsg.2013.10.005

Janaway, T.M., Parnel, J., 1989. Carbonate production within the Orcadian basin, northern Scotland: a petrographic and geochemical study. Palaeogeography, Palaeoclimatology, Palaeoecology 70, 89-105.

Jiang, W.-T., Peacor, D.R., Árkai, P., Tóth, M., Kim, J.W., 1997. TEM and XRD determination of crystallite size and lattice strain as a function of illite crystallinity in pelitic rocks. Journal of Metamorphic Geology 15, 267–281. https://doi.org/10.1111/j.1525-1314.1997.00016.x

Johnston, S.T., Gutierrez-Alonso, G., 2010. The North American Cordillera and West European Variscides: Contrasting interpretations of similar mountain systems. Gondwana Research 17, 516–525.

Jongmans, W.J., 1951. Las floras carboníferas de España. Estudios Geológicos 7, 281-330.

Jost, A.B., Mundil, R., He, B., Brown, S.T., Altiner, D., Sun, Y., DePaolo, D.J., Payne, J.L., 2014. Constraining the cause of the end-Guadalupian extinction with coupled records of carbon and calcium isotopes. Earth and Planetary Science Letters 396, 201–212. https://doi.org/10.1016/j.epsl.2014.04.014

Juncal, M., Diez, J.B., de la Horra, R., Galán-Abellán, B., Borruel-Abadía, V., Barrenechea, J.F., Arche, A., López-Gómez, J., 2018. Palynostratigraphy of the Middle Triassic (Anisian) Eslida Formation, SE Iberian Ranges, Spain. Palynology 42, 149–157. https://doi.org/10.1080/01916122.2017.1310766

Juncal, M.A., Lloret, J., Diez, J.B., López-Gómez, J., Ronchi, A., De la Horra, R., Barrenechea, J.F., Arche, A., 2019. New Upper Carboniferous palynofloras from Southern Pyrenees (NE Spain): Implications for palynological zonation of Western Europe. Palaeogeography, Palaeoclimatology, Palaeoecology 516, 307–321. https://doi.org/10.1016/j.palaeo.2018.12.010

Keller, W.D., 1970. Environmental Aspects of Clay Minerals. SEPM Journal of Sedimentary Research Vol. 40. https://doi.org/10.1306/74D720A4-2B21-11D7-8648000102C1865D

Kerp, H., Fichter, J., 1985. Die Makrofloren des saarpfälzischen Rotliegenden (?Ober-Karbon-Unter-Perm; SW-Deutschland) Mainzer Geowissenschaften Mitteilungen 14, 159–286.

Kerp, H., 1996. Post-Variscan Late Palaeozoic Northern Hemisphere gymnosperms: the onset to the Mesozoic. Rev. Palaeobot. Palynol. 90, 263–285.

Kindle, E.M., 1917. Recent and fossil ripple marks. Musuem Bull. Cam. Geol. Surv. 25, 1–56.

Kirkham, D., and W. L Powers, 1972. Advanced Soil Physics. New York, NY: Wiley-Interscience. xvii + pp. 534.

Knoll, A.H., Bambach, R.K., Payne, J.L., Pruss, S., Fischer, W.W., 2007. Paleophysiology and end-Permian mass extinction. Earth and Planetary Science Letters 256, 295–313. https://doi.org/10.1016/j.epsl.2007.02.018

Kolasinski, J., Rogers, K., Frouin, P., 2008. Effects of acidification on carbon and nitrogen stable isotopes of benthic macrofauna from a tropical coral reef. Rapid Commun. Mass Spectrom. 22, 2955–2960. https://doi.org/10.1002/rcm.3694

Körner, F., Schneider, J.W., Hoernes, S., Gand, G., Kleeberg, R., 2003. Climate and continental sedimentation in the Permian of the Lodève Basin (Southern France). Boll. Soc. Geol. It. Volume speciale n. 2, 185–191.

Kraus, M.J., 1999. Paleosols in clastic sedimentary rocks: their geologic applications. Earth-Science Reviews 47, 41–70. https://doi.org/10.1016/S0012-8252(99)00026-4

Krull, E.S., Retallack, G.J., 2000. δ13C depth profiles from paleosols across the Permian-Triassic boundary: Evidence for methane release. GSA Bulletin 112, 1459–1472. https://doi.org/10.1130/0016-7606(2000)112<1459:CDPFPA>2.0.CO;2

Kürschner W.M., Waldemaar Herngreen G.F., 2010. Triassic palynology of central and northwestern Europe: a review of palynofloral diversity patterns and biostratigraphic subdivisions. Geological Society, London, Special Publications 2010, 334, 263-283.

Kustatscher E., Manfrin S., Mietto P., Posenato R., Roghi G., 2006. New biostratigraphic data on Anisian (Middle Triassic) palynomorphs from the Dolomites, Italy. Review of Palaeobotany and Palynology 140, 79-90.

Kustatscher E., Roghi G., 2006. Anisian palynomorphs from the Dont Formation of the Kühwiesenkopf/Monte Prà Della Vacca Section (Northern Italy). Micropaleontology 52 (3), 223-244.

Lago, M., Arranz, E., Pocoví, A., Galé, C., Gil-Imaz, A., 2004. Permian magmatism and basin dynamics in the southern Pyrenees: a record of the transition from late Variscan transtension to early Alpine extension. In: Wilson, M., Neumann, E.-R., Davies, G.R., Timmerman, M.J., Heeremans, M., Larsen, B.T. (Eds.), Permo-Carboniferous Magmatism and Rifting in Europe. Geological Society, London, Special Publications 223, pp. 439–464.

Lambiase, J.J., 1990. A model for tectonic control of lacustrine stratigraphic sequences in continental rift basins. In: Katz, B.J. (Ed.), Lacustrine Exploration: Case Studies and Modern Analogues. American Association of Petroleum Geologists, Canada, Memoir 50, pp. 265–276.

Langford, R.P., Chan, M.A., 1989. Fluvial-aeolian interactions: Part II, ancient systems. (Sedimentology). 36, 1037–1051.

Lefournier, J., 1980. Dépôts de pré-ouverture de l'Atlantique Sud. Comparaison avec la sédimentation actuelle dans la branche occidentale des Rifts Est-Africain. Recherche géologique en Afrique 5, 127–130.

Lemoigne, Y., Doubinger, J., 1984. Réflexion sur la coexistence de flores hygrophile, mésophile et mésoxérophile durant le Paléozoïque Supérieur en Euramérie. Geobios 17, 365–369.

Li, G., Wang, Y., Shi, G.R., Liao, W., Yu, L., 2016. Fluctuations of redox conditions across the Permian–Triassic boundary—New evidence from the GSSP section in Meishan of South China. Palaeogeography, Palaeoclimatology, Palaeoecology 448, 48–58. https://doi.org/10.1016/j.palaeo.2015.09.050

Lindgreen, H., Surlyk, F., 2000. Upper Permian–Lower Cretaceous clay mineralogy of East Greenland: provenance, paleoclimate and volcanicity. Clay Minerals 35, 791–806.

Linol, B., Bercovici, A., Bourquin, S., Diez, J.B., López-Gómez, J., Broutin, J., Durand, M., Villanueva-Amadoz, U., 2009. Late Permian to Middle Triassic correlations and palaeogeographical reconstructions in south-western European basins: New sedimentological data from Minorca (Balearic Islands, Spain). Sedimentary Geology 220, 77–94. https://doi.org/10.1016/j.sedgeo.2009.06.003

Lloret, J., Juncal, M., 2018. Primeros datos palinológicos del Carbonífero superior en el Pirineo Oriental (Argestues, Lleida, España). Geogaceta 64, 91–94.

Lloret, J., Ronchi, A., López-Gómez, J., Gretter, N., De la Horra, R., Barrenechea, J.F., Arche, A., 2018. Syn-tectonic sedimentary evolution of the continental late Palaeozoic-early Mesozoic Erill Castell-Estac Basin and its significance in the development of the central Pyrenees Basin. Sedimentary Geology 374, 134–157. https://doi.org/10.1016/j.sedgeo.2018.07.014

Looy, C.V., Kerp, H., Duijnstee, I.A.P., DiMichele, W.A., 2014. The Late Paleozoic ecological-evolutionary laboratory, a land-plant fossil record perspective. The Sedimentary Record 12, 4–10.

López-Gómez, J., Arche, A., Pérez-López, A., 2002. Permian and Triassic. In: Gibbons, W., Moreno, T. (Eds.), The Geology of Spain. Geological Society, London, pp. 185–212.

López-Gómez, J., Martín-González, F., Heredia, N., de la Horra, R., Barrenechea, J.F., Cadenas, P., Juncal, M., Diez, J.B., Borruel-Abadía, V., Pedreira, D., García-

Sansegundo, J., Farias, P., Galé, C., Lago, M., Ubide, T., Fernández-Viejo, G., Gand, G., 2019. New lithostratigraphy for the Cantabrian Mountains: A common tectono-stratigraphic evolution for the onset of the Alpine cycle in the W Pyrenean realm, N Spain. Earth-Science Reviews 188, 249–271. https://doi.org/10.1016/j.earscirev.2018.11.008

Maaleki-Moghadam, M., Rafiei, B., Richoz, S., Woods, A.D., Krystyn, L., 2019. Anachronistic facies and carbon isotopes during the end-Permian biocrisis: Evidence from the mid-Tethys (Kisejin, Iran). Palaeogeography, Palaeoclimatology, Palaeoecology 516, 364–383. https://doi.org/10.1016/j.palaeo.2018.12.007

Machette, M.N., 1985. Calcic soils of the southwestern United States, in: Geological Society of America Special Papers. Geological Society of America, pp. 1–22. https://doi.org/10.1130/SPE203-p1

Marfil, R., La Iglesia, A., Herrero, M.J., Scherer, M., Delgado, A., 2015. Clay mineral occurrence and burial transformations: reservoir potential of the Permo-Triassic sediments of the Iberian Range. Basin Research 27, 295–309. https://doi.org/10.1111/bre.12074

Marocchi, M., Morelli, C., Mair, V., Klotzli, U., Bargossi, G.M., 2008. Evolution of large silicic magma systems: remarks new U-Pb zircon data on the NW Permian Athesian Volcanic Group (Southern Alps, Italy). The Journal of Geology 116, 480–498.

Marriott, S.B., Wright, V.P., 1993. Paleosols as indicators of geomorphic stability in two Old Red Sandstone alluvial suites, South Wales. J. Geol. Soc. London 150, 1109–1120.

Martí, J., 1986. El vulcanisme explosiu del tardihercinià del Pirineu Català. Ph.D. thesis, Universitat de Barcelona, Barcelona, Spain.

Martí, J., Mitjavilla , J.M., 1988. El volcanismo tardihercínico del Pirineo catalán, II: caracterización de la actividad explosiva. Acta geológica hispánica 23, 21–32.

Martí, J., 1996. Genesis of crystal-rich volcaniclastic facies in the Permian red beds of the Central Pyrenees (NE Spain). Sedimentary Geology 106, 1–19.

Martín-Closas, C., Galtier, J., 2005. Plant taphonomy and paleoecology of Late Pennsylvanian intramontane wetlands in the Graissessac-Lodève basin (Languedoc, France). PALAIOS 20, 249–265.

Martín-Closas, C., Martínez-Roig, D., 2007. Plant taphonomy and palaeoecology of Stephanian limnic wetlands in the eastern Pyrenees (Catalonia, Spain). Comptes Rendus Palevol 6, 437–449.

Matte, P., 1986. Tectonics and plate tectonics model for the Variscan belt of Europe. Tectonophysics 126, 329–374.

Matte, P., 2001. The Variscan collage and orogeny (480–290 Ma) and the tectonic definition of the Armorica microplate: a review. Terra Nova 13, 122–128.

Maynard, J.R., Hofmann, W., Dunay, R.E., Benthan, P.N., Dean, K.P., Watson, I., 1997. The Carboniferous of Western Europe; the development of a petroleum system. Petroleum Geoscience 3, 97–115.

McCann, T., Pascal, C., Timmerman, M.J., Krzywiec, P., López-Gómez, J., Wetzel, L., Krawczyk, C.M., Rieke, H., Lamarche, J., 2006. Post-Variscan (end Carboniferous-Early Permian) basin evolution in Western and Central Europe. In: Gee, D.G., Stephenson, R.A. (Eds.), European Lithosphere Dynamics. Geological Society, London, Memoirs 32, pp. 355–388.

Ménard, G., Molnar, P., 1988. Collapse of a Hercynian Tibetan Plateau into a late Palaeozoic European Basin and Range province. Nature 334, 235-237.

Menéndez-Amor, J., 1952. Algunas plantas fósiles permianas de la provincia de Lérida. Notas y Comunicaciones Instituto Geológico y Minero de España 28, 117–123.

Merino-Tomé, O., Gutiérrez-Alonso, G., Villa, E., Fernández-Suárez, J., Llaneza, J.M., Hofmann, M., 2017. LA-ICP-MS U-Pb dating of Carboniferous ash layers in the Cantabrian Zone (N Spain): stratigraphic implications. Journal of the Geological Society 174, 836–849. https://doi.org/10.1144/jgs2016-119

Mey, P.H.W., Nagtegaal, P.J.C., Roberti, K.J., Hartevelt, J.J., 1968. Lithostratigraphic subdivision of post-Variscan deposits in the South-Central Pyrenees, Spain. Leidse Geologische Mededelingen 41, 221–228.

Miall, A., 1996. The Geology of Fluvial Deposits - Sedimentary Facies, Basin, 1st ed. Springer-Verlag, Berlin, Heidelberg.

Miall, A., 2014. Fluvial Depositional Systems, 1st ed. Springer Geology. Springer International Publishing, Switzerland.

Michel, L.A., Tabor, N.J., Montañez, I.P., Schmitz, M.D., Davydov, V.I., 2015. Chronostratigraphy and Paleoclimatology of the Lodève Basin, France: Evidence for a pan-tropical aridification event across the Carboniferous–Permian boundary. Palaeogeography, Palaeoclimatology, Palaeoecology 430, 118–131.

Mii, H., Grossman, E.L., Yancey, T.E., 1997. Stable carbon and oxygen isotope shifts in Permian seas of West Spitsbergen-Global change or diagenetic artifact? Geology 25, 227–230. https://doi.org/10.1130/0091-7613(1997)025<0227:SCAOIS>2.3.CO;2

Morelli, A., Bruno, L., Cleveland, D.M., Drexler, T.M., Amorosi, A., 2017. Reconstructing Last Glacial Maximum and Younger Dryas paleolandscapes through subsurface paleosol stratigraphy: An example from the Po coastal plain, Italy. Geomorphology 295, 790–800. https://doi.org/10.1016/j.geomorph.2017.08.013

Mortazavi, M., Moussavi-Harami, R., Brenner, R.L., Mahboubi, A., Nadjafi, M., 2013. Stable isotope record in pedogenic carbonates in northeast Iran: Implications for Early Cretaceous (Berriasian–Barremian) paleovegetation and paleoatmospheric P(CO2) levels. Geoderma 211–212, 85–97. https://doi.org/10.1016/j.geoderma.2013.07.008

Mujal, E., Fortuny, J., Oms, O., Bolet, A., Galobart, À., Anadón, P., 2016a. Palaeoenvironmental reconstruction and early Permian ichnoassemblage from the NE Iberian Peninsula (Pyrenean Basin). Geological Magazine 153, 578–600.

Mujal, E., Gretter, N., Ronchi, A., López-Gómez, J., Falconnet, J., Diez, J.B., De la Horra, R., Bolet, A., Oms, O., Arche, A., Barrenechea, J.F., Steyer, J.-S., Fortuny, J., 2016b. Constraining the Permian/Triassic transition in continental environments: Stratigraphic and paleontological record from the Catalan Pyrenees (NE Iberian Peninsula). Palaeogeography, Palaeoclimatology, Palaeoecology 445, 18–37.

Mujal, E., Fortuny, J., Bolet, A., Oms, O., López, J.Á., 2017a. An archosauromorph dominated ichnoassemblage in fluvial settings from the late Early Triassic of the Catalan Pyrenees (NE Iberian Peninsula). PLOS ONE 12 (4), e0174693, https://doi.org/10.1371/journal.pone.0174693.

Mujal, E., Fortuny, J., Pérez-Cano, J., Dinarès-Turell, J., Ibáñez-Insa, J., Oms, O., Vila, I., Bolet, A., Anadón, P., 2017b. Integrated multi-stratigraphic study of the Coll de Terrers late Permian–Early Triassic continental succession from the Catalan Pyrenees (NE Iberian Peninsula): A geologic reference record for equatorial Pangaea. Global and Planetary Change 159, 46–60.

Mujal, E., Fortuny, J., Marmi, J., Dinarès-Turell, J., Bolet, A., Oms, O., 2018. Aridification across the Carboniferous-Permian transition in central equatorial Pangea: The Catalan Pyrenees succession (NE Iberian Peninsula). Sedimentary Geology 363, 48-68.

Müller, R., Nystuen, J.P., Wright, V.P., 2004. Pedogenic Mud Aggregates and Paleosol Development in Ancient Dryland River Systems: Criteria for Interpreting Alluvial Mudrock Origin and Floodplain Dynamics. Journal of Sedimentary Research 74, 537–551. https://doi.org/10.1306/010704740537

Muñoz, J.A., 1992. Evolution of a continental collision belt: ECORS-Pyrenees crustal balanced cross-section. In: McClay, K.R. (Ed.), Thrust Tectonics. Springer Netherlands, pp. 235-246.

Munsell, A.H., 1905. A Color Notation. G. H. Ellis Company, Harvard, USA.

Muttoni, G., Gaetani, M., Kent, D.V., Sciunnach, D., Angiolini, L., Berra, F., Garzanti, E., Mattei, M., Zanchi, A., 2009. Opening of the Neo-Tethys Ocean and the Pangea B to Pangea A transformation during the Permian 14, 17–48. https://doi.org/10.7916/D8SF2TXF

Nagtegaal, P.J.C., 1969. Sedimentology, paleoclimatology, and diagenesis of Post- Hercynian continental deposits in the south-central Pyrenees, Spain. Leidse Geologische Mededelingen 42, 143–238.

Neumann, E.-R., Wilson, M., Heeremans, M., Spencer, E.A., Obst, K., Timmerman, M.J., Kirstein, L., 2004. Carboniferous-Permian rifting and magmatism in southern Scandinavia, the North Sea and northern Germany: a review. In: Wilson, M., Neumann, E.-R., Davies, G.R., Timmerman, M.J., Heeremans, M., Larsen, B.T. (Eds.),

Permo-Carboniferous Magmatism and Rifting in Europe. Geological Society, London, Special Publications 223, pp. 11–40.

Nevin, C.M., Trainer, D.W., 1927. Laboratory Study in Delta-building. Geological Society of America Bulletin 38, 451–458. https://doi.org/10.1130/GSAB-38-451

Newell, A.J., Benton, M.J., Kearsey, T., Taylor, G., Twitchett, R.J., Tverdokhlebov, V.P., 2012. Calcretes, fluviolacustrine sediments and subsidence patterns in Permo-Triassic salt-walled minibasins of the south Urals, Russia. Sedimentology 59, 1659–1676. https://doi.org/10.1111/j.1365-3091.2012.01320.x

North, C.P., Davidson, S.K., 2012. Unconfined alluvial flow processes: Recognition and interpretation of their deposits, and the significance for palaeogeographic reconstruction. Earth-Science Reviews 111, 199–223.

Orłowska-Zwolińska, T., 1984. Palynostratigraphy of the buntsandstein of Western Poland. Acta Palaeontologica Polonica 29 (3-4), 161-194.

Orłowska-Zwolińska, T., 1985. Palynological zones of the Polish epicontinental Triassic. Bulletin of the Polish Academy of Science, Earth Sciences 33 (3-4), 107-117.

Owen, A., Ebinghaus, A., Hartley, A.J., Santos, M.G.M., Weissmann, G.S., 2017. Multi-scale classification of fluvial architecture: An example from the Palaeocene-Eocene Bighorn Basin, Wyoming. Sedimentology 64, 1572–1596.

Paquette, Y., Doubinger, J., Courel, L., 1980. Étude palynologique de la couche du toit du bassin autunien de l'Aumance (Assise de Buxières); liaison avec des milieux sédimentaires. Bulletin de la Société d'histoire Naturelle d'Autun 95, 85-101.

Parham, W.E., 1969. Formation of halloysite from feldspar: Low temperature, artificial weathering versus natural weathering. Clays and Clay Minerals 17, 1322. https://doi.org/10.1346/CCMN.1969.0170104

Pellenard, P., Gand, G., Schmitz, M., Galtier, J., Broutin, J., Stéyer, J-S., 2017. High-precision U-Pb zircon ages for explosive volcanism calibrating the NW European continental Autunian stratotype. Gondwana Research 51, 118-136.

Pereira, M.F., Castro, A., Chichorro, M., Fernández, C., Díaz-Alvarado, J., Martí, J., Rodríguez, C., 2014. Chronological link between deep-seated processes in magma chambers and eruptions: Permo-Carboniferous magmatism in the core of Pangaea (Southern Pyrenees). Gondwana Research 25, 290–308.

Platt, N.H., 1989. Lacustrine carbonates and pedogenesis: sedimentology and origin of palustrine deposits from the Early Cretaceous Rupelo Formation, W Cameros Basin, N Spain. Sedimentology 36, 665–684. https://doi.org/10.1111/j.1365-3091.1989.tb02092.x

Platt, N.H., Keller, B., 1992. Distal alluvial deposits in a foreland basin setting—the Lower Freshwater Miocene), Switzerland: sedimentology, architecture and palaeosols. Sedimentology 39, 545–565.

Poblet, J., 1991. Estructura hercínica i alpina del vessant sud de la zona axial del Pirineu Central. Ph.D. thesis, Universitat de Barcelona, Barcelona, Spain.

Puigdefàbregas, C., Souquet, P., 1986. Tecto-sedimentary cycles and depositional sequences of the Mesozoic and Tertiary from the Pyrenees. Tectonophysics, The Geological Evolution of the Pyrenees 129, 173–203. https://doi.org/10.1016/0040-1951(86)90251-9

Ramos, A., Sopena, A., Perez-Arlucea, M., 1986. Evolution of Buntsandstein Fluvial Sedimentation in the Northwest Iberian Ranges (Central Spain). Journal of Sedimentary Research 56, 862-875.

Reinhardt, J., Wayne, R.S., 1988. Paleosols and Weathering Through Geologic Time: Principles and Applications, Geological Society of America Special Papers. Geological Society of America. https://doi.org/10.1130/SPE216

Retallack, G.J., 1984. Completeness of the rock and fossil recor: some estimates unsing fossil soils. Paleobiology 10, 59–78.

Retallack, G.J., 1988. Field recognition of paleosols, in: Geological Society of America Special Papers. Geological Society of America, pp. 1–20. https://doi.org/10.1130/SPE216-p1

Retallack, G.J., 1994. A pedotype approach to latest Cretaceous and earliest Tertiary paleosols in eastern Montana. GSA Bulletin 106, 1377–1397. https://doi.org/10.1130/0016-7606(1994)106<1377:APATLC>2.3.CO;2

Retallack, G.J., 1995. Permian-Triassic Life Crisis on Land. Science 267, 77–80. https://doi.org/10.1126/science.267.5194.77

Retallack, G.J., Veevers, J.J., Morante, R., 1996. Global coal gap between Permian-Triassic extinction and Middle Triassic recovery of peat-forming plants. Bulletin of the Geological Society of America 108, 195–207. https://doi.org/10.1130/0016-7606(1996)108<0195:GCGBPT>2.3.CO;2

Retallack, G.J., 1997. A color guide to paleosols. John Wiley & Sons, Chichaster, UK.

Retallack, G.J., 2001. Soils of the Past, Second. ed. Blackwell Publishing Ltd., Oxford.

Retallack, G.J., Jahren, A.H., Sheldon, N.D., Chakrabarti, R., Metzger, C.A., Smith, R.M.H., 2005. The Permian–Triassic boundary in Antarctica. Antarctic Science 17, 241–258. https://doi.org/10.1017/S0954102005002658

Retallack, G.J., Metzger, C.A., Greaver, T., Jahren, A.H., Smith, R.M.H., Sheldon, N.D., 2006. Middle-Late Permian mass extinction on land. Geological Society of America Bulletin 118, 1398–1411. https://doi.org/10.1130/B26011.1

Retallack, G.J., 2013. Permian and Triassic greenhouse crises. Gondwana Research 24, 90–103. https://doi.org/10.1016/j.gr.2012.03.003

Rey, P., 1993. Seismic and tectono-metamorphic characters of the lower continental crust in Phanerozoic areas: A consequence of post-thickening extension. Tectonics 12, 580–590.

Richard, Z.D., Pollard, D., Kump, L.R., White, T.S., 2018. Anomalously low δ18O values of high-latitude Permo-Triassic paleosol siderite. Palaeogeography, Palaeoclimatology, Palaeoecology 492, 26–40. https://doi.org/10.1016/j.palaeo.2017.11.062

Robles, S., Llompart, C., 1987. Analisis paleogeográfico y consideraciones paleoicnologicas del Pérmico Superior y Triasico Inferior en la transversal del rio Sebre (Alt Urgell, Pirineo de Lérida). Cuadernos Geología Ibérica 11, 115–130.

Rodríguez-Méndez, L., Cuevas, J., Tubía, J.M., 2016. Post-Variscan basin evolution in the central Pyrenees: Insights from the Stephanian–Permian Anayet Basin. Comptes Rendus Geoscience 348, 333–341.

Roger, P., 1965. Etude stratigraphique et struturale de la zona des Nogueras entre l'Esera et l'Isabena (Huesca-Espagne). Actes de la Société linnéenne de Bordeaux 102, 3–27.

Roghi G., 1995. Analisi palinologica del Trias medio del Sudalpino. Tesi di dottorato di Ricerca in Scienze della Terra. Università degli Studi di Padova, Italia, pp. 121. Unpublished.

Ronchi, A., Saria, E., Broutin, J., 2008. The "Autuniano Sardo": basic features for a correlation through the Western Mediterranean and Paleoeurope. Bollettino della Società Geologica Italiana 127, 655–681.

Ronchi, A., Lloret, J., Gretter, N., López-Gómez, J., De, la H., Barrenechea, J., Arche, A., Diez, J.B., 2018. Comment on "Integrated multi-stratigraphic study of the Coll de Terrers late Permian–Early Triassic continental succession from the Catalan Pyrenees (NE Iberian Peninsula): A geologic reference record for equatorial Pangaea" by Eudald Mujal, Josep Fortuny, Jordi Pérez-Canoa, Jaume Dinarès-Turell, Jordi Ibáñez-Insa, Oriol Oms, Isabel Vila, Arnau Bolet, Pere Anadón. Global and Planetary Change 159 (2017) 46–60. Global and Planetary Change. https://doi.org/10.1016/j.gloplacha.2018.06.010

Roscher, M., Schneider, J.W., 2006. Permo-Carboniferous climate: Early Pennsylvanian to Late Permian climate development of central Europe in a regional and global context. Geological Society, London, Special Publications 265, 95–136. https://doi.org/10.1144/GSL.SP.2006.265.01.05

Royer, D.L., 1999. Depth to pedogenic carbonate horizon as a paleoprecipitation indicator? Geology 27, 1123. https://doi.org/10.1130/0091-7613(1999)027<1123:DTPCHA>2.3.CO;2

Rust, B.R., Gibling, M.R., Legun, A.S., 1985. Coal Deposition in an Anastomosing-Fluvial System: The Pennsylvanian Cumberland Group South of Joggins, Nova Scotia, Canada. In: Rahmani, R.A., Flores, R.M. (Eds.), Sedimentology of Coal and Coal-Bearing Sequences. Blackwell Publishing Ltd., Oxford, UK, pp. 105–120.

Sahney, S., Benton, M.J., Falcon-Lang, H.J., 2010. Rainforest collapse triggered Carboniferous tetrapod diversification in Euramerica. Geology 38, 1079–1082.

Salas, R., Casas, A., 1993. Mesozoic extensional tectonics, stratigrapy and crustal evolution during the Alpine cycle of the eastern Iberian basin. Tectonophysics 228, 33-55.

Sambrook Smith, G.H., Best, J.L., Leroy, J.Z., Orfeo, O., 2016. The alluvial architecture of a suspended sediment dominated meandering river: the Río Bermejo, Argentina. Sedimentology 63, 1187–1208. https://doi.org/10.1111/sed.12256

Saura, E., 2004. Anàlisis estructural de la zona de les Nogueres Pirineus Centrals. Ph.D. thesis, Universitat Autònoma de Barcelona, Barcelona, Spain.

Saura, E., Teixell, A., 2006. Inversion of small basins: effects on structural variations at the leading edge of the Axial Zone antiformal stack (Southern Pyrenees, Spain). Journal of Structural Geology 28, 1909–1920.

Schaltegger, U., Brack, P., 1999. Radiometric age constraints on the formation of the Collio Basin (Brescian Prealps). In Cassinis, G.; Cortesogno, L.; Gaggero, L.; Massari, F.; Neri, C.; Nicosia, U.; and Pittau, P., (Eds.), Stratigraphy and facies of the Permian deposits between eastern Lombardy and the western Dolomites. Field Trip Guidebook, International Field Conference on the Continental Permian of the Southern Alps and Sardinia (Italy), Brescia, September 15–25, p. 71.

Schaltegger, U., Brack, P., 2007. Crustal-scale magmatic systems during intracontinental strike-slip tectonics: U, Pb and Hf isotopic constraints from Permian magmatic rocks of the Southern Alps. Int. Journal of Earth Science 96: 1131–1151.

Schlische, R.W., Olsen, P.E., 1990. Quantitative Filling Model for Continental Extensional Basins with Applications to Early Mesozoic Rifts of Eastern North America. The Journal of Geology 98, 135–155.

Schlische, R.W., 1991. Half-graben basin filling models: new constraints on continental extensional basin development. Basin Research 3, 123–141.

Schmidt, G., 1931. Das Paläozoikum der spanischen Pyrenäen. Abhandlungen Gesellschaft der Wissenschaften Göttingen, Mathematisch-Physische Klasse III (5), 980–1065. [Spanish translation, 1943: El Paleozoico del Pirineo español. Publicaciones alemanas sobre Geología de España II, 101–195.]

Schneider, J.W., Körner, F., Roscher, M., Kroner, U., 2006. Permian climate development in the northern peri-Tethys area — The Lodève basin, French Massif Central, compared in a European and global context. Palaeogeography, Palaeoclimatology, Palaeoecology 240, 161–183. https://doi.org/10.1016/j.palaeo.2006.03.057

Schnurrenberger, D., Russell, J., Kelts, K., 2003. Classification of lacustrine sediments based on sedimentary components. Journal of Paleolimnology 29, 141–154.

Schobben, M., van de Velde, S., Gliwa, J., Leda, L., Korn, D., Struck, U., Ullmann, C.V., Hairapetian, V., Ghaderi, A., Korte, C., Newton, R.J., Poulton, S.W.,

Wignall, P.B., 2017. Latest Permian carbonate carbon isotope variability traces heterogeneous organic carbon accumulation and authigenic carbonate formation. Clim. Past 13, 1635–1659. https://doi.org/10.5194/cp-13-1635-2017

Scotese, C.R., Langford, R.P., 1995. Pangea and the Paleogeography of the Permian. In: Scholle, P.A., Peryt, T.M., Ulmer-Scholle, D.S. (Eds.), The Permian of Northern Pangea. Springer, Berlin, Heidelberg, pp. 3–19.

Scotese, C.R., 2003. PALEOMAP, Earth History, Jurassic [WWW Document]. Early Jurassic, the Dinosaurs spread across Pangea. URL http://www.scotese.com/jurassic.htm (accessed 12.1.17).

Sheldon, N.D., 2005. Do red beds indicate paleoclimatic conditions?: A Permian case study. Palaeogeography, Palaeoclimatology, Palaeoecology 228, 305–319. https://doi.org/10.1016/j.palaeo.2005.06.009

Sheldon, N.D., Tabor, N.J., 2009. Quantitative paleoenvironmental and paleoclimatic reconstruction using paleosols. Earth-Science Reviews 95, 1–52. https://doi.org/10.1016/j.earscirev.2009.03.004

Sheldon, N.D., Chakrabarti, R., Retallack, G.J., Smith, R.M.H., 2014. Contrasting geochemical signatures on land from the Middle and Late Permian extinction events. Sedimentology 61, 1812–1829. https://doi.org/10.1111/sed.12117

Sibuet, J.-C., Srivastava, S.P., Spakman, W., 2004. Pyrenean orogeny and plate kinematics. Journal of Geophysical Research: Solid Earth 109, B08104. doi:10.1029/2003JB002514

Sikes, N.E., Ashley, G.M., 2007. Stable isotopes of pedogenic carbonates as indicators of paleoecology in the Plio-Pleistocene (upper Bed I), western margin of the Olduvai Basin, Tanzania. J. Hum. Evol. 53, 574–594. https://doi.org/10.1016/j.jhevol.2006.12.008

Simancas, J.F., Tahiri, A., Azor, A., Lodeiro, F.G., Martínez Poyatos, D.J., El Hadi, H., 2005. The tectonic frame of the Variscan–Alleghanian orogen in Southern Europe and Northern Africa. Tectonophysics 398, 181–198.

Simon, S.S.T., Gibling, M.R., 2017. Fine-grained meandering systems of the Lower Permian Clear Fork Formation of north-central Texas, USA: Lateral and oblique accretion on an arid plain. Sedimentology 64, 714–746.

Singer, A. and Stoffers, P., 1980. Clay-mineral diagenesis in two East African lake sediments. Clay Miner., 15:291-307.

Singer, A., 1984. The paleoclimatic interpretation of clay minerals in sediments - a review. Earth-Science Reviews 21, 251–293. https://doi.org/10.1016/0012-8252(84)90055-2

Smith, N.D., Cross, T.A., Dufficy, J.P., Clough, S.R., 1989. Anatomy of an avulsion. Sedimentology 36, 1–23.

Smith, R., Botha, J., 2005. The recovery of terrestrial vertebrate diversity in the South African Karoo Basin after the end-Permian extinction. Comptes Rendus Palevol 4, 623–636. https://doi.org/10.1016/j.crpv.2005.07.005

Smooth, J.P., Olsen, P.E., 1988. Chapter 10 - Massive mudstones in basin analysis and paleoclimatic interpretation of the Newark Supergroup. In: Manspeizer, W. (Ed.), Developments in Geotectonics, Triassic-Jurassic Rifting. Elsevier, Amsterdam, Netherlands, pp. 249–274.

Soil Survey Staff, 1999. Soil Taxonomy - A Basic System of Soil Classification for Making and Interpreting Soil Surveys, 2nd ed. Superintendent of Documents, U.S. Government Printing Office.

Soriano, C., Martí, J., Casas, J.-M., 1996. Palinspastic reconstruction of Permo-Carboniferous basins involved in Alpine deformation: the Erill Castell-Estac basin, Southern Pyrenees, Spain. Geologie en Mijnbouw 75, 43–55.

Soula, J.-C., Lucas, C., Bessiere, G., 1979. Genesis and evolution of Permian and Triassic basins in the Pyrenees by regional simple shear acting on older Variscan structures: field evidence and experimental models. Tectonophysics 58, T1–T9.

Speksnijder, A., 1985. Anatomy of a strike-slip fault controlled sedimentary basin, Permian of the Southern Pyrenees, Spain. Sedimentary Geology 44, 179–223.

Stampfli, G.M., Borel, G.D., 2002. A plate tectonic model for the Paleozoic and Mesozoic constrained by dynamic plate boundaries and restored synthetic oceanic isochrons. Earth and Planetary Science Letters 196, 17–33.

Stampfli, G.M., von Raumer, J.F., Wilhem, C., 2011. The distribution of Gondwana derived terranes in the early Paleozoic. In: Gutiérrez-Marco, J.C., Rábano, I., García-Bellido, D. (Eds.), The Ordovician of the World, Cuadernos Del Museo Geominero. Instituto Geológico y Minero de España (IGME), Madrid, Spain, pp. 567–574.

Stear, W.M., 1983. Morphological Characteristics of Ephemeral Stream Channel and Overbank Splay Sandstone Bodies in the Permian Lower Beaufort Group, Karoo Basin, South Africa. In: Collinson, J.D., Lewin, J. (Eds.), Modern and Ancient Fluvial Systems. Blackwell Publishing Ltd., Oxford, UK, pp. 405–420.

Stephenson, M.H., 2016. Permian palynostratigraphy: a global overview, in: Lucas, S.G., Shen, S.Z. (Eds.), The Permian Timescale. Geological Society, London, Special Publications, 450.

Strahler, A.N., 1970. Introduction to physical geography. Wiley. 502 pp.

Sun, K-Q., 2006. The Cathaysia Flora and the mixed Late Permian Cathaysian–Angaran Floras in East Asia. Journal of Integrative Plant Biology 48, 381–389.

Szymański, W., Szkaradek, M., 2018. Andesite weathering and soil formation in a moderately humid climate: A case study from the Western Carpathians (southern Poland). Carpathian journal of earth and environmental sciences 13, 93–105.

Tabor, N.J., Montañez, I.P., 2002. Shifts in late Paleozoic atmospheric circulation over western equatorial Pangea: Insights from pedogenic mineral ʕ18O compositions 4.

Takeuchi, A., Hren, M.T., Smith, S.V., Chamberlain, C.P., Larson, P.B., 2010. Pedogenic carbonate carbon isotopic constraints on paleoprecipitation: Evolution of desert in the Pacific Northwest, USA, in response to topographic development of the Cascade Range. Chemical Geology 277, 323–335. https://doi.org/10.1016/j.chemgeo.2010.08.015

Talbot, M.R., 1988. The origins of palustrine oil source rocks: evidence from the lakes of tropical Africa. In: Fleet, A.J., Kelts, K., Talbot, M.R. (Eds.), Lacustrine Petroleoum Source Rocks. Geological Society, London, Special Publications 40, pp. 23-43.

Talbot, M. R., Holm, K., Williams, M.A.J., 1994. Sedimentation in low-gradient desert margin systems: A comparison of the Late Triassic of northwest Sumerset (England) and Late Quaternary of east-central Australia. In: Rosen, M.R (Ed), Paleoclimate and Basin Evolution of Playa Systems. Geological Society of America Special Papers 289, Boulder, CO, USA, pp. 97-117.

Talens, J., Wagner, R.H., 1995. Stratigraphic implications of late Carboniferous and early Permian megafloras in Lérida, south-central Pyrenees; comparison with the Cantabrian Mountains. Coloquios de Paleontología, Universidad Complutense 47, 177–192.

Tanner, L.H., Lucas, S.G., 2017. Paleosols of the upper Paleozoic Sangre de Cristo Formation, north-central New Mexico: Record of early Permian palaeoclimate in tropical Pangaea. Journal of Palaeogeography 6, 144–161. https://doi.org/10.1016/j.jop.2017.02.001

Terzaghi Karl (1924). Soil Mechanics in Engineering Practice, Wiley-Interscience; 3 Sub-edition (January 1996).

Thomas, S.G., Tabor, N.J., Yang, W., Myers, T.S., Yang, Y., Wang, D., 2011. Palaeosol stratigraphy across the Permian–Triassic boundary, Bogda Mountains, NW China: Implications for palaeoenvironmental transition through earth's largest mass extinction. Palaeogeography, Palaeoclimatology, Palaeoecology 308, 41–64. https://doi.org/10.1016/j.palaeo.2010.10.037

Thomas, B.A., Cleal, C.J., 2017. Distinguishing Pennsylvanian-age lowland, extra- basinal and upland vegetation. Palaeobiodiveristy and Palaeoenvironments 97, 1–21.

Valero-Garcés, B., Gisbert, J., 1992. Shallow carbonate lacustrine facies models in the Permian of the aragon-bearn basin (Western Spanish-French Pyrenees). Carbonates and Evaporites 7, 94-107.

Valero-Garcés, B., Morellón, M., Moreno, A., Corella, J.P., Martín-Puertas, C., Barreiro, F., Pérez, A., Giralt, S., Mata-Campo, M.P., 2014. Lacustrine carbonates of

Iberian Karst Lakes: Sources, processes and depositional environments. Sedimentary Geology 299, 1–29.

Van Den Driessche, J., Brun, J.-P., 1989. Un modèle cinématique de l'extension paléozoique supérieur dans le Sud du Massif Central. Comptes rendus de l'Académie des sciences, Mécanique, Physique, Chimie, Sciences de l'univers, Sciences de la Terre 309, 1607–1613.

Van Wees, J.D., Arche, A., Beijdorff, C.G., López-Gómez, J., Cloetingh, S.A.P.L., 1998. Temporal and spatial variations in tectonic subsidence in the Iberian Basin (eastern Spain): inferences from automated forward modelling of high-resolution stratigraphy (Permian–Mesozoic). Tectonophysics 300, 285–310.

Vandervoort, D.S., 1997. Stratigraphic response to saline lake-level fluctuations and the origin of cyclic nonmarine evaporite deposits: The Pleistocene Blanca Lila Formation, northwest Argentina. Geological Society of America Bulletin 109, 210–224.

Vargas, H., Gaspar-Escribano, J.M., López-Gómez, J., Van Wees, J.-D., Cloetingh, S., de La Horra, R., Arche, A., 2009. A comparison of the Iberian and Ebro Basins during the Permian and Triassic, eastern Spain: A quantitative subsidence modelling approach. Tectonophysics 474, 160–183

Veevers, J.J., Conaghan, P.J., Shaw, S.E., 1994. Turning point in Pangean environmental history at the Permian/Triassic (P/Tr) boundary, in: Klein, G.O. (Ed.), Pangea: Paleoclimate, Tectonics, and Sedimentation During Accretion, Zenith, and Breakup of a Supercontinent, Special Paper. Geological Society of America, pp. 187–196.

Vergés, J., Martínez, A., 1988. Corte compensado del Pirineo oriental: Geometria de las cuencas de antepais y edades de emplazamiento de los mantos de corrimiento. Acta Geológica Hispánica 23, 95–105.

Virgili, C., Cassinis, G., Broutin, J., 2006. Permian to Triassic sequences from selected continental areas of southwestern Europe. In: Spencer, G.L., Cassinis, G., Schneider, J.W. (Eds.), Non-Marine Permian Biostratigraphy and Biochronology. Geological Society, London, Special Publications 265, pp. 231–259.

Voigt, S., Haubold, H., 2015. Permian tetrapod footprints from the Spanish Pyrenees. Palaeogeography, Palaeoclimatology, Palaeoecology 417, 112–120.

Wagner, R.H., 1984. Megafloral Zones of the Carboniferous. Compte Rendu 9e Congrès International de Stratigraphie et Géologie du Carbonifère, Washington and Champaign-Urbana 1979, 2, 109–134.

Wagner, R.H., 2004a. Climatic changes as mirrored by Carboniferous and Permian floral distributions. Monografías del Jardín Botánico de Córdoba 11, 29–39.

Wagner, R.H., 2004b. Gondomaria grandeuryi (Zeiller) Wagner & Castro, 1998, in the context of an upper Stephanian flora from Surroca (prov. Girona, Catalonia, Spain). Treballs del Museu de Geologia de Barcelona 12, 53–67.

Wagner, R.H., Álvarez-Vázquez, C., 2010. The Carboniferous floras of the Iberian Peninsula: A synthesis with geological connotations. Review of Palaeobotany and Palynology 162, 239–324.

Wakelin-King, G.A., Webb, J.A., 2007. Upper-Flow-Regime Mud Floodplains, Lower-Flow-Regime Sand Channels: Sediment Transport and Deposition in a Drylands Mud-Aggregate River. Journal of Sedimentary Research 77, 702–712.

Wignall, P.B., 2001. Large igneous provinces and mass extinctions. Earth-Science Reviews 53, 1–33. https://doi.org/10.1016/S0012-8252(00)00037-4

Wu, C., Ullah, M.S., Lu, J., Bhattacharya, J.P., 2016. Formation of point bars through rising and falling flood stages: Evidence from bar morphology, sediment transport and bed shear stress. Sedimentology 63, 1458–1473.

Xu, G., Feng, Q., Deconinck, J.F., Shen, J., Zhao, T., Young, A.L., 2017. High-resolution clay mineral and major elemental characterization of a Permian-Triassic terrestrial succession in southwestern China: Diagenetic and paleoclimatic/paleoenvironmental significance. Palaeogeography, Palaeoclimatology, Palaeoecology 481, 77–93. https://doi.org/10.1016/j.palaeo.2017.05.027

Yakimenko, E., Inozemtsev, S., Naugolnykh, S., 2004. Upper Permian paleosols (Salarevskian Formation) in the central part of the Russian Platform: paleoecology and paleoenvironment. Revista Mexicana de Ciencias Geológicas 21.

Yin, H., Feng, Q., Lai, X., Baud, A., Tong, J., 2007. The protracted Permo-Triassic crisis and multi-episode extinction around the Permian–Triassic boundary. Global and Planetary Change, Environmental and Biotic Changes during the Paleozoic-Mesozoic Transition 55, 1–20. https://doi.org/10.1016/j.gloplacha.2006.06.005

Ziegler, A.M., 1990. Phytogeographic patterns and continental configurations during the Permian Perio in: McKerrow, W.S., Scotese, C.R. (Eds.), Palaeozoic Palaeogeography and Biogeography. Geological Society, Memoir 12, 363–379.

Zwart, H.J., 1986. The variscan geology of the Pyrenees. Tectonophysics, The Geological Evolution of the Pyrenees 129, 9–27. https://doi.org/10.1016/0040-1951(86)90243-X
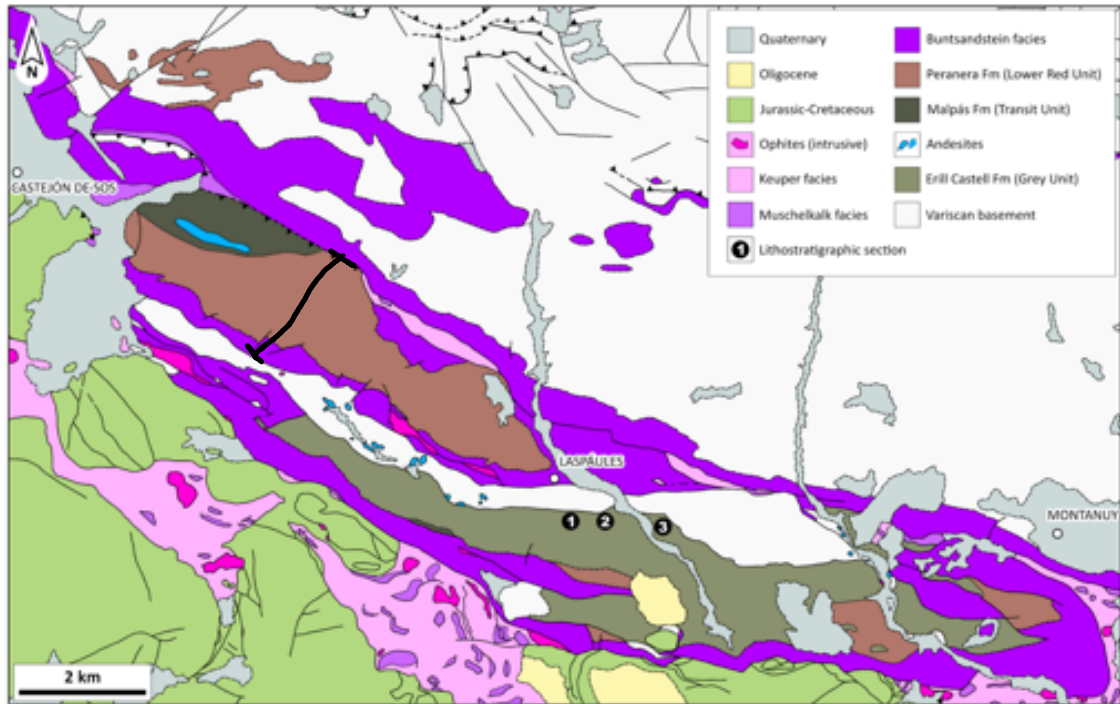
Appendix I

Figure 1 Appenix I. Geological map of Castejón-Laspaúles basin and the location of Villarrué-Suils section. Modified from Robles et al. (online).
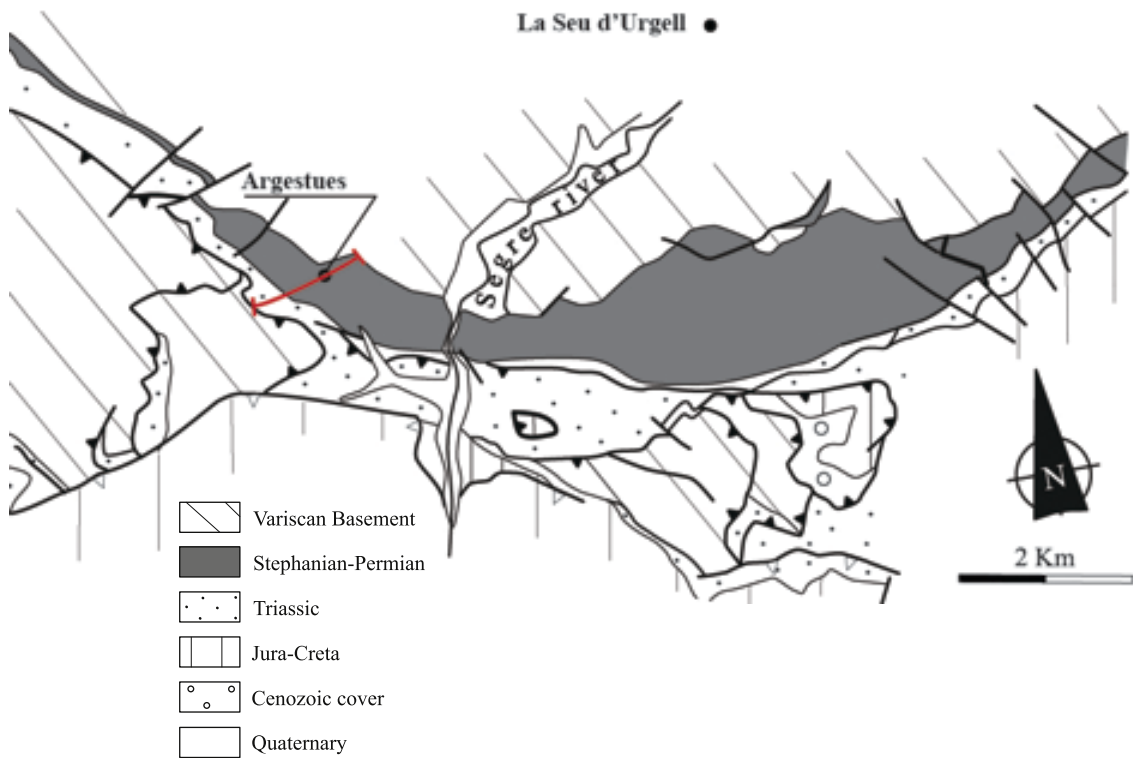
Figure 2 Appenix I. Geological map of Gramós basin and the location of Pallarols section. Modified from Gretter et al. (2015).

224
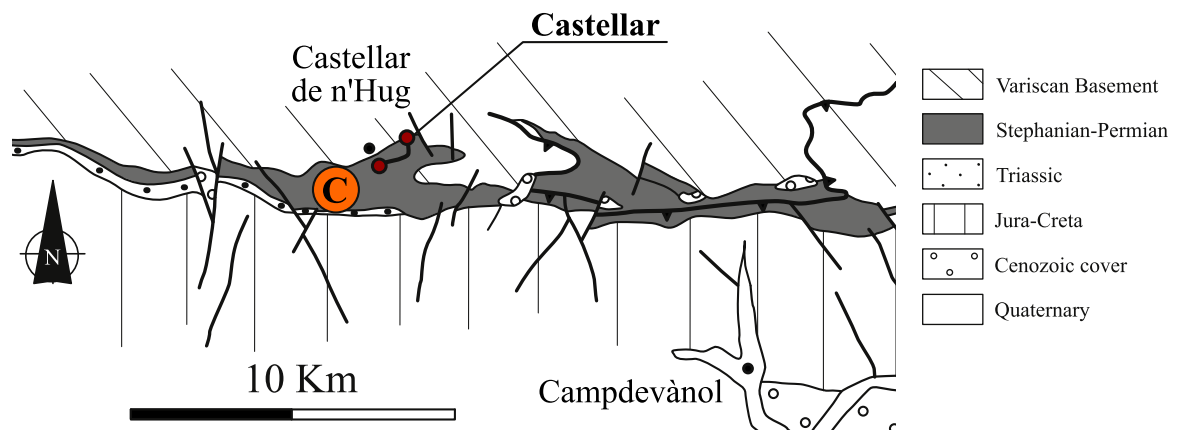
Figure 3 Appenix I. Geological map of Castellar de n'Hugs basin and the location of the section. Modified from Gretter et al. (2015).

Figure 4. Baró stratigraphic section.

Figure 5 Appendix I. Castellars stratigraphic section (I).
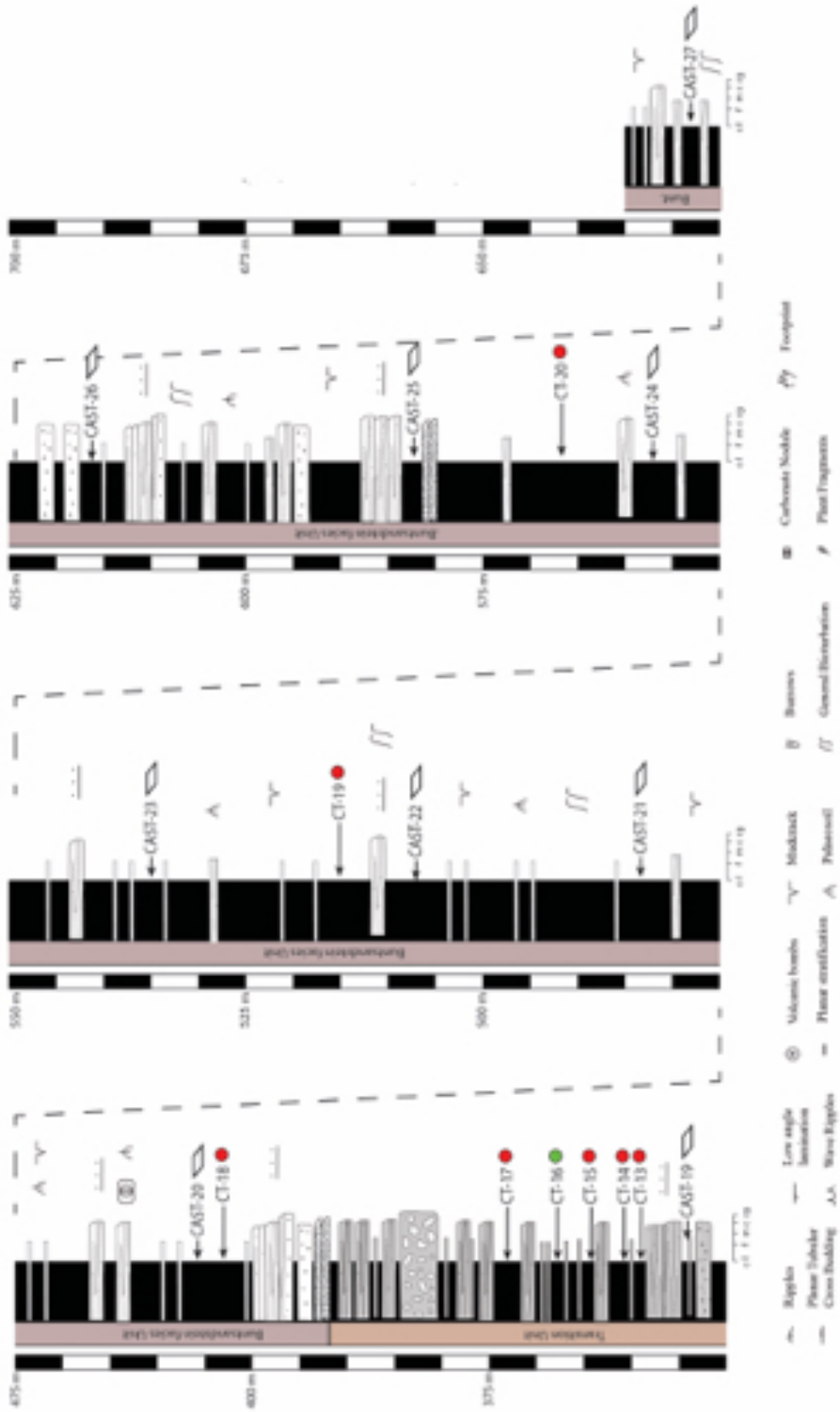
Figure 6 Appendix I. Castellars stratigraphic section (2).

Figure 7 Appendix I. Collada de Pui Cavaller stratigraphic section (1).
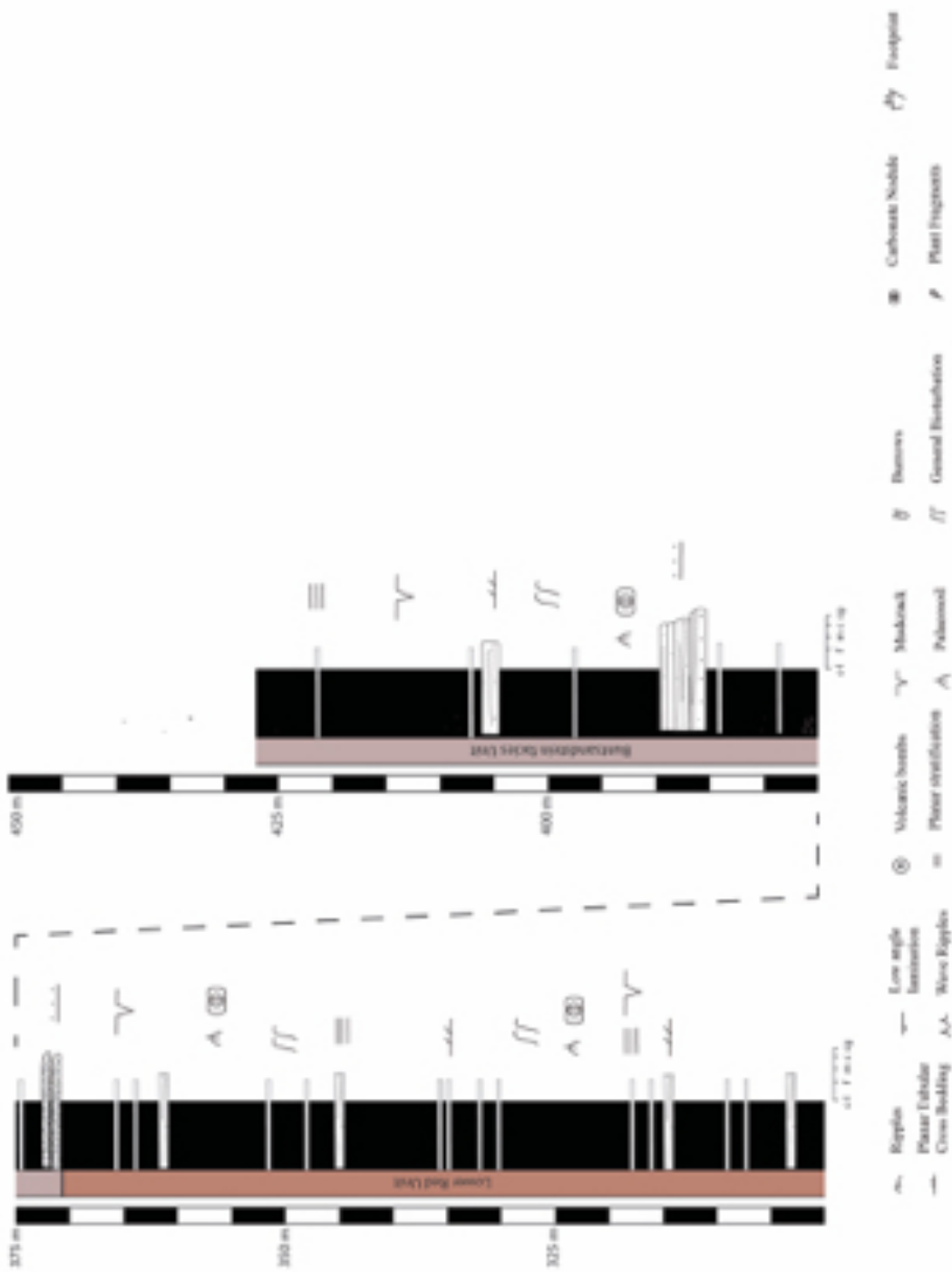
Figure 8 Appendix I. Collada de Pui Cavaller stratigraphic section (2).

Figure 9 Appendix I. Estac stratigraphic section (1).

Figure 10 Appendix I. Estac stratigraphic section (2).

Figure 11 Appendix I. Gotarta stratigraphic section.
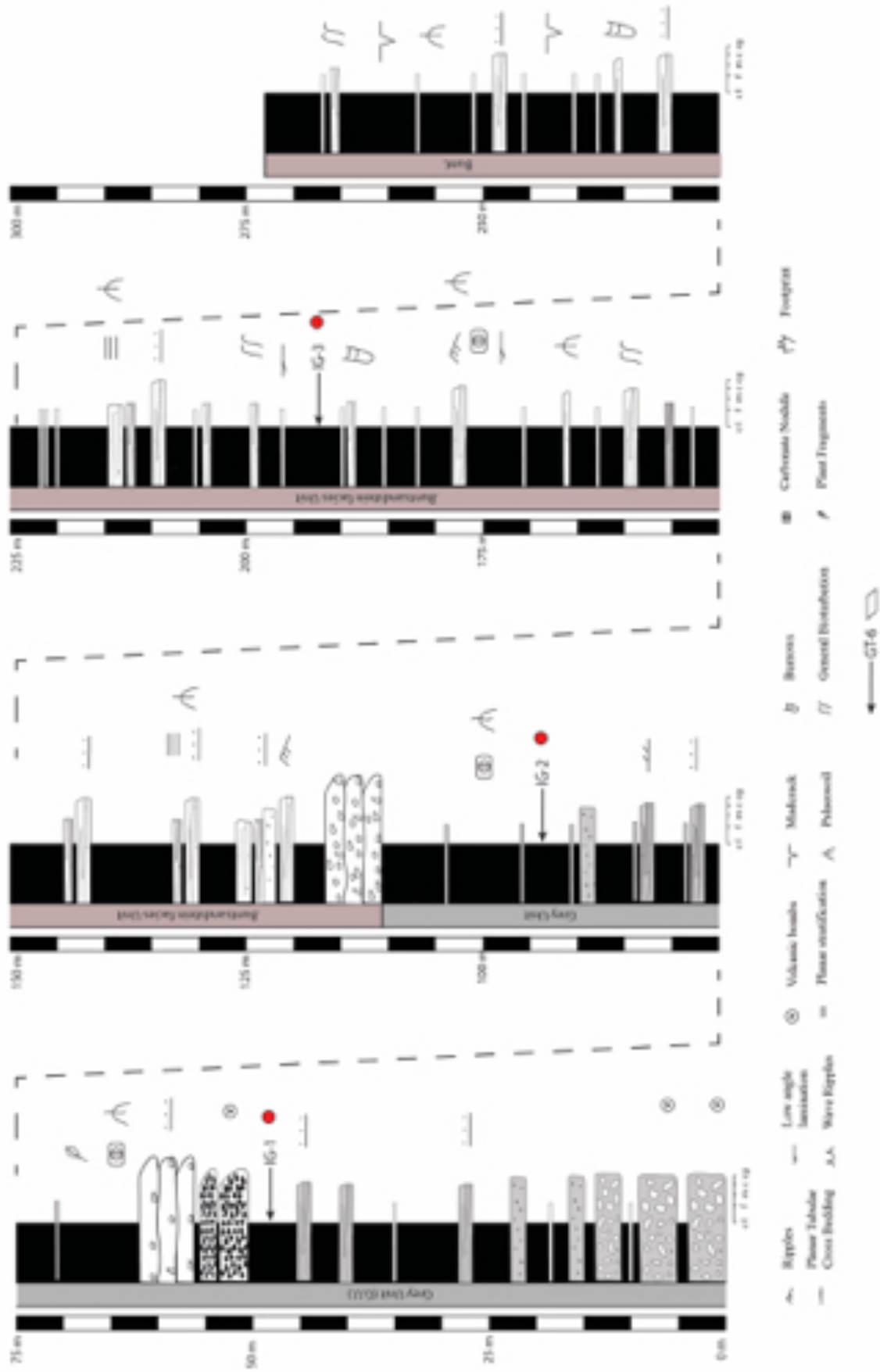
Figure 12 Appendix I. Igüerri stratigraphic section.
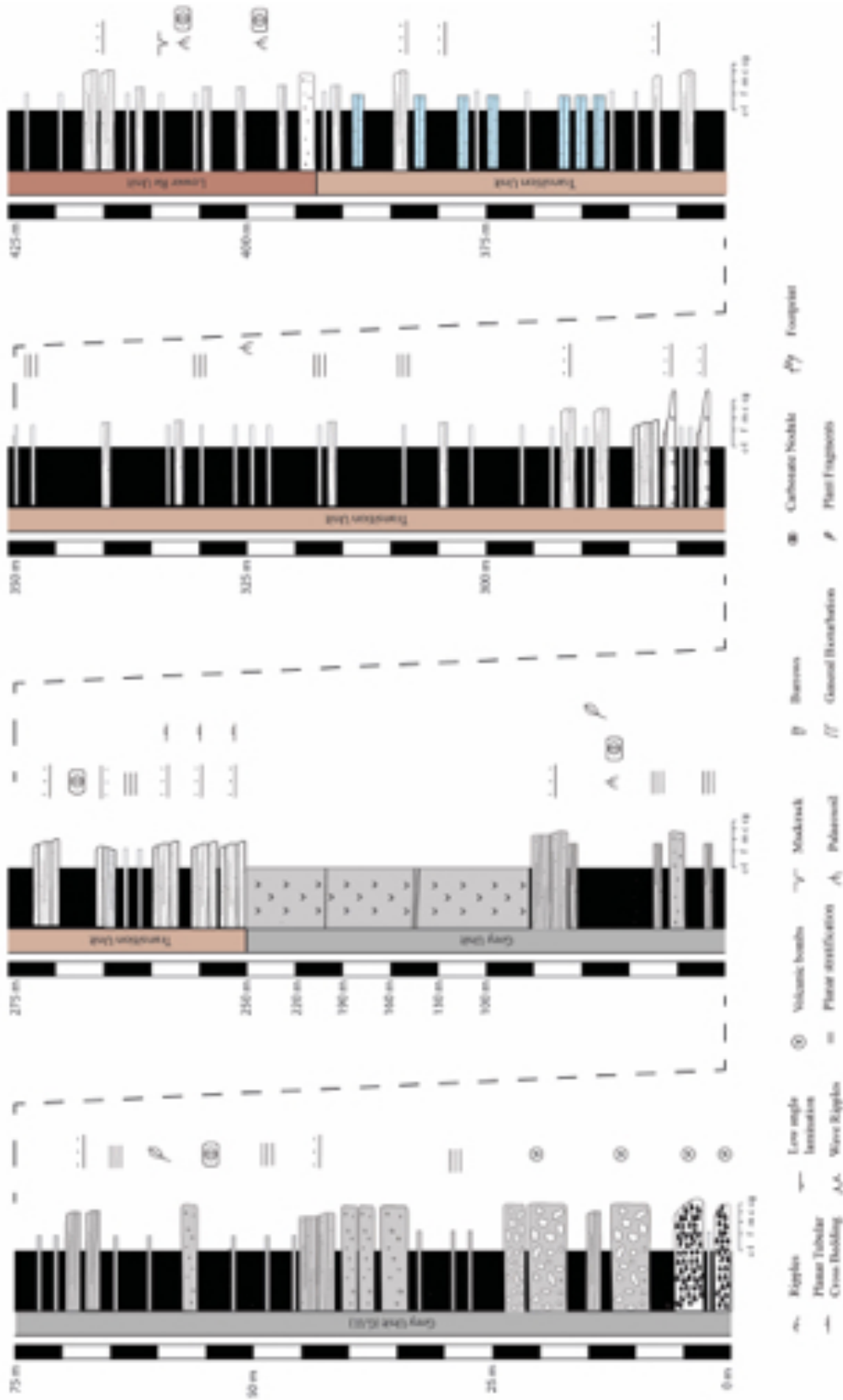
Figure 13 Appendix I. Malpàs (Erill Castell) stratigraphic section (1).
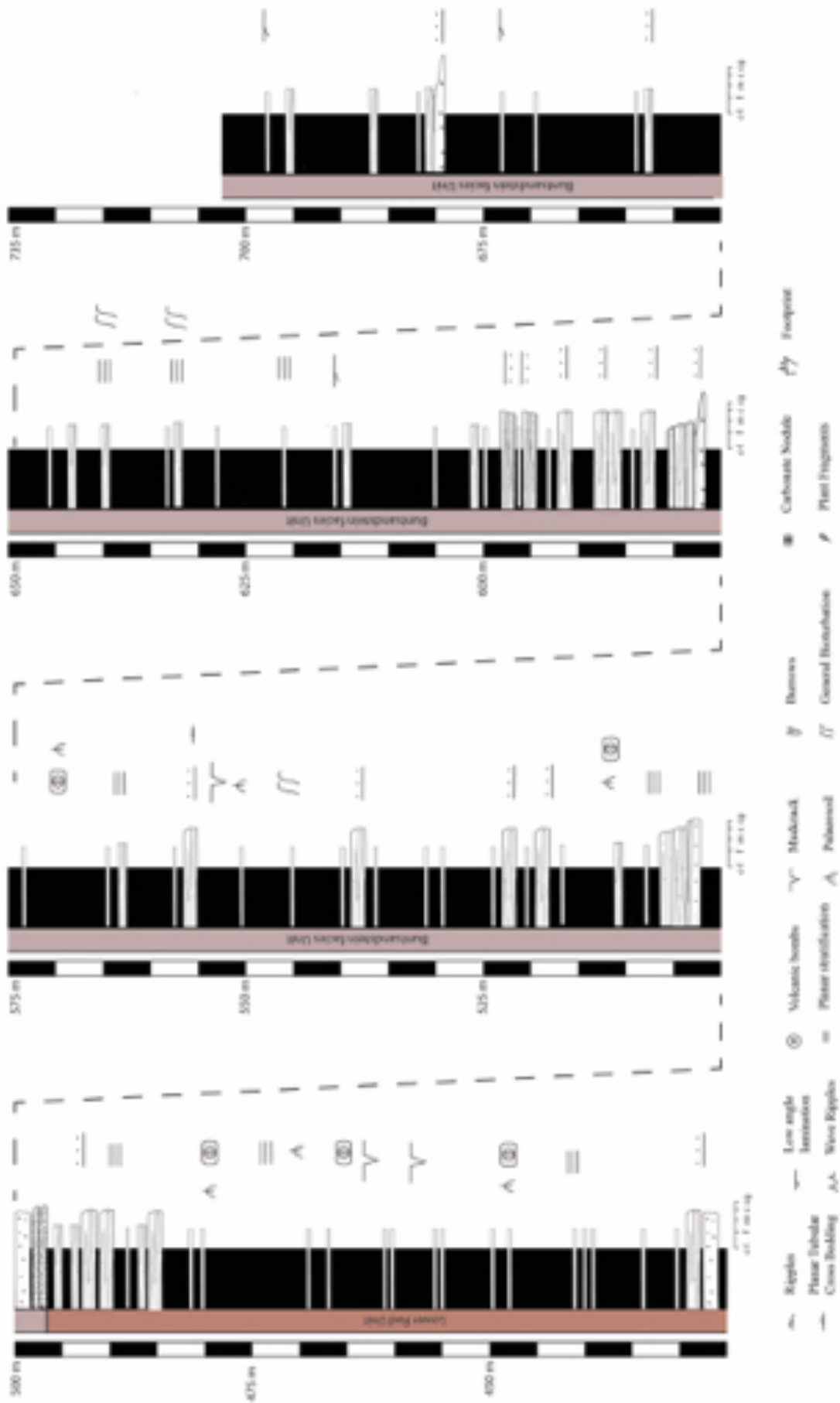
Figure 14 Appendix I. Malpàs (Erill Castell) stratigraphic section (2).

236
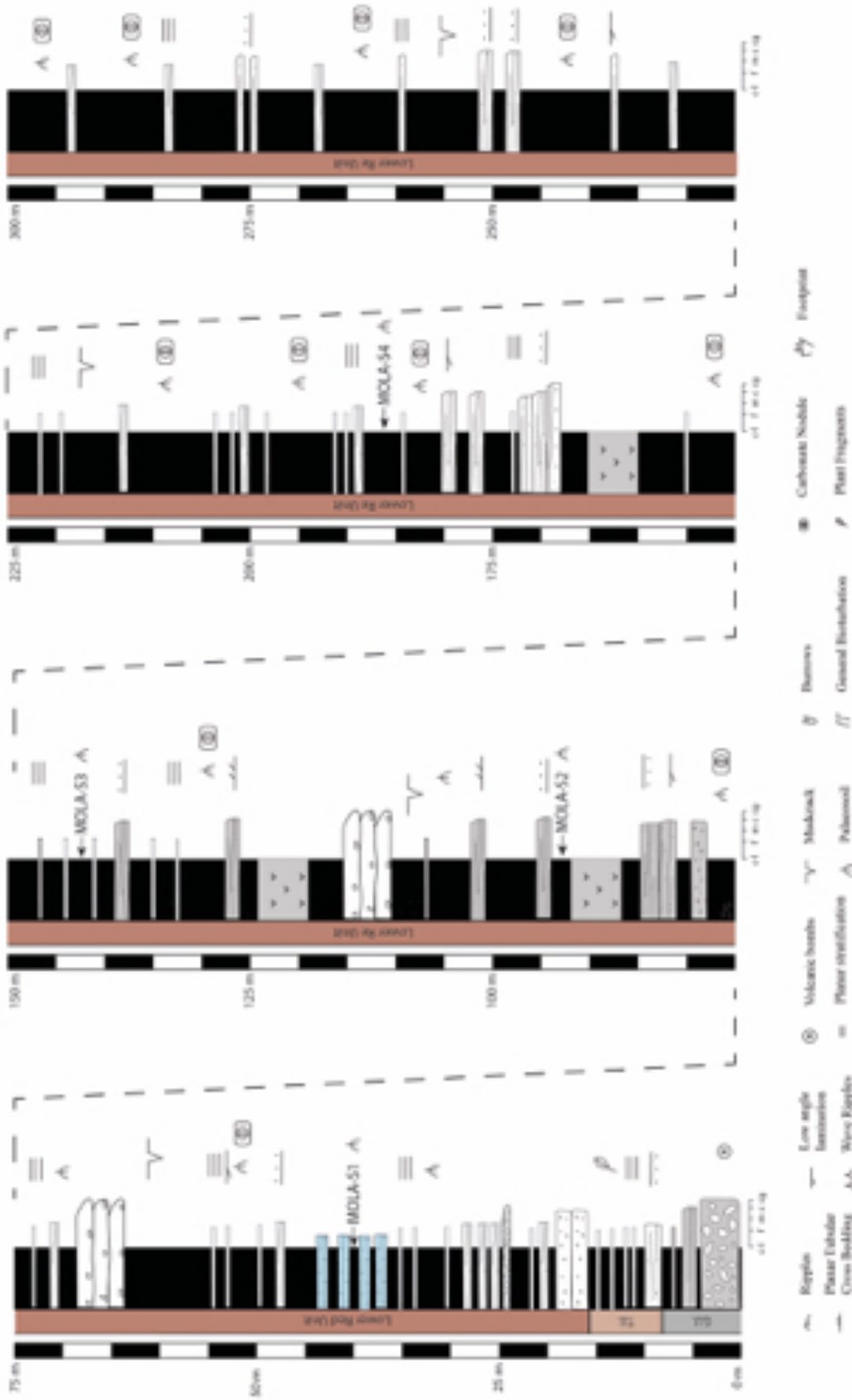
Figure 15 Appendix I. La Mola d'Amunt stratigraphic section (1).
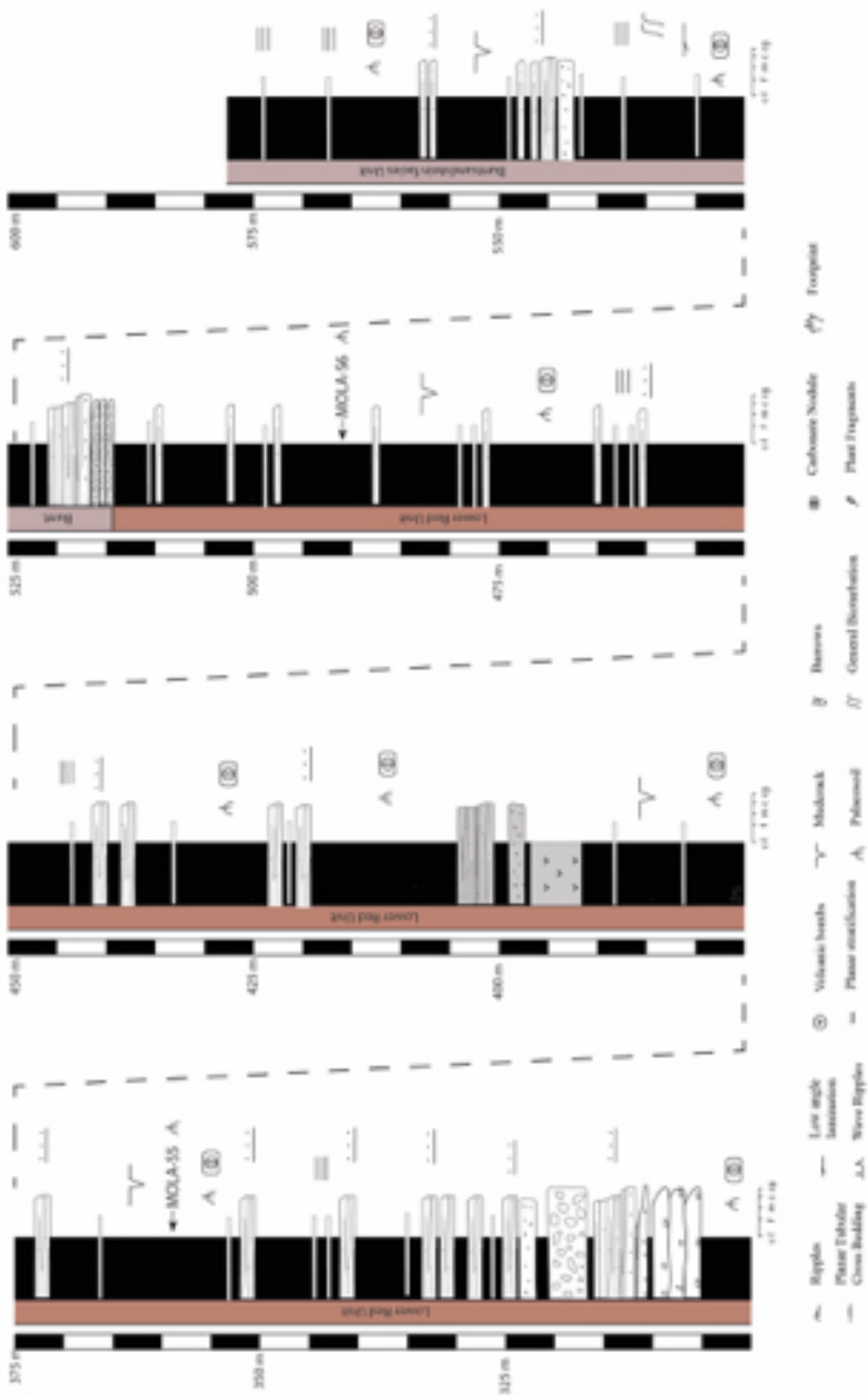
Figure 16 Appendix I. La Mola d'Amunt stratigraphic section (2).

Figure 17 Appendix I. Castellar de N'Hug stratigraphic section (1).

239
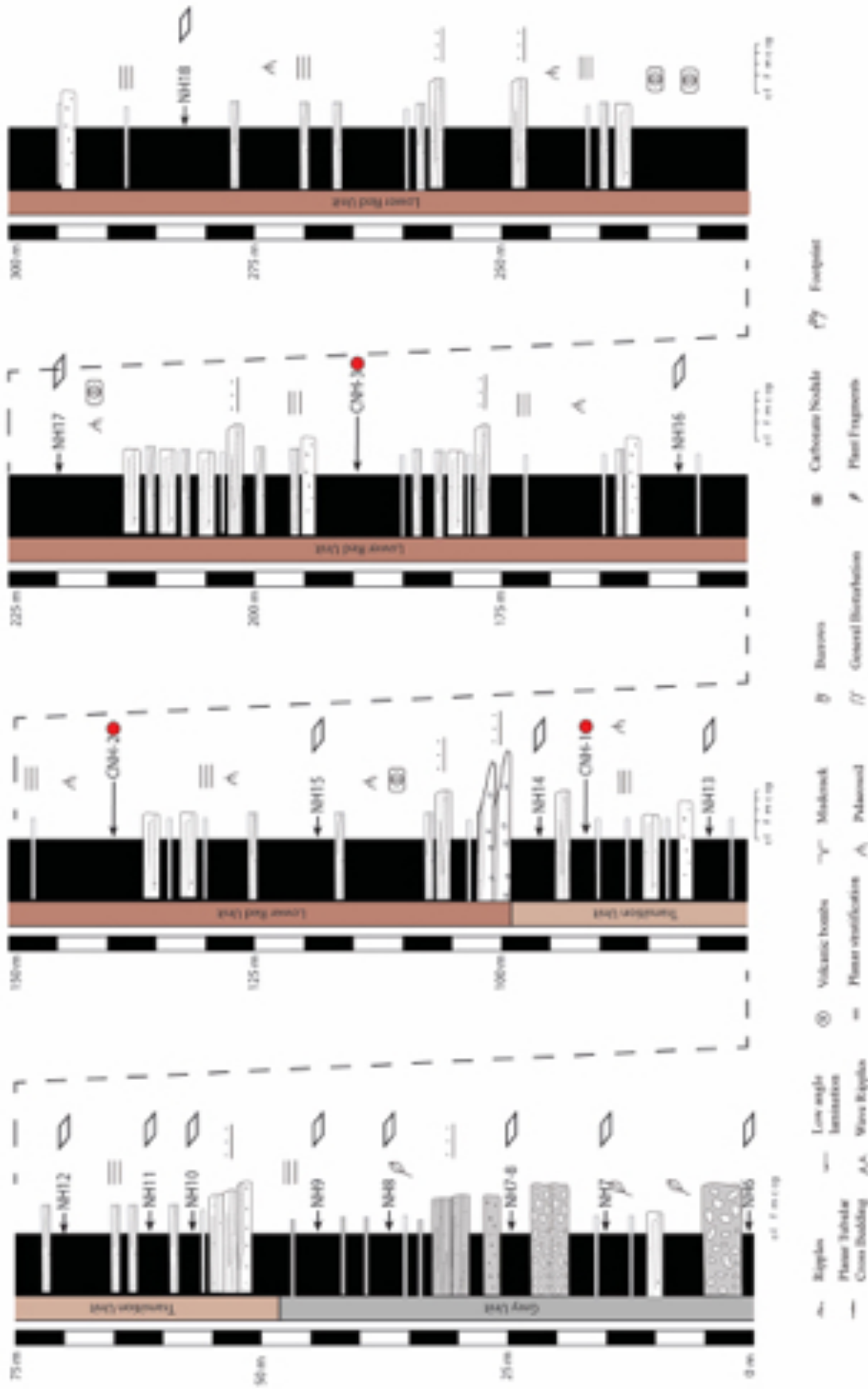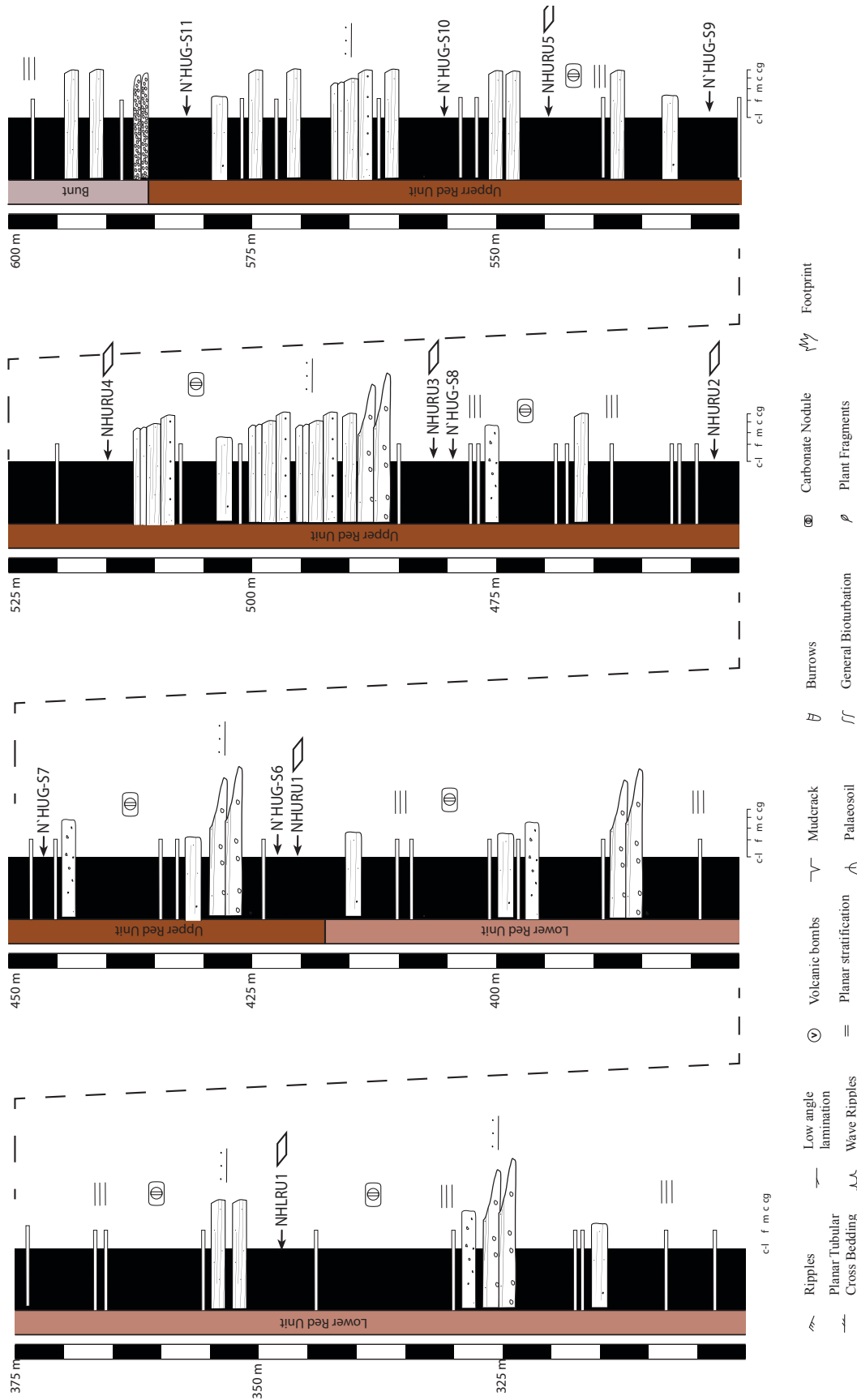
Figure 18 Appendix I. Castellar de N'Hug stratigraphic section (2).
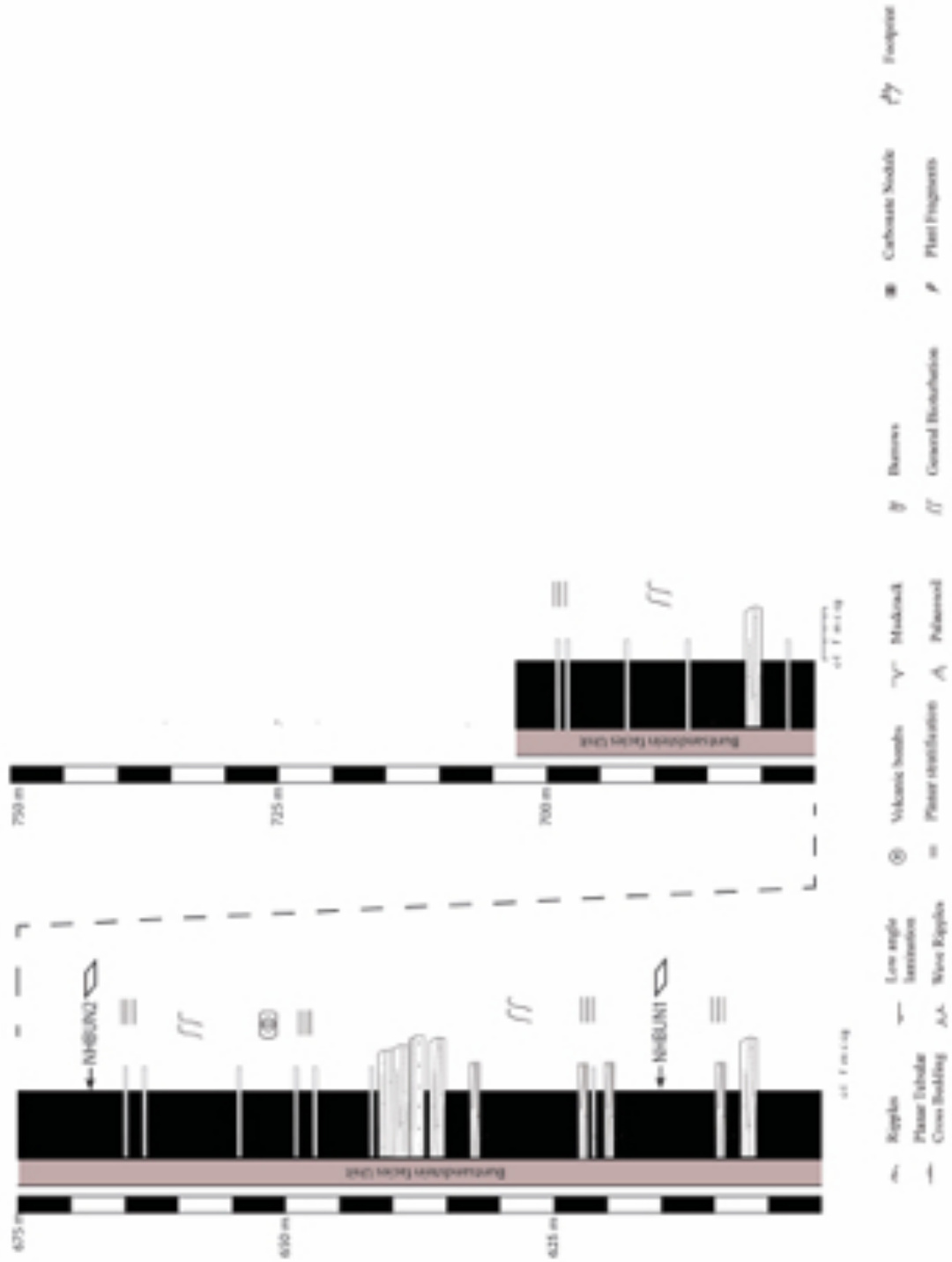
Figure 19 Appendix I. Castellar de N'Hug stratigraphic section (3).
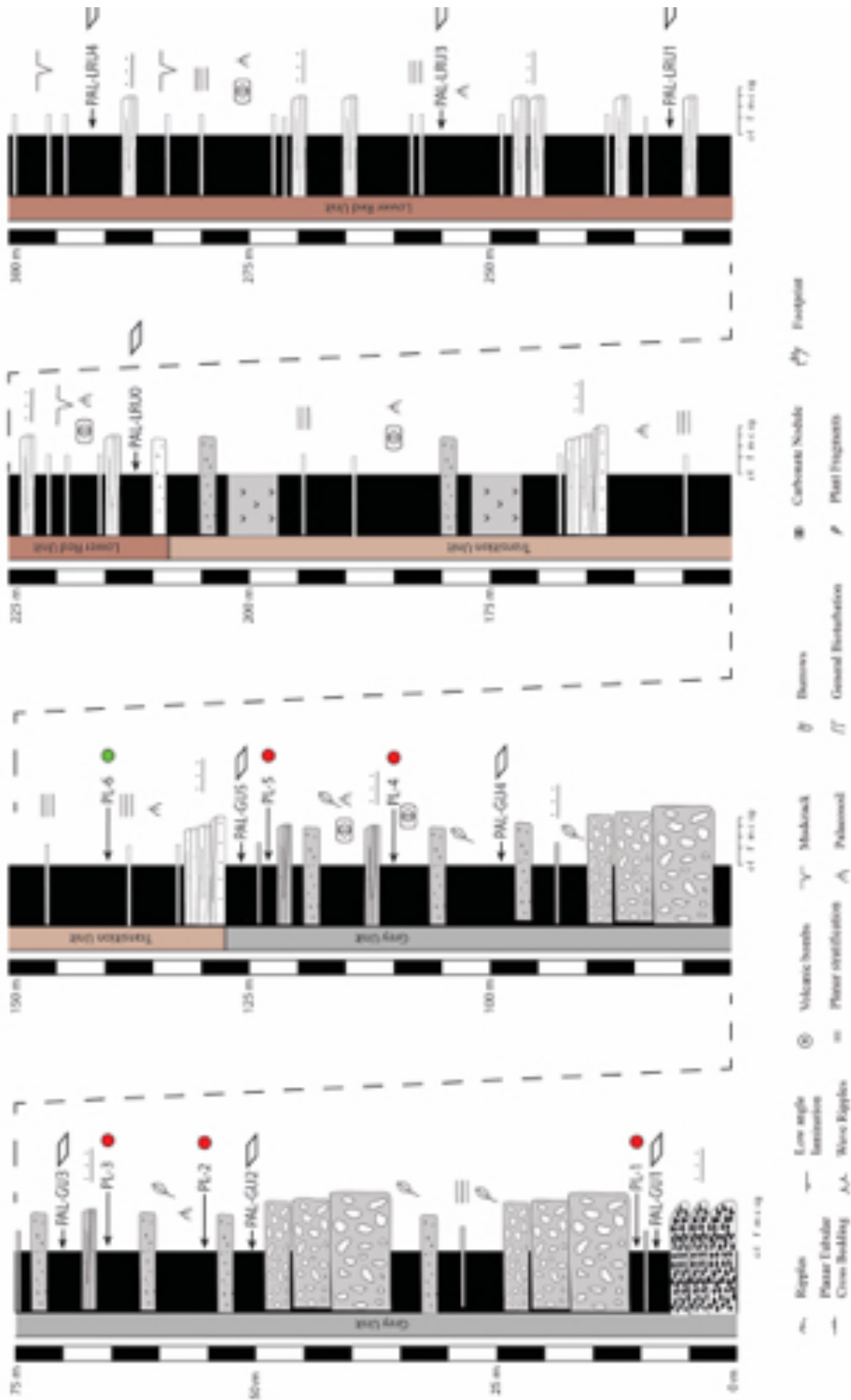
Figure 20 Appendix I. (Rio) Pallarols stratigraphic section (1).

Figure 21 Appendix I. (Rio) Pallarols stratigraphic section (2).
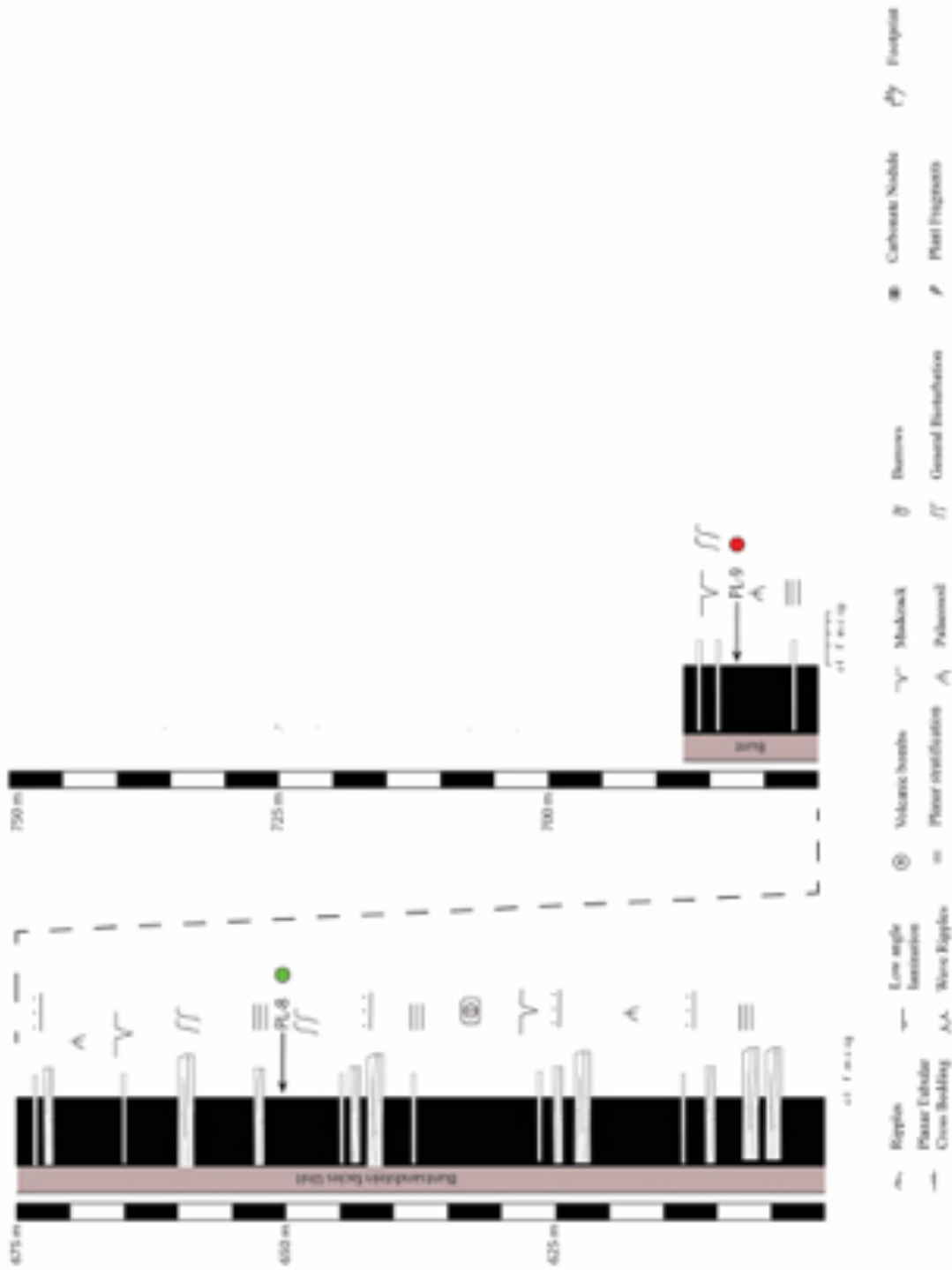
Figure 22 Appendix I. (Rio) Pallarols stratigraphic section (3).
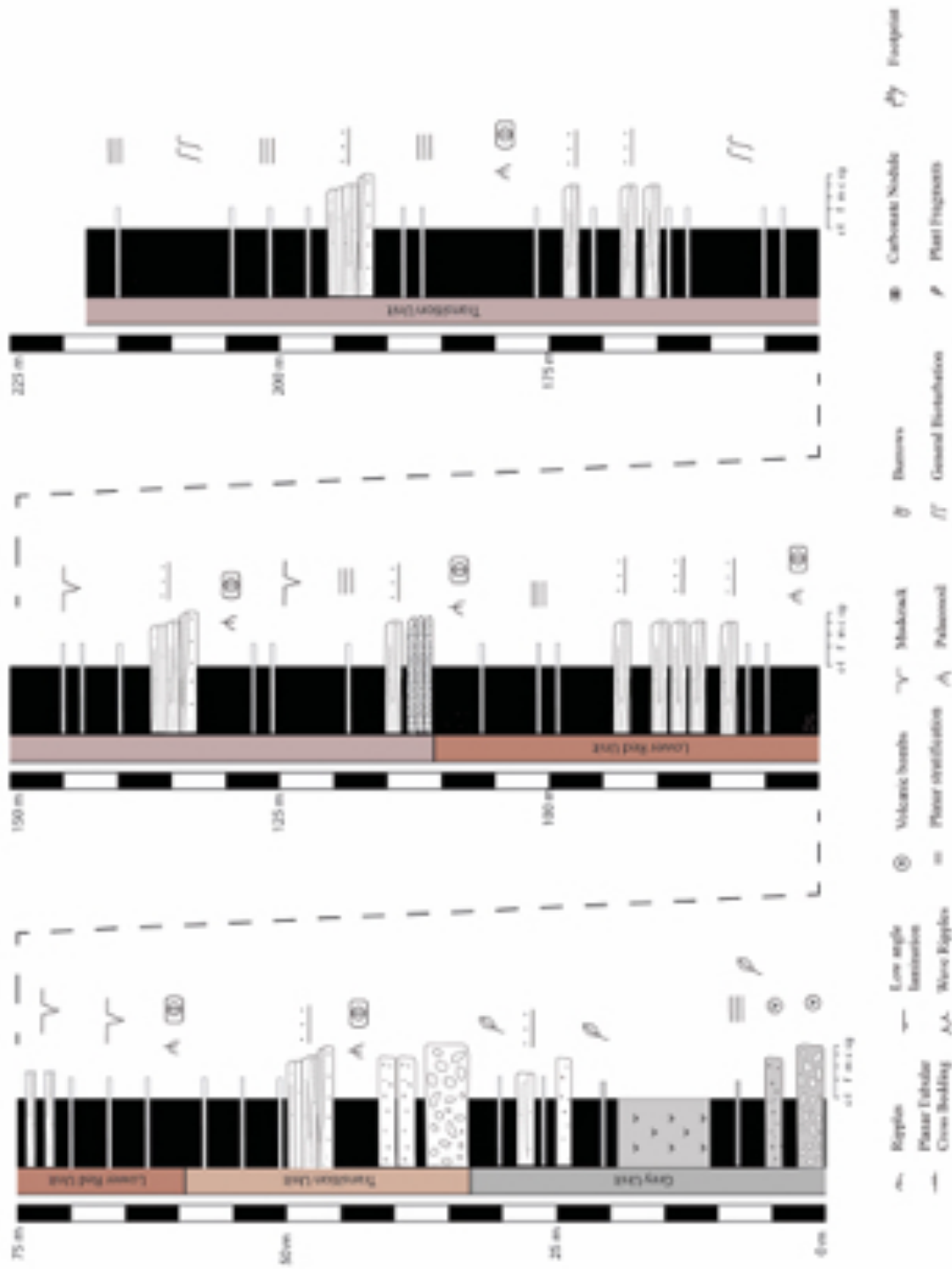
Figure 23 Appendix I. Roca de les creus stratigraphic section.
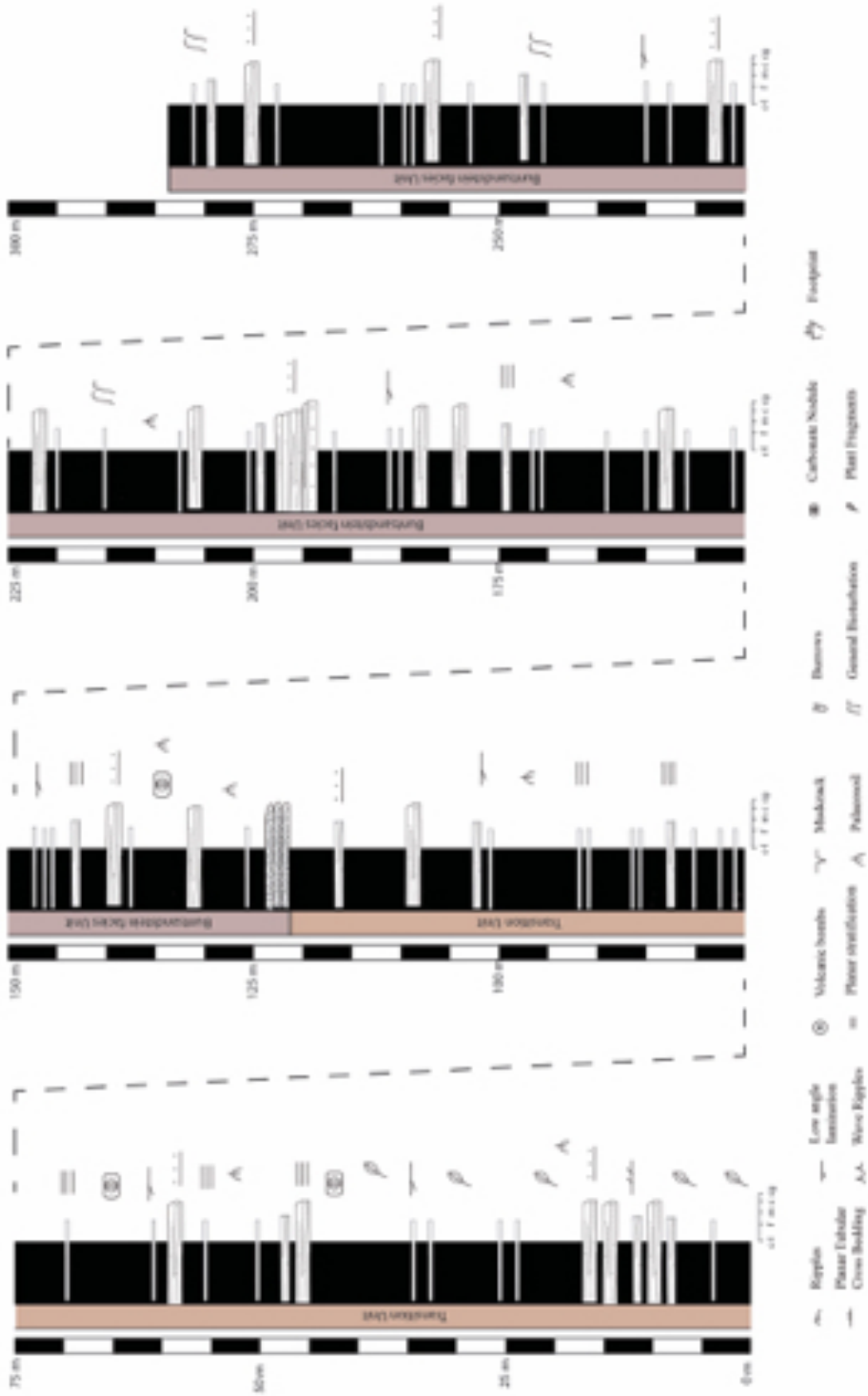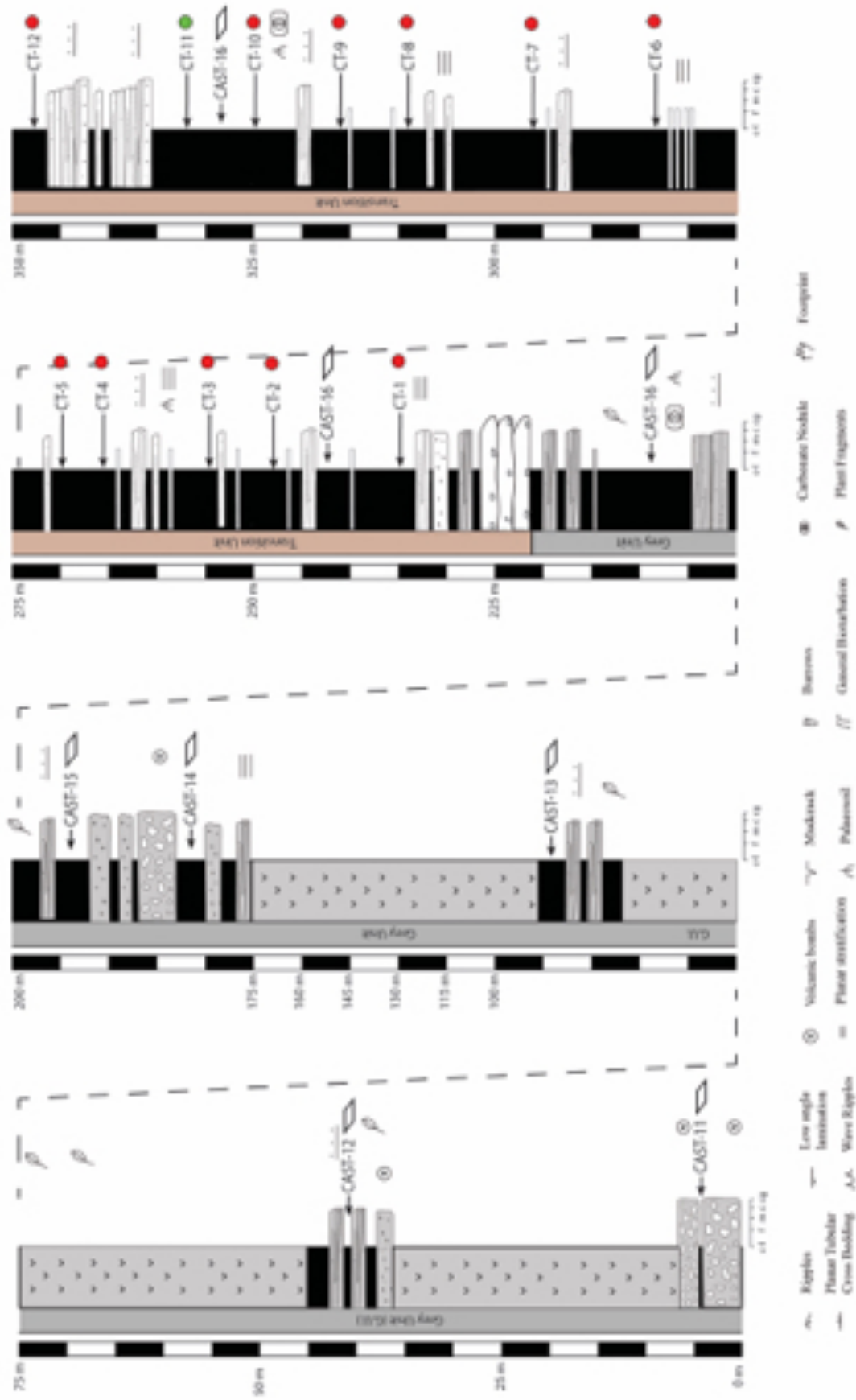
Figure 24 Appendix I. Sas stratigraphic section (1).
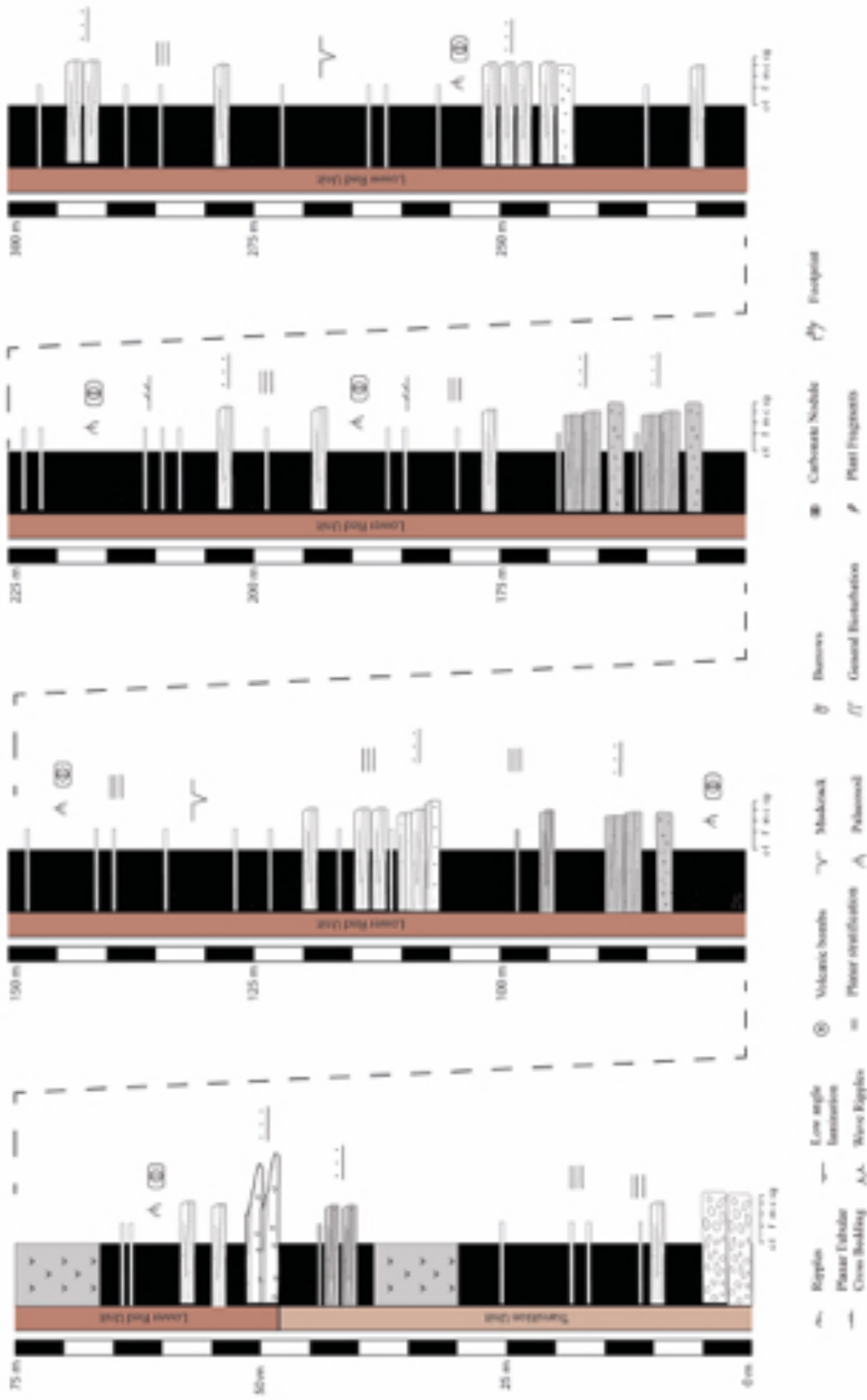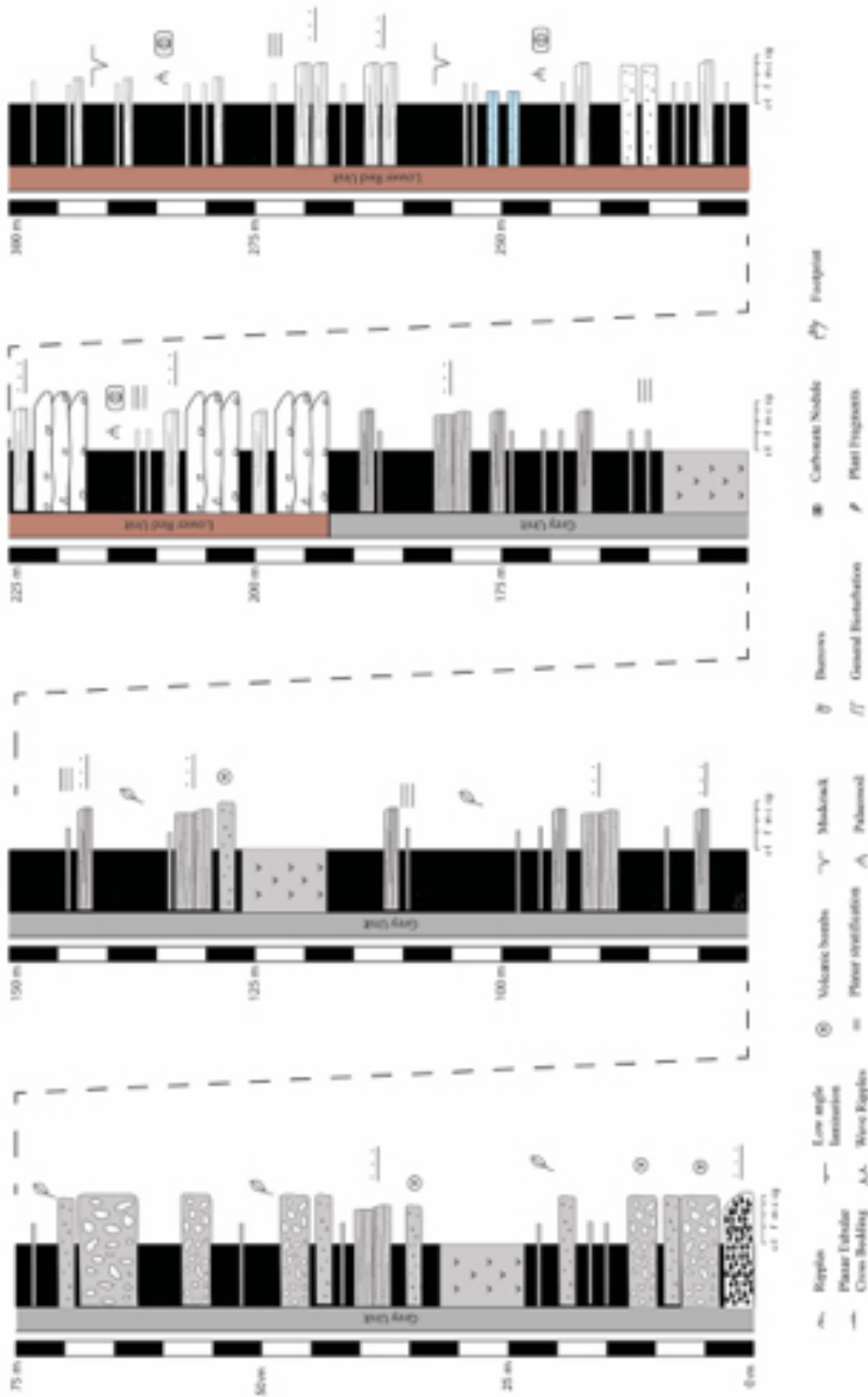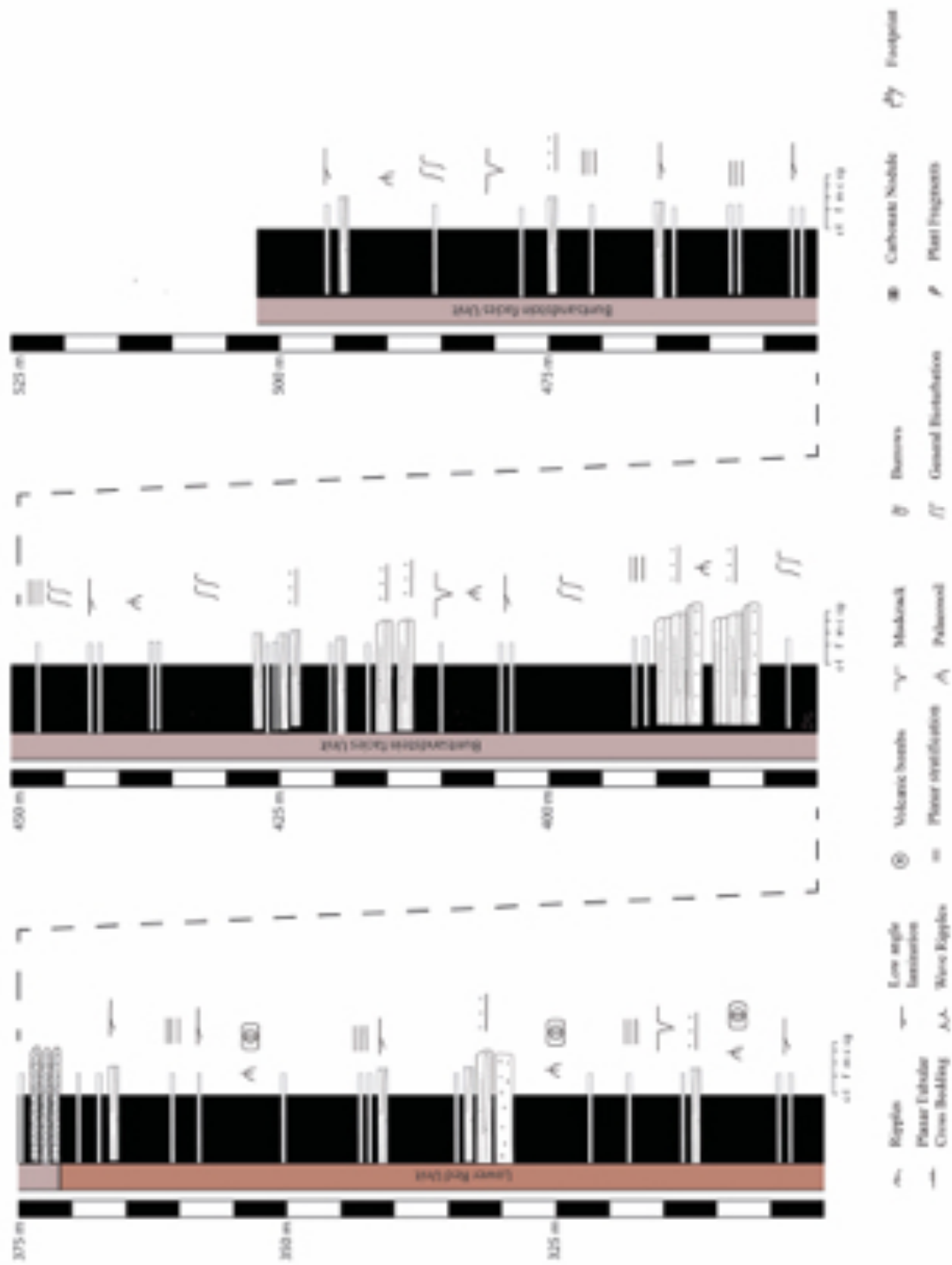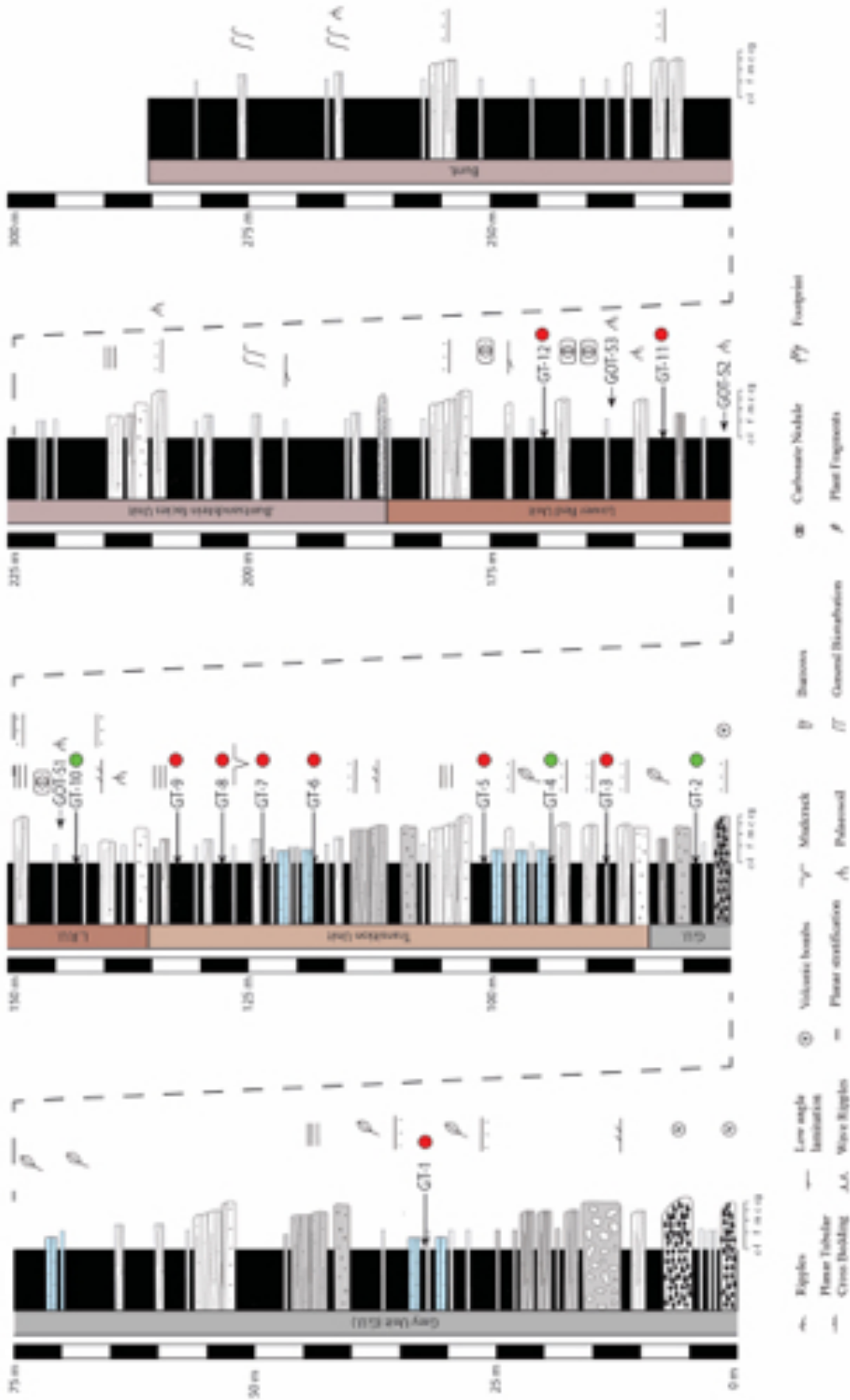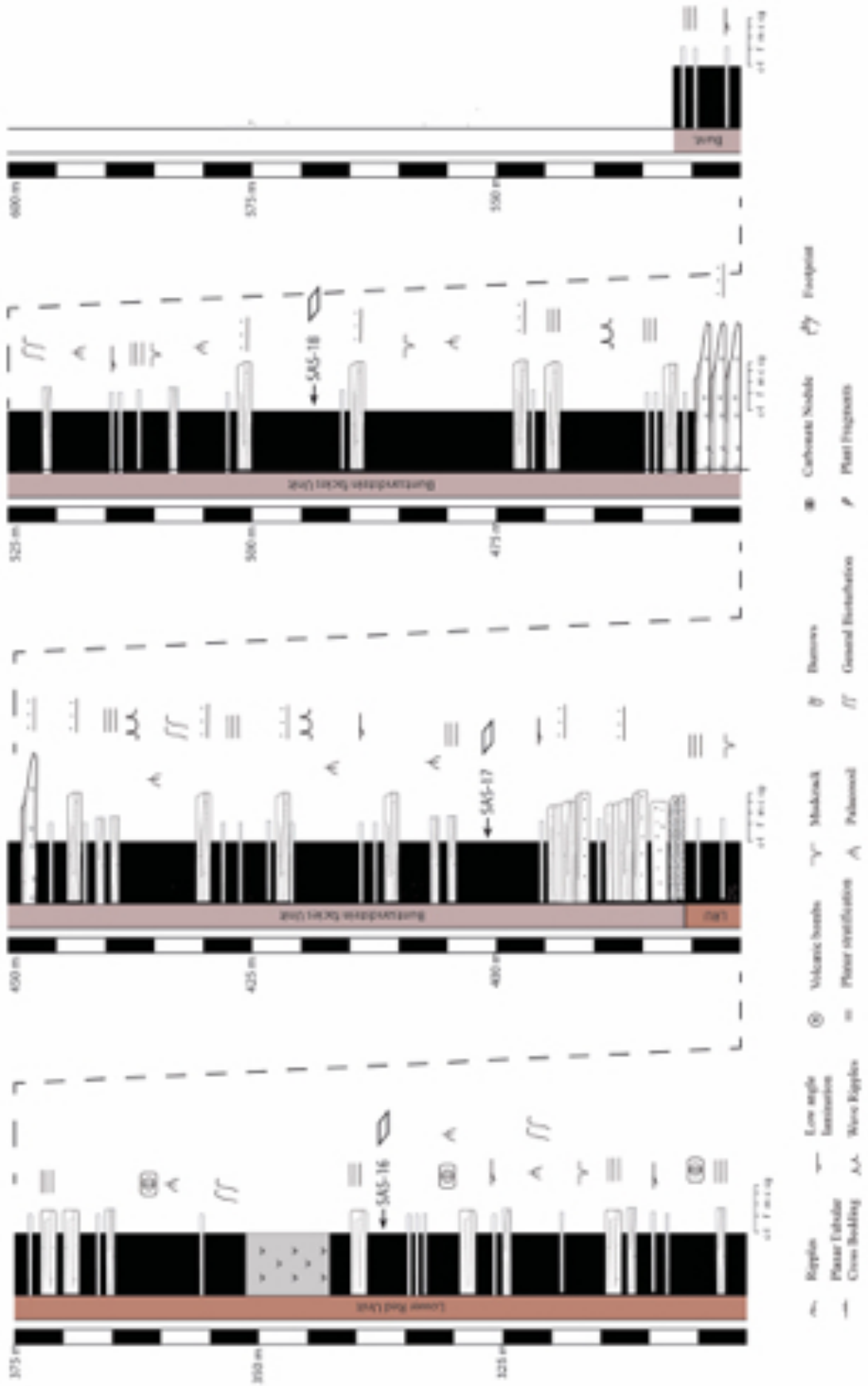
Figure 25 Appendix I. Sas stratigraphic section (2).
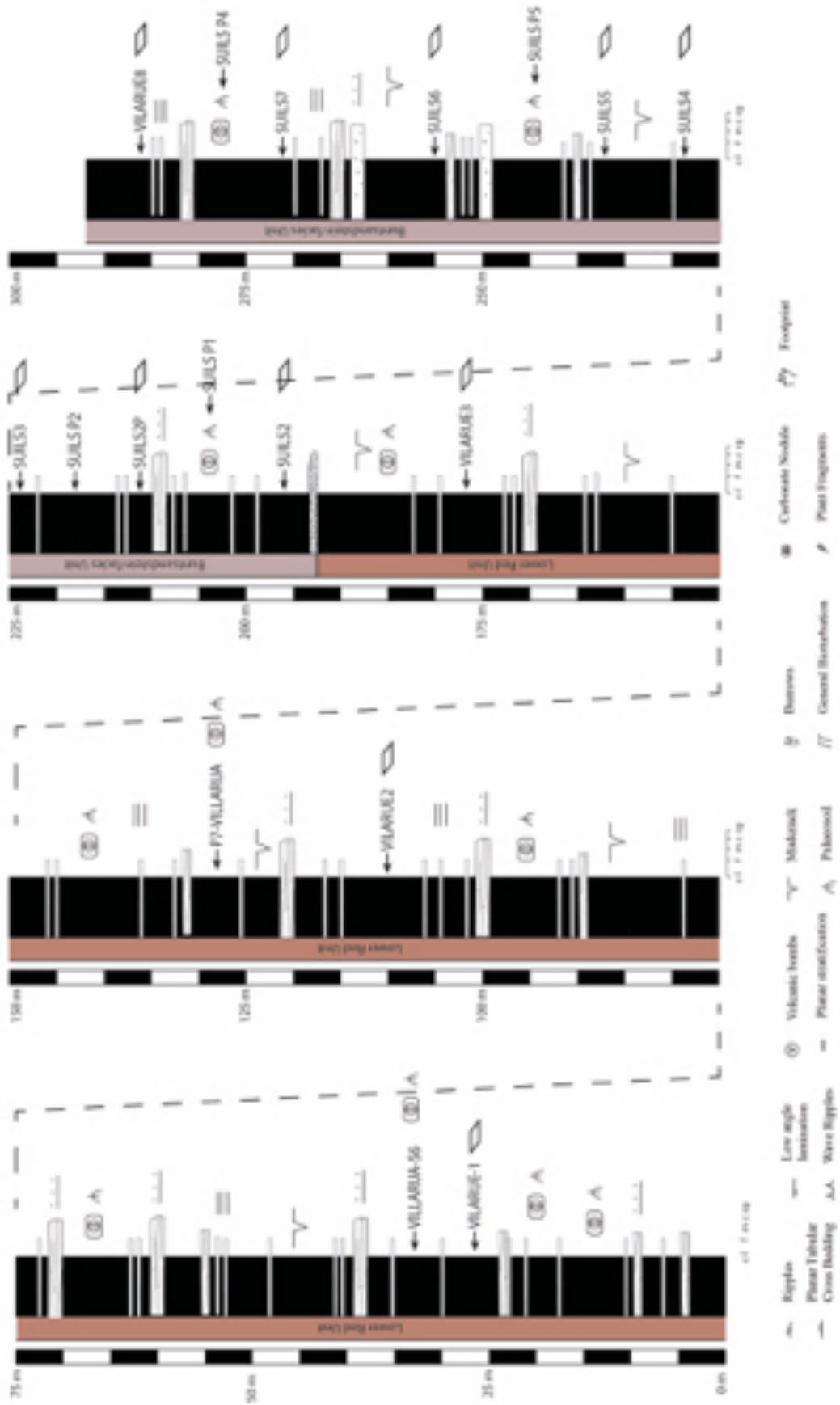
Figure 26 Appendix I. Villarrué-Suils stratigraphic section.

Appendix II

Sample	d^{13}C	± (1 s)	d^{18}O	± (1 s)
CO7-10	2,36	0,01	-2,10	0,01
CO7-31	2,27	0,01	-1,79	0,01
NHUG-S10AB	-4,06	0,01	-2,18	0,01
NHUG-S10BA	-3,54	0,02	-2,80	0,02
NHUG-S10BB	-3,69	0,01	-2,54	0,01
NHUG-S10BC	-3,84	0,01	-3,22	0,01
NHUG-59AB	-6,65	0,01	-8,59	0,01
NHUG-58C	-6,43	0,01	-7,82	0,01
NHUG-58A	-6,50	0,02	-7,28	0,01
MOLA-54CA	-1,65	0,01	-7,42	0,02
MOLA-53BC	-2,11	0,02	-9,27	0,02
MOLA-53AC	-4,86	0,01	-9,55	0,01
MOLA-53AB	-5,54	0,01	-8,85	0,02
MOLA-52CC	-6,51	0,01	-9,16	0,01
NHUG-59AA	-5,74	0,02	-9,46	0,03
MOLA-53BB	-3,41	0,01	-9,23	0,03
NHUG-59BB	-5,79	0,01	-9,22	0,02
NHUG-58B	-6,23	0,01	-7,63	0,01
MOLA-53AA	-3,25	0,01	-9,88	0,02
MOLA-52CB	-7,01	0,01	-8,96	0,01
MOLA-52AA	-6,48	0,01	-9,25	0,02
MOLA-52AB	-6,11	0,01	-10,26	0,02
MOLA-52CA	-6,59	0,01	-9,57	0,02
MOLA-52AC	-6,09	0,01	-10,24	0,02
MOLA-51CA	-6,71	0,01	-10,06	0,02
MOLA-51CB	-6,16	0,01	-8,30	0,01
MOLA-51CC	-6,34	0,01	-10,14	0,02
170-5A	-5,97	0,01	-7,47	0,01
170-5B	-5,83	0,01	-8,15	0,01
170-6A	-5,81	0,01	-7,85	0,01
170-6B	-5,07	0,01	-10,36	0,02
GOT-S2BB	-6,33	0,02	-9,44	0,01
GOT-S2BC	-6,11	0,01	-8,78	0,03
GOT-S3BA	-6,72	0,02	-8,47	0,02
NHU6-S10AC	-4,52	0,02	-7,19	0,03
NHU6-S10AA	-5,92	0,02	-8,67	0,02
MOLA-54CC	-2,04	0,01	-9,32	0,01
MOLA-53BA	-2,33	0,01	-9,59	0,02
NHU6-59AA	-5,76	0,01	-9,39	0,01

Table 1 Appenix II. Isotopic data.

Sample	d^{13}C	± (1 s)	d^{18}O	± (1 s)
NHU6-59BB	-5,70	0,01	-9,00	0,02
MOLA-54CB	-0,89	0,01	-5,26	0,02
170-5C	-6,17	0,01	-8,54	0,02
170-6C	-5,67	0,01	-9,06	0,01
MOLA-56CA	-3,02	0,02	-7,40	0,01
MOLA-56BC	-3,80	0,01	-9,33	0,01
GOT-53BB	-6,95	0,00	-9,68	0,01
GOT-5BBC	-7,08	0,01	-9,90	0,02
170-1A	-3,66	0,01	-12,19	0,01
170-1B	-3,53	0,01	-12,88	0,02
170-1C	-3,55	0,01	-12,03	0,01
VIP6DA	-2,91	0,02	-10,66	0,01
VIP6DB	-3,36	0,02	-10,48	0,02
VIP6DC	-3,34	0,02	-10,70	0,02
VIP7A	-4,61	0,01	-9,60	0,01
VIP7B	-4,90	0,01	-10,05	0,01
VIP7C	-4,94	0,01	-10,22	0,01
GOT-S2BA	-5,37	0,01	-10,00	0,02
VIP6CC	-2,68	0,01	-10,48	0,01
VIP6CB	-3,11	0,01	-9,59	0,01
VIP6CA	-3,03	0,01	-9,65	0,02
VIPP6BC	-2,81	0,01	-10,62	0,01
VIP6BB	-1,93	0,01	-9,37	0,02
VIP6BA	-2,39	0,01	-10,51	0,02
SU-P2 2B2C	-7,73	0,01	-10,89	0,01
SU-P2 2B2B	-7,59	0,01	-10,36	0,01
SU-P2 2BCC	-8,79	0,01	-10,29	0,01
SU-P2 2BCB	-8,44	0,01	-9,04	0,01
SU-P2 2BCA	-8,54	0,01	-10,46	0,01
NHU6-59AC	-6,76	0,01	-8,88	0,02
MOLA-56BA	-3,86	0,02	-9,00	0,02
SU-P2 2B2A	-7,61	0,02	-11,01	0,03
NP1-1A	-0,40	0,02	-4,68	0,01
NP1-1B	1,85	0,01	-11,32	0,01
NP1-1C	-0,24	0,01	-3,46	0,02
N0-10A	-5,06	0,01	-6,77	0,01
N0-10B	-5,22	0,01	-6,95	0,01
N0-10C	-5,25	0,01	-6,88	0,01
N0-11A	-5,26	0,01	-8,10	0,01
N0-11B	-5,28	0,01	-8,15	0,00
N0-11C	-5,13	0,02	-7,85	0,01
N0-12A	-5,00	0,01	-6,66	0,00
N0-12B	-5,00	0,01	-7,35	0,01
N0-12C	-5,04	0,01	-7,37	0,02
TRAV-1A	-5,16	0,01	-6,65	0,00
TRAV-1B	-4,96	0,01	-6,09	0,02
TRAV-1C	-5,62	0,01	-7,54	0,01
SAS-01A	-4,07	0,01	-7,10	0,01
SAS-01B	-5,07	0,01	-7,79	0,01
SAS-01C	-5,55	0,01	-7,30	0,02

Table 2 Appenix II. Isotopic data.

Appendix III

Sample	IC	Section	Unit
PAL-GU1	1,16	Pallarols	GU
PAL-LRU0	1,26	Pallarols	LRU
PAL-LRU1	1,26	Pallarols	LRU
PAL-LRU4	1,35	Pallarols	LRU
PAL-LRU5	0,61	Pallarols	LRU
PAL-URU1	1,15	Pallarols	URU
PAL-URU2	1,19	Pallarols	URU
PAL-URU3	0,99	Pallarols	URU
PAL-URU4	1,34	Pallarols	URU
PAL-URU5	0,88	Pallarols	URU
PAL-BUNT1	0,51	Pallarols	Bunt
PAL-BUNT2	0,62	Pallarols	Bunt
PAL-BUNT3	0,67	Pallarols	Bunt
NHBUN2	0,67	Castellar de N'Hug	Bunt
NHBUN1	0,74	Castellar de N'Hug	Bunt
NHURU5	0,66	Castellar de N'Hug	URU
NHURU4	0,77	Castellar de N'Hug	URU
NHURU3	0,77	Castellar de N'Hug	URU
NHURU1	0,51	Castellar de N'Hug	URU
NH18	0,89	Castellar de N'Hug	LRU
NH17	0,8	Castellar de N'Hug	LRU
NH16	0,62	Castellar de N'Hug	LRU
NH15	0,6	Castellar de N'Hug	LRU
NH14	0,67	Castellar de N'Hug	LRU
NH13	0,7	Castellar de N'Hug	LRU
NH12	0,71	Castellar de N'Hug	LRU
NH11	0,87	Castellar de N'Hug	LRU
NH10	0,77	Castellar de N'Hug	LRU
NH9	1,05	Castellar de N'Hug	TU
NH7	0,68	Castellar de N'Hug	TU
NH6	0,77	Castellar de N'Hug	TU
SAS1	1,23	Sas	GU
SAS2	0,92	Sas	TU
SAS3	1,24	Sas	TU

Table 1 Appendix III. IC index of the samples studied for the clay mineralogu

Sample	IC	Section	Unit
SAS4	0,75	Sas	TU
SAS5	0,83	Sas	TU
SAS8	0,6	Sas	LRU
SAS9	0,55	Sas	LRU
SAS10	0,63	Sas	LRU
SAS11	0,62	Sas	LRU
SAS12	0,66	Sas	LRU
SAS14	0,58	Sas	Bunt
SAS16	0,58	Sas	Bunt
SAS17	0,55	Sas	Bunt
SAS18	0,57	Sas	Bunt
SUILS2	0,64	Villarrué-Suils	Bunt
SUILS2P	0,56	Villarrué-Suils	Bunt
SUILS3	0,55	Villarrué-Suils	Bunt
SUILS4	0,56	Villarrué-Suils	Bunt
SUILS5	0,58	Villarrué-Suils	Bunt
SUILS7	0,55	Villarrué-Suils	Bunt
CAST12	1,08	Castellar	GU
CAST14	1,17	Castellar	GU
CAST15	1,29	Castellar	TU
CAST16	1,23	Castellar	TU
CAST17	0,98	Castellar	TU
CAST18	0,56	Castellar	TU
CAST19	0,55	Castellar	Bunt
CAST20	0,54	Castellar	Bunt
CAST21	0,43	Castellar	Bunt
CAST22	0,55	Castellar	Bunt
CAST23	0,49	Castellar	Bunt
CAST24	0,58	Castellar	Bunt
CAST25	0,59	Castellar	Bunt
CAST26	0,64	Castellar	Bunt
CAST27	0,6	Castellar	Bunt
VILARUE1	0,71	Villarrué-Suils	LRU
VILARUE2	0,62	Villarrué-Suils	LRU
VILARUE4	0,99	Villarrué-Suils	LRU

Table 2 Appendix III. IC index of the samples studied for the clay mineralogu

Unit	Sample	Quartz	Calcite	Hematite	Feldespates	Illite	Chlorite
BUNT	NHBUN2	24	0	3	3	57	13
BUNT	NHBUN1	31	0	5	2	51	12
URU	NHURU5	28	3	3	3	63	0
URU	NHURU4	34	9	5	3	50	0
URU	NHURU3	27	8	5	2	58	0
URU	NHURU2	33	6	4	6	51	0
URU	NHURU1	25	10	4	12	31	18
LRU	NHLRU1	52	0	3	0	45	0
LRU	NH18	33	0	4	4	5	53
LRU	NH17	33	0	4	4	6	52
LRU	NH16	44	7	3	9	24	12
LRU	NH15	44	6	3	5	29	12
TU	NH14	32	7	5	4	37	15
TU	NH13	13	11	5	5	54	12
TU	NH12	35	6	3	11	29	16
TU	NH11	24	2	6	5	53	10
TU	NH10	32	14	2	10	30	12
GU	NH9	24	0	5	7	57	8
GU	NH8	32	14	4	17	33	0
GU	NH7-8	35	5	5	12	43	0
GU	NH7	34	0	4	6	44	11
GU	NH6	27	0	4	4	65	0

Table 3 Appenix III. Clay mineralogy results of Castellar de N'Hug sector.

Unit	Sample	Quartz	Calcite	Hematite	Feldespates	Illite	Chlorite
GU	SAS1	28	0	0	1	53	18
GU	SAS2	36	0	0	3	46	15
GU	SAS3	18	0	0	0	82	0
TU	SAS4	16	16	0	5	51	11
TU	SAS5	30	0	5	3	57	5
TU	SAS6	20	57	0	0	23	0
TU	SAS8	12	0	5	3	75	5
TU	SAS9	43	6	2	10	27	12
LRU	SAS10	40	0	1	7	38	14
LRU	SAS11	28	0	5	3	58	6
LRU	SAS12	41	0	5	2	44	8
LRU	SAS14	24	7	4	4	44	16
LRU	SAS16	30	7	3	5	45	9
BUNT	SAS17	31	0	5	5	50	9
BUNT	SAS18	28	0	5	5	53	8

Table 4 Appenix III. Clay mineralogy results of Sas sector.

Unit	Sample	Quartz	Dolomite	Calcite	Hematite	Feldespates	Illite	Chlorite	Halloysite	Dickite
GU	CAST11	5	0	0	0	0	5	85	5	0
GU	CAST12	17	0	0	0	0	3	56	24	0
GU	CAST13	42	0	0	0	0	2	37	19	0
GU	CAST14	24	0	0	0	0	3	0	36	37
GU	CAST15	26	0	0	0	0	6	0	34	34
GU	CAST16	28	0	0	0	0	5	0	67	0
TU	CAST17	24	0	0	0	0	45	31	0	0
TU	CAST18	20	0	5	8	5	50	12	0	0
TU	CAST19	35	0	4	3	4	46	7	0	0
BUNT	CAST20	31	0	4	4	4	49	8	0	0
BUNT	CAST21	35	0	3	5	3	39	14	0	0
BUNT	CAST22	26	0	5	5	5	46	15	0	0
BUNT	CAST23	25	0	5	5	5	47	13	0	0
BUNT	CAST24	21	0	5	4	5	50	15	0	0
BUNT	CAST25	23	0	4	5	4	54	10	0	0
BUNT	CAST26	26	6	5	4	5	47	8	0	0
BUNT	CAST27	38	3	0	4	4	43	8	0	0

Table 5 Appenix III. Clay mineralogy results of Castellars sector.

Unit	Sample	Quartz	Calcite	Hematite	Feldespates	Illite	Chlorite	Halloysite
GU	PAL-GU1	42	0	0	3	2	23	30
GU	PAL-GU2	36	7	0	14	10	33	0
GU	PAL-GU3	41	0	0	9	2	25	23
GU	PAL-GU4	23	0	0	10	2	28	37
GU	PAL-GU5	40	0	0	6	4	0	49
LRU	PAL-LRU0	25	6	3	5	56	5	0
LRU	PAL-LRU1	22	10	4	4	46	14	0
LRU	PAL-LRU3	23	17	3	3	37	17	0
LRU	PAL-LRU4	23	18	3	3	45	8	0
LRU	PAL-LRU5	16	0	6	3	75	0	0
URU	PAL-URU1	22	2	4	6	55	11	0
URU	PAL-URU2	22	17	4	0	44	13	0
URU	PAL-URU3	30	5	5	6	46	9	0
URU	PAL-URU4	26	6	4	4	49	11	0
URU	PAL-URU5	16	0	6	3	75	0	0
BUNT	PAL-BUNT1	53	0	4	0	29	14	0
BUNT	PAL-BUNT2	48	0	4	4	36	8	0
BUNT	PAL-BUNT3	23	4	6	4	55	8	0

Table 6 Appenix III. Clay mineralogy results of Pallarols sector.

Unit	Sample	Quartz	Dolomite	Calcite	Hematite	Feldespates	Illite	Chlorite
BUNT	**SUILS2**	40	0	0	6	3	42	9
BUNT	**SUILS2P**	28	0	19	6	4	38	5
BUNT	**SUILS3**	45	0	5	7	5	32	7
BUNT	**SUILS4**	52	0	13	2	1	22	10
BUNT	**SUILS5**	19	26	0	5	3	42	5
BUNT	**SUILS6**	31	0	5	4	3	55	1
BUNT	**SUILS7**	20	0	16	0	3	53	7
BUNT	**SUILS8**	37	0	0	6	4	44	8
LRU	**VILARUE1**	20	0	20	3	5	40	12
LRU	**VILARUE2**	37	0	6	3	6	34	14
LRU	**VILARUE4**	34	0	8	3	1	47	7

Table 7 Appenix III. Clay mineralogy results of Suils-Villarrué sector.